# PDE based models of electric field sensors and their corresponding inverse problems




Timothy James Westwood

The Queen's College
University of Oxford

A thesis submitted for the degree of

*Doctor of Philosophy*

Trinity Term 2020

# Contents


Abstract iii

Acknowledgements v

Chapter 1. Introduction 1

1.1. Dielectric and conductive materials 8

1.2. Electric field sensing 13

1.3. Motivating applications 22

1.4. Thesis aims, limitations, and overview 25

Chapter 2. Modelling of electric field sensors 30

2.1. The sensor geometry and the sensing domain 31

2.2. Modelling of materials 33

2.3. Maxwell's equations 36

2.4. Modelling the sensor input and sensor measurements 48

2.5. Summary of the models 60

Chapter 3. Mathematical analysis of the models 67

3.1. Preliminaries 67

3.2. Frequency space models 75

3.3. Time dependent models 82

Chapter 4. Numerical solution and validation of the models 101

4.1. Preliminaries 101

4.2. Numerical solution in the frequency domain 108

4.3. Numerical solution in the time domain 118

4.4. Fitting of the model parameters 125

4.5. Comparison of the models to real data 137

Chapter 5. ECT as an inverse problem 140

5.1. The $\Lambda_\gamma$ and $N_\gamma$ operators 149

5.2. The finite dimensional DtN and NtD operators 156

5.3. Estimation of $\widetilde{\Lambda}_\gamma$ and $\widetilde{S}_\gamma$ from data 160

Chapter 6. Reconstruction algorithms 174

6.1. Parameter reconstruction in the full data case 177

6.2. Parameter reconstruction in the partial data case 193

Chapter 7. Conclusion and next steps 204

7.1. Next steps 205

Appendices 208

A. Code to define geometry and mesh 208

B. Code for the solution of Model 1 and Model 2 210

C. Code for the solution of Model 3 and Model 4 212

D. Code for the solution of Model 5 212

Bibliography 214

**Abstract**

This thesis is concerned with the forward and inverse problems associated with Electrical Capacitance Tomography (ECT) and Electrical Impedance Tomography (EIT). We collectively refer to these paradigms, and other associated modalities, as Electric Field Sensing (EFS). Common to all EFS modalities is the aim to determine the conductivity and permittivity of the material inside a volume from measurements of the electric potential and electric flux taken on the boundary of the volume. EFS modalities have many applications in industrial processes and medical diagnostics due mainly to the non-invasive, non-ionising, and non-destructive property of electric field measurements.

For each application the choice of electrode configuration and sensor input are critical: the shape of the generated electric field and the measurement sensitivity and material specificity are dependent on these choices. We are particularly motivated to study planar configurations of electrodes with time-dependent voltage impulses applied sequentially to different subsets of the electrodes.

We derive five PDE models that describe the electric field in either the frequency or the time domain. In particular, we propose a novel choice of boundary conditions, determined by a coupled ODE, to model additional circuit components and parasitic capacitances inherent in all EFS sensors. For each model, we prove existence and uniqueness results. We also discuss the numerical solution of each model using the Finite Element Method (FEM).

We then consider the inverse problems associated to each of the five models. We detail four, practically inspired, measurement paradigms and prove equivalence by explicitly constructing bijections between them. Our unified approach of combining sequential measurements can be applied to each of the five models. Most notably, we prove the equivalence between sequential measurements taken on two electrodes with measurements taken concurrently on all electrodes. We also discuss the partial data case where not all electrode pairs are sampled.

Finally, in the case of the partial data, we discuss novel methods for estimating the missing data using known measurements of a closely related parameter distribution: the benefit being reconstruction algorithms developed for the full data problem can then be applied to the partial data case.

**Acknowledgements**

The journey that led to the completion of the thesis has been, for want of a better description, tumultuous. Many times I have come close to giving up but I have always been encouraged to continue by one person or another. It is, therefore, fitting to thank my colleagues, family, and friends.

Firstly, I would like to thank Professor Yves Capdeboscq not only for the insights that began this project many moons ago, but also for the endless optimism that this thesis would be completed (eventually). I appreciate you sticking by me and correcting my many mistakes, mathematical and otherwise, with such humour. Secondly, I would like to thank Professor Colin Please who gently nudged me away from idealism and towards pragmatism. Without this push and all the helpful comments on the many previous drafts, I doubt this manuscript would have been finished.

I would also like to thank Professors Patrick Farrell, Chris Farmer, Endre Süli, Kathryn Gillow, and Andreas Münch whose feedback on early versions of this manuscript has led to improvements both to the quality of the mathematics and its presentation. Furthermore, I would like to thank Professor Endre Süli and Professor William Lionheart for agreeing to examine this thesis.

I must also thank my colleagues at Zedsen Ltd who have given me unfettered access to the technology that has been a source of inspiration for this work.

I have been lucky to have such a supportive family. All the mechanical construction toys and home science kits have not gone to waste: this variety of interests has certainly contributed to the multidisciplinary nature of this thesis. Thanks to you all.

I am also grateful to have such great friends. I have to thank Miles and Sarah for their support, particularly during the tough times; they have been there both day and night. Thanks must also go to Joe for allowing me cathartic opportunities to moan and groan over a pint (or two). I am indebted to Tom and Nat for their friendship and

for enabling my regular escapes to the Cornish coast when it all got a bit too much. I must thank Hannah for not only her encouragement and support over the past few months but also for the companionship that I have come to treasure so dearly.

And to everyone else I have befriended over my time in Oxford. There are too many to mention by name but I thank you all, all the same. My time in Oxford has been memorable and I will look back fondly on the time spent in this city amongst friends. Cheers.

CHAPTER 1

# Introduction

In this thesis we are interested in developing models that describe the electric fields generated by Electrical Capacitance Tomography (ECT) and Electrical Impedance Tomography (EIT) devices. There are many practical applications which has resulted in the simultaneous development of similar devices in different scientific and engineering disciplines under a multitude of different names: Electrical Capacitance Volume Tomography (ECVT), Electrical Impedance Spectroscopy (EIS), Electrical Resistive Tomography (ERT), Induced Polarisation Tomography (IPT) to name a few. As we shall see, considered through a mathematical lens these modalities are incredibly similar—the same mathematical equations and models can be used to describe the generated electric field in all cases. For the purposes of highlighting this generality, in this thesis we adopt the umbrella term of Electric Field Sensing (EFS) to describe such modalities.

We define an EFS device as a physical device consisting of an array of electrodes that is capable of generating an electric field that extends into a sensing volume whilst being able to take measurements of the current flux or voltage at distinct points in space. This is most often achieved by driving a current or voltage impulse on an electrode (or set of electrodes) and measuring the resulting charge, current, or voltage on another electrode (or set of electrodes). The electrodes can either be internal or external the object under test leading to both interior and exterior measurement configurations. In these thesis we will specialise to considering exterior measurements only. The shape and distribution of the electrodes—the electrode geometry—is designed to be application specific and many configurations have been developed. In order to preserve the generality, the specific shape and location of the electrodes is not prescribed, allowing for the models to be applicable to a wide range of devices.

The measurements taken by EFS are dependent on the electrode geometry, the sensor input, and the material in the sensing volume. Most commonly, EFS devices are used to determine the electrical conductivity and dielectric permittivity of materials in the sensing volume. Throughout this document the conductivity and permittivity at point $x$ at time $t$ will be denoted by $\sigma(t, x)$ and the permittivity by $\varepsilon(t, x)$ respectfully. We discuss models, written in terms of Partial Differential Equations (PDEs), that describe the sensor input, the response of the materials, and the sensor measurements in both the frequency and time domains. Given a set of electric field measurements and fixed electrode geometry, reconstruction algorithms can be used to determine the conductivity and permittivity of the materials exposed to the electric field. In other words, this thesis considers the forward and inverse problems associated with EFS.

PROBLEM (*Forward problem of EFS*). *Given $\varepsilon$ and $\sigma$, the permittivity and conductivity of the material in the sensing volume, describe the relationship between the sensor input and the sensor output.*

PROBLEM (*Inverse problem of EFS*). *Given the sensor inputs, outputs, and the relationship between them, determine the unknown material parameters $\varepsilon$ and $\sigma$ in the sensing volume.*

**1.0.1. Mathematical modelling.** A mathematical model is a representation of a real-world situation written using mathematics. The use of such models is not limited to the natural sciences and are widely used in economics, business, engineering, as well as the political and social sciences. The advantages of mathematical models are numerous: a model can be used to further understand and explain the behaviour of a system as well as to make predictions of the system in different states or at later times. On the other hand, the modelling process implicitly and explicitly makes many assumptions that may or may not be independently verifiable. As a result, there is a significant risk that the model used may be too simplistic and fail to describe the nuances of the physical phenomena, or unnecessarily complex and difficult to use. It is, therefore, good practice to be explicit with any assumptions being made and to remain cognisant that the model validity is dependent on these assumptions. In an

ideal situation each of the assumptions should be independently verified and tested, however, we accept that this is often not feasible or practical.

The development of accurate models can aid the development of electric field sensors by offering a test environment where the effect on the measurements due to hardware or operational changes can be determined. For example, a model can be used to investigate the impact of electrode shape and placement enabling the sensor design to be optimised. Additionally, many of the reconstruction algorithms developed for EFS applications rely on a particular model and consequently the accuracy of the reconstruction is limited by the accuracy of the model. It is hoped that the models presented in this thesis can be used to further optimise sensor design and refine reconstruction algorithms.

In this thesis, we choose to ignore thermodynamic, convective, or fluidic effects of the materials being considered. This simplification is made to reduce the model complexity of the generated electric fields. While in general the material properties are temperature-dependent, we assume that the environment under which the sensor operates is maintained at constant conditions. We also ignore the effect of ohmic heating in the electrodes and assume the devices are operating at low power. In most applications, and for most devices known to the author, these assumptions are valid.

Finally, we remark that the models discussed in this thesis are inherently deterministic. While this neglects to consider the true uncertainty present in all physical measurements, we believe that much can be achieved by developing a deterministic approach. However, this choice is not dichotomous: it is possible to combine a deterministic model with a probabilistic model of the measurement process and uncertainty. This bipartite approach likely possesses many advantages of both deterministic and probabilistic methods by being accurate, mathematically tractable, easily implemented in a computational environment, and empirically verifiable with real sensor data.

**1.0.2. Inverse problems.** Inverse problems are paramount to the scientific pursuit of knowledge. Many problems in science reduce to determining a priori unknown

causes from measurements of the effects. Taking this viewpoint, this thesis will consider the material parameters as the 'cause' and the distortion of the electric field, which is measured indirectly, as the 'effect'.

Formally, let $\mathcal{P}$ be the space of all admissible parameter distributions and $\mathcal{M}$ be the space of all admissible measurements. The forward problem of EFS is then a function

$$\mathcal{F} : \mathcal{P} \longrightarrow \mathcal{M}.$$

An example of such an operator $\mathcal{F}$, although tautological, is the sensor itself. In this generality the problem is intractable: little can be said in mathematical terms unless further information is known about the function $\mathcal{F}$, the parameter space $\mathcal{P}$, and the space of measurements $\mathcal{M}$. We introduce a mathematical structure by supposing the parameter space $\mathcal{P}$ and the measurement space $\mathcal{M}$ can be modelled by Hilbert spaces or, more generally, by Banach spaces. We denote the function spaces representing $\mathcal{P}$ and $\mathcal{M}$ by $P$ and $M$ respectively. The model of the forward problem is then an operator between function spaces:

$$F : P \longrightarrow M.$$

In this framework the forward and inverse problems are reduced to functional analysis. There is then a wealth of mathematical techniques that can be used to investigate properties of $F$. In particular, we are interested in the existence and resulting properties of the inverse operator

$$F^{-1} : M \longrightarrow P.$$

The ultimate goal is to choose an operator $F$ that is explicitly computable and accurate to the true forward problem $\mathcal{F}$. Furthermore, we require $F$ to be invertible with inverse operator $F^{-1}$ closely resembling the true—but unknown—operator $\mathcal{F}^{-1}$.

In most cases the forward problem is well-posed (in the sense of Hadamard) whereas the inverse problem is ill-posed (not well-posed). A problem is well-posed in the sense of Hadamard if for every $p \in P$ there is a unique $m \in M$ such that $F(p) = m$ where $m$ depends continuously on $p$ in a suitable topology [82]. Conventionyl, almost

all physical problems, and the mathematical models thereof, are well-posed. Inverse problems, on the other hand, are non-physical and fail to be well-posed. In terms of functional analysis, this can manifest when the forward operator is not an injective mapping from the parameter space $P$ into the measurement space $M$. In this situation, knowledge of the measurement is insufficient to determine the unknown parameter and the inverse problem is in need of regularisation. Many regularisation strategies are used by practitioners and most require restricting $F$ to a subset of the parameter space or imposing additional criteria to select a unique parameter from the set of possible parameters. Example criteria include choosing the parameter with the smallest $L^2$ norm, or with the parameter with the least total variation. The choice of regularisation strategy not only has a significant effect on the solvability of the inverse problem but also on the practical utility of the solution and is of critical importance and interest to practitioners.

This description of an inverse problem is purposefully abstract: mathematical inverse problems arise in many fields including statistics, computer science, and physics. We refer the reader to the extensive literature in the field for a deeper discussion [96, 103, 112, 170]. For the remainder of this thesis, we shall assume that all forward problems are operators acting between function spaces, and leave behind the more general abstract framework.

The mathematical study of inverse problems is centred around four themes: the identifiability of the parameters, the stability of the inverse problem, the development of numerical reconstruction algorithms, and the use of partial data [112]. The problem of identifiability, often referred to as the solvability of the inverse problem, is concerned with establishing the existence (or not) of a one-to-one correspondence between the elements of the parameter space $P$ and elements of the measurement space $M$.

Closely related to identifiability is the question of stability. Ideally, it is hoped that 'close' measurements, interpreted in a suitable sense, result from 'close' material parameters. We make the meaning of 'close' precise in Chapter 5. If similar measurements can result from dramatically different material parameters, then a *useful*

solution of the inverse problem is unlikely to be obtained in practice due to the resulting sensitivity to measurement noise. We remark that the stability and identifiability are independent concepts: an inverse problem can be solvable and yet unstable and vice versa.

Of direct practical importance is the development of numerical reconstruction algorithms to determine the unknown parameter(s) from measurements. The accuracy of such numerical algorithms, should they exist, is limited by the sensitivity of the measurements to changes in the parameter, the noise in the sensor measurements, and the choice of numerical methods used. Due to the ill-posedness of the inverse problem it is often necessary to regularise the problem. Therefore, the choice of regularisation scheme affects both the computational performance and accuracy of the reconstruction algorithm. The most common approach is to use a Tikhonov regularisation method [112], however, many other methods and approaches have been developed. A notable alternative is the so-called 'regularisation by discretisation' [112]. In this case, the chosen discretisation procedure has implicitly regularised the problem by restricting the space of possible parameters to functions that conform to this discretisation. We discuss numerical methods to solve the inverse problem relating to EFS in more detail in Chapter 6.

Finally, it is often the case in practice that only part of the information needed to solve the inverse problem is known—the so-called 'partial data' problem. This 'missing data' may be inherent to the measurement modality used or the particular application considered. For example, part of the domain may be inaccessible, the rate of data acquisition slower than the target phenomena, or simply that physical measurements are local averages and thus have limited spatial resolution. All three of these possibilities can occur in the case of EFS.

We discuss in more detail the inverse problem of EFS in Chapter 5 and Chapter 6. Before continuing, we discuss the so-called 'inverse crimes'.

**1.0.3. Inverse crimes.** The concept of an 'inverse crime', as defined by Colton and Kress [56], occurs when theoretical ingredients of the forward model are encoded

into the solution of the inverse problem, which results in the inverse problem becoming less ill-posed than it actually is. Consequently, overly optimistic convergence and accuracy results are likely to be reported [103]. Common inverse crimes relevant to EFS are the following [120]:

(1) the same discretisation used in the solution of the forward problem is used in the inversion of the problem;
(2) the same model used to produce the simulated data is used to invert the data;
(3) post-hoc tweaking of regularisation parameters.

Common approaches used to avoid committing such crimes include adding random noise (or error) to the simulated measurements (for example [30]), using different discretisations of the forward and inverse problems (for example [41]), or using entirely different physical models for the forward and inverse problems (for example [48]).

In this thesis we make an active effort to avoid committing these crimes. When testing numerical reconstruction algorithms, we ensure that the simulated data is measured on a significantly finer mesh to the one used in the reconstruction. Despite this, we acknowledge that the reconstructions of the simulated parameters will continue to be overly optimistic due to the unquantified model error. It is likely, despite our best efforts, that the simulated forward problem more closely resembles the inverse problem than the true, but unknown, forward problem. This is unavoidable, however, statistical inversion theory offers an alternative: significant progress has been made in the development of techniques to estimate both the model error and its effects on the reconstruction. See [38, 175] for a general introduction or [103, 189] for a specific application to electric field sensing. However, while methodical testing of the reconstruction algorithms on simulated data is important, this analysis is only a proxy for the use of real sensor data.

The true test of a reconstruction algorithm is the application to real-world data collected in the environment of the intended sensor application. Even laboratories, while convenient, are often unrealistic test environments: the data will be collected by experienced practitioners in controlled environmental conditions and measurements

can be repeated as many times as desired. In applications, these conditions are not practical or even feasible to replicate. However, the development of a robust testing procedure to verify the numerical reconstruction algorithms is beyond the scope of this thesis.

## 1.1. Dielectric and conductive materials

We briefly describe the material parameters that are of interest to this study, namely the dielectric permittivity and the electric conductivity of a material. The presentation here follows closely [116] and similar descriptions can be found in [98]. It is widely known that all materials are made of atoms, molecules and ions. The type, arrangement, and interaction between the particles in a material—the microscopic properties—determine the behaviour of the material in response to an external electric or magnetic field—the macroscopic properties. Broadly speaking, materials can be classified and distinguished by the response to external electric and magnetic fields. While it is conceivable that materials exist that do not follow this pattern, we remark that these materials are not commonly encountered. We suppose for simplicity that all materials discussed in this thesis are not magnetic and each material can be identified by a unique, possibly time or frequency dependent, permittivity and conductivity.

While we allow for complex conglomerations of materials in the sensing volume, we suppose that each material component is homogeneous. This is particularly relevant when considering solutes dissolved in liquids where we assume there is no concentration gradient or separation occuring due to differing densities. Finally, we assume that the objects in the sensing volume are in thermal equilibrium and neglect thermodynamic effects. We now briefly describe the microscopic origin of the dielectric permittivity and the conductivity. We postpone a discussion of the mathematical model for these materials until Chapter 2.2.

**1.1.1. Polarisation processes in dielectric materials.** Dielectric materials, also known as electrical insulators, or simply insulators, are poor conductors of electrical current and thus the effects of polarisation dominate the response to electric fields. The specific molecular mechanism that generates this polarisation depends on

the molecular and atomic structure of the material [98]. More precisely, dielectrics consisting of molecules with a permanent dipole, also called polar dielectrics, will behave differently to dielectrics whose constituent molecules do not have a permanent dipole, also called non-polar dielectrics. Furthermore, polar dielectrics in the liquid or gas phase will behave differently to solid dielectrics.

In non-polar dielectrics the predominant polarisation process is often called electronic polarisation. In this case, the external electric field distorts the electron cloud distribution of each atom or molecule, or electrical equilibrium of the bond joining atoms, in order to oppose the external electric field. This forms a dipole moment across the molecular or atomic unit. The combined effect of all the dipoles results in a non-uniform distribution of charge on the surface of the material and the material is said to be polarised. The dielectric permittivity of a material, denoted by $\varepsilon$, is a measure of how easily a material polarises, or equivalently, the amount of energy that can be stored in the material [154]. A diagrammatic representation of electronic polarisation is shown in Figure 1.1.1.

Alternatively, when exposed to an external electric field the molecules in polar dielectrics reorient (if they are able) so that the permanent molecular dipole opposes the electric field. This is particularly relevant when liquids or gases are being considered. The rate of this alignment is determined by the relaxation time and the permittivity is described by a Debye model [105], or one of the many variants [18], and is critical in biomedical applications of [76, 107, 172]. In the case when the polar molecules are not free to move, anisotropic polarisation will occur with permittivity being dependent on the direction of the electric field.

All materials become polarised when placed in an external electric field although the magnitude and direction of the polarisation is dependent on the type and arrangement of the constituent particles in the material. Dielectric materials, also known as electrical insulators, or simply insulators, are poor conductors of electricity and thus the effects of polarisation dominate the response to electric fields.

The permittivity of a material is dependent on the frequency of the applied electric field. This is due to the non-instantaneous response of a material to the electric

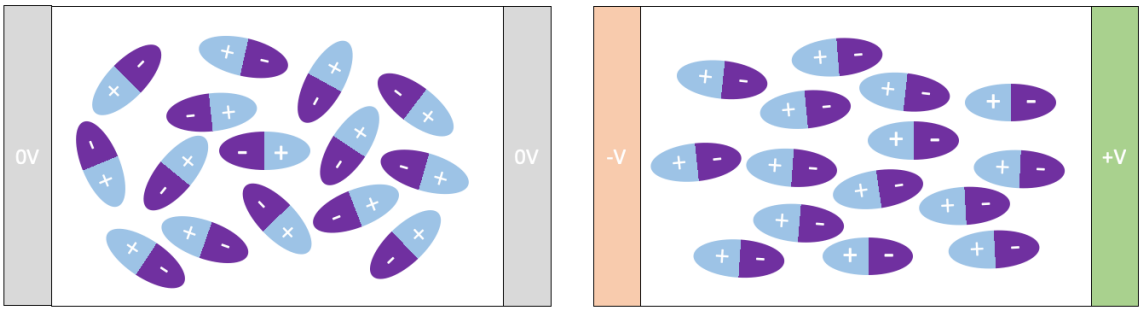



FIGURE 1.1.1. Diagrammatic representation of a dielectric material with a permanent dipole with no external field (left) and in an external field (right).

field—the dielectric relaxation [98]. In particular, as the frequency increases, there is insufficient time for the material to become polarised, and thus the permittivity of the material is reduced. This phenomenon is fundamental to spectroscopic modalities of electric field sensing: materials can be detected by applying electric fields with specific frequencies even in the presence of other confounding materials. The dielectric relaxation of a material, the observed lag in the response of a material to a varying electric field, is often modelled by the idealised Debye model or one of the many variants [18].

The dielectric permittivity of a material is often expressed relative to the permittivity of the vacuum, denoted $\varepsilon_0$. In this case, the permittivity is referred to as the relative permittivity. The permittivity of the vacuum is a physical constant, measured empirically to be $8.854 \times 10^{-12}$ $\mathrm{Fm}^{-1}$ (4 s.f.). By definition the relative permittivity is a real number greater than 1 and is a convenient quantity to compare materials: Table 1 shows the relative permittivity of some common materials. We shall assume in this thesis that all references to the permittivity unless otherwise stated, should be interpreted as the relative quantity.

Furthermore, the relative permittivity of a material is known to be frequency dependent. In particular, biological matter and tissues exhibit unusual frequency dependence of both the dielectric constant and the conductivity. Visually there are three distinct stages that occur at different frequency bands and are termed alpha, beta, and gamma dispersions [155].

| Material | Relative permittivity |
|---|---|
| PTFE (Teflon) | 2.1 |
| Polyamide | 2.8 |
| Marble | 8 |
| Ammonia (at 20°C) | 17 |
| Glycerol | 47 |
| Water (at 20°C) | 80 |
| Sulfuric acid (at 20°C) | 84 |

TABLE 1. Relative permittivity of common materials (unknown frequency) [178].

- Alpha dispersion occurs at low frequencies less than 1kHz. At these frequencies, the polarisation of the tissue interfaces dominates the measured signal [155].
- Beta dispersion occurs at radio frequencies between 1kHz and 100MHz range. The polarisation is associated with cellular membranes, proteins, and other organic molecules [73].
- Gamma dispersion occurs at microwave frequencies. In this high frequency regime, the polarisation of the material is closely associated with the polarisation of water molecules [60].

A typical relationship between the dielectric permittivity and frequency in the beta dispersion range can be seen in Figure 1.1.2. Three characteristic regions are denoted by I, II, and III on the diagram. During phase I the permittivity remains constant as frequency increases before entering a transient period in phase II, where the permittivity is highly frequency dependent. Phase III is characterised by another region of constant permittivity, however, at a lower value than observed in Phase I. Similar characteristic relationships are seen for alpha and gamma dispersion cases leading to the permittivity decreasing, as the frequency increases, in a step-like manner [155]. Characterising the dispersion relationships is a critical approach to identifying and analysing the dielectric properties of biological samples [76, 80, 143, 159].

**1.1.2. Conductive materials.** Conductive materials are characterised by the presence of freely moving charge carriers. The freedom enjoyed by these charged carriers determines the effectiveness of the material to conduct electrical charge. For

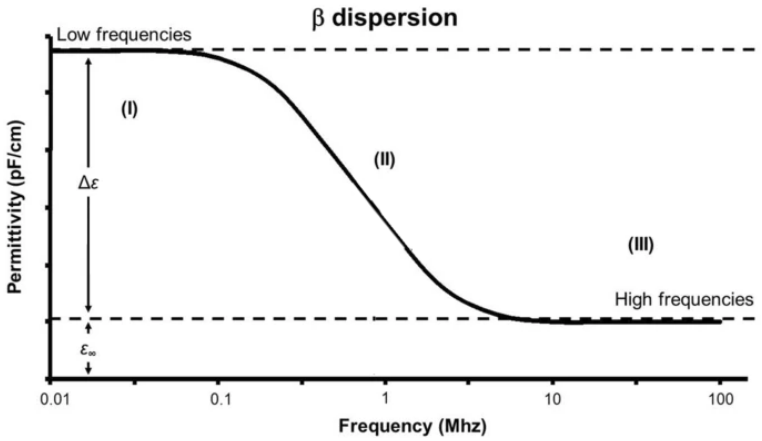



FIGURE 1.1.2. Schematic representation of the beta dispersion of a cell suspension where the characteristic three phases I, II, and III are marked. Reproduced by permission from [73].

example, metals have many delocalised electrons that are free to move through the material and so are good conductors of electrical current, see Figure 1.1.3. We consider a perfect conductor to be an idealised conductive material where the conduction of current is instantaneous. Although such a material does not physically exist, in highly conductive materials the conduction occurs at time-scales smaller than the sampling rate of EFS devices. Essentially, the conduction process appears instantaneous.

Materials where the current transfer is not instantaneous are called weak-conductors or semi-conductors. Whilst such materials do exist in the solid phase, they are more commonly encountered as ionic compounds in aqueous solution. For example, sodium chloride (NaCl) readily disassociates in water producing equal quantities of sodium ($Na^+$) and chloride ($Cl^-$) ions that act as charge carriers. The resulting solution is able to conduct electrical current due, in part, to the bulk ion transfer through the material. This is despite the opposing charge species existing in equal concentrations: the more massive chloride ion experiences a greater resistive force during transit through the solvent than the less massive sodium ion. A simplified graphical representation of this phenomenon is shown in Figure 1.1.3. Additionally, the clustering of solvent molecules around the ions and the partial ionisation of the solvent are also expected to play a significant role. The net compound effect can be represented as a macroscopic quantity known as the material's conductivity.

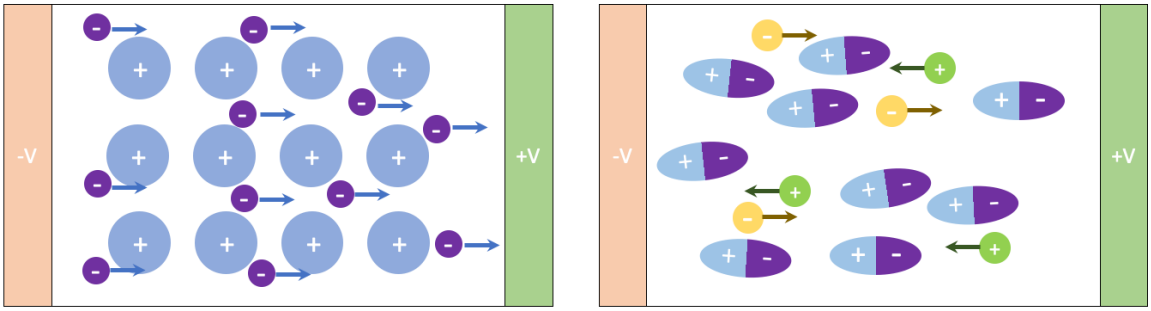



FIGURE 1.1.3. Diagrammatic representation of a metal (left) and ions in solvent (right).

Materials with a high conductivity value are good conductors (e.g. metals) and materials with a low conductivity are poor conductors (e.g. saline). The conductivity values for common materials are given in Table 2.

| Material | Electrical conductivity $\mathrm{Sm}^{-1}$ |
|---|---|
| Deionised water | $5.50 \times 10^{-6}$ |
| Saline | $4.50 - 5.50$ |
| Gold | $4.52 \times 10^{7}$ |
| Copper | $5.96 \times 10^{7}$ |
| Silver | $6.30 \times 10^{7}$ |

TABLE 2. Electrical conductivity of common materials. All values taken from [177].

We remark that the conductivity is highly dependent on the kinetic energy of the particles, or in other words, the temperature of the material. In this thesis, for simplicity, we shall assume that the materials are in thermal equilibrium and neglect the effect of temperature.

## 1.2. Electric field sensing

The principle of electric field sensing is to determine the material properties inside a region of space by measuring the distortion, caused by the object, of a generated electric field. The use of electric fields to interrogate and identify materials is not a new idea—Maxwell himself remarked that distinguishing materials was possible by measurements of the distorted electric field [132].

Many devices, intended for a wide range of applications, have been developed that seek to measure this distortion. As new devices are developed, distinct sub-modalities of electric field sensing arise: namely, Electrical Impedance Tomography (EIT), Electrical Capacitance Tomography (ECT), Electrical Capacitance Volume Tomography (ECVT), Electrical Resistivity Tomography (ERT), Induced Polarisation Tomography (IPT), and Electrical Impedance Spectroscopy (EIS). While each of these submodalities differ, they share many commonalities: each seeks to determine electrical properties of materials using measurements of a generated electric field external to the object [1, 29, 49].

In general, EFS has many advantages over other imaging and sensing modalities. In particular EFS devices are low-cost, portable, non-ionising, and non-destructive. EFS can also be described as a non-invasive imaging modality as all measurements are taken external to the object in the sensing volume. Furthermore, the fast rate of data acquisition possible makes them—in principle—ideal to image rapidly changing objects such as the flow of fluid for example. EFS devices can be operated in difficult to reach regions or environments with high-temperatures or pressures where many other modalities would fail.

There are of course limitations and challenges with these technologies [24]. Most fundamentally, is the so-called 'soft-field' nature of electric fields: electric fields rapidly decay and disperse away from the sources of charge. Furthermore, it is difficult to focus electric fields, unlike magnetic fields, and thus the resolution of electric field sensing is inherently lower than other imaging modalities that use magnetic fields. Ultimately, these affect sensor accuracy and performance.

To complicate matters further, the generated electric fields are affected by parasitic (stray) electric fields generated either from the sensor electronics or from other objects near the sensor [153]. To limit this effect, it is common to use grounded metal plates to shield both the sensing volume and the sensor electrodes from such extraneous electric fields [110]. Despite this intervention reducing the noise of the measurement signal, it is expected that the sensitivity of the signal to material changes in the sensing domain is also reduced. This is likely affect the resulting parameter reconstruction.

Despite these challenges, the potential benefits offered by EFS modalities continues to attract proponents and ensures that EFS continues to be a highly-active field of research.

**1.2.1. Description of electric field sensors.** Electric field sensors typically contain three parts: the sensor, the sensor electronics, and a measurement processing unit. The sensor subunit consists of a fixed number of highly conductive electrodes arranged in a fixed configuration that surrounds the volume of space where the material properties are to be determined. We refer to this region of space as the sensing volume. The sensor electronics are responsible for generating the sensor input whilst simultaneously measuring the charge, voltage, or received current on (or through) the electrodes. Finally, the sensor measurements are processed and interpreted in the measurement processing unit. Figure 1.2.1 shows this general configuration along with the typical flow of data and information.

The geometry of the sensor and the spatial arrangement of the electrodes is often designed with a particular application in mind. In many cases, the electrodes are mounted onto a fixed, rigid support surrounding the object in the sensing volume with the electrodes either in direct contact with the object or separated by a thin dielectric barrier material. The sensor input can be either a direct current (DC) or alternating current (AC) voltage signal applied between pairs of electrodes. The resulting charge density on the electrodes is typically measured forming a capacitance measurement. Alternatively, current can be injected into the domain, again in DC or AC form, via the electrodes, in which case the resulting potential difference between pairs of electrodes is measured forming an impedance measurement.

The shape of the generated electric field is dependent on the choice of electrodes. By driving different combinations of electrodes, the entire sensing volume can be scanned producing a set of measurements that depends on the spatial distribution of the material parameters in the domain. This dependence is known to be highly non-linear and the interpretation of the measurements is a non-trivial problem. Many reconstruction

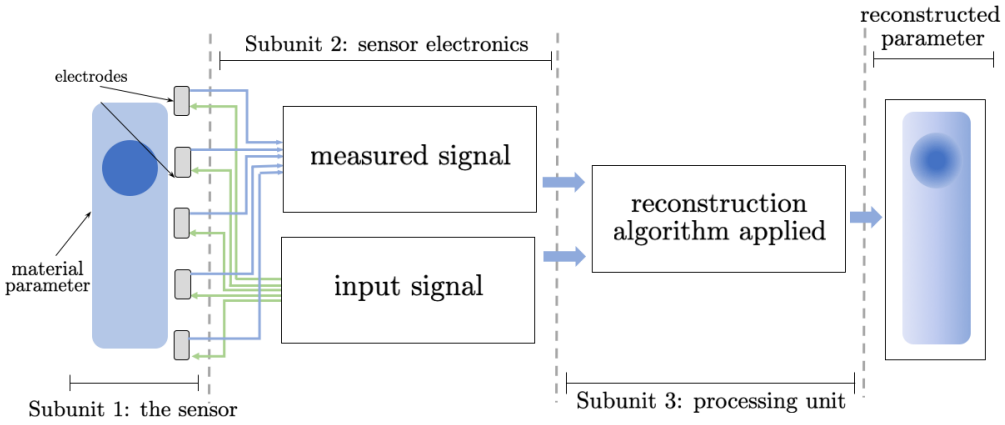



FIGURE 1.2.1. Diagrammatic representation of the subunits of a planar EFS device. The direction of the arrows indicates the flow of data between subunits.

algorithms have been proposed, developed, and tested with the aim to generate a spatial approximation of the material properties inside the sensing volume (see Chapter 6). The wide range of intended applications has resulted in a variety of sensor geometries and variants of this configuration being developed [40, 91, 122, 186, 200, 204].

**1.2.2. EIT, EIS, ERT, IPT, ECT, and ECVT.** Electrical impedance tomography (EIT) and electrical resistivity tomography (ERT) seek to determine the impedance or resistivity of a material [136, 190]. In these modalities, the electrodes are placed in direct contact with the object's surface and a DC signal is injected into the domain. The resulting potential difference between each pair of electrodes is measured in succession forming a complete set of EIT measurements. The principle of EIT has been discussed by many authors, see the review papers [1, 29, 49] for further information.

Electrical Impedance Spectroscopy (EIS) is identical to EIT except that an AC input is used often across a wide range of specifically chosen frequencies. The aim is to determine the frequency dependence of the materials in the sensing volume, which is particularly useful when the imaging domain contains a complex mixture of materials

as the electrical properties of each constituent material will respond differently to others at specific frequencies [155]. We refer the interested reader to the review papers [22, 80, 208] and the references therein.

A significant practical difficulty in using EIT and EIS arises from the imperfect contact between the electrodes and the object surface. It is widely accept by practitioners that such contact impedances cause distortion and introduce artifacts in the reconstructed parameter distribution particularly at low frequencies. This inherent difficulty led to the development of the Complete Electrode Model (CEM) for the electrodes [50, 161], however, the accurate estimation of the contact impedance parameters in this model is vital [114].

A similar modality, used in geophysical applications, is known as induced polarisation tomography (IPT) [28]. This approach injects current into the domain, and the subsequent voltage response is measured either in the frequency domain [209] or in the time domain [118]. From this the resistivity or the charge storage capability of the material in the domain can be determined [210].

Other EFS modalities rely on capacitative sensing principles. Examples include Electrical Capacitance Tomography (ECT), which seeks to estimate two-dimensional cross-sections of materials in the domain, and Electrical Capacitance Volume Tomography (ECVT) that images three dimensional objects. In contrast to EIT/EIS/ERT, the electrodes in ECT/ECVT are not placed in direct contact with the object boundary but separated by a small distance or by an electrically insulating material. This distance eliminates the problem of the parasitic contact impedances at the expense of not being able to inject current into the object directly. A DC or AC voltage source can be applied between a pair of electrodes and the resulting charge measured: the combination of the applied voltage and the resulting charge forms a complete capacitance measurement. This measurement process is repeated for each pair of electrodes forming a complete set of capacitance measurements which combined with a reconstruction algorithm can be used to infer the spatial permittivity in the domain.

EFS sensors are often described as tomographic whereby they measure two-dimensional slices of three-dimensional objects. The validity of this interpretation relies on the

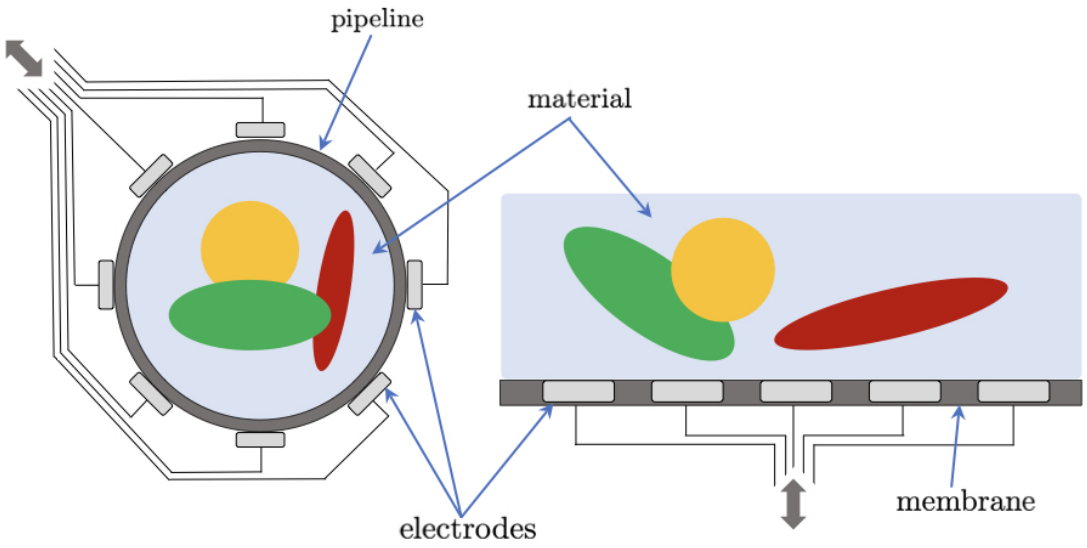



FIGURE 1.2.2. Diagrammatic representation of the two-dimensional cross section of a cylindrical ECT sensor (left) and planar ECT sensor (right). The material parameter distribution and the electrodes are indicated.

choice of sensor geometry and the electrode arrangement. Furthermore, the so-called fringing fields, caused by the finite length of the electrodes, must also be neglected [110]. Partly for this reason, most often EFS sensors are cylindrical or planar [8]—typical cylindrical and planar sensor are shown in Figure 1.2.2. In either case, the measurements on the electrodes correspond to an average of the electric field over the surface area of the electrode and thus EFS sensors are not sensitive to spatial variations in the electric field parallel to the electrodes or on scales smaller than the size of the electrodes. Therefore, it is correct to say that EFS modalities image a two-dimensional projection of the material properties onto the plane with normal vector in the plane of the electrodes, rather than a tomographic slice through the material.

**1.2.3. Hybridised ECT sensors.** A combined approach using different imaging modalities with complementary properties has also been proposed and studied. In particular, ECT sensors, suffering with limited spatial resolution, can be coupled with one that has a high spatial resolution [9, 115]. A common combination is to combine Ultrasound Transmission Tomography (UTT) with ECT. UTT seeks to estimate the

spatial the distribution of the acoustic impedance distribution inside the domain from which it is possible to infer, to high accuracy and precision, the phase boundaries between different materials. Given the material boundaries in the sensing volume, ECT sensors are then able to estimate the material parameters with greater accuracy. A UTT–ECT hybridised sensor has demonstrated improved material parameter estimation [165]. The difficulty being that the models describing both modalities and the measurements are non-trivial [4, 5, 115]. We do not discussed such hybridised modalities in this thesis but note that the models developed can be used in the modelling of hybridised sensors..

**1.2.4. Description of Zedsen's ECT sensor.** The work contained within this thesis has been motivated by an application to the ECT sensors being developed by Zedsen Ltd. However, our approach and results apply more generally to other EFS devices and modalities. We now give a high-level description of a Zedsen ECT sensor.

A Zedsen ECT sensor consists of two arrays of parallel electrodes encased in a thin, flexible dielectric membrane and arranged perpendicular to each otheras in Figure 1.2.3. The electrodes in both arrays are controlled by proprietary electronics that make use of multiplexors to rapidly generate and measure electric fields. The sensors are capable of high-resolution time series measurements of the generated electric field.

During a single measurement a pair of electrodes, which can be on either electrode array, are chosen: one of the electrodes acts as the 'transmitter' and the other as the 'receiver'. The transmitter is connected to a signal generator while the receiver is connected via a measurement circuit to ground. The remaining electrodes are connected to ground but by a sufficiently high resistor that, to a first approximation, they can be considered floating (not grounded).

When a voltage signal is applied to the transmitting electrode a time-dependent electric field is created that extends into the sensing volume. In order to oppose this electric field, the materials in the sensing volume become polarised and charge accumulates on the receiver. The potential difference between the receiver and ground is measured at pre-determined points in time, converted to a digital output, and

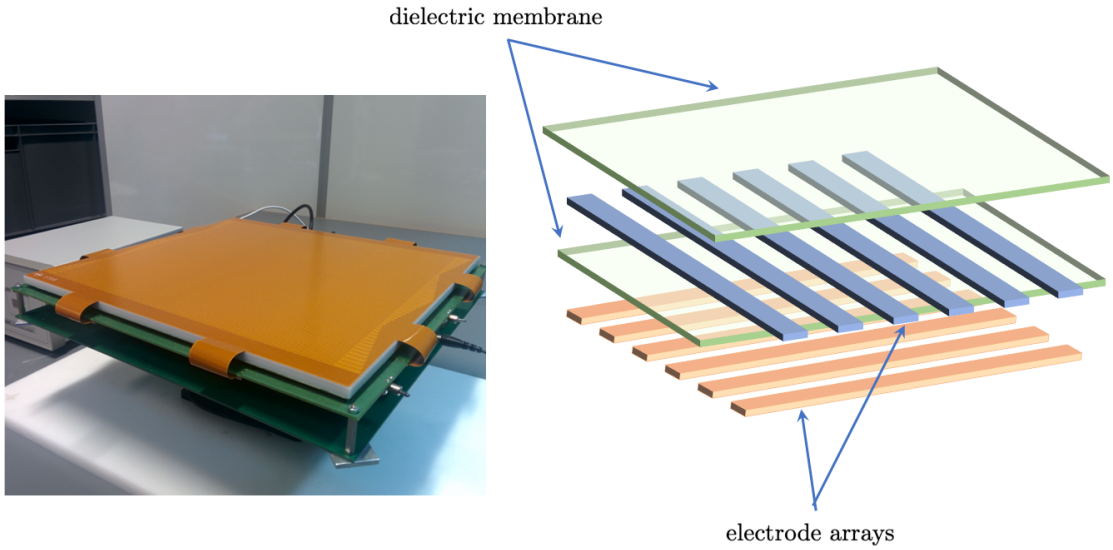



FIGURE 1.2.3. Photograph of a Zedsen sensor (left) and a diagram of the electrode configuration (right). Reproduced with permission.

recorded as a time series of integers. This process is then repeated sequentially for each pair of electrodes. This procedure is also described in [42].

As with other capacitance sensors, the measurements are dependent on the permittivity and conductivity of materials in the sensing volume. Additionally, since the receiver is connected to ground through a resistor, the rate of charge accumulation will be dependent on the resistance value. Furthermore, the additional capacitive load added to the circuit due to the presence of parasitic capacitances and from the multiplexors also needs to be considered. Building a framework to understand this complexity is one motivation for this work. Empirically,by comparing sensor measurements taken using the same sensor construction material properties in the sensing volume can be distinguished.

Due to the temperature, humidity, and pressure of the environment affecting capacitance measurements, it is useful to consider the difference between measurements with and without the object in the sensing volume. Since both of these measurements are taken sequentially using the same sensor electronics, it is thought that the numerical difference is sufficient to eliminate the measurement dependence on the sensor

electronics and the environment. We will make it clear where necessary when difference or absolute measurements are being used.

A novelty of Zedsen's sensors lies in the ability to apply a custom transmit pulse and measure the temporal evolution of the electric field as a high-resolution time series. The measurements can be taken both during and immediately after the transmit pulse. This is similar to the measurement techniques used in Induced Polarisation Tomography (IPT). Preliminary testing of Zedsen's device has demonstrated that the received signals are dependent on both the permittivity and conductivity of materials in the sensing volume, although the explicit relationships are yet to be determined.

Data collected by Zedsen sensors has been considered and evaluated by other authors with mixed results [42, 61, 150]. This could be due to the standard models for ECT not being directly applicable to these novel sensors and, in particular, the time series measurements. Indeed, the most promising study using Zedsen's data to date took the approach of considering static measurements and neglecting the time series data [42]. It is hoped that the time-dependent models discussed and developed in this thesis will enable the full set of time-series measurements to be used in parameter reconstruction.

A further difficulty of applying pre-existing models to Zedsen sensors is the behaviour of the electrodes, other than the transmitter and receiver pair, during a measurement scan. As far as the author is aware, other ECT devices connect the remaining electrodes directly to ground, whereas Zedsen sensors have the remaining electrodes non-grounded. While this paradigm has the benefit of larger measurement signals there is a cost: there is no immediate super-position principle for the measurements obtained in this way as mixed boundary are used. We account for this complexity by a suitable choice of boundary conditions in our model and a careful consideration of the inverse problem. This is the motivation for considering the *two electrode problem* in this thesis.

## 1.3. Motivating applications

The advantages of EFS have resulted in many devices being developed and applied to a wide range of applications. We motivate the work in this thesis by briefly mentioning applications of electric field sensors of the type discussed in this thesis. We consider the application to geophysics, industrial processes, and medical diagnostics.

**1.3.1. Geophysical applications.** Historically the first use of electric potential measurements was to determine the presence (or not) of oil deposits. This work was conducted by the Schlumberger brothers in the 1920's [164]. Since then numerous developments to both the hardware and reconstruction algorithms have occurred [63, 93, 123]. Now EFS are used for many other geophysical applications including the development of sensors to detect soil characteristics [27], estimate water content [34], detect and monitor archaelogical sites [43], and to detect landmines [52, 196].

**1.3.2. Industrial processes.** The high-speed data acquisition of ECT devices makes ECT an ideal technology for the imaging of fast-moving or changing materials common in many industrial processes. Example applications include the real-time monitoring of crude resource processing and the monitoring of fluid flow and separation in pipelines [3, 24]. In particular, ECT sensors have been used to monitor the solid deposits formed on the inner layer of pipelines [195]. The deposits increase the turbulence of the flow and restricts the pipeline volume, which results in more power being needed to maintain the flow-rate, ultimately increasing the production costs and constituting a safety hazard.

The use of PDE models and reconstruction algorithms have been used extensively in the development, testing, and deployment of ECT sensors to multiphase flows [3, 97, 100, 201, 204]. More recently, the use of neural networks to post-process the reconstructed tomographic images from pipelines has been considered and the results are promising [81, 197].

Other industrial applications include the imaging of a combustion chamber [187] and measuring concentration and distribution of solids in fluidized beds [122]. However, the wide-scale deployment of ECT sensors is yet to be reported and many ECT sensors remain in early stages of development.

**1.3.3. Medical diagnostics.** The most mature and widely used clinical application of EIT is the continuous monitoring of lung ventilation and perfusion [26, 74, 99]. Other, less developed, applications include the imaging of cardiac activity [95], and imaging of severe acute stroke [133]. An intriguing application is the use of EIT to distinguish ischaemic and hemorrhagic strokes in an emergency situation [66, 151].

The connection between the electrical properties of healthy and diseased tissues was first observed in 1926 [75] and replicated in many subsequent studies [67, 76, 172, 205]. In particular, the it has been established that the dielectric properties of brain tumours (glioma), breast carcinomas, and colon cancers differ significantly from healthy tissues in the frequency range of 500 MHz to 5 GHz [205]. The selection of the frequency is imperative to ensure the specificity of the sensing modality [155]. This has led to electric field sensors being developed and tested to measure these parameters non-invasively [139].

The physiology and composition of the biological tissue, the constituents of the extracellular fluid, and metabolic differences between healthy and diseased tissue are responsible for the observed differences in electrical properties [78, 155]. In particular, cancer cells have a higher water and sodium content than healthy cells. Since the water and sodium content of a cell changes the permittivity and conductivity of the local tissue [117], electric field measurements can distinguish between cancerous and healthy cells, therefore, EFS has the potential to screen for and/or diagnose cancers non-invasively [78].

The use of EIT sensors in the screening and detection of breast cancers has been considered [128, 143, 211]. The most promising EIT devices developed for this application is the TransScan TD2000 device described in [12, 134]. Clinical studies using this device in vivo have been reported in [124–126] and replicated independently in

[130, 192]. However, these studies were unable to demonstrate a sufficient sensitivity and specificity to be used as a screening device but did demonstrate the benefit of using EIT in combination with other imaging modalities. The TransScan TD2000 has been approved by the FDA as an adjunct modality to be used in combination with mammography [89]. Alternative EIT devices for breast cancer detection are discussed in [47, 86, 162, 206].

Developments have been made in order to develop EIT devices with greater sensitivity and specificity. Most notable is the use of multiple frequency inputs. In particular, the use of high frequency measurements has been shown to measure the impedance of breast phantoms to an accuracy of 99.7% [84]. However, the author is not aware of studies where these high-frequency devices have been used in vivo.

EIT has also been considered as an imaging modality of non-mammographically detectable breast cancers or identifying risk factors before tumours develop [166–168]. Combining EIT with thermography and the data analysed in conjunction is also showing promise [212].

While there has clearly been significant interest in EIT as an imaging, screening, and diagnostic modality, the technology is yet to make a significant contribution to patient care. This is, in part, due to the high levels of accuracy required being difficult to obtain due to the inherent non-specificity and low-resolution properties of electric fields. There is also evidence that confounding variables such as hormone levels can impact EIT measurements in vivo [142, 144]. It is hoped that improvements in the mathematical modelling of these devices, and the biological tissues being sensed, can overcome these difficulties.

The technology and applications of EIT are much more developed than those of ECT, However, ECT devices are being developed for medical applications [149]. We leave the discussion of potential applications here and progress to discussing the aims of the thesis.

## 1.4. Thesis aims, limitations, and overview

The narrative of this thesis naturally separates into two parts: the first part develops PDE models to describe the electric fields generated by EFS devices, while the second part discusses the associated inverse problem in both the full and partial data scenarios. Before elucidating further, we discuss the limitations of this thesis.

**1.4.1. Limitations of this thesis.** In this thesis, the sensor operation is simplified and abstracted in order to produce a tangible and useful model that describes the generated electric fields to a *reasonable* accuracy. However, there remain other electronic components and sensor features that are not accounted for in the model. The quantitative effect these components have on the the electric field remains unclear.

Most notable, is the existence of parasitic capacitances and resistances inherent in the electronic components themselves. While it is the author's belief that, at least in part, these systematic errors are incorporated into the parameters of the model during the calibration process, there is no guarantee this will be the case for the operation of the sensor in all environments and for all materials. For example, if the tolerances of the components are temperature dependent, then using the model in an environment where the temperature varies will likely result in poor model accuracy. It is, therefore, good practice to fit the model parameters to data collected in the environmental conditions expected for the intended application. We accept that this may not be feasible or even possible to achieve in all cases.

The models considered here are written in terms PDEs and thus familiarity with PDE analysis and the finite element method (FEM) is useful to understand the arguments in this thesis. However, we make every effort to make the presentation, and in particular the conclusions, as widely accessible as possible. Additionally, we provide the numerical code used in this thesis in the appendices.

It is worth noting that the implementation of the reconstruction algorithms developed by the author and used in this thesis, are not intended to be optimal in the sense of convergence or accuracy. We are primarily interested in establishing the feasibility of a reconstruction for a specific planar sensor geometry with few assumptions made

on the material parameters, rather than obtaining an optimal reconstruction in a specific setting. We expect that the accuracy of the reconstructions can be significantly improved by incorporating a priori information into the reconstruction algorithm.

Finally, we remark that for the reconstruction algorithms presented to be useful in practice they must be optimised to offer real-time reconstructions of the material parameters. While there is the potential for the sensor data to be processed on external computers, cloud computing systems, or supercomputers there is a commercial appetite for embedded algorithms to run on resource-light architectures. The difficulties and challenges of implementing reconstruction algorithms, most notably the numerical solution of PDEs, in a distributed computing environment or embedding algorithms into sensor firmware is a non-trivial problem that is beyond the scope of this thesis.

**1.4.2. Roadmap of the thesis.** The disparate and multi-disciplinary nature of EFS is unavoidably reflected in this thesis: each chapter has a different emphasis and uses techniques and language from a variety fields and perspectives. In each chapter, every effort is made to explain concepts, introduce terminology, and review relevant literature where necessary. Consequently, each chapter can more or less be read and understood independently. In the first few chapters of this thesis, reference to Sobolev function spaces is made for completeness. However, a detailed understanding of these is not necessary for following the modelling process. All of the function spaces used are defined rigorously at the start of Chapter 3 before the models are analysed mathematically. We now describe the structure of the thesis.

In Chapter 2, we derive and describe five boundary-valued PDE models for EFS sensors. The derivation of the models requires the quasi-static form of Maxwell's equations. We discuss this form of the equations and offer a novel justification of the quasi-static assumption in terms of energy estimates. We describe models in both the frequency domain (Model 1 and Model 2) and the time domain (Model 3, Model 4, and Model 5).

We pay particular attention to the choice of boundary conditions for each model. In particular, Model 1 and Model 3 suppose that the electrode can be described by local

boundary conditions. While convenient mathematically, this model of the electrodes is not physically realistic. In contrast, Model 2 and Model 4 impose additional constraints on the boundary conditions to ensure the electrodes are modelled as perfect conductors. Model 5 couples the PDE describing the electric field inside the sensing volume with an ODE that models the charging of a simple measurement circuit in the time domain.

We provide a mathematical analysis of each model in Chapter 3. In each case, we establish the existence and uniqueness of a solution and, where appropriate, we discuss the regularity of the solution. In addition, we establish a decay estimate for Model 3, Model 4, and as a corollary, for Model 5.

The analysis of the forward problem concludes with Chapter 4. In this chapter, we detail the numerical solution of models 1-5 using the Finite Element Method (FEM). We demonstrate and discuss accuracy and convergence properties of the solvers. In the case of Model 5, we describe and implement a procedure to estimate the model hyper-parameters using empirical sensor data. We compare the simulated data to data supplied by Zedsen Ltd.

Chapter 5 considers the inverse problem associated to each of the forward models. After expressing the inverse problemin terms of the Dirichlet-to-Neumann (or Neumann-to-Dirichlet) operator the connection to the classical Calderón problem is explained. We summarise the literature on the Calderón problem that has implications on the inverse problems considered here. We end this chapter with a definition and discussion of the specific two electrode problem considered in this thesis.

In Chapter 6, we discuss numerical reconstruction algorithms that can be used to solve the inverse problems. We consider solving the inverse problem by linearisation as well as by a non-linear, PDE-constrained minimisation approach. Both of these algorithms are described, implemented, and tested using simulated data. We then consider the partial data problem deduced from the two electrode problem and develop and test constructive algorithms to estimate the missing data.

We summarise the conclusions of this work in Chapter 7 and discuss avenues for future developments.

**1.4.3. Summary of the main results.** We summarise the main results developed in this thesis and their locations within the document.

(1) We justify the use of the quasi-static assumption in a novel way by estimating the energy in the magnetic field in terms of the energy in the electric field (Chapter 2).
(2) We establish a novel time-dependent PDE model for the electric fields generated by an ECT device with boundary conditions described by an ODE. (Chapter 2)
(3) We rigorously prove existence to the time dependent problem. We extend this result to establish existence and uniqueness results in the case when the boundary conditions are determined by an ODE using a fixed point argument. (Chapter 3)
(4) We describe a procedure to estimate the model parameters from real sensor data and test the validity of the model with real data collected from a planar sensor. (Chapter 4)
(5) We describe multiple procedures to estimate the missing data in the partial data two electrode problem. The accuracy of each approach is estimated numerically. (Chapter 5)

These results have been compiled into the following papers:

- The analysis of the time dependent model is presented in:
  - Y. Capdeboscq and T. Westwood. The existence and uniqueness of a time dependent PDE with time dependent parameters. In preparation.
- The statement of the time dependent model and the experimental verification is included in:
  - Y. Capdeboscq, C. Please, and T. Westwood. A coupled PDE-ODE model for Electrical Capacitance Tomography in the time domain. In preparation.
- The results and algorithms to solve the two electrode problem are discussed in:

– Y. Capdeboscq and T. Westwood. On a Electrical Capacitance Tomography using Two Electrode Measurements. In preparation.

CHAPTER 2

# Modelling of electric field sensors

In this chapter we present five models that seek to describe the electric fields generated by EFS devices. We shall denote the relationship between the sensor input and output, assuming a known material distribution,, by $\mathcal{S}^i$ for $i = 1, \ldots, 5$—the index corresponding to the model number.

We make the choice, as do many practitioners, to model the electric field generated by the sensor as the unique solution to a Partial Differential Equation (PDE). PDE models of electric fields have many advantages: they provide a description of the complex shape of the electric fields; are numerically solvable using the Finite Element Method (FEM); and, are amenable to mathematical analysis.

We choose as the domain of the PDE an open, bounded volume of $\mathbb{R}^3$ that encloses the sensing volume, the region of interest (ROI) and the electrodes. The electrodes will be modelled as segments of the boundary and, in this framework, the sensor input, the current or voltage impulse on the transmitter electrode, corresponds to a particular choice of boundary conditions for the PDE. As one would expect, the choice of boundary conditions is crucial to the accuracy and well-posedness of the resulting model. For the models developed in this chapter, we discuss the motivation and rationale behind each choice of boundary condition. We postpone the discussion of well-posedness of the models until Chapter 3 where the models are analysed mathematically.

Alternative approaches to model electric fields have been explored in the literature: including using ODE based circuit models [72], statistical models [140, 188, 189, 198], and Neural Networks [59]. While these alternative approaches have been used to some success, it has been demonstrated that significant improvements can be achieved by combining different approaches. For example, a statistical model requiring the computation of likelihood ratios often involves the solution of PDEs [140]. Alternatively, statistical methods can be used to describe the error distribution of a PDE model

[189]. Furthermore, neural networks can be used to model the material parameters in a PDE model [152]. We do not explore such combined approaches in this thesis but advocate their use to both researchers and practitioners.

There are five aspects of an electric field sensor that we need to consider; the sensor geometry, the materials in the sensing volume, the generated electric field, the sensor input, and the sensor measurement. We address each of these in turn before concluding with a summary of the five models that will be discussed in this thesis.

## 2.1. The sensor geometry and the sensing domain

Maxwell's equations of electromagnetism describe the behaviour of the electric and magnetic fields in $\mathbb{R}^3$. However, since electric and magnetic fields are known to decay away from the source of charge, we choose to model the electric fields generated by an ECT sensor in a bounded domain. Let $\Omega_B \subset \mathbb{R}^3$ be an open-bounded, simply connected domain with smooth boundary $\partial\Omega_B$. Defined in this way, $\mathbb{R}^3$ is partitioned into a bounded component, $\Omega_B$, and an unbounded component, $\Omega_B^c$. We shall suppose that $\Omega_B$ is sufficiently large so that the electric field generated by the sensor are negligible in $\Omega_B^c$. Similarly, we suppose that there are no sources of charge in $\Omega_B^c$ that interact with the electric fields in $\Omega$. More concisely, we make the following assumption:

Assumption 1. *There are no sources of charge external to $\Omega_B$.*

We suppose that the sensor has $N \in \mathbb{N}$ (metallic) electrodes that are perfect conductors with sufficiently smooth boundaries. While this is an idealised case, we expect that this can be achieved during the manufacturing process of the electrodes.

Assumption 2. *All electrodes are perfect conductors with smooth boundaries.*

We model the electrodes as disjoint connected volumes, denoted $E_1, \ldots, E_N \subset \Omega_B$, such that for each $i = 1, \ldots, N$ the boundary $\partial E_i$ is a hyper-surface that maps to $S^{d-1}$ by a $C^1$ diffeomorphism. Furthermore, we shall assume that for some $\delta_1 > 0$ the volumes $E_1, \ldots, E_N$ are separated by at least $\delta_1$: for any $i, j = 1, \ldots, N$ with $i \neq j$,

we assume

$$\inf_{x\in E_i, y\in E_j} |x-y|_{\mathbb{R}^3} > \delta_1 > 0.$$

It is often convenient to assume the electrodes are identical in size and shape, however, this is not necessary in our model framework. We denote the surface area of electrode $E_i$ by $|\partial E_i|$ for $i = 1, \ldots, N$. Furthermore, by assuming that the electrodes are perfect conductors we enforce that the electric field inside $E_i$ is spatially uniform. Therefore, it is sufficient to consider only the electric field external to the electrodes—the potential in the interior is determined by the potential on the electrode's surface. Wedefine $\Omega \subset \Omega_B$ to be the space exterior to the electrodes

$$\Omega := \Omega_B \setminus \bigcup_{k=1}^{N} E_k,$$

which decomposes the boundary of $\Omega$ into the disjoint union

$$\partial\Omega = \partial\Omega_B \cup \bigcup_{k=1}^{N} \partial E_k.$$

We shall often refer to $\partial\Omega_B$ as the boundary of the computational domain, or simply as the computational boundary.

Henceforth, we will consider the electric field in the domain $\Omega$ where the sensor input, applied to the electrodes, will be modelled as boundary conditions on $\bigcup_{k=1}^{N} \partial E_k$. Furthermore, we denote the region of interest (ROI) by a smooth open, simply-connected subset of the interior of $\Omega$, denoted by $\Omega'$, such that for some $\delta_2 > 0$,

$$\inf_{x\in\Omega'} \operatorname{dist}(x, \partial\Omega) > \delta_2 > 0.$$

This condition ensures that $\Omega'$ is separated away from the electrode boundaries and corresponds physically to the volume where the object being sensed will be placed. Example domains are illustrated in Figure 2.1.1.

**2.1.1. A 2D model.** For particular sensor geometries, modelling the electric field in the three dimensional domain $\Omega$ can be reduced to considering only the two dimensional cross-section of the domain. If the sensor geometry is such that the generated

field will be uniform in one direction, for example a sufficiently long cylindrical sensor, then the electric field is approximately constant along the axis parallel to the electrodes. As a result, the spatial variation of the electric field can be described as a function of two coordinates and, if required, extended to three dimensions trivially.

However, if the ratio of the electrode length to the sensor width (or diameter) is close to one, the electric fields will not be well approximated by an electric field that is constant in the direction parallel to the electrodes. The electric field around the ends of the electrodes, often called the fringing effect, is not negligible and cannot be ignored.

For the most part, we specialise to such cases: let $\Omega \subset \mathbb{R}^2$ be an open-bounded connected set and the electrodes be disjoint regions $E_1, \ldots, E_N \subset \Omega$ enclosed by planar curves $\partial E_k$ for $k = 1, \ldots, N$. We remark that the domain $\Omega$ remains connected but is not simply connected as it was in the $\mathbb{R}^3$. Two example sensor geometries that motivate this thesis can be seen in Figure 2.1.1.

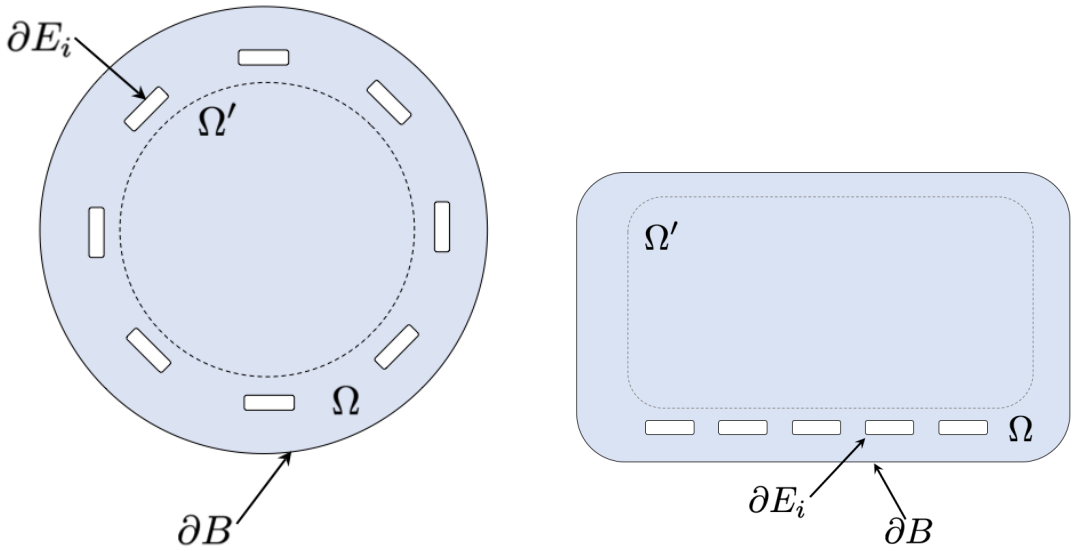
The main benefit of considering the two dimensional domain is computational: the numerical solution of the three dimensional electric field, although computationally possible, is a much larger numerical problem. In contrast, the two dimensional electric field is a more convenient problem for prototyping the analysis and reconstruction algorithms.

## 2.2. Modelling of materials

In this thesis we model the dielectric permittivity and conductivity of materials as bounded functions in $L^\infty(\Omega)$ mapping into $\mathbb{R}_+$. For this to be applicable, we make the assumption:

ASSUMPTION 3. *All materials in $\Omega$ are isotropic and piecewise homogeneous.*

Additionally, we assume that all materials are non-magnetic (the magnetic permeability being equal to the vaccuum $\mu = \mu_0$) and are in thermal equilibrium with both the environment and the sensor.




(A) A cross section of a cylindrical sensor. (B) A cross section of a planar sensor.

FIGURE 2.1.1. Examples of two dimensional sensor geometries considered in this work. In each case the domain $\Omega$, the ROI $\Omega'$, the electrodes $\partial E_i$, and the computational boundary $\partial\Omega_B$ are indicated.

In the simplest case, we suppose that the conductivity and permittivity of the material are independent of the applied frequency. This situation also occurs more generally when an EFS device is operated at a single frequency and thus only the permittivity and conductivity of a material at that frequency can be measured.

More generally, the permittivity and conductivity of a material, particularly of biological tissues, are known to depend on frequency [19]. For broadband sensors all materials exhibit some form of frequency dependence that needs to be considered. Furthermore, for practical applications involving mixtures of materials, understanding the frequency dependence of the permittivity and conductivity has been long known to be critical for biological applications [155]. The development of EFS devices that operate in the time domain is a more recent consideration and in this thesis we include a special focus on this case [19, 57].

In the single frequency case, we shall model the conductivity of the material by a positive scalar function, $\sigma \in L^\infty(\Omega; \mathbb{R}^+)$ supported in $\Omega'$. The set of all admissible

conductivity distributions is given by

$$\mathcal{A}_{\mathrm{c}} := \{\sigma \in L^{\infty}(\Omega) : \sigma(x) \geq 0 \text{ for a.e. } x \in \Omega' \text{ and } \sigma(x) = 0 \text{ for a.e. } x \in \Omega \setminus \Omega'\}. \tag{2.2.1}$$

Let $\varepsilon_0 > 0$ be a fixed constant. The set of all permittivity distributions in $\Omega$ is given by

$$\mathcal{A}_{\mathrm{p}} := \{\varepsilon \in L^{\infty}(\Omega) : \varepsilon(x) \geq \varepsilon_0 > 0 \text{ for a.e. } x \in \Omega \text{ and } \nabla\varepsilon = 0 \text{ in } \Omega \setminus \Omega'\}. \tag{2.2.2}$$

We highlight that, unlike the conductivity, the support of each permittivity is the whole of $\Omega$ although we suppose that near the boundary, we assume the permittivity is constant.

In the multi-frequency situation, the permittivity and conductivity can be modelled by functions in $\varepsilon \in C^1(\mathbb{R}_+; \mathcal{A}_{\mathrm{p}}) \cap L^{\infty}(\mathbb{R}; \mathcal{A}_{\mathrm{p}})$ and $\sigma \in C^1(\mathbb{R}_+; \mathcal{A}_{\mathrm{c}}) \cap L^{\infty}(\mathbb{R}; \mathcal{A}_{\mathrm{p}})$ respectively. We do not assert that this regularity is optimal in a mathematical sense, however, this is general enough to include physically relevant dispersion relations such as those described in Chapter 1.1.1.

In the time domain, we suppose that $\varepsilon \in C^1(\mathbb{R}; \mathcal{A}_{\mathrm{p}})$ and $\sigma \in C^1(\mathbb{R}; \mathcal{A}_{\mathrm{c}})$ with the additional constraint that the permittivity and conductivity cannot grow indefinitely in time. We define the space for some $T_0 > 0$

$$\mathcal{A}_{\mathrm{TD}} := \left\{(\varepsilon, \sigma) : \sigma \in C^1(\mathbb{R}; \mathcal{A}_{\mathrm{c}}) \text{ and } \varepsilon \in C^1(\mathbb{R}; \mathcal{A}_{\mathrm{p}}) \text{ s.t. } (\partial_t \varepsilon) = (\partial_t \sigma) = 0 \text{ for } t \geq T_0\right\}. \tag{2.2.3}$$

When we consider the electric field in the frequency domain, we shall introduce the so-called complex permittivity: define

$$\mathcal{A}_{\mathrm{FD}} := \left\{\widehat{\varepsilon} - \mathrm{i}\,\omega^{-1}\widehat{\sigma} : (\varepsilon, \sigma) \in \mathcal{A}_{\mathrm{TD}}\right\} \tag{2.2.4}$$

where $\widehat{\cdot}$ denotes the Fourier transform.

The definitions of permittivity and conductivity can be extended to the case of anisotropic materials where material response depends on the direction of the applied

electric field. To illustrate this we consider the case of a single frequency. Mathematically, an anisotropic permittivity would be represented by a tensor $\varepsilon \in L^\infty(\Omega; \mathbb{R}^{3\times 3})$ such that for some $c > 0$

$$c^{-1} \|v\|^2 \leq v \cdot \varepsilon v \leq c \|v\|^2$$

holds for all $v \in \mathbb{R}^3$ and a.e. $x \in \Omega$. Similarly, an anisotropic conductivity would be modelled as a tensor $\sigma \in L^\infty(\Omega; \mathbb{R}^{3\times 3})$ such that for some $c > 0$

$$0 \leq v \cdot \sigma v \leq c \|v\|^2$$

for all $v \in \mathbb{R}^3$ and a.e. $x \in \Omega$. Finally, we remark that for the models presented to be used for EIT or ERT, the conductivity distribution $\sigma$ must be contained within $\mathcal{A}_\mathrm{p}$ and not $\mathcal{A}_\mathrm{c}$ to ensure the PDE is well posed.

## 2.3. Maxwell's equations

Maxwell's equations [132] are a system of coupled PDEs that describe the time evolution of the electric field $E$, the magnetic field $H$, the electric displacement field $D$, and the magnetic displacement field $B$ given sources of electrical charge $\rho$ and current $J$. Maxwell's system of equations can be stated on the infinite domain $\mathbb{R}^3$ or on a connected, open and bounded domain $\Omega \subset \mathbb{R}^3$. For the system to be well posed on an infinite domain, decay at infinity conditions are required, whereas on a bounded domain, boundary conditions suffice. We consider exclusively the case of a bounded domain and consider $E, H, D, B, \rho$, and $J$ as functions mapping $\mathbb{R}^+ \times \Omega$ into $\mathbb{R}$.

More precisely, let $\Omega \subset \mathbb{R}^3$ be an open, bounded, and simply-connected domain with smooth boundary $\partial\Omega$. The macroscopic form of Maxwell equations in a domain are

$$\begin{cases} -\operatorname{div}(D) = \rho \\ -\operatorname{div}(B) = 0 \\ \nabla \times E = -\partial_t B \\ \nabla \times H = \partial_t D + J \end{cases} \quad \text{in } \Omega \times \mathbb{R}^+ \tag{2.3.1}$$

subject to the boundary conditions

$$D \cdot \hat{n} = 0 \text{ and } H \cdot \hat{n} = 0 \text{ on } \mathbb{R}^+ \times \partial\Omega, \tag{2.3.2}$$

and initial conditions

$$E(0, x) = E_0 \text{ and } H(0, x) = H_0 \text{ in } \Omega. \tag{2.3.3}$$

We also suppose that $\rho$ and $J$ are compactly supported in time: there exists a $T^* > 0$ such that

$$\rho(t, \cdot) = J(t, \cdot) = 0 \text{ for all } t > T^*.$$

The first equation in (2.3.1) is often referred to as Gauss' law, the second as Gauss' Law of Magnetism, the third as Faraday's law of induction, and the final equation as Ampère's law [98]. We remark the boundary condition (2.3.2) is not the only choice: equation (2.3.2) can be replaced with

$$E \times \hat{\nu} = 0 \text{ and } B \cdot \hat{n} = 0 \text{ on } \mathbb{R}^+ \times \partial\Omega. \tag{2.3.4}$$

The choice of boundary condition (2.3.4) is often referred to as a *perfectly conducting* boundary condition whereas (2.3.2) is an *insulating* condition.

In this work we consider the situation when the $D$ and $B$ fields are determined by the $E$ and $H$ fields. This functional relationship is called a constituent law and can be chosen to reflect physical characteristics of the materials in the sensing domain.

**2.3.1. Constituent laws.** We begin by discussing constituent laws governing the relationship between the $E$ and $D$ fields, and between the $B$ and $H$ fields. We denote the dielectric permittivity and magnetic permeability of the vacuum by $\varepsilon_0$ and by $\mu_0$ respectively. We suppose that the pair $(D, B)$ are dependent on $(E, H)$ at time $t \in \mathbb{R}^+$ but not directly on the past $0 \leq t^* < t$. Equivalently, we suppose that the material response is instantaneous to the change in the electric and/or magnetic field. Formally,

we adopt constituent laws of the form

$$\begin{cases} D(t,x) = \varepsilon_0 E(t,x) + P(t,x) \\ B(t,x) = \mu_0 H(t,x) + M(t,x) \end{cases} \tag{2.3.5}$$

for all $t \in \mathbb{R}^+$ where $P$ is the polarisation field and $M$ is the magnetisation field [36, 163]. Alternative forms of the constituent laws have been considered by other authors. For example, the case when the $D$ field depends directly on the past has also been considered in [14, 18, 19].

2.3.1.1. *Linear dielectric materials.* We now describe a form of the polarisation and the magnetisation fields $P$ and $M$ respectively for linear dielectric materials. If we assume that the material has a linear response proportional to the dielectric permittivity and magnetic permeability [65], we can write (2.3.5) as

$$\begin{cases} D(t,x) = \varepsilon E(t,x) \\ B(t,x) = \mu H(t,x). \end{cases} \tag{2.3.6}$$

It is often convenient to consider the relative permittivity, denoted $\varepsilon_r$, and relative permeability, denoted $\mu_r$, relative to the vacuum [98] with

$$\varepsilon = \varepsilon_0 \varepsilon_r \text{ and } \mu = \mu_0 \mu_r.$$

Throughout the thesis we shall refer to the relative permittivity and the permittivity synonymously.

2.3.1.2. *Dynamic material response.* More generally, the polarisation term $P(t,x)$ is not constant in time and the material has a dynamic response to the electric field $E$. In this case, we suppose that the polarisation term $P(t,x)$ evolves according to an evolution equation, see for example [10]. A widely known example is the Debye model for dipole relaxation.

We suppose that there are two polarisation mechanisms occurring in a material. The first occurs instantaneously, which we denote by $P_e$, and the other, denoted by $P_\mu$, is the time dependent polarisation. For a material characterised by a single relaxation

time $\tau > 0$, the polarisation term can be decomposed by

$$P(t,x) = P_e + P_\mu(t,x), \tag{2.3.7}$$

where $P_\mu \in C^1\left(0,T;H^1(\Omega)\right)$ evolves according to

$$\tau\partial_t P_\mu(t,x) + P_\mu(t,x) = P_\infty - P_e, P_\mu(0,x) = 0 \tag{2.3.8}$$

for some $P_\infty \in H^1(\Omega)$.

Then as a function of $t$, the polarisation term can be written

$$P_\mu(t,x) = \tau^{-1}\int_0^t \left(P_\infty - P_0\right) e^{-(t-s)/\tau} E(s,x)\,\mathrm{d}s. \tag{2.3.9}$$

In the case of a constant electric field $E_0 \in H^1(\Omega)$, 2.3.9 becomes

$$P(t,x) = P_e + \left(P_\infty - P_e\right)\left(1 - e^{-t/\tau}\right). \tag{2.3.10}$$

Expressing $P_\infty \in H^1(\Omega)$ and $P_e \in H^1(\Omega)$ by

$$P_\infty(x) = \varepsilon_0\left(\varepsilon_L - 1\right)E_0(x) \text{ and } P_e(x) = \varepsilon_0\left(\varepsilon_I - 1\right)E_0(x)$$

for some $\varepsilon_L \in \mathcal{A}_\mathrm{p}$ and $\varepsilon_I \in \mathcal{A}_\mathrm{p}$. The susceptibility function can then be written

$$\chi(t) = \left(\varepsilon_L - \varepsilon_I\right)\mathrm{e}^{-\tau^{-1}t}. \tag{2.3.11}$$

More generally, it is often convenient to express the polarisation term directly as a convolution with the electric field

$$P(t,x) = \varepsilon_0\int_0^t \chi(t-s)E(s,x)\,\mathrm{d}s \tag{2.3.12}$$

for some appropriate function $\chi(t)$ which is referred to as the time-dependent susceptibility.

In the Fourier domain, the instantaneous permittivity $\varepsilon_I$ is often thought as the infinite frequency limit response and written $\varepsilon_\infty$. Similarly, the long-time limit of the permittivity $\varepsilon_L$ is thought of as the static (DC) permittivity and denoted $\varepsilon_s$. In this

case, the constitutive law can be written as

$$\widehat{D}(\omega, x) = \varepsilon_0 \left( \varepsilon_\infty + \frac{\varepsilon_s - \varepsilon_\infty}{1 + \mathrm{i}\omega\tau} \right) \widehat{E}(\omega, x), \tag{2.3.13}$$

and the susceptibility function becomes

$$\widehat{\chi}(\omega) = \frac{\chi_0}{1 + \mathrm{i}\omega\tau} \tag{2.3.14}$$

where $\chi_0$ is the static susceptibility [104]. This can be recognised as the Debye model. More generally, mixtures of molecules with different relaxation times results in the Cole-Cole relationships are described by

$$\widehat{D}(\omega, x) = \varepsilon_0 \left( 1 + \frac{1}{1 + (\mathrm{i}\omega\tau)^{1-\alpha}} \right) \widehat{E}(\omega, x) \tag{2.3.15}$$

for some $\alpha > 0$ [107, 176]. Furthermore, complex mixtures of materials with different relaxation times can be considered by the summation of (2.3.14) with different relaxation times [191]. We do not consider these cases in detail in this thesis, however, the results can be easily extended to such cases.

More generally, a dynamic material response can be modelled by more general evolution equations, see for example [10].

2.3.1.3. *Conductive materials.* The third constituent law adopted relates the current density $J$ with the electric field $E$. Suppose that $J$ depends linearly on $E$ such that

$$J = \sigma E \tag{2.3.16}$$

for some $\sigma \in \mathcal{A}_{\mathrm{c}}$. This equation is often referred to as Ohm's law and can be generalised for anisotropic materials [98].

We make a brief digression to motivate Ohm's law from a molecular viewpoint in the isotropic case; we refer the reader to [141, Chapter 25] for a more detailed explanation. When a conductive material with free charged particles is placed in an external electric field, an electromotive force is generated that moves the charged particles to oppose the external field. If the effect of the magnetic field is neglected,

the force exerted on a free charged body is proportional to the electric field $E$:

$$f = \pm |q_{\pm}| E. \tag{2.3.17}$$

Under the action of this force, the charged particles will accelerate up to a velocity $v \in \mathbb{R}^3$ whereby the opposing resistive force, caused by the charged particles moving through the material, is equal in magnitude to the electromotive force. In an homogeneous material, the resistive force is proportional to the velocity and

$$f = \nu v \tag{2.3.18}$$

for some constants $\nu > 0$.

Let there be $N_+ \in \mathbb{N}$ free positively charged species each with a charge $q_+ > 0$ travelling at the constant velocity $v_+ \in \mathbb{R}^3$ and $N_- \in \mathbb{N}$ negatively charged species with charge $q_- < 0$. The total current density can then be described as

$$J = N_+ |q_+| v_+ - N_- |q_-| v_-. \tag{2.3.19}$$

Using (2.3.17) and (2.3.18) this becomes

$$J = \left( \frac{1}{\nu_+} N_+ |q_+|^2 + \frac{1}{\nu_-} N_- |q_-|^2 \right) E, \tag{2.3.20}$$

where the resistive force experienced by the positively (resp. negatively) charged species is $\nu_+$ (resp. $\nu_-$). We remark that the quantity in the brackets is independent of the electric field $E$ and can, therefore, be considered a property of the material. We refer to this quantity as the material's conductivity and define

$$\sigma := \frac{1}{\nu_+} N_+ |q_+|^2 + \frac{1}{\nu_-} N_- |q_-|^2 . \tag{2.3.21}$$

It follows that $\sigma \in \mathcal{A}_c$ as required.

2.3.1.4. *Maxwell's equations for linear, dielectric and conductive media.* Coupled with equations (2.3.6) and (2.3.16), Maxwell's equations (2.3.1) can be expressed as

functions of the electric field $E$ and the magnetic field $H$:

$$\begin{cases} -\operatorname{div}(\varepsilon E) = \rho \\ -\operatorname{div}(\mu H) = 0 \\ \nabla \times E = -\partial_t(\mu H) \\ \nabla \times H = \partial_t(\varepsilon E) + \sigma E \end{cases} \quad \text{in } \Omega \times \mathbb{R}^+, \text{ in } \Omega \times \mathbb{R}^+, \tag{2.3.22}$$

together with the boundary conditions

$$\varepsilon E \cdot \hat{n} = 0 \text{ and } \mu H \cdot \hat{n} = 0 \text{ on } \mathbb{R}^+ \times \partial\Omega, \tag{2.3.23}$$

and initial conditions

$$E(0,x) = E_0 \text{ and } H(0,x) = H_0 \text{ in } \Omega. \tag{2.3.24}$$

For the remainder of this document we refer to the system of equations (2.3.22) simply as Maxwell's equations. We state the following theorem which ensures that the Maxwell's equations are well-posed. We refer the reader to [45] for a more in-depth discussion of well-posedness in more general cases of Maxwell's equations.

THEOREM 1. *Suppose that $\Omega \subset \mathbb{R}^3$ is an open-bounded connected domain with $C^1$ boundary $\partial\Omega$. Given a source term $\rho \in H^1(0,T;L^2(\Omega))$, a permittivity distribution $\varepsilon \in \mathcal{A}_p$, a permeability distribution $\mu \in \mathcal{A}_p$, and a conductivity $\sigma \in \mathcal{A}_c$. Then there exists a unique pair of fields $(E,H) \in \left[C^1([0,\infty);L^2(\Omega)) \cap C^0([0,\infty);V)\right]^2$, where $V$ is a complete subspace of $H(curl,\Omega)$, that are the unique weak solutions to (2.3.22) subject to (2.3.23) and (2.3.24).*

The space $V$ can be defined more precisely to incorporate the boundary condition see [146]. We do not go into details here as we will prove independently that the models considered in this thesis are well-posed.

**2.3.2. Time harmonic form.** Maxwell's equations can be equivalently stated in time harmonic form. We denote the Fourier transform of $f$ by $\widehat{f}$, provided it exists. For simplicity, we suppose that at $t = 0$, $E = 0$ and $H = 0$ and $\rho(t) = 0$ for $t \leq 0$. By taking the Fourier transform of Maxwell's equations (2.3.22), we obtain for each

frequency $\omega \in \mathbb{R}$

$$\begin{cases} -\operatorname{div}\left(\varepsilon\widehat{E}\right) = \widehat{\rho} \\ -\operatorname{div}\left(\mu\widehat{H}\right) = 0 \\ \qquad \nabla \times \widehat{E} = -\,\mathrm{i}\,\omega\mu\widehat{H} \\ \qquad \nabla \times \widehat{H} = \mathrm{i}\,\omega\varepsilon\widehat{E} + \sigma\widehat{E} \end{cases} \quad \text{in } \Omega \times \mathbb{R}, \tag{2.3.25}$$

with boundary conditions given by

$$\varepsilon\widehat{E}(\omega, x) \cdot \hat{n} = 0 \text{ and } \mu\widehat{H}(\omega, x) \cdot \hat{n} = 0 \text{ on } \partial\Omega \times \mathbb{R} \tag{2.3.26}$$

where we have extended $\rho(t) = 0$ for $t \leq 0$. We remark that we have assumed that the permittivity, permeability, and the conductivity of the material are frequency independent. It is a classical result that in this form, Maxwell's equations are well-posed. The following theorem has been established by several authors [4, 5, 135].

THEOREM 2. *Let $\varepsilon, \mu \in \mathcal{A}_p$ and $\sigma \in \mathcal{A}_c$. Suppose also that $\widehat{\rho} \in L^2(\Omega; \mathbb{C}^3)$ and $\omega > 0$. Then there exists a unique pair of fields $\left(\widehat{E}, \widehat{H}\right) \in \left[H(curl, \Omega; \mathbb{C}^3)\right]^2$ that are the weak solutions to (2.3.25) satisfying the boundary conditions (2.3.26). Furthermore, this solution satisfies the inequality*

$$\left\|\widehat{E}\right\|_{H(curl,\Omega;\mathbb{C}^3)} + \left\|\widehat{H}\right\|_{H(curl,\Omega;\mathbb{C}^3)} \leq C\left(\|\widehat{\rho}\|_{L^2(\Omega;\mathbb{C}^3)}\right) \tag{2.3.27}$$

*for some constant $C > 0$ depending on $\Omega$, $\omega$, $\varepsilon_0$, and $\mu_0$.*

If further assumptions are made on the distribution of parameters then it can be shown that the $\widehat{E}$ and $\widehat{H}$ fields are more regular [5]. Furthermore, the well-posedness of Maxwell's equations also holds in the anisotropic case [45].

**2.3.3. The quasi-static assumption.** We are particularly interested in the case when the magnetic field does not vary significantly—the so-called quasi-static regime. The validity of the assumption is dependent on the frequency of the applied electric field. Many practitioners choose to adopt the quasi-static form of Maxwell's equations, where the effect of the magnetic field is neglected, as a model of the electric fields generated by EFS devices [24, 92]. In this section, we establish a precise bound on the range of frequencies where the energy in the magnetic field is controlled by the energy

in the electric field. In other words, we prove that for a range of frequencies, the quasi-static form of Maxwell's equations, given subsequently, are a suitable approximation to the full Maxwell's equations.

Suppose $\Omega \subset \mathbb{R}^3$ is an open-bounded, simply connected domain. We begin by recalling the strong Helmholtz decomposition [156],. Another classical reference of this result is [11, Section 6].

LEMMA 1. *Let $\Omega \subset \mathbb{R}^3$ be a simply connected, open, and bounded domain with $C^1$ boundary $\partial\Omega$. Then for any $E \in L^2(\Omega;\mathbb{C}^3)$ with $E \cdot \hat{n} = 0$ on $\partial\Omega$, there exist $u \in H^1(\Omega;\mathbb{C})$ and $A \in H^1(\Omega;\mathbb{C}^3)$ with $\nabla \cdot A = 0$ such that*

$$E = -\nabla u + \nabla \times A. \tag{2.3.28}$$

If we take $\widehat{E} \in H(\mathrm{curl},\Omega;\mathbb{C}^3) \subset L^2(\Omega;\mathbb{C}^3)$ to be the solution of (2.3.25), then the Helmholtz decomposition holds and we assert that

$$\widehat{E} = -\nabla \widehat{u} + \nabla \times A \tag{2.3.29}$$

for some $\widehat{u} \in H^1(\Omega;\mathbb{C})$ and $A \in H(\mathrm{curl},\Omega;\mathbb{C})$ with $\nabla \cdot A = 0$. If it were that $\nabla \times A$ is zero, then the electric field is the gradient of a scalar field and $\nabla \times E = 0$. It follows that the influence of the magnetic field on the electric field is zero because

$$\partial_t (\mu H) = 0. \tag{2.3.30}$$

In principle, $\nabla \times A$ is never zero but can be considered to be small and thus $\widehat{E} = -\nabla\widehat{u}$ is a reasonable approximation. We now state and prove the main result of this section. In this lemma all derivatives are to be interpreted in the sense of distributions.

LEMMA 2. *Let $\left(\widehat{E},\widehat{H}\right) \in [H^1(\Omega;\mathbb{C}^3)]^2$ be the solutions to Maxwell's equations (2.3.22) in a bounded domain $\Omega \subset \mathbb{R}^3$, such that*

$$\widehat{E} \cdot \hat{n} = f \text{ and } \widehat{H} \cdot \hat{n} = 0 \text{ on } \partial\Omega$$

*with* $f \in H^{1/2}(\partial\Omega;\mathbb{C})$ *such that* $\int_{\partial\Omega} f\, ds = 0$. *Let* $\varepsilon \in \mathcal{A}_p$, $\sigma \in \mathcal{A}_c$, *and* $\mu \in \mathbb{R}_{>0}$ *model the permittivity, conductivity, and permeability in* $\Omega$ *respectively. Define*

$$\omega_0 = \sqrt{\frac{\lambda_1^N}{\mu \left\|\varepsilon\right\|_{L^\infty(\Omega;\mathbb{R})}}}, \tag{2.3.31}$$

*where* $\lambda_1^N$ *is the first strictly positive eigenvalue of the negative Laplacian on* $\Omega$, *with Neumann boundary conditions. If* $0 < \omega < \omega_0$, *then*

$$\left\|\nabla \times A\right\|_{L^2(\Omega;\mathbb{C}^3)} \leq \frac{\omega}{(\omega_0^2 - \omega^2)} \sqrt{\left(1 + \omega^2 \frac{\left\|\sigma\right\|_{L^\infty(\Omega;\mathbb{R})}^2}{\left\|\varepsilon\right\|_{L^\infty(\Omega;\mathbb{R})}^2}\right)} \left\|\nabla u\right\|_{L^2(\Omega;\mathbb{C}^3)}, \tag{2.3.32}$$

*where* $A \in H^1(\Omega;\mathbb{C}^3)$ *and* $u \in H^1(\Omega;\mathbb{C})$ *are such that* $\widehat{E} = \nabla \times A - \nabla u$.

Proof. For the proof we use the time harmonic form of Maxwell's equations given by (2.3.25). Taking the curl of

$$\nabla \times \widehat{E} = -\,\mathrm{i}\,\omega\mu\widehat{H} \tag{2.3.33}$$

we establish

$$\nabla \times \left(\nabla \times \widehat{E}\right) = -\,\mathrm{i}\,\omega(\nabla \times \mu\widehat{H}).$$

Since $\mu$ is constant, this becomes

$$\nabla \times \left(\nabla \times \widehat{E}\right) = -\,\mathrm{i}\,\omega\mu\left(\nabla \times \widehat{H}\right).$$

Eliminating $\widehat{H}$ by substitution, we obtain

$$\begin{aligned} \nabla \times \left(\nabla \times \widehat{E}\right) &= -\,\mathrm{i}\,\omega\mu\left(\mathrm{i}\,\omega\varepsilon\widehat{E} + \sigma\widehat{E}\right) \\ &= (\omega^2\mu\varepsilon - \mathrm{i}\,\omega\mu\sigma)\widehat{E}. \end{aligned} \tag{2.3.34}$$

Expressing $\widehat{E} = \nabla \times A - \nabla u$ using (2.3.28), the left hand side can be written

$$\begin{aligned} \left(\nabla \times \left(\nabla \times \widehat{E}\right)\right) &= (\nabla \times (\nabla \times (\nabla \times A - \nabla u))) \\ &= (\nabla \times (\nabla \times (\nabla \times A))), \end{aligned}$$

where the second line follows since the curl of a gradient is zero. Using the identity

$$\nabla \times (\nabla \times A) = \nabla (\nabla \cdot A) - \Delta A$$

where $\Delta$ is the vector Laplacian, we deduce

$$\begin{aligned} \left(\nabla \times \left(\nabla \times \widehat{E}\right)\right) &= -\Delta (\nabla \times A) + \nabla (\operatorname{div} (\nabla \times A)) \\ &= -\Delta (\nabla \times A) \end{aligned} \tag{2.3.35}$$

since the divergence of a curl is always zero. Define $q := \omega^2 \mu\varepsilon - \mathrm{i}\,\omega\mu\sigma$ then $q \in L^\infty(\Omega; \mathbb{C})$,

$$\|q\|^2_{L^\infty(\Omega)} = \omega^2 \mu^2 \left(\omega^2 \|\varepsilon\|^2_{L^\infty(\Omega)} + \|\sigma\|^2_{L^\infty(\Omega)}\right). \tag{2.3.36}$$

Combining (2.3.34) and (2.3.35), we obtain

$$-\Delta (\nabla \times A) = q (\nabla \times A - \nabla u).$$

By the definition of the decomposition (2.3.28), each component of $\nabla \times A$ must satisfy a Helmholtz equation. Namely, denote the $i$th component by $w_i := (\nabla \times A)_i$ then

$$\begin{aligned} -\Delta w_i - q w_i &= q h_i \text{ in } \Omega \\ \nabla w_i \cdot \hat{n} &= 0 \text{ on } \partial\Omega, \end{aligned} \tag{2.3.37}$$

where $h_i = -(\nabla u)_i$. We now look to bound each component $w_i$ by $u_i$: testing equation (2.3.37) against $\overline{w}_i$ and integrating by parts yields

$$\int_\Omega |\nabla w_i|^2 \, \mathrm{d}x - \int_\Omega \operatorname{Re}(q) |w_i|^2 \, \mathrm{d}x = \operatorname{Re}\left(\int_\Omega q h_i \overline{w}_i \, \mathrm{d}x\right) \text{ and} \tag{2.3.38}$$

$$\int_\Omega \operatorname{Im}(q) |w_i|^2 \, \mathrm{d}x = \operatorname{Im}\left(\int_\Omega q h_i \overline{w}_i \, \mathrm{d}x\right). \tag{2.3.39}$$

Applying the Cauchy-Schwarz inequality to equation (2.3.38),

$$\|\nabla w_i\|^2_{L^2(\Omega;\mathbb{C})} - \|\operatorname{Re}(q)\|_{L^\infty(\Omega)} \|w_i\|^2_{L^2(\Omega;\mathbb{C})} \leq \|q\|_{L^\infty(\Omega;\mathbb{C})} \|h_i\|_{L^2(\Omega;\mathbb{C})} \|w_i\|_{L^2(\Omega;\mathbb{C})}. \tag{2.3.40}$$

We recall Poincaré's inequality with an optimal coefficient of $1/\lambda_1^N$, where $\lambda_1^N$ is the first—necessarily strictly positive—eigenvalue of the Neumann Laplace operator on $H^1(\Omega;\mathbb{C})/\mathbb{R}_{>0}$, is given by

$$\lambda_1^N \|w_i\|^2_{L^2(\Omega;\mathbb{C})} \leq \|\nabla w_i\|^2_{L^2(\Omega;\mathbb{C})}\,.$$

By rearranging (2.3.31), we obtain

$$\lambda_1^N = \omega_0^2 \mu \|\varepsilon\|_{L^\infty(\Omega)}\,,$$

and (2.3.40) becomes

$$(\omega_0^2 - \omega^2)\mu \|\varepsilon\|_{L^\infty(\Omega)} \|w_i\|^2_{L^2(\Omega;\mathbb{C})} \leq \|q\|_{L^\infty(\Omega;\mathbb{C})} \|h_i\|_{L^2(\Omega;\mathbb{C})} \|w_i\|_{L^2(\Omega;\mathbb{C})}\,. \tag{2.3.41}$$

Using (2.3.36), (2.3.41) becomes

$$\|w_i\|_{L^2(\Omega;\mathbb{C})} \leq \frac{\omega}{(\omega_0^2 - \omega^2)} \sqrt{\left(1 + \omega^2 \frac{\|\sigma\|^2_{L^\infty(\Omega)}}{\|\varepsilon\|^2_{L^\infty(\Omega)}}\right)} \|h_i\|_{L^2(\Omega;\mathbb{C})}\,.$$

Moreover, this inequality holds for all of the components of the vector field $\nabla \times A$; taking the maximum over all indices $i$ we obtain that

$$\|\nabla \times A\|_{L^2(\Omega;\mathbb{C}^3)} \leq \frac{\omega}{(\omega_0^2 - \omega^2)} \sqrt{\left(1 + \omega^2 \frac{\|\sigma\|^2_{L^\infty(\Omega)}}{\|\varepsilon\|^2_{L^\infty(\Omega)}}\right)} \|\nabla u\|_{L^2(\Omega;\mathbb{C}^3)}$$

holds provided that

$$0 < \omega < \omega_0$$

as required. □

**2.3.4. Summary of the equations for the electric potential.** For the rest of this work we shall adopt the quasi-static assumption which allows us to assume that the electric field $E$ can be approximately written as $E = -\nabla u$ for some scalar function $u : \Omega \to \mathbb{K}$ in the frequency domain, or $E(t,\cdot) = -\nabla u(t,\cdot)$ for a.e. $t \in [0,T]$ in the time domain. For sufficiently small frequencies, the error is controlled by the norm of $E$ as in (2.3.32).

Taking the divergence of the final equation in (2.3.25), we deduce

$$\operatorname{div}(\nabla \times H) = -\operatorname{div}\left((\mathrm{i}\,\omega\varepsilon + \sigma)\,\nabla u\right)$$

holds at a.e. $x \in \Omega$. Similarly, in the time domain taking the divergence of the final equation in (2.3.22) we establish

$$\operatorname{div}(\nabla \times H) = -\operatorname{div}\left(\partial_t\left(\varepsilon\nabla u\right) + \sigma\nabla u\right).$$

Since the divergence of a curl is always zero, we arrive at equations that describe the electric potential in the time and frequency domains in the quasi-static regime.

To summarise, we have derived two models of the electric potential in $\Omega$. The first of these describes the evolution of the electric field in time: given $\varepsilon \in \mathcal{A}_{\mathrm{p}}$ and $\sigma \in \mathcal{A}_{\mathrm{c}}$, the electric potential $u(t,x) : [0,T] \times \Omega \to \mathbb{R}$ satisfies

$$-\operatorname{div}\left(\partial_t\left(\varepsilon\nabla u\right)\right) - \operatorname{div}\left(\sigma\nabla u\right) = 0 \quad \text{in } [0,T] \times \Omega, \tag{2.3.42}$$

for an appropriate choice of boundary and initial conditions. The second equation describes in the electric potential in the frequency domain: for a fixed frequency $\omega \in \mathbb{R}_+$ and given $\gamma = \varepsilon - \mathrm{i}\,\omega^{-1}\sigma \in \mathcal{A}(\omega)$ the electric potential $u(x) : \Omega \to \mathbb{C}$ satisfies

$$-\operatorname{div}(\gamma(\omega)\nabla u) = 0 \quad \text{in } \Omega, \tag{2.3.43}$$

subject to appropriate boundary conditions.

## 2.4. Modelling the sensor input and sensor measurements

In this section we describe how the sensor inputcan be modelled as boundary conditions for equations (2.3.42) and (2.3.43). We suppose that the sensor input corresponds to applying a voltage on the electrodes, injecting current through the electrodes, or a combination of both. Heuristically, a voltage input condition corresponds to a Dirichlet boundary condition and an injected current to a Neumann condition. In the following chapter we establish that a solution to either (2.3.42) or (2.3.43) exists for each choice of boundary condition.

In addition to the choice of boundary condition corresponding to the sensor input, we also require that the boundary conditions model the physical properties of the electrodes. Namely, we assume that the electrodes are perfect conductors.

ASSUMPTION 4. *All electrodes are perfect conductors.*

In a perfect conductor, the electric potential is spatially uniform whilst the charge, or current, is uniformly distributed over the surface of the conductor. As we shall see, boundary conditions can be chosen to ensure both of these properties hold.

Modelling electrodes as boundary conditions is not new and has been applied and developed by many different authors [50, 161]. We review the electrode models that, by consensus, have become wide-spread and commonplace before introducing a novel choice of boundary conditions in the time domain. In this case, the relationship between the electric potential and charge on each electrode is described by an ODE.

For the following sections, it is convenient to define

$$\mathbb{K}^N_\diamond := \left\{ x \in \mathbb{K}^N \text{ such that } \sum_{k=1}^N x_k = 0 \right\}$$

for $\mathbb{K} = \mathbb{R}$ or $\mathbb{C}$.

**2.4.1. Boundary conditions in the frequency domain.** In the frequency domain the material parameters are denoted by $\gamma \in \mathcal{A}(\omega)$ for $\omega \in \mathbb{R}_+$. In this section we shall suppose that the electric potential, denoted $u$, is the solution of (2.3.43) subject to appropriate boundary conditions that we will now describe. In all cases we shall assume a zero Neumann condition is imposed on the computational boundary $\partial\Omega_B$:

$$\gamma \nabla u \cdot \hat{n} = 0 \text{ on } \partial\Omega_B. \tag{2.4.1}$$

*The continuum model.* This is the most abstract electrode model used for EFS devices and is primarily considered due to the connection with the Calderón problem, see Chapter 5 and [29, 37, 49, 50, 180]. In this model, the sensor input is described by either

$$\gamma \nabla u \cdot \hat{n} = f \text{ on } \bigcup_{i=1}^N \partial E_i, \tag{2.4.2}$$

where $f \in H^{-1/2}(\partial\Omega;\mathbb{C})$ with $\int_{\partial\Omega} f\,\psi\,\mathrm{d}s = 0$ for all $\psi \in H^{1/2}(\partial\Omega)$, or by

$$u = \varphi \text{ on } \bigcup_{i=1}^{N} \partial E_i, \tag{2.4.3}$$

for some $\varphi \in H^{1/2}(\partial\Omega;\mathbb{C})$. While mathematically convenient—the existence and uniqueness of the electric field follows immediately from classical elliptic regularity [69]—this model does not accurately match experimentally observed data. Primarily, this is due to the choice of boundary condition being non-physical: the current or the electrical potential cannot be imposed point-wise.

However, by restricting the space of boundary conditions, (2.4.3) can ensure the electric potential is uniform on the electrodes. Suppose that $U \in \mathbb{C}^N$ and define

$$\varphi = \sum_{k=1}^{N} U_k\,\chi_k \tag{2.4.4}$$

where $\chi_k$ is the characteristic function of the $k$th electrode. Imposing this choice of $\varphi$ in (2.4.3), we enforce the potential field to be spatially uniform on each electrode reflecting the assumption that the electrodes are perfect conductors. Equivalently, we impose

$$u = U_k \text{ on } \partial E_k \text{ for } k = 1,\dots,N. \tag{2.4.5}$$

While it is tempting to analogously replace (2.4.2) with

$$\gamma\nabla u\cdot\hat{n} = Q_k \text{ on } \partial E_k \text{ for } k = 1,\dots,N, \tag{2.4.6}$$

for some $Q = (Q_k)_{k=1}^N \in \mathbb{C}^N_\diamond$, this is not sufficient to ensure that the electric potential is constant on each electrode. For $u$ to be is constant on each electrode, additional constraints need to be imposed: this is the so-called 'shunt model' [50]. Before, describing the shunt model, we discuss the model of the sensor measurements in the continuum case.

When the boundary condition (2.4.2) is imposed, the sensor measurements will be modelled as the trace of the function $u$ on the boundary $\partial\Omega$, denoted by $u|_{\partial\Omega}$. Similarly, when (2.4.3) is used as a boundary condition, the boundary flux is considered the sensor

measurements, namely $\gamma \nabla u \cdot \hat{n}|_{\partial\Omega}$. This action of the sensor is then an evaluation of either the Dirichlet-to-Neumann (DtN) or the Neumann-to-Dirichlet (NtD) map, when (2.4.4) or (2.4.6) are imposed respectively. We will discuss this interpretation further in Chapter 5 when the associated inverse problems are discussed.

Alternatively, when the discretised boundary conditions given by (2.4.4) are applied, the average boundary flux on each electrode is used as the measurement: namely, the measurements are given by the vector $m \in \mathbb{C}^N_\diamond$ defined component-wise by

$$m_k = |\partial E_k|^{-1} \int_{\partial E_k} \gamma \nabla u \cdot \hat{n} \, \mathrm{d}s \quad \text{for} \quad k = 1, \ldots, N. \tag{2.4.7}$$

Similarly, when (2.4.6) is used as the boundary condition, we take as the measurement the average electric potential on the electrode surface. In this case, $m \in \mathbb{C}^N_\diamond$ becomes

$$m_k = |\partial E_k|^{-1} \int_{\partial E_k} u \, \mathrm{d}s \quad \text{for} \quad k = 1, \ldots, N. \tag{2.4.8}$$

We remark that in this discretised case the action of the sensor becomes a mapping from $U \in \mathbb{C}^N$ to $m \in \mathbb{C}^N_\diamond$ given by (2.4.7) in the Dirichlet case, and $Q \in \mathbb{C}^N_\diamond$ to $m \in \mathbb{C}^N_\diamond$ given by (2.4.8) in the Neumann case.

*The shunt model.* We now describe a weaker choice of boundary condition where only the average boundary flux is imposed on the electrodes. Additionally, we constrain the electric potential to be constant on each electrode. Given a vector, $Q \in \mathbb{C}^N_\diamond$, we impose

$$|\partial E_k|^{-1} \int_{\partial E_k} \gamma \nabla u \cdot \hat{n} \, \mathrm{d}S = Q_k \text{ on } \partial E_k \text{ for } k = 1, \ldots, N \tag{2.4.9}$$

as the input of the system. Additionally, we constrain that

$$u = U_k \text{ on } \partial E_k \text{ for } k = 1, \ldots, N, \tag{2.4.10}$$

for some a priori *unknown* voltage distribution given by $U \in \mathbb{C}^N_\diamond$. The shunt model then consists of imposing (2.4.9) and restricting to the space of solutions where (2.4.10) holds. The vector $U \in \mathbb{C}^N_\diamond$ is to found as part of the solution of the equation and constitues the sensor measurements in this case.

Unfortunately, for EIT devices in particular, the shunt model fails to accurately predict sensor measurements due imperfect contact between the electrodes and the conductive objects generating variable surface impedances [50]. When these surface impedances are present it is preferable to use the Complete Electrode Model (CEM). In this more accurate case, the shunt model can be realised as the limit as the surface impedance at the interface between the object and the electrode tends to zero. When this is the case, or the electrodes are not in direct contact with the object, the shunt model becomes a reasonable electrode model.

*The complete electrode model.* The CEM is similar to the shunt model in the sense that the average flux on the electrodes is prescribed as the sensor input. However, (2.4.10) is replaced by a Robin condition with a configurable parameter to model the surface impedance on each electrode. Let $Z \in \mathbb{C}^N$ be a given vector of surface impedances and $Q = \mathbb{C}^N_\diamond$ be the vector of prescribed average flux on the electrodes. We impose

$$\int_{\partial E_k} \gamma \nabla u \cdot \hat{n} \, \mathrm{d}S = Q_k \text{ on } \partial E_k \text{ for } k = 1, \ldots, N \tag{2.4.11}$$

and

$$u + Z_k \gamma \nabla u \cdot \hat{n} = U_k \text{ on } \partial E_k \text{ for } k = 1, \ldots, N \tag{2.4.12}$$

where $U \in \mathbb{C}^N$ is an unknown vector of voltages that is found as part of the solution. The well-posedness of this model is described in detail in [161]. The parameters $Z \in \mathbb{C}^N$ are usually estimated empirically by fitting simulated measurements to real sensor measurements for a known material distribution. We describe a similar method for fitting model parameters in Chapter 4.

For EIT sensors it has been shown that the CEM can be tuned to agree with measured data to a high accuracy [111, 184] and in some cases measurement precision [50]. An application to ECT has been more recently discussed [71], although the accuracy of the CEM has not yet established for this modality.

*Summary of the boundary conditions and measurements.* To summarise, in the frequency domain, we have six choices of sensor input and measurement (output) pairs. We collate these in Table 1. For each choice of boundary condition, the electric

potential is the unique solution of (2.3.43) (see Chapter 3). We remark that any of these conditions can be imposed on distinct sections of the boundary to produce a mixed model.

| | **Sensor input (boundary condition)** | **Sensor output (measurement)** |
|---|---|---|
| Case 1 | $\gamma\nabla u\cdot\hat{n}=f$ on $\partial\Omega$ for $f\in H^{-1/2}(\partial\Omega)$ | $u\vert_{\partial\Omega}\in H^{1/2}(\partial\Omega)$ |
| Case 2 | $u=\varphi$ on $\partial\Omega$ for $\varphi\in H^{1/2}(\partial\Omega)$ | $\gamma\nabla u\cdot\hat{n}\vert_{\partial\Omega}\in H^{-1/2}(\partial\Omega)$ |
| Case 3 | $\gamma\nabla u\cdot\hat{n}=Q_k$ on $\partial E_k$ for $Q\in\mathbb{C}^N$ with $\sum_{k=1}^N Q_k=0$ | $\vert\partial E_k\vert^{-1}\int_{\partial E_k}u\,\mathrm{d}s$ on $\partial E_k$ for $k=1,\dots,N$ |
| Case 4 | $u=U_k$ on $\partial E_k$ for $U\in\mathbb{C}^N$ | $\vert\partial E_k\vert^{-1}\int_{\partial E_k}\gamma\nabla u\cdot\hat{n}\,\mathrm{ds}$ on $\partial E_k$ for $k=1,\dots,N$ |
| Case 5 | $\vert\partial E_k\vert^{-1}\int_{\partial E_k}\gamma\nabla u\cdot\hat{n}\,\mathrm{ds}=Q_k$ and $u=U_k$ on $\partial E_k$ for $k=1,\dots,N$ | $U\in\mathbb{C}^N$ where $u=U_k$ on $\partial E_k$ for $k=1,\dots,N$ |
| Case 6 | $\vert\partial E_k\vert^{-1}\int_{\partial E_k}\gamma\nabla u\cdot\hat{n}\,\mathrm{d}S=Q_k$ and $u+Z_k\gamma\nabla u\cdot\hat{n}=U_k$ on $\partial E_k$ for $k=1,\dots,N$ | $U\in\mathbb{C}^N$ where $u=U_k$ on $\partial E_k$ for $k=1,\dots,N$ |

TABLE 1. Summary of the boundary condition and measurement pairs in the frequency domain. As discussed previously, Case 1, 2, and 3 are non-physical. We will adopt Case 4 in Model 1 and Case 5 in Model 2 introduced below. We do not consider Case 6 in this thesis.

**2.4.2. The time dependent boundary conditions.** In this section boundary conditions for the time dependent equation are discussed. We consider analogous boundary conditions to those discussed above in the frequency domain. We then consider the coupled PDE-ODE model that is novel to this work.

In the time domain the material parameters are taken to be $\varepsilon\in\mathcal{A}_{\mathrm{p}}$ and $\sigma\in\mathcal{A}_{\mathrm{c}}$. For each choice of boundary condition discussed, we suppose that $u(t,x)\to\mathbb{R}$ is the

solution to (2.3.42). In all cases we impose

$$\varepsilon \nabla u \cdot \hat{n} = 0 \text{ on } [0,T] \times \partial\Omega_B.$$

*Continuum model of the electrodes in the time dependent case.* In the most abstract case, we suppose that either a potential difference or the boundary flux is imposed onto the electrodes. This corresponds to imposing either

$$u = \varphi \text{ on } (0,T] \times \bigcup_{k=1}^{N} \partial E_k \tag{2.4.13}$$

with $\varphi \in H^1\left(0,T; H^{1/2}(\partial\Omega)\right)$, or

$$\varepsilon \nabla u \cdot \hat{n} = f \text{ on } (0,T] \times \bigcup_{k=1}^{N} \partial E_k \tag{2.4.14}$$

$f \in H^1\left(0,T; H^{-1/2}(\partial\Omega)\right)$ such that $\int_{\partial\Omega} f\,\psi\,\mathrm{d}s = 0$ for all $\psi \in H^{1/2}(\partial\Omega)$. However, for reasons discussed previously this choice of boundary conditions is not physically relevant or applicable. Instead, we restrict to a subspace of admissible boundary conditions that can be decomposed into

$$\varphi(t,x) = \phi(t)\xi(x) \tag{2.4.15}$$

for $\phi \in C^1([0,T])$ and $\xi \in H^{1/2}(\partial\Omega;\mathbb{R})$ in the Dirichlet case and $\xi \in H^{-1/2}(\partial\Omega;\mathbb{R})$ with $\int_{\partial\Omega} \xi\,\psi\,\mathrm{d}s = 0$ for all $\psi \in H^{1/2}(\partial\Omega)$ in the Neumann case. Given a vector $U \in \mathbb{R}^N$, we let

$$\xi(x) = \sum_{k=1}^{N} U_k\,\chi_k \tag{2.4.16}$$

where $\chi_k$ is the characteristic function of $\partial E_k$. This choice of $\xi$ imposes that the electric potential is spatially uniform on the electrode surface for each $t \in [0,T]$. Similarly, choosing a vector $Q \in \mathbb{R}^N_\diamond$ and expressing

$$\xi(x) = \sum_{k=1}^{N} Q_k\,\chi_k \tag{2.4.17}$$

in (2.4.15) imposes that the total flux on each electrode is given by $\phi(t)Q_k$ at each $t \in [0,T]$. To summarise, combining (2.4.15) with (2.4.16) we impose

$$u = \phi(t)U_k \text{ on } \partial E_k \text{ for } k = 1, \dots, N. \tag{2.4.18}$$

Alternatively, combining (2.4.15) with (2.4.17) we impose

$$\varepsilon \nabla u \cdot \hat{n} = \phi(t)Q_k \text{ on } \partial E_k \text{ for } k = 1, \dots, N. \tag{2.4.19}$$

We now describe the corresponding sensor measurements. When the Dirichlet boundary conditions of (2.4.13) or (2.4.18) are used, the corresponding sensor measurement is the average flux on the electrodes: namely, the measurements are given by the function $m \in C\left([0,T]\,;\mathbb{R}^N_\diamond\right)$ where

$$(m(t))_k := \left(|\partial E_k|^{-1} \int_{\partial E_k} \varepsilon \nabla u(t,\cdot) \cdot \hat{n}\, \mathrm{d}s\right) \text{ for } k = 1, \dots, N. \tag{2.4.20}$$

Analogously, when the Neumann conditions of (2.4.14) or (2.4.19) are imposed, the average voltage on the electrodes is measured and $m \in C\left(0,T;\mathbb{R}^N\right)$ becomes

$$(m(t))_k := \left(|\partial E_k|^{-1} \int_{\partial E_k} u\, \mathrm{d}s\right) \text{ for } k = 1, \dots, N. \tag{2.4.21}$$

In practice, the measurement function $m$, given by either (2.4.20) or (2.4.21), is sampled at $N_T \in \mathbb{N}$ discrete time points, denoted by $t_1, \dots, t_{N_T}$, producing a vector valued time-series. This time series will be denoted by the matrix $M \in \mathbb{R}^{N_T \times N}$ defined by

$$M_{ik} := (m(t_i))_k \text{ for } i = 1, \dots, N_T \text{ and } k = 1, \dots, N.$$

However, as in the frequency dependent case the choice of boundary condition (2.4.19) is not sufficient to impose that the electric potential is spatially uniform on each electrode. We describe a time-dependent analogue of the shunt electrode conditions that imposes this constraint.

*The shunt model of the electrodes.* Suppose we are given a vector $Q \in \mathbb{R}^N_\diamond$ and a function $\phi \in H^1(0,T)$. The average flux imposed on the electrodes is given by

$$|\partial E_k|^{-1} \int_{\partial E_k} \varepsilon \nabla u \cdot \hat{n} \, \mathrm{d}s = \phi(t) Q_k \text{ on } (0,T] \times \partial E_k \text{ for } k = 1, \ldots, N. \tag{2.4.22}$$

Additionally, we constrain the electric potential to be

$$u = (U(t))_k \text{ on } \partial E_k \text{ for } k = 1, \ldots, N \tag{2.4.23}$$

for some function $U \in H^1\left(0,T;\mathbb{R}^N_\diamond\right)$ that is a priori unknown. The shunt model in the time domain then becomes imposing (2.4.22) and restricting to the space of solutions where (2.4.23) holds.

*The ODE model of the electrodes.* The boundary conditions described above have two limitations: firstly, each case supposes that the potential difference between electrodes can indeed be measured, and secondly, no charge can accumulate on any of the electrodes from other sources. In practice, one or both of these phenomena manifest. For example, during the temporal measurement process electrodes must be connected to ground via a predefined measurement circuit in order. In the simplest case, this circuit is an RC circuit see Figure 2.4.1. As a result, when a transmit pulse is applied to the transmitting electrode, charge accumulates on the remaining electrodes at a rate proportional to both the capacitance and resistance in the connected RC circuit as well as the material in the sensing volume.

Furthermore, during the measurement process the remaining electrodes are connected to ground, albeit through a large resistance, and thus charge accumulates on the other electrodes in the sensor. The rate and magnitude of the charge accumulated is dependent on the unknown object in the sensing domain. In practice, this accumulation of charge is not measured. Fundamentally, this results in additional, unaccounted for, charge entering the domain and violates a modelling assumption.

Our proposal to model the electrodes seeks to address both of these cases: we couple the PDE with $N$ ODEs, one for each electrode, to describe charge through the measurement circuit. For expository purposes, we consider the simplest measurement

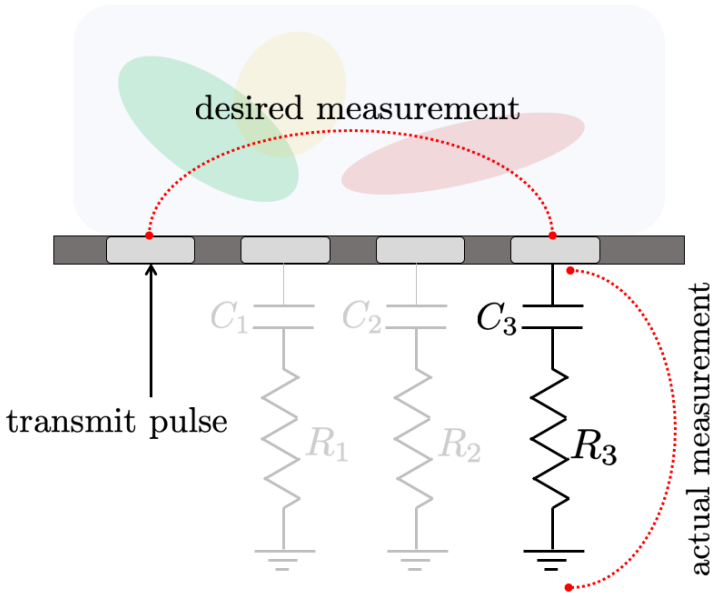



FIGURE 2.4.1. Schematic diagram showing the additional RC circuits being modelled in the planar case, the desired measurement, and the actual measurement.

circuit of an RC series circuit. with the resistance and capacitance in each ODE being model hyper-parameters that can be either predefined or estimated empirically, we discuss this further in Chapter 4.

In more detail, we suppose that $\mathcal{I} \subset \{1, \dots, N\}$ is the set of indices where the potential difference is imposed. Given a $\phi(t) \in H^1(0,T)$, we impose a Dirichlet condition on the electrodes corresponding to $\mathcal{I}$:

$$u = \phi(t) \text{ on } \partial E_k \text{ for } k \in \mathcal{I}. \tag{2.4.24}$$

On the electrodes with indices corresponding to $\mathcal{I}^c := \{1, \dots, N\} \setminus \mathcal{I}$, we constrain

$$\begin{cases} u = (U(t))_k \\ |\partial E_k|^{-1} \displaystyle\int_{\partial E_k} \gamma \nabla u(t,\cdot) \cdot \hat{n} \, \mathrm{d}s = (Q(t))_k \end{cases} \quad \text{for } k \in \mathcal{I}^c \text{ and } t \in (0,T] \tag{2.4.25}$$

for some a priori unknown functions $U(t) \in \mathbb{R}^N$ and $Q(t) \in \mathbb{R}^N$. We remark that if the vector $Q(t)$ is known, then this reduces to the shunt model discussed previously.

Rather than assume $U(t)$ or $Q(t)$ is known, we enforce for every $t \in [0, T]$ a relationship between $U(t)$ and $Q(t)$ given by

$$\partial_t Q_k + (R_k C_k)^{-1} Q_k = C_k^{-1} \left( U_k(t) - U_0 \right) \text{ for } k \in \mathcal{I}^c, \tag{2.4.26}$$

with $R_k, C_k > 0$ being known fixed parameters. To ensure this system is well-posed, we suppose the initial charge and voltage on the electrodes is given. For simplicity, we assume that initially the voltage and charge on each of the electrodes is zero:

$$U_k(0) = Q_k(0) = 0 \text{ for all } k = 1, \dots, N, \tag{2.4.27}$$

which implicitly supposes the initial conditions $\phi(0) = 0$ and $u(0, \cdot) = 0$ in $\Omega$.

We remark that an RC circuit is the simplest circuit model to be used, and more complex circuit models can be imposed in the same way. A natural extension would be to include parallel capacitances between electrodes to model any 'cross talk' in the system. This would require a coupled system of $N$ ODEs, which although being more complex is certainly feasible.

We combine the time-dependent equation (2.3.42) with (2.4.24), (2.4.26), (2.4.25), and the initial conditions (2.4.27) to form a model of the electric field generated by sensors with schematics given by 2.4.1. In this case, we shall suppose that the measurements are given by $U \in H^1(0, T; \mathbb{R}^N)$ as in (2.4.25). Similarly to the models discussed previously, this measurement may only be known as a time series.

We prove that this model is well-posed in Chapter 3.3.3. A numerical scheme to solve the equation is given in Chapter 4.3.3. The accuracy of this model compared with empirically collected sensor data is discussed in Chapter 4.5.

*Summary of the boundary conditions and measurements.* To summarise, in the time domain we have six choices of sensor input and output pairs: summarised in Table 2. For each choice of boundary the electric potential is the unique solution of (2.3.42) (see Chapter 3). We remark that although the dependence of the measurement on $\sigma$ is not explicit, since the measurements are taken on the boundary where $\sigma = 0$, the function $u$ is a non-linear function of both $\sigma$ and $\varepsilon$. This is perhaps the first indication that the corresponding inverse problem is non-trivial.

| | **Sensor input (boundary condition)** | **Sensor output (measurement)** |
|---|---|---|
| Case 1 | $\varepsilon\nabla u \cdot \hat{n} = f$ on $\bigcup_{k=1}^{N} \partial E_k$ for $f \in H^1\left(0,T; H^{-1/2}(\partial\Omega)\right)$ | $u\|_{\partial\Omega} \in H^1\left(0,T; H^{1/2}(\partial\Omega)\right)$ |
| Case 2 | $u = \varphi$ on $\bigcup_{k=1}^{N} \partial E_k$ for $\varphi \in H^1\left(0,T; H^{1/2}(\partial\Omega)\right)$ | $\varepsilon\nabla u \cdot \hat{n}\|_{\partial\Omega} \in H^1\left(0,T; H^{-1/2}(\partial\Omega)\right)$ |
| Case 3 | $\varepsilon\nabla u(t,\cdot) \cdot \hat{n} = \phi(t) Q_k$ on $(0,T] \times \partial E_k$ for $k = 1, \ldots, N$ | $\|\partial E_k\|^{-1} \int_{\partial E_k} u(t_i,\cdot)\, \mathrm{d}s$ for $k = 1, \ldots, N$ and $i = 1, \ldots, N_T$ |
| Case 4 | $u = \phi(t) U_k$ on $(0,T] \times \partial E_k$ for $k = 1, \ldots, N$ | $\|\partial E_k\|^{-1} \int_{\partial E_k} \gamma\nabla u(t_i,\cdot) \cdot \hat{n}\, \mathrm{d}s$ for $k = 1, \ldots, N$ and $i = 1, \ldots, N_T$ |
| Case 5 | $\|\partial E_k\|^{-1} \int_{\partial E_k} \gamma\nabla u(t,\cdot) \cdot \hat{n}\, \mathrm{d}s = (Q(t))_k$ and $u = (U(t))_k$ on $(0,T] \times \partial E_k$ for $k = 1, \ldots, N$ | $M \in \mathbb{R}^{N_T \times N}$ where $M_{ik} = (U(t_i))_k$ for $k = 1, \ldots, N$ and $i = 1, \ldots, N_T$ |
| Case 6 | $u = \phi(t)$ on $\partial E_k$ for $k \in \mathcal{I}$ and (2.4.26), (2.4.25) hold on $\partial E_k$ for $k \in \mathcal{I}^c$ | $M \in \mathbb{R}^{N_T \times N}$ where $M_{ik} = (U(t_i))_k$ for $k = 1, \ldots, N$ and $i = 1, \ldots, N_T$ |

TABLE 2. Summary of the boundary condition and measurement pairs in the time domain. As discussed previously, Case 1, 2, and 3 are non-physical. We will adopt Case 4 in Model 3, Case 5 in Model 4, and Case 6 in model 5 introduced below.

## 2.5. Summary of the models

We collate the above information to give a concise statement of each of the five models considered in this thesis. We begin with the models stated in the frequency domain. For each model we describe the input of the model, the PDE that describes the electric potential potential field, and the modelled sensor measurements. We defer the discussion of uniqueness and existence of the PDEs until the next chapter and a detailed discussion of the associated inverse problem until Chapter 5. For clarity, we summarise all of the models in the full data case: the partial data case can be recovered when only some of the measurement vector or matrix is known. The reader may find it useful to refer back to this summary when considering later chapters.

**2.5.1. Model 1: Frequency space model with discrete electrode conditions.** We consider the mixed model formed by combining Case 3 and Case 4 in Table 1: let $\partial\Omega_D$ be the union of the electrodes where the voltage can be controlled and $\partial\Omega_N$ to be union of the electrodes where the flux can be controlled. In other words, let the electrodes comprising $\partial\Omega_D$ be indexed by $\mathcal{I} \subset \{1, \dots, N\}$ and $\partial\Omega_N$ by $\mathcal{I}^c := \{1, \dots, N\} \setminus \mathcal{I}$:

$$\partial\Omega_D := \bigcup_{k\in\mathcal{I}} \partial E_k \text{ and } \partial\Omega_N := \bigcup_{k\in\mathcal{I}^c} \partial E_k.$$

Given a vector $U \in \mathbb{C}^N$ and a vector $Q \in \mathbb{C}^N$, we model the voltage distribution as the weak solution $u : \Omega \to \mathbb{C}$ to

$$\begin{cases} -\operatorname{div}(\gamma\nabla u) = 0 \quad \text{in } \Omega, \\ \qquad\qquad u = U_k \text{ on } \partial E_k \text{ for } k \in \mathcal{I} \\ \gamma\nabla u \cdot \hat{n} = Q_k \text{ on } \partial E_k \text{ for } k \in \mathcal{I}^c, \\ \gamma\nabla u \cdot \hat{n} = 0 \quad \text{on } \partial\Omega_B. \end{cases} \tag{2.5.1}$$

In the particular case when $\mathcal{I} = \emptyset$—the pure Neumann case—we require additionally that $\sum_{k=1}^N Q_k = 0$ and $\int_\Omega u \, \mathrm{d}x = 0$ for the solution to be unique. We remark that the

entries $U_k$ for $k \in \mathcal{I}^c$ and $Q_k$ when $k \in \mathcal{I}$ are not required for the model to be well posed.

The sensor measurements then can be described by $m \in \mathbb{C}^N$ defined as

$$m_k = \begin{cases} |\partial E_k|^{-1} \displaystyle\int_{\partial E_k} u \, \mathrm{d}s & \text{for } k \in \mathcal{I}^c, \\ |\partial E_k|^{-1} \displaystyle\int_{\partial E_k} \gamma \nabla u \cdot \hat{n} \, \mathrm{d}s & \text{for } k \in \mathcal{I}, \end{cases} \tag{2.5.2}$$

where $u$ solves (2.5.1). We are then able to define the operator $S^1_\gamma$ that describes the mapping of the sensor input to the sensor output.

Definition 1 (Model 1). Fix a frequency $\omega \in \mathbb{R}_+$, a parameter distribution $\gamma(\omega) \in \mathcal{A}(\omega)$, and a subset of the indices $\mathcal{I} \subset \{1, \ldots, N\}$ corresponding to $\partial\Omega_D$. The domain boundary is decomposed as

$$\partial\Omega = \partial\Omega_B \cup \partial\Omega_D \cup \partial\Omega_N.$$

We model the sensor by the operator

$$\mathcal{S}^1_\gamma : \mathbb{C}^N \longrightarrow \mathbb{C}^N$$

$$X \longmapsto m$$

where the vector $m$ is given by (2.5.2).

Finally, we remark that this model is similar to the complex impedance model introduced in [119] or [57].

**2.5.2. Model 2: Frequency space model with shunt electrode conditions.** In this case we consider the boundary conditions to be described by Case 5 in Table 1—the so-called shunt boundary conditions.

Fix a frequency $\omega \in \mathbb{R}_+$, an admissible material parameter distribution $\gamma \in \mathcal{A}$ and a vector $Q \in \mathbb{C}^N_\diamond$. We model the electric potential, denoted $u$, and the potential on the electrodes, denoted $U \in \mathbb{C}^N$, as the weak solution to

$$\begin{cases} -\operatorname{div}(\gamma\nabla u) = 0 \quad \text{in } \Omega, \\ u = U_k \text{ on } \partial E_k \text{ for } k = 1, \dots, N \\ |\partial E_k|^{-1} \displaystyle\int_{\partial E_k} \gamma\nabla u \cdot \hat{n}\, \mathrm{d}s = Q_k \text{ on } \partial E_k \text{ for } k = 1, \dots, N \\ \gamma\nabla u \cdot \hat{n} = 0 \quad \text{on } \partial\Omega_B, \end{cases} \tag{2.5.3}$$

subject to the additional constraint that $\sum_{k=1}^{N} U_k = 0$ to ensure uniqueness.

For this model the sensor measurements are taken to be $U \in \mathbb{C}^N$ that are found as part of the solution. The mapping between the sensor input and output is defined to be $S^2_\gamma$.

Definition 2 (Model 2). Fix a frequency $\omega \in \mathbb{R}_+$ and a parameter distribution $\gamma(\omega) \in \mathcal{A}(\omega)$. We model the sensor by the operator

$$\begin{aligned} \mathcal{S}^2_\gamma : \mathbb{C}^N_\diamond &\longrightarrow \mathbb{C}^N_\diamond \\ Q &\longmapsto U \end{aligned}$$

where $\left(u, (U_k)_{k=1}^N\right)$ solves (2.5.3) for the given $Q$.

**2.5.3. Model 3: Time domain model with discrete electrode conditions.** We consider the time dependent analogue of Model 1. Once again, let $\mathcal{I} \subset \{1, \dots, N\}$ be the indices of electrodes corresponding to $\partial\Omega_D$ and the remainder corresponding to $\partial\Omega_N$. Then necessarily

$$\partial\Omega_D := \bigcup_{k\in\mathcal{I}} \partial E_k \text{ and } \partial\Omega_N = \bigcup_{k\in\mathcal{I}^c} \partial E_k.$$

We suppose that $\varepsilon \in \mathcal{A}_{\mathrm{p}}$, $\sigma \in \mathcal{A}_{\mathrm{c}}$ , $\phi \in C^1([0,T])$, a vector $U \in \mathbb{C}^N$ and $Q \in \mathbb{C}^N$ are given. We remark that the entries of $U_k \in \mathcal{I}^c$ are irrelevant and will not be imposed. Similarly, for the entries $Q_k$ when $k \in \mathcal{I}$. Suppose the initial electric potential $u_0 \in H^1(\Omega)$ is known. We model the electric potential field, $u : [0,T] \times \Omega \to \mathbb{R}$, as the weak solution to

$$\begin{cases} -\operatorname{div}\left(\partial_t\left(\varepsilon\nabla u\right)\right) - \operatorname{div}\left(\sigma\nabla u\right) = 0 & \text{in } [0,T]\times\Omega, \\ u = \phi(t)U_k & \text{on } (0,T]\times\partial E_k \text{ for } k\in\mathcal{I}, \\ \varepsilon\nabla u\cdot\hat{n}\,\mathrm{d}s = \phi(t)Q_k & \text{on } (0,T]\times\partial E_k \text{ for } k\in\mathcal{I}^c, \\ \varepsilon\nabla u\cdot\hat{n} = 0 & \text{on } (0,T]\times\partial\Omega_B, \\ u(0,\cdot) = u_0 & \text{in } \Omega. \end{cases} \tag{2.5.4}$$

In the case when $\mathcal{I}=\emptyset$, the full Neumann problem, we require additionally that $\sum_{k=1}^{N} Q_k = 0$ and constrain the solution to satisfy $\int_\Omega u(t,\cdot)\,\mathrm{d}x = 0$ for each $t\in[0,T]$.

The measurement $m \in H^1\left(0,T;\mathbb{R}^N\right)$ is then defined component-wise for each $t\in[0,T]$ by

$$\left(m(t)\right)_k = \begin{cases} |\partial E_k|^{-1}\displaystyle\int_{\partial E_k} u(t,\cdot)\,\mathrm{d}s & \text{for } k\in\mathcal{I}^c, \\ |\partial E_k|^{-1}\displaystyle\int_{\partial E_k} \varepsilon\nabla u(t,\cdot)\cdot\hat{n}\,\mathrm{d}s & \text{for } k\in\mathcal{I}. \end{cases}$$

However, we suppose that the measurement $m$ is known only at finitely many, distinct time points denoted $t_1,\ldots,t_{N_T}$ for some $N_T>0$ with $t_1=0$ and $t_{N_T}=T$. Without loss of generality we suppose that the set $\{t_1,\ldots,t_{N_T}\}$ are ordered so that $t_1 < t_1 < \cdots < t_{N_T}$. The measurement then becomes a matrix $M\in\mathbb{R}^{N_T\times N}$ defined by

$$M_{ij} := \left(m(t_i)\right)_j \text{ for } i=1,\ldots,N_T \text{ and } j=1,\ldots,N. \tag{2.5.5}$$

Definition 3 (Model 3). Suppose $\varepsilon\in\mathcal{A}_{\mathrm{p}}$ and $\sigma\in\mathcal{A}_{\mathrm{c}}$. Fix the sampling time points as $\{t_1,\ldots,t_{N_T}\}$ for some $N_T>0$ and a function $\phi(t)\in C^1\left([0,T]\right)$. Let $\mathcal{I}\subset\{1,\ldots,N\}$ be a subset of indices corresponding to $\partial\Omega_D$ and $\mathcal{I}^c$ to $\partial\Omega_N$. We model the sensor by the operator

$$\mathcal{S}^3 : H^1(0,T)\times\mathbb{R}^N \longrightarrow \mathbb{R}^{N_T\times N}$$

$$\phi\cdot X \longmapsto M$$

where $u$ solves (2.5.4) with boundary conditions given explicitly by

$$\begin{cases} u = \phi(t)X_k & \text{on } (0,T] \times \partial E_k \text{ for } k \in \mathcal{I} \\ \varepsilon \nabla u \cdot \hat{n} = \phi(t) X_k & \text{on } (0,T] \times \partial E_k \text{ for } k \in \mathcal{I}^c \end{cases}$$

and $M$ is defined by 2.5.5.

**2.5.4. Model 4: Time domain model with discrete electrode conditions.** We consider the analogue of the shunt boundary conditions in the time domain. Suppose we are given $u_0 \in H^1(\Omega)$, $\phi \in H^1(0,T)$ and a vector $Q \in \mathbb{R}^N_\diamond$. Then the electric potential $u : [0,T] \times \Omega \to \mathbb{R}$ and the voltage on the electrodes $U : [0,T] \to \mathbb{R}^N$ is modelled as the weak solution to

$$\begin{cases} -\operatorname{div}\left(\partial_t \left(\varepsilon \nabla u\right)\right) - \operatorname{div}\left(\sigma \nabla u\right) = 0 & \text{in } [0,T] \times \Omega, \\ u = U_k & \text{on } (0,T] \times \partial E_k \text{ for } k = 1, \dots, N, \\ |\partial E_k|^{-1} \displaystyle\int_{\partial E_k} \varepsilon \nabla u \cdot \hat{n} \, \mathrm{d}s = \phi(t) Q_k & \text{on } (0,T] \times \partial E_k \text{ for } k = 1, \dots, N, \\ \varepsilon \nabla u \cdot \hat{n} = 0 & \text{on } (0,T] \times \partial \Omega_B, \\ u(0,\cdot) = u_0 & \text{in } \Omega, \end{cases} \tag{2.5.6}$$

subject to the additional constraint that $U(t) \in \mathbb{R}^N_\diamond$ for all $t \in [0,T]$. The measurements correspond to the function $U : [0,T] \to \mathbb{R}^N_\diamond$ to be found as part of the solution. In practice, we suppose that $U(t)$ is sampled at the time points $t_1, \dots, t_{N_T}$ as in Model 3.

Definition 4 (Model 4). Suppose $\varepsilon \in \mathcal{A}_{\mathrm{p}}$ and $\sigma \in \mathcal{A}_{\mathrm{c}}$. Fix the sampling time points as $\{t_1, \dots, t_{N_T}\}$ for some $N_T > 0$. Denote by $\mathbb{R}^N_\diamond$ the set of vectors that sum to zero. We model the sensor by the operator

$$\begin{aligned} \mathcal{S}^4 : H^1(0,T) \times \mathbb{R}^N_\diamond &\longrightarrow \mathbb{R}^{N_T \times N} \\ (\phi, Q) &\longmapsto \left(U(t_i)\right)_k \end{aligned}$$

where $(u, U)$ solves (2.5.6).

**2.5.5. Model 5: Time domain model with ODE boundary conditions.** In this model we suppose the receiving electrode is connected via an RC circuit to ground, which is at a voltage $U_0 \in \mathbb{R}$. As discussed previously, the voltage $U_k$ and charge $Q_k$ at time $t \in [0,T]$ on the $k$-th electrode are related by the ODE

$$U_k(t) - U_0 = C_k \partial_t Q_k + R_k^{-1} Q_k \tag{2.5.7}$$

for some choice of constants $C_k, R_k > 0$. This is the purpose of Model 5: to combine the ODE (2.5.7) with a PDE model of the electric field in $\Omega$.

In actuality, the charge on the $k$-th electrode at time $t \in [0,T]$, expressed in terms of the voltage field $u$, can be written as

$$Q_k(t) = |\partial E_k|^{-1} \int_{\partial E_k} \varepsilon \nabla u \cdot \hat{n} \, \mathrm{d}s.$$

Suppose that the transmit pulse, $\phi \in C^1([0,T])$, is applied to the electrodes $\mathcal{I} \subset \{1,\dots,N\}$. Typically, we consider the case when $\mathcal{I}$ is a singleton set. The potential field inside the sensing volume, $u : [0,T] \times \Omega \longrightarrow \mathbb{R}$, the electric potential on the electrodes $U(t) \in \mathbb{R}^N$, and the flux on the electrodes $Q(t) \in \mathbb{R}^N_\diamond$ is modelled as the weak solution satisfying

$$\begin{cases} -\operatorname{div}\left(\partial_t\left(\varepsilon \nabla u\right)\right) - \operatorname{div}\left(\sigma \nabla u\right) = 0 & \text{in } [0,T] \times \Omega, \\ u(t,\cdot) = \phi(t) & \text{on } (0,T] \times \partial E_k \text{ for } k \in \mathcal{I} \\ u(t,\cdot) = \left(U(t)\right)_k & \text{on } (0,T] \times \partial E_k \text{ for } k \in \mathcal{I}^c, \\ |\partial E_k|^{-1} \displaystyle\int_{\partial E_k} \varepsilon \nabla u(t,\cdot) \cdot \hat{n} \mathrm{d}s = \left(Q(t)\right)_k & \text{on } (0,T] \times \partial E_k \text{ for } k \in \mathcal{I}^c, \\ \partial_t Q_k + \left(R_k C_k\right)^{-1} Q_k = C_k^{-1}\left(U_k - U_0\right) & \text{for } t \in (0,T] \text{ and } k \in \mathcal{I}^c, \\ Q_k(0) = Q_0 & \text{for } k \in \mathcal{I}^c, \\ u(0,\cdot) = u_0 & \text{in } \Omega, \end{cases} \tag{2.5.8}$$

for given constants $C_k > 0$, $R_k > 0$, a known ground voltage $U_0 \in \mathbb{R}$.

The sensor measurements correspond to $U \in C\left([0,T];\mathbb{R}^N\right)$, which is found as part of the solution. As in Model 3 and Model 4, we suppose that $U(t) \in \mathbb{R}^N$ is known as a time series sampled at the points $t_1, \ldots, t_{N_T}$.

Definition 5 (Model 5). Suppose $\varepsilon \in \mathcal{A}_{\mathrm{p}}$ and $\sigma \in \mathcal{A}_{\mathrm{c}}$. Fix the sampling time points as $\{t_1, \ldots, t_{N_T}\}$ for some $N_T > 0$ and a function $\phi(t) \in C^1([0,T])$ with $\phi(0) = 0$. Let $\mathcal{I} \subset \{1, \ldots, N\}$ be a subset of electrode indices where the transmit pulse is imposed. Suppose the initial charge is given by $Q_0 \in \mathbb{R}^N_\diamond$. We model the sensor by the operator

$$\mathcal{S}^4 : H^1(0,T) \times \mathbb{R}^N \longrightarrow \mathbb{R}^{N_T \times N}$$

$$(\phi, Q_0) \longmapsto (U(t_i))_k$$

where the triple $(u, U, Q)$ solves (2.5.8).

CHAPTER 3

# Mathematical analysis of the models

In this chapter we prove existence and uniqueness each of the PDEs associated to each of the five models introduced previously. In other words, we establish that each of the models are well-posed. We consider each of the equations (2.5.1), (2.5.3), (2.5.4), (2.5.6), and (2.5.8) separately since different approaches and results are needed in each case. However, there are similarities: all of the results rely on the function space satisfying a Poincaré-type inequality, the celebrated Lax–Milgram lemma, and suitable uniform energy estimates. In this functional analytic approach, existence of a solution follows by the Lax–Milgram lemma and uniqueness follows directly from uniform energy estimates. The regularity of the solutions given in the statement of each result is sufficient for practical applications but is not mathematically optimal—determining the optimal regularity of the solutions to each PDE is beyond the scope of this thesis. In order to state the main results of this chapter, we introduce the function spaces used and establish Poincaré inequalities in these spaces. We also discuss the form of the Lax–Milgram lemma used later.

## 3.1. Preliminaries

Let $\Omega \subset \mathbb{R}^d$ for $d = 2$ or 3 be an open, bounded, connected set with a piecewise $C^1$–boundary. We suppose that the boundary is decomposed into $N \in \mathbb{N}$ disjoint connected hypersurfaces denoted $\partial E_1, \ldots, \partial E_N$ that represent the surface of each electrode denoted $E_1, \ldots, E_N$. Furthermore, we suppose that such that each $\partial E_i$ is mapped to $S^{d-1}$ by a $C^1$ diffeomorphism. See Figure 2.1.1 for examples when $d = 2$. As a result, the boundary $\partial\Omega$ can be decomposed as

$$\partial\Omega = \partial\Omega_B \cup \bigcup_{k=1}^{N} \partial E_k,$$

where $\partial\Omega_B$ is the boundary of the domain not covered by the electrodes.

We group the electrodes into two distinct categories, denoted by $\partial\Omega_D$ and $\partial\Omega_N$, corresponding to the Dirichlet and the Neumann parts of the boundary respectively. This distinction is physically motivated: Dirichlet boundary conditions correspond to the voltage on the electrodes whereas Neumann boundary conditions correspond to the flux (or charge) on the electrode surface. Each of the electrodes will be contained in either $\partial\Omega_D$ or $\partial\Omega_N$. From this perspective, there is an alternative decomposition of $\partial\Omega$ as

$$\partial\Omega = \partial\Omega_B \cup \partial\Omega_D \cup \partial\Omega_N.$$

We consider the time domain to be $[0, T]$ for some maximal time $T > 0$ and we define

$$Q_T := [0, T] \times \Omega.$$

The set $Q_T$ is referred to as the parabolic cylinder. Throughout we shall suppose the field $\mathbb{K}$ is either $\mathbb{R}$ or $\mathbb{C}$.

**3.1.1. Functions and function spaces.** Denote the Sobolev space of weakly differentiable, square integrable functions $u : \Omega \longrightarrow \mathbb{K}$ by $H^1(\Omega; \mathbb{K})$. We extend this definition to $H^s\left(\mathbb{R}^N; \mathbb{K}\right)$ for any $s > 0$, by defining the space of functions

$$H^s\left(\mathbb{R}^N; \mathbb{K}\right) := \left\{ u \in L^2\left(\mathbb{R}^N; \mathbb{K}\right) : \int_\Omega \left(1 + |\xi|^{2s}\right) |\widehat{u}(\xi)|^2 \, \mathrm{d}\xi < \infty \right\},$$

where $\widehat{u}$ denotes the Fourier transform of the function $u$. Equipped with the norm

$$\|u\|_{H^s(\mathbb{R}^N;\mathbb{K})} := \left\| \left(1 + |\xi|^2\right)^{s/2} \widehat{u} \right\|_{L^2(\mathbb{R}^N;\mathbb{K})},$$

the space $H^s\left(\mathbb{R}^N; \mathbb{K}\right)$ is a Hilbert space. Analogously, when $s < 0$ we define

$$H^s\left(\mathbb{R}^N; \mathbb{K}\right) := \left\{ u \in \mathcal{L}'\left(\mathbb{R}^N; \mathbb{K}\right) : \int_\Omega \left(1 + |\xi|^{2s}\right) |\widehat{u}(\xi)|^2 \, \mathrm{d}\xi < \infty \right\}$$

where $\mathcal{L}'\left(\mathbb{R}^N; \mathbb{K}\right)$ denotes the dual space to $L^2\left(\mathbb{R}^N; \mathbb{K}\right)$. By the Plancherel theorem, one can show that $(H^s)'$, the dual space of $H^s$, can be identified with $H^{-s}$ for any $s \in \mathbb{R}$. For each $s \in \mathbb{R}$, this definition can be extended to any Lipschitz domain

$\Omega \subset \mathbb{R}^N$ by

$$H^s(\Omega;\mathbb{K}) = \left\{u|_{\partial\Omega} : u \in H^s\left(\mathbb{R}^N;\mathbb{K}\right)\right\}$$

with the norm

$$\|u\|_{H^s(\Omega;\mathbb{K})} := \inf\left\{\|w\|_{H^s(\mathbb{R}^N;\mathbb{K})} : w|_\Omega = u\right\}.$$

We refer the reader to [69, 70] or [62] for further details of these function spaces and the trace theorem.

3.1.1.1. *The spaces $H^1_\diamond(\Omega;\mathbb{K})$ and $H^1_U(\Omega;\mathbb{K})$.* We define the following subspaces of $H^1(\Omega;\mathbb{K})$. Let $H^1_\diamond(\Omega;\mathbb{K})$ be the space of all weakly differentiable, square integrable functions with average zero on the boundary:

$$H^1_\diamond(\Omega;\mathbb{K}) := \left\{f \in H^1(\Omega;\mathbb{K}) : \int_{\partial\Omega} f\,\mathrm{d}s = 0\right\}. \tag{3.1.1}$$

We equip $H^1_\diamond(\Omega;\mathbb{K})$ with the quotient norm

$$\|u\|_{H^1_\diamond(\Omega;\mathbb{K})} := \inf_{C\in\mathbb{R}}\left\{\|u+C\|_{H^1(\Omega;\mathbb{K})}\right\}.$$

We shall denote the dual space to $H^1_\diamond(\Omega;\mathbb{K})$ by $H^{-1}_\diamond(\Omega;\mathbb{K})$.

Suppose that $U \subset \partial\Omega$ be an open set that decomposes $\partial\Omega$ into disjoint subsets

$$\partial\Omega := U \cup \widetilde{U}.$$

We define

$$H^1_U(\Omega;\mathbb{K}) := \left\{f \in H^1(\Omega;\mathbb{K}) : f|_U = 0\right\}, \tag{3.1.2}$$

to be the space of $H^1$ functions that have zero trace on the segment of the boundary denoted by $U$. We endow $H^1_U(\Omega;\mathbb{K})$ with the canonical norm on $H^1(\Omega;\mathbb{K})$. In the case when $U = \partial\Omega$, $H^1_{\partial\Omega}(\Omega;\mathbb{K})$ is more commonly denoted by $H^1_0(\Omega;\mathbb{K})$. The dual space to $H^1_U(\Omega;\mathbb{K})$ shall be similarly denoted $H^{-1}_U(\Omega;\mathbb{K})$.

3.1.1.2. *The function spaces $\dot{H}^1(\Omega;\mathbb{K})$ and $\overline{H^1}(\Omega;\mathbb{K})$.* Let $N \in \mathbb{N}$ be fixed and correspond to the the number of electrodes. Suppose $(X, \|\cdot\|_X)$ and $(Y, \|\cdot\|_Y)$ are Banach spaces. The direct sum, written $X \oplus Y$, is the space of tuples $(x, y)$ where

$x \in X$ and $y \in Y$:

$$X \oplus Y := \{(x, y) \text{ such that } x \in X \text{ and } y \in Y\}.$$

Equipped with the norm defined by

$$\|\cdot\|_{X\oplus Y} := \|\cdot\|_X + \|\cdot\|_Y,$$

the space $X \oplus Y$ is also a Banach space.

We define the space $H^1_\oplus(\Omega;\mathbb{K})$ to be the direct sum between $H^1(\Omega;\mathbb{K})$ and $\mathbb{K}^N$

$$H^1_\oplus(\Omega;\mathbb{K}) := H^1(\Omega;\mathbb{K}) \oplus \mathbb{K}^N.$$

By the above, the space $H^1_\oplus(\Omega;\mathbb{K})$ is a Banach space with the appropriate norm. We consider two subspaces of $H^1_\oplus(\Omega;\mathbb{K})$: the space of functions that differ by a constant denoted $\dot{H}^1(\Omega;\mathbb{K})$ and the space of functions taking prescribed values on $\partial\Omega$ denoted $\overline{H^1}(\Omega;\mathbb{K})$. We define these two spaces formally. Denote the vector of ones in $\mathbb{K}^N$ by $\mathbf{1}$.

Let $\sim$ be the equivalence relation defined on elements of $H^1_\oplus(\Omega;\mathbb{K})$ by

$$(u_1, U_1) \sim (u_2, U_2) \iff u_1 = u_2 + c \text{ and } U_1 = U_2 + c\mathbf{1} \text{ for some } c \in \mathbb{K}.$$

Equivalently, we say that two elements of $H^1_\oplus(\Omega;\mathbb{K})$ are equivalent if they differ by a constant $c \in \mathbb{K}$. We define $\dot{H}^1(\Omega;\mathbb{K})$ to be the quotient space

$$\dot{H}^1(\Omega;\mathbb{K}) := {}^{H^1_\oplus(\Omega;\mathbb{K})}\!/_{\sim}$$

endowed with the quotient norm

$$\|(u, U)\|_{\dot{H}^1(\Omega;\mathbb{K})} := \inf_{c\in\mathbb{K}} \left\{ \|u - c\mathbf{1}\|_{H^1(\Omega;\mathbb{K})} + \|U - c\mathbf{1}\|_{\mathbb{K}^N} \right\}.$$

Finally, we introduce the subspace of functions $(u, U) \in H^1_\oplus(\Omega;\mathbb{K})$ where $u$ and $U$ are equal on the electrodes, $\partial E_1, \ldots, \partial E_N$: more precisely we define

$$\overline{H^1}(\Omega;\mathbb{K}) := \left\{(u, U) \in H^1_\oplus(\Omega;\mathbb{K}) \text{ such that } u|_{\partial E_k} = U_k \text{ for all } k = 1, \ldots, N\right\}.$$

3.1.1.3. *Function spaces involving time.* We now consider the spaces of functions involving time. We write such functions as $u(t,x) : Q_T \to \mathbb{K}$. We will typically suppose that for a.e. $t \in [0,T]$, $u(t,\cdot) \in X$ for some suitable choice of Banach space $X$. When this is the case, it is often convenient to consider such $u(t,x)$ not as a function of $t \in [0,T]$ and $x \in \Omega$, but rather as a mapping from $[0,T]$ into the Banach space $X$. We shall denote such functions in bold typeface. For example, given a function $u(t,x) : Q_T \to \mathbb{K}$ for a.e. $t \in [0,T]$, we associate the function

$$\mathbf{u} : [0,T] \to X$$

defined by

$$[\mathbf{u}(t)](x) := u(t,x) \text{ for a.e. } t \in [0,T] \text{ and } x \in \Omega.$$

Let $L$ be a Banach space on $[0,T]$ with norm $\|\cdot\|_L$. We denote the function spaces $L(0,T;X)$ to be

$$L(0,T;X) := \left\{ \mathbf{u} : [0,T] \to X \text{ such that } \left\| \|\mathbf{u}(t)\|_X \right\|_L < \infty \right\}.$$

Then $L(0,T;X)$ is itself a Banach space with the norm defined by

$$\|\mathbf{u}\|_{L(0,T;X)} := \left\| \|\mathbf{u}(t)\|_X \right\|_L \text{ for all } \mathbf{u} \in L(0,T;X).$$

Examples of such function spaces are $L^2(0,T;H^1_\diamond(\Omega;\mathbb{K}))$ and $C^1([0,T];H^1_U(\Omega;\mathbb{K}))$. Further details and definitions of such function spaces can be found in [69, Chapter 5.9.2].

**3.1.2. Poincaré's inequality.** Poincaré's inequality allows for the $L^2$ norm of a function to be controlled by the $L^2$ norm of its weak derivative (or more generally the $L^p$ norm of the function controlled by the $L^p$ norm of the weak derivative). However, this is certainly not true for a general function in $H^1(\Omega;\mathbb{K})$. Typically, Poincaré's inequality is stated (see [69, 70]) for functions in $H^1_0(\Omega;\mathbb{K})$—functions that have zero trace on the boundary, although, the more general Poincaré–Wirtinger inequality holds for all functions in $H^1(\Omega;\mathbb{K})$. However, Poincaré's inequality holds for other subspaces of $H^1(\Omega;\mathbb{K})$. We state and prove Poincaré's inequality in the function spaces $H^1_\diamond(\Omega;\mathbb{K})$,

$H^1_U(\Omega;\mathbb{K})$, $\dot{H}^1(\Omega;\mathbb{K})$ , and $\overline{H^1}(\Omega;\mathbb{K})$ introduced above. The proof in the case $\dot{H}^1(\Omega;\mathbb{K})$ is adapted from [161].

THEOREM 3 (Poincaré's inequality). *Let $\Omega \subset \mathbb{R}^d$ be an open, bounded, and connected domain with a $C^1$ boundary. Let $V \subset \partial\Omega$ be an open set with positive measure. Then the following hold.*

(1) For any $u \in H^1_\diamond(\Omega;\mathbb{K})$ or $u \in H^1_V(\Omega;\mathbb{K})$ there exists a constant $C > 0$ such that

$$\|u\|_{L^2(\Omega;\mathbb{K})} \leq C \|\nabla u\|_{L^2(\Omega;\mathbb{K})}, \tag{3.1.3}$$

where $C$ depends only on $d$, $\Omega$ and $V$.

(2) Similarly, if $(u, U) \in \dot{H}^1(\Omega;\mathbb{K})$ then

$$\|u\|_{\dot{H}^1(\Omega;\mathbb{K})} \leq C \left( \|\nabla u\|^2_{L^2(\Omega)} + \sum_{k=1}^{N} \int_{\partial E_k} |u(x) - U_k|^2 \, \mathrm{d}s \right)^{1/2} \tag{3.1.4}$$

where $C$ depends only on $d$, $\Omega$.

(3) Finally, for any $(u, U) \in \overline{H^1}(\Omega;\mathbb{K})$

$$\|u\|_{\overline{H^1}(\Omega;\mathbb{K})} \leq C \|\nabla u\|_{L^2(\Omega;\mathbb{K})} \tag{3.1.5}$$

where $C$ depends only on $d$ and $\Omega$.

PROOF. 1. We begin with the case when $u \in H^1_V(\Omega;\mathbb{K})$. Suppose for a contradiction that for every $k \in \mathbb{N} \setminus \{0\}$ there exists $u_k \in H^1_V(\Omega;\mathbb{K})$ such that

$$\|u_k\|_{L^2(\Omega;\mathbb{K})} > k \|\nabla u_k\|_{L^2(\Omega;\mathbb{K})}. \tag{3.1.6}$$

We may further assume by linearity that $\|u_k\|_{L^2(\Omega;\mathbb{K})} = 1$. In particular the functions $\{u_k\}_{k\in\mathbb{N}}$ are bounded in $H^1(\Omega;\mathbb{K})$. By applying the Rellich–Kondrachov theorem, we extract a subsequence $u_{k_j}$ and a limit function $u \in L^2(\Omega;\mathbb{K})$ such that $u_{k_j} \to u$ in $L^2(\Omega;\mathbb{K})$ and $\nabla u_{k_j} \rightharpoonup \nabla u$ in $L^2(\Omega;\mathbb{K})$. Then using (3.1.6), we deduce $\left\|\nabla u_{k_j}\right\|_{L^2(\Omega;\mathbb{K})} \to 0$ as $j \to \infty$. Since the norm is weakly lower semi-continuous,

$$\|\nabla u\|_{L^2(\Omega;\mathbb{K})} \leq \liminf_{n\to\infty} \left\|\nabla u_{k_j}\right\|_{L^2(\Omega;\mathbb{K})} = 0.$$

Therefore, $\nabla u = 0$ a.e. in $\Omega$. Furthermore,

$$u = 0 \text{ on } V \text{ and } \|u\|_{L^2(\Omega;\mathbb{K})} = 1. \tag{3.1.7}$$

By the fundamental theorem of calculus, which holds since $\Omega$ is connected, we conclude that $u$ is constant in $\Omega$. Since as $u = 0$ on $V$, it must be that $u = 0$ a.e. in $\Omega$. This conclusion contradicts (3.1.7).

Similarly, if $u \in H^1_\diamond(\Omega;\mathbb{K})$, following the same argument as above we obtain that the limit function $u$ is such that $\nabla u = 0$ a.e. in $\Omega$. Using $\|u\|_{L^2(\Omega;\mathbb{K})} = 1$ we obtain $u = 1/\sqrt{|\Omega|}$. Calculating the integral over the boundary, we compute

$$\int_{\partial\Omega} u \, \mathrm{d}s = |\partial\Omega| \, / \sqrt{|\Omega|} \neq 0,$$

a contradiction as required.

2. We denote the right hand side of inequality (3.1.4) by

$$|(u,U)| := C \left( \|\nabla u\|^2_{L^2(\Omega)} + \sum_{k=1}^{N} \int_{\partial E_k} |u(x) - U_k|^2 \, \mathrm{d}s \right)^{1/2}.$$

Let $(u,U) \in \dot{H}^1(\Omega;\mathbb{K})$ and suppose for a contradiction that there exists a sequence $\left\{(u_n,U_n) \in \dot{H}^1(\Omega;\mathbb{K})\right\}_{n\in\mathbb{N}}$ such that

$$\|(u_n,U_n)\|_{\dot{H}^1(\Omega;\mathbb{K})} = 1, \quad |(u_n,U_n)| < \frac{1}{n}.$$

Choose a sequence of constants $\{c_n\}_{n\in\mathbb{N}}$ such that the sequence $\left\{(w_n,W_n) \in \dot{H}^1(\Omega;\mathbb{K})\right\}_{n\in\mathbb{N}}$, defined by $(w_n,W_n) = (u_n - c_n, U_n - c_n\mathbf{1})$ satisfies

$$1 \leq \|w_n\|^2_{H^1(\Omega;\mathbb{K})} + \|W_n\|^2_{\mathbb{K}^N} < 1 + \frac{1}{n}. \tag{3.1.8}$$

By Rellich–Kondrachov there exists a subsequence, still indexed by $n$, that converges to some $w \in L^2(\Omega;\mathbb{K})$. Furthermore, since

$$\|\nabla w_{n_k}\|_{L^2(\Omega;\mathbb{K})} < \frac{1}{n},$$

for each $n$, $w_n$ converges in $H^1(\Omega;\mathbb{K})$ to a constant function $w = c_0$ for some $c_0 \in \mathbb{K}$. Since $H^1(\Omega;\mathbb{K}) \hookrightarrow L^2(\partial\Omega;\mathbb{K})$ with a compact embedding, $w_n \to c_0$ in $L^2\left(\cup_{k=1}^N \partial E_k;\mathbb{K}\right)$. We have

$$\sum_{k=1}^{N} \|w_n - W_n\|_{L^2(\partial E_k)} \leq |(w_n, W_n)| = |(u_n, U_n)| < \frac{1}{n},$$

the sequence $W_n$ also converges to $c_0 \in \mathbb{K}$ as $n \longrightarrow \infty$. Using (3.1.8) and the definition of $\|\cdot\|_{\dot{H}^1(\Omega;\mathbb{K})}$ ,

$$1 = \|(u_n, U_n)\|_{\dot{H}^1(\Omega;\mathbb{K})} \leq \|w_n - c_0\mathbf{1}\|^2_{H^1(\Omega;\mathbb{K})} + \|W_n - c_0\mathbf{1}\|^2_{\mathbb{K}^N} \to 0$$

which is a contradiction.

3. Finally, since $\overline{H^1}(\Omega;\mathbb{K}) \subset \dot{H}^1(\Omega;\mathbb{K})$ and $u|_{\partial E_k} = U_k$ for each $k = 1, \ldots, N$, the second term on the right hand side of (3.1.4) vanishes and the result follows. □

**3.1.3. Lax–Milgram lemma.** We state (without proof) the celebrated Lax–Milgram lemma that we shall use repeatedly to prove existence to the PDE models. A proof can be found in [69] for example.

THEOREM 4 (Lax–Milgram Lemma). *Let $X$ be a Hilbert space. Suppose the functional $B : X \times X \to \mathbb{K}$ satisfies the following conditions:*

*a) sesquilinearity: for all $\lambda, \mu \in \mathbb{C}$ and $x_1, x_2, x \in X$*

$$B(\lambda x_1 + \mu x_2, x) = \lambda B(x_1, x) + \mu B(x_2, x),$$

$$B(x, \lambda x_1 + \mu x_2) = \overline{\lambda} B(x, x_1) + \overline{\mu} B(x, x_2);$$

*b) boundedness: there exists a $C > 0$ such that $|B(x_1, x_2)| \leq C \|x_1\|_X \|x_2\|_X$ for all $x_1 \in X$ and $x_2 \in X$;*

*c) coercivity: there exists a $\delta > 0$ such that $|B(x, x)| \geq \delta \|x\|^2_X$ for all $x \in X$.*

*Then, for any continuous linear functional $f : X \to \mathbb{K}$ there exists a unique $x \in X$ such that $B(x, y) = f(y)$ for all $y \in X$.*

## 3.2. Frequency space models

In this section we consider the existence and uniqueness of solutions to Model 1 and Model 2. In this section all of the functions are complex valued and $\mathbb{K} = \mathbb{C}$. To simplify the notation, we drop the explicit reference to the field.

**3.2.1. Model 1.** The following theorem is sufficient to establish that a solution to (2.5.1) with boundary conditions given by (2.4.2) or (2.4.3) exists and is unique.

THEOREM 5. *Suppose $\Omega$ is a bounded, open domain in $\mathbb{R}^3$ with Lipschitz boundary denoted by $\partial\Omega$ that can be decomposed into disjoint components as*

$$\partial\Omega = \partial\Omega_D \cup \partial\Omega_N.$$

*Suppose $\gamma \in \mathcal{A}(\omega)$ for a fixed $\omega \in \mathbb{R} \setminus \{0\}$. We consider two cases:*

*Case 1.* *If $\partial\Omega_D$ has positive measure, then there exists a unique weak solution $u \in H^1(\Omega)$ to*

$$\begin{cases} -\operatorname{div}(\gamma\nabla u) = f & \text{in } \Omega, \\ u = \varphi & \text{on } \partial\Omega_D, \\ \gamma\nabla u \cdot \hat{n} = \psi & \text{on } \partial\Omega_N, \end{cases} \tag{3.2.1}$$

*for any $\varphi \in H^{1/2}(\partial\Omega_D)$ and $\psi \in H^{-1/2}(\partial\Omega_N)$, and $f \in H^{-1}(\Omega)$. Furthermore, there exists $C > 0$, depending on $\gamma$ and $\Omega$, such that*

$$\|u\|_{H^1(\Omega)} \leq C\left(\|\varphi\|_{H^{1/2}(\partial\Omega_D)} + \|\psi\|_{H^{-1/2}(\partial\Omega_N)} + \|f\|_{H^{-1}(\Omega)}\right). \tag{3.2.2}$$

*Case 2.* *If $\partial\Omega_D$ has zero measure, then there exists a unique weak solution $u \in H^1_\diamond(\Omega)$ to*

$$\begin{cases} -\operatorname{div}(\gamma\nabla u) = f & \text{in } \Omega, \\ \gamma\nabla u \cdot \hat{n} = \psi & \text{on } \partial\Omega_N, \end{cases} \tag{3.2.3}$$

*for any $\psi \in H^{-1/2}(\partial\Omega;\mathbb{C})$ and $f \in H^{-1}_\diamond(\Omega)$ such that*

$$\int_\Omega f\,dx + \int_{\partial\Omega} \psi\,ds = 0.$$

*Furthermore, there exists $C > 0$, depending on $\gamma$ and $\Omega$ such that*

$$\|u\|_{H^1(\Omega)} \leq C \left( \|\psi\|_{H^{-1/2}(\partial\Omega_N)} + \|f\|_{H^{-1}(\Omega)} \right). \tag{3.2.4}$$

The proof of Theorem 5 is not a direct application of the Lax-Milgram lemma since the given boundary data $\varphi \in H^{1/2}(\partial\Omega_D; \mathbb{C})$ is not necessarily in $H^{1/2}(\partial\Omega; \mathbb{C})$. If this condition is satisfied, when $\partial\Omega_N = \emptyset$ for example, then the proof of the theorem is a direct application of the Lax-Milgram lemma.

Proof of Theorem 5. We begin the proof by establishing the result for a homogeneous Dirchlet boundary condition: $\varphi = 0$. In this case, we seek a solution in the space $H^1_{\partial\Omega_D}(\Omega)$ and for concision, we write simply $H^1_D(\Omega)$ and denote the dual space by $H^{-1}_D(\Omega)$.

Testing (3.2.1) against $v \in H^1_D(\Omega)$ and using Green's theorem we establish the weak form of (3.2.1): $u \in H^1_D(\Omega)$ is a weak solution to (3.2.1) if and only if

$$\int_\Omega \gamma \nabla u \cdot \nabla \overline{v} \, \mathrm{d}x = \int_\Omega f \, \overline{v} \, \mathrm{d}x + \int_{\partial\Omega_N} \psi \, \overline{v} \, \mathrm{d}s \quad \text{for all} \quad v \in H^1_D(\Omega).$$

We define the sesquilinear form $B : H^1_D(\Omega) \times H^1_D(\Omega) \to \mathbb{C}$ by

$$B(u, v) := \int_\Omega \gamma \nabla u \cdot \nabla \overline{v} \, \mathrm{d}x \tag{3.2.5}$$

and the linear functional $L : H^1_D(\Omega) \mapsto \mathbb{C}$ by

$$L(v) := \int_\Omega f \, \overline{v} \, \mathrm{d}x + \int_{\partial\Omega_N} \psi \, \overline{v} \, \mathrm{d}s. \tag{3.2.6}$$

We check that $B$ and $L$ satisfy the conditions of the Lax-Milgram lemma.

- The boundedness of the bilinear form follows by the Cauchy-Schwarz inequality, namely,

$$|B(u, v)| \leq \|\gamma\|_{L^\infty(\Omega;\mathbb{C})} \left( \|\nabla u\|_{L^2(\Omega)} \, \|\nabla v\|_{L^2(\Omega)} \right). \tag{3.2.7}$$

Using Young's inequality, we establish that there exists a constant $C > 0$, depending on $\|\gamma\|_{L^\infty(\Omega)}$, such that

$$|B(u,v)| \leq C\left(\|u\|^2_{H^1_D(\Omega)} + \|v\|^2_{H^1_D(\Omega)}\right) \tag{3.2.8}$$

for all $u, v \in H^1_D(\Omega)$.

- Coercivity of $B(u,u)$ follows from the Poincaré-type inequality (3.1.3) established in Theorem 3. More verbosely,

$$\begin{aligned} B(u,u) &= \int_\Omega \gamma \left|\nabla u\right|^2 \\ &\geq c_0 \left\|\nabla u\right\|^2_{L^2(\Omega)} \\ &\geq \frac{c_0}{(1+c_p^2)} \left\|u\right\|^2_{H^1_D(\Omega),} \end{aligned} \tag{3.2.9}$$

  where $c_0$ is the lower bound on $\gamma \in \mathcal{A}$ and $c_p$ is the Poincaré constant.

- The boundedness of the linear functional $L(v)$ follows by definition of dual spaces: for any $v \in H^1_D(\Omega)$ we have

$$|L(v)| \leq \|f\|_{H_D^{-1}(\Omega)} \|v\|_{H^1_D(\Omega)} + \|\psi\|_{H^{-1/2}(\partial\Omega_N)} \|v\|_{H^{1/2}(\partial\Omega_N)}. \tag{3.2.10}$$

  By applying the trace inequality, for all $v \in H^1(\Omega)$ there exists a $C > 0$ such that $\|v\|_{H^{1/2}(\partial\Omega_N)} \leq C \|v\|_{H^1(\Omega;\mathbb{C})}$,, we establish that $L$ is bounded and

$$|L(v)| \leq \left(\|f\|_{H_D^{-1}(\Omega)} + \|\psi\|_{H^{-1/2}(\partial\Omega_N)}\right) \|v\|_{H^1_D(\Omega)}, \tag{3.2.11}$$

  holds for all $v \in H^1_D(\Omega)$.

The conditions of the Lax-Milgram theorem are satisfied and so we conclude that there exists a unique $u \in H^1_D(\Omega)$ satisfying $B(u,v) = 0$ for all $v \in H^1_D(\Omega)$.

We now consider the general case for a boundary condition given by $\varphi \in H^{1/2}(\partial\Omega_D)$. Let $G \in H^1(\Omega)$ be an extension, or lift, of $\varphi$ in $\Omega$ i.e. $G \in H^1(\Omega)$ satisfies $G|_{\partial\Omega_D} = \varphi$ and

$$\|G\|_{H^1(\Omega;\mathbb{C})} \leq \|\varphi\|_{H^{1/2}(\partial\Omega_D;\mathbb{C})}. \tag{3.2.12}$$

Furthermore, we have that

$$\operatorname{div}(\gamma \nabla G) \in H_D^{-1}(\Omega; \mathbb{C}) \tag{3.2.13}$$

and

$$\gamma \nabla G \cdot \hat{n}|_{\partial\Omega_N} \in H^{-1/2}(\partial\Omega_N; \mathbb{C}). \tag{3.2.14}$$

Let $w \in H_D^1(\Omega; \mathbb{C})$ be the weak solution to the equation

$$\begin{cases} -\operatorname{div}(\gamma \nabla w) = \widetilde{f} & \text{in } \Omega, \\ w = 0 & \text{on } \partial\Omega_D, \\ \gamma \nabla w \cdot \hat{n}\, \mathrm{d}s = \widetilde{\psi} & \text{on } \partial\Omega_N, \end{cases} \tag{3.2.15}$$

with $\widetilde{f} := f + \operatorname{div}(\gamma \nabla G) \in H_D^{-1}(\Omega)$ and $\widetilde{\psi} := \psi + \gamma \nabla G \cdot \hat{n} \in H^{-1/2}(\partial\Omega_N)$. We have already established that $w \in H_D^1(\Omega; \mathbb{C})$ exists and is unique. We define $u \in H^1(\Omega)$ by $u := w + G$. Using the linearity of the divergence operator, we establish that $u$ is the unique weak solution to (3.2.1).

We complete the proof of the Theorem by establishing the required bound on the $\|u\|_{H^1(\Omega)}$. Testing (3.2.15) against $\overline{w} \in H_D^1(\Omega)$, we establish

$$\int_\Omega \gamma \left|\nabla w\right|^2 \mathrm{d}x = \int_\Omega f \cdot \overline{w}\, \mathrm{d}x - \int_\Omega \gamma \nabla G \cdot \nabla \overline{w}\, \mathrm{d}x + \int_{\partial\Omega_N} \widetilde{\psi} \cdot \overline{w}\, \mathrm{d}s.$$

Thus

$$\int_\Omega \gamma \left|\nabla w\right|^2 \mathrm{d}x \leq C \left( \|f\|_{H_D^{-1}(\Omega)} + \|\psi\|_{H^{-1/2}(\partial\Omega_N)} + \|G\|_{H^1(\Omega)} \right) \|w\|_{H_D^1(\Omega)}$$

holds for some $C > 0$. Applying Poincaré's inequality, we deduce

$$\|w\|_{H_D^1(\Omega)}^2 \leq C \left( \|f\|_{H_D^{-1}(\Omega)} + \|\psi\|_{H^{-1/2}(\partial\Omega_N)} + \|G\|_{H^1(\Omega)} \right) \|w\|_{H_D^1(\Omega)}.$$

Using Young's inequality for some $\delta > 0$ and the triangle inequality the $\|w\|_{H_D^1(\Omega)}$ term on the right hand side can be incorporated into the left, and

$$\|w\|_{H_D^1(\Omega)}^2 \leq \frac{C}{\delta(1-\delta)} \left( \|f\|_{H_D^{-1}(\Omega)}^2 + \|\psi\|_{H^{-1/2}(\partial\Omega_N)}^2 + \|G\|_{H^1(\Omega)}^2 \right).$$

Finally, we establish that

$$\|u\|^2_{H^1(\Omega)} \leq C\left(\|f\|^2_{H_D^{-1}(\Omega)} + \|\psi\|^2_{H^{-1/2}(\partial\Omega_N)} + \|\varphi\|^2_{H^{1/2}(\partial\Omega_D)}\right)$$

holds for some $C > 0$ depending on $\gamma$ and $\Omega$. The required estimate then follows immediately. □

**3.2.2. Model 2.** We turn out attention to the existence and uniqueness of a solution to (2.5.3). The previous result cannot be applied in this case as only the average surface flux on each electrode is imposed. The novelty of this model is that only the total surface flux on each of the electrodes are imposed. In itself this is not well-posed, however, it turns out that constraining the voltage on the electrodes to be constant is sufficient to ensure existence and uniqueness. We state and prove this result.

THEOREM 6. *Given $\gamma \in \mathcal{A}(\omega)$ for a fixed frequency $\omega \in \mathbb{R}\setminus\{0\}$ and given $Q \in \mathbb{C}^N_\diamond$, there exists a unique solution $\left(u, (U_k)_{k=1}^N\right) \in \overline{H^1}(\Omega)$ such that*

$$\begin{cases} -div\,(\gamma(\omega)\nabla u) = 0 \quad \text{in } \Omega, \\ \qquad\qquad u = U_k \ \text{ on } \partial E_k \text{ for } k = 1,\dots,N, \\ \displaystyle\int_{\partial E_k} \gamma\nabla u\cdot\hat{n}\,ds = Q_k \ \text{ on } \partial E_k \text{ for } k = 1,\dots,N, \\ \qquad \gamma\nabla u\cdot\hat{n}\,ds = 0 \quad \text{on } \partial B. \end{cases} \tag{3.2.16}$$

Before we embark on a direct proof of this theorem, it is useful to establish the associated sesquilinear form to (3.2.16).

PROPOSITION 1. *Fix $\gamma \in \mathcal{A}$. If we assume $\left(u, (U_k)_{k=1}^N\right) \in \overline{H^1}(\Omega)$ is a weak solution to (3.2.16) for a given choice of $(Q_k)_{k=1}^N \in \mathbb{C}^N_\diamond$, then, for any $(v, V) \in \overline{H^1}(\Omega)$*

$$B((u,U),(v,V)) = \sum_{k=1}^N Q_k\overline{V}_k, \tag{3.2.17}$$

*with* $B : \overline{H^1}(\Omega) \times \overline{H^1}(\Omega) \to \mathbb{C}$ *defined by*

$$B((u,U),(v,V)) := \int_\Omega \gamma \nabla u \cdot \nabla \overline{v}\, dx. \tag{3.2.18}$$

*Conversely, if* $(u,U) \in \overline{H^1}(\Omega)$ *satisfies (3.2.17) for all* $(v,V) \in \overline{H^1}(\Omega)$ *and a given choice of* $(Q_k) \in \mathbb{C}^N_\diamond$*, then* $(u,U)$ *also satisfies (3.2.16).*

PROOF. Testing equation (3.2.16) against $(v,V) \in \overline{H^1}(\Omega)$ and using Green's theorem, we obtain

$$\int_\Omega \gamma \nabla u \cdot \nabla \overline{v}\, \mathrm{d}s - \int_{\partial\Omega} \gamma \nabla u \cdot \hat{n} \overline{v}\, \mathrm{d}s = 0. \tag{3.2.19}$$

Furthermore, since $\overline{v}|_{\partial E_k} = \overline{V}_k$ for each $k = 1, \dots, N$, the boundary integral term can be written as

$$\int_{\partial\Omega} \gamma \nabla u \cdot \hat{n} \overline{v}\, \mathrm{d}s = \sum_{k=1}^N \overline{V}_k \int_{\partial E_k} \gamma \nabla u \cdot \hat{n}\, \mathrm{d}s,$$

which in terms of $Q_k$ becomes

$$\int_{\partial\Omega} \gamma \nabla u \cdot \hat{n} \overline{v}\, \mathrm{d}s = \sum_{k=1}^N Q_k \overline{V}_k. \tag{3.2.20}$$

Note that since $\sum_{k=1}^N Q_k = 0$, the above identity does not depend on the choice of the representative in the class $(v,V)$. Combining, (3.2.19) and (3.2.20), we establish $\left(u, (U_k)_{k=1}^N\right) \in \overline{H^1}(\Omega)$ must satisfy (3.2.17) as required.

Conversely, suppose that $(u,U) \in \overline{H^1}(\Omega)$ satisfies (3.2.17) for all $(v,V) \in \overline{H^1}(\Omega)$. Choosing $v \in H^1(\Omega;\mathbb{C})$ such that $\mathrm{supp}(v) \subset \mathrm{int}(\Omega)$, where $\mathrm{int}(\Omega)$ denotes the interior of $\Omega$, and setting $V = 0$ then (3.2.17) becomes

$$\int_\Omega \gamma \nabla u \cdot \nabla v\, \mathrm{d}x = 0,$$

i.e. $u$ satisfies $-\mathrm{div}(\gamma \nabla u) = 0$ weakly in $\Omega$. Applying Green's theorem together with (3.2.17), it follows

$$\int_\Omega \gamma \nabla u \cdot \nabla \overline{v}\, \mathrm{d}x + \int_{\partial\Omega} \gamma \nabla u \cdot \hat{n} \overline{v}\, \mathrm{d}s = \sum_{k=1}^N Q_k \overline{V}_k$$

as required. □

We now prove Theorem 6.

PROOF OF THEOREM (6). Combining Proposition 1 and the Lax-Milgram lemma, it suffices to prove that $B$ is a bounded, coercive sesquilinear form that satisfies the assumptions of the Lax-Milgram lemma and that the functional

$$f\left(\left(v, V_{k=1}^{N}\right)\right) = \sum_{k=1}^{N} Q_k \cdot \overline{V_k}$$

is well-defined and continuous. We begin by considering the functional $f$.

Suppose that $(v, V) \sim (v_2, V_2)$ in $\overline{H^1}(\Omega)$, then $(v_1, V_1)$ and $(v_2, V_2)$ differ by a constant, which we denote by $k \in \mathbb{C}$. Since $\sum_{k=1}^{N} Q_k = 0$,

$$f(v_1, V_1) = \sum_{k=1}^{N} Q_k \cdot \overline{V_1} = \sum_{k=1}^{N} Q_k \cdot \left(\overline{V_1} - k\right) = \sum_{k=1}^{N} Q_k \cdot \overline{V_2} = f(v_2, V_2)$$

thus $f$ is well-defined. Using the definition of the infimum, for $(v, V) \in \overline{H^1}(\Omega)$ and every $c \in \mathbb{C}$ there exists $\varepsilon > 0$ such that

$$\left(\|v - c\|_{H^1(\Omega)}^2 + \|V - c\mathbf{1}\|_{\mathbb{C}^N}^2\right)^{1/2} \leq \|(v, V)\|_{\overline{H^1}(\Omega)} + \varepsilon. \tag{3.2.21}$$

Then for any $(v, V) \in \overline{H^1}(\Omega)$,

$$|f(v, V)| \leq \|Q\|_{\mathbb{C}^N} \|V - c\mathbf{1}\|_{\mathbb{C}^N},$$

which, using (3.2.21), becomes

$$|f(v, V)| \leq \|Q\|_{\mathbb{C}^N} \left(\|(v, V)\| + \varepsilon\right).$$

Passing to the limit as $\varepsilon \to 0$, we establish $f$ is a continuous linear functional on $\overline{H^1}(\Omega)$. By similar arguments to the above, $B$ can be shown to be a bounded, coercive sesquilinear form. □

We conclude this section by remarking that the above proof can be adapted to prove that the complete electrode model is well-posed. In this case, the solution

$(u, U) \in \dot{H}^1(\Omega)$ is given as the weak solution to

$$B((u,U),(v,V)) = \sum_{k=1}^{N} Q_k \overline{V}_k$$

with the sesquilinear form given by

$$B((u,U),(v,V)) := \int_\Omega \gamma \nabla u \cdot \nabla \overline{v} \, \mathrm{d}x + \sum_{k=1}^{N} \frac{1}{z_k} \int_{\partial E_k} (u - U_k)(\overline{v} - \overline{V}_k) \, \mathrm{d}s.$$

We omit the details of the proof here but refer the reader to [161].

## 3.3. Time dependent models

We turn our attention to the well-posedness of the models in the time domain. In this section, we set $\mathbb{K} = \mathbb{R}$ throughout. For convenience, we define $\mathcal{A}$ be the set of pairs of admissible permittivity and conductivity distributions that do not depend on time:

$$\mathcal{A} := \{(\varepsilon, \sigma) \in \mathcal{A}_\mathrm{p} \times \mathcal{A}_\mathrm{c}\},$$

where $\mathcal{A}_\mathrm{p}$ is defined by (2.2.2) and $\mathcal{A}_\mathrm{c}$ by (2.2.1). More generally, we consider parameters that evolve in time. Recall the definition of $\mathcal{A}_\mathrm{TD}$ given by (2.2.3):

$$\mathcal{A}_\mathrm{TD} := \left\{(\varepsilon,\sigma) : \sigma \in C^1(\mathbb{R}; \mathcal{A}_\mathrm{c}) \text{ and } \varepsilon \in C^1(\mathbb{R}; \mathcal{A}_\mathrm{p}) \text{ s.t. } (\partial_t \varepsilon) = (\partial_t \sigma) = 0 \text{ for } t \geq T_0\right\}$$

for some $T_0 > 0$.

By this definition, for each parameter $(\varepsilon, \sigma) \in \mathcal{A}_\mathrm{TD}$ we have $\partial_t \varepsilon(t, \cdot) = 0$ for sufficiently large $t$. Therefore, for $t > T_0$, $(\varepsilon(t,\cdot), \sigma(t,\cdot)) \in \mathcal{A}$ and long-time existence for parameters in $\mathcal{A}_\mathrm{TD}$ can be established from the existence of solutions to $\mathcal{A}$, provided short-time existence of solutions holds for parameters in $\mathcal{A}_\mathrm{TD}$. We use this framework and establishing the existence and uniqueness result in two parts: firstly, we establish existence and uniqueness of a solution with $(\varepsilon, \sigma) \in \mathcal{A}$, and as a corollary establish existence for a solution with $\varepsilon, \sigma \in \mathcal{A}_\mathrm{TD}$.

**3.3.1. Model 3.** We begin by defining a weak solution to (2.5.4). We generalise the PDE slightly: for any parameter $(\varepsilon, \sigma) \in \mathcal{A}_\mathrm{TD}$ and $T > 0$, we denote by $u$ :

$[0,T]\times\Omega\to\mathbb{R}$ the weak solution of

$$\begin{cases} -\operatorname{div}\left(\partial_t\left(\varepsilon\nabla u\right)+\sigma\nabla u\right)=f & \text{in } [0,T]\times\Omega,\\ u=\varphi & \text{on } (0,T]\times\partial\Omega_D,\\ \partial_t\left(\varepsilon\nabla u\right)\cdot\hat{n}=\psi & \text{on } (0,T]\times\partial\Omega_N,\\ u(0,x)=u_0 & \text{in } \Omega, \end{cases} \tag{3.3.1}$$

where the time dependent boundary conditions $\varphi(t,x)$ and $\psi(t,x)$, the source term $f(t,x)$, and initial condition $u_0$ are given. Testing against $v\in H^1(\Omega)$ and using Green's theorem, we establish for a.e. $t\in[0,T]$

$$\int_\Omega \varepsilon\partial_t\left(\nabla\mathbf{u}\right)\cdot\nabla v\,\mathrm{d}x+\int_\Omega\left[\left(\partial_t\varepsilon\right)+\sigma\right]\nabla\mathbf{u}\cdot\nabla v\,\mathrm{d}x=\int_{\partial\Omega_D}\left[\varepsilon\partial_t\left(\nabla\mathbf{u}\right)\cdot\hat{n}\;+\left(\partial_t\varepsilon\right)\nabla\mathbf{u}\cdot\hat{n}\right]v\,\mathrm{d}s + \int_{\partial\Omega_N}\psi v\,\mathrm{d}s+\int_\Omega\mathbf{f}v\,\mathrm{d}x. \tag{3.3.2}$$

Note that $\int_{\partial\Omega}\sigma\nabla u\cdot\hat{n}v\,\mathrm{d}s=0$ for any $u,v\in H^1(\Omega)$ by virtue of $\sigma\equiv 0$ near $\partial\Omega$. We use this identity in the definition of a weak solution to equation (3.3.1) in $[0,T]\times\Omega$.

Definition 6. Let $(\varepsilon,\sigma)\in\mathcal{A}_{\mathrm{TD}}$ be fixed. Suppose $H(\Omega)\subset H^1(\Omega)$ is a subspace of functions where the Poincaré inequality holds. Denote the dual space to $H(\Omega)$ by $H^{-1}(\Omega)$. We say that a function

$$u\in L^\infty\left(0,T;H(\Omega)\right),\ \text{with } \partial_t u\in L^2\left(0,T;H(\Omega)\right),$$

is a weak solution of (3.3.1) provided:

(i) $f\in L^2(0,T;H^{-1}(\Omega))$, $\varphi\in C^1\left([0,T];H^{1/2}\left(\partial\Omega_D\right)\right)$, $\psi\in C^1\left([0,T];H^{-1/2}\left(\partial\Omega_N\right)\right)$, and $u_0\in H(\Omega)$;

(ii) (3.3.2) holds for each $v\in H$ and a.e. $t\in[0,T]$;

(iii) $u|_{\partial\Omega_D}(t)=\varphi(t)$ for all $t\in[0,T]$;

(iv) and, $\mathbf{u}(0,\cdot)=u_0$.

If $\partial\Omega_D$ is empty, we also require that

(v) $\int_{\partial\Omega}\psi\,\mathrm{d}s+\int_\Omega f\,\mathrm{d}x=0$ holds for a.e. $t\in[0,T]$.

We now state and prove the main result of this chapter.

THEOREM 7. *Fix $(\varepsilon, \sigma) \in \mathcal{A}_{TD}$, $f \in L^2(0,T;H^{-1}(\Omega))$ and $T > 0$.*

*Case 1.* *If $\partial\Omega_D$ has positive measure, then, for any $\varphi \in H^1\left(0,T;H^{1/2}\left(\partial\Omega_D\right)\right)$ and $\psi \in H^1\left(0,T;H^{-1/2}(\partial\Omega_N)\right)$ there exists a unique $u \in H^1\left(0,T;H^1(\Omega)\right)$ that is the weak solution to (3.3.1). Furthermore,*

$$\begin{aligned}\max_{t\in[0,T]} \|u\|_{H^1(\Omega)} \leq C \Big(\sqrt{T}\left(\|f\|_{L^2(0,T;H^{-1}(\Omega))} + \|\psi\|_{L^2\left(0,T;H^{-1/2}(\partial\Omega_N)\right)}\right) \\ + \left(1+\sqrt{T}\right)\|\varphi\|_{H^1\left(0,T;H^{1/2}(\partial\Omega_D)\right)} + \|u_0\|_{H^1_D(\Omega)}\Big)\end{aligned} \tag{3.3.3}$$

*and*

$$\begin{aligned}\|\partial_t u\| \leq C \Big(\|f\|_{L^2(0,T;H^{-1}(\Omega))} + \|\psi\|_{L^2\left(0,T;H^{-1/2}(\partial\Omega_N)\right)} \\ + \|u_0\|_{H^1_D(\Omega)} + \|\varphi\|_{H^1\left(0,T;H^{1/2}(\partial\Omega_D)\right)}\Big).\end{aligned} \tag{3.3.4}$$

*Case 2.* *If $\partial\Omega_D$ has zero measure, then, for any $\psi \in H^1\left(0,T;H^{-1/2}_{\diamond}(\partial\Omega_N)\right)$ there exists $u \in H^1(0,T;H^1_{\diamond}(\Omega))$ that is the unique weak solution to (3.3.1) provided*

$$\int_\Omega f\, dx + \int_{\partial\Omega} \psi\, ds = 0.$$

*Furthermore,*

$$\max_{t\in[0,T]} \|u\|_{H^1(\Omega)} \leq C\left(\sqrt{T}\left(\|f\|_{L^2(0,T;H^{-1}(\Omega))} + \|\psi\|_{L^2\left(0,T;H^{-1/2}(\partial\Omega_N)\right)}\right) + \|u_0\|_{H^1_D(\Omega)}\right)$$

*and*

$$\|\partial_t u\|_{L^2(0,T;H^1(\Omega))} \leq C\left(\|f\|_{L^2(0,T;H^{-1}(\Omega))} + \|\psi\|_{L^2\left(0,T;H^{-1/2}(\partial\Omega_N)\right)} + \|u_0\|_{H^1_D(\Omega)}\right) \tag{3.3.5}$$

*In both cases, the constant $C > 0$ depends on $\Omega$, the norms of $\varepsilon$ and $\sigma$, and the coercivity bound on $\varepsilon$ only.*

REMARK. We remark that that using the Cauchy-Schwarz inequality,

$$\begin{aligned}\frac{1}{\sqrt{T}+1}\left\|u\right\|_{H^1(0,T;H^1(\Omega))} &\leq \max_{t\in[0,T]}\left\|u\right\|_{H^1(\Omega)} + \left\|\partial_t u\right\|_{L^2(0,T;H^1(\Omega))} \\ &\leq \left(T^{-\frac{1}{4}} + T^{\frac{1}{4}}\right)^2 \left\|u\right\|_{H^1(0,T;H^1(\Omega))} .,\end{aligned}$$

Therefore,

$$\max_{t\in[0,T]}\left\|\cdot\right\|_{H^1(\Omega)} + \left\|\partial_t\cdot\right\|_{L^2(0,T;H^1(\Omega))}$$

is equivalent to the canonical norm on $H^1\left(0,T;H^1(\Omega)\right)$.

The proof of this result follows from a Galerkin argument; similar proofs can be found in standard graduate texts on PDE theory, see for example [69]. The aim is to prove the convergence of a bounded sequence of approximate solutions, extract a weakly convergent subsequence using a compactness result, and finally, demonstrate that the limit function also satisfies the PDE. Uniqueness of the solution then follows by an energy argument.

We give details of this argument in the homogeneous case when $\varphi = 0$ on $\partial\Omega_D$. The full result follows by choosing an extension operator of a $\varphi \in H^1\left(0,T;H^{1/2}\left(\partial\Omega_D\right)\right)$ as in the proof of Theorem 5 and modifying the source term accordingly. Therefore, we prove existence in the space $H^1_{\partial\Omega_D}(\Omega)$, defined in (3.1.2), which we denote by $H^1_D(\Omega)$. We denote the dual space by $H^{-1}_D(\Omega)$ with the the duality pairing between $H^1_D(\Omega)$ and $H^{-1}_D(\Omega)$ by $\langle\langle\cdot,\cdot\rangle\rangle$.

PROOF. We begin by constructing the of approximate solutions. We denote by $\varepsilon_\infty \in \mathcal{A}_{\mathrm{p}}$ the $t\to\infty$ limit of $\varepsilon(t)$. Let $w_k \in H^1_D(\Omega)$ be the eigenfunctions of the self-adjoint operator $\operatorname{div}\left(\varepsilon_\infty\nabla\cdot\right) : H^1_D(\Omega) \to H^{-1}_D(\Omega)$, with associated eigenvalues $\lambda_k \in \mathbb{R}$. Without loss of generality, the eigenfunctions are chosen to form an orthonormal basis of $L^2(\Omega)$ and an orthogonal basis of $H^1_D(\Omega)$. We suppose that the eigenfunctions are ordered so that $\lambda_k$ form an increasing sequence. Define the finite subspaces of $E_m \subset H^1_D(\Omega)$ for $m \in \mathbb{N}$ to be

$$E_m := \operatorname{span}_{k=1,\ldots,m}\left\{w_k\right\}.$$

We seek coefficients such that the approximate solutions, $u_m \in H_D^1(\Omega)$, can be expressed in this basis: namely, for some some absolutely continuous functions $d_k^m : [0,T] \to \mathbb{R}$

$$u_m(t,x) = \sum_{k=1}^{m} d_k^m(t) w_k(x). \tag{3.3.6}$$

By a direct calculation, $u_m$ is a solution of (3.3.1) if and only if $d_k^m$ satisfy the initial value problem

$$\sum_{j=1}^{m} A_{kj} \frac{\mathrm{d}}{\mathrm{d}t} d_j^m(t) = \left[ \psi_k + f_k - \sum_{j=1}^{m} B_{kj} d_j^m(t) \right], \; d_k^m(0) = \langle u_0, w_k \rangle_{L^2(\Omega)}, \tag{3.3.7}$$

for a.e. $0 \leq t \leq T$ and every $k = 1, ..., m$, where

$$A_{kj}(t) = \int_\Omega \varepsilon \nabla w_k \cdot \nabla w_j \, \mathrm{d}x, \tag{3.3.8}$$

$$B_{kj}(t) = \int_\Omega (\sigma + \partial_t \varepsilon) \nabla w_k \cdot \nabla w_j \, \mathrm{d}x, f_k(t) = \langle f(\cdot,t), w_k \rangle_{H^{-1}(\Omega), H^1(\Omega)}, \tag{3.3.9}$$

and

$$\psi_k(t) = \langle \psi(t,\cdot), w_k \rangle_{H^{-1/2}(\partial\Omega_N), H^{1/2}(\partial\Omega_N)}. \tag{3.3.10}$$

We note that by the definition of the eigenfunctions $w_k$, $A$ can be factorised with $A = Q\Lambda Q^T$ where $Q \in \mathbb{R}^{m \times m}$ is an orthogonal matrix and $\Lambda \in \mathbb{R}^{m \times m}$ is a diagonal matrix with positive diagonal elements. The ODE then becomes

$$\frac{\mathrm{d}}{\mathrm{d}t} d^m = Q\Lambda^{-1} Q^T \left[ \psi + f - B d^m \right] \tag{3.3.11}$$

in vectorised form.

By Caratheodory's theorem, there exists an absolutely continuous solution to (3.3.11) in the subinterval $[0, T^*)$ for some $0 < T^* \leq T$. Using the energy inequality (3.3.13), we establish that the solution cannot blow up at $t = T^*$. By iteratively applying this argument, an increasing sequence of wider intervals can be written that eventually covers the whole interval $[0,T]$. Therefore, for each $m \in \mathbb{N}$ the function defined by (3.3.6) is an approximate solution to the PDE in the space $E_m$. Moreover, since (3.3.7) is linear, the solution is unique.

We remark that in situation when $(\varepsilon, \sigma) \in \mathcal{A}$ the analysis simplifies by choosing $w_k \in H^1_D(\Omega)$ to be eigenfunctions of the operator $-\mathrm{div}\,(\varepsilon\nabla\cdot) : H^1_D(\Omega) \to H^{-1}_D(\Omega)$. Denote the corresponding eigenvalue by $\lambda_k > 0$. In which case, ODE (3.3.7) becomes

$$\frac{\mathrm{d}}{\mathrm{d}t} d_k^m(t) = \frac{1}{\lambda_k}\left[\psi_k + f_k - \sum_{j=1}^{m} a_{kj} d_j^m(t)\right], \quad d_k^m(0) = \langle u_0, w_k\rangle_{L^2(\Omega)},$$

for each $k = 1, \ldots, m$ with

$$a_{kj} = \int_\Omega \sigma\nabla w_k \cdot \nabla w_j \,\mathrm{d}x. \tag{3.3.12}$$

Applying Caratheodory's theorem in the same manner using an analogous inequality (3.3.13), existence of approximate solutions can be established.

LEMMA 3. *For every $m \in \mathbb{N}$, there exists a unique approximate solution $u_m \in W^{1,1}([0,T]; E_m)$ of equation (3.3.1).*

In order to pass to the limit as $m \to \infty$ and establish existence of the solutions on $[0,T]$, it is necessary to establish uniform energy estimates. We state the energy estimates in the following lemma and postpone the proof until after the proof of the main theorem.

LEMMA 4. *Let $(u_m)_{m\in\mathbb{N}}$ be the sequence of approximate solutions whose existence is established in Lemma 3. Then for all $m \in \mathbb{N}$ there holds*

$$\begin{aligned}\|u_m\|_{L^\infty\left(0,T;H^1_D(\Omega)\right)} + \|\partial_t u_m\|_{L^2\left(0,T;H^1_D(\Omega)\right)} \le C\Big(&\|f\|_{L^2(0,T;H^{-1}(\Omega))} \\ &+ \|\psi\|_{L^2\left(0,T;H^{-1/2}(\partial\Omega_N)\right)} + \|u_0\|_{H^1_D(\Omega)}\Big),\end{aligned} \tag{3.3.13}$$

*for some constant $C > 0$ depending on $T$, $\Omega$, the norms of $\varepsilon$ and $\sigma$, and the coercivity bound on $\varepsilon$ only. Furthermore,*

$$\|\partial_t u_m\|^2_{L^2\left(0,T;H^1_D(\Omega)\right)} \le C\left(\|f\|^2_{L^2(0,T;H^{-1}(\Omega))} + \|\psi\|^2_{H^1\left(0,T;H^{-1/2}(\partial\Omega_N)\right)} + \|u_0\|^2_{H^1_D(\Omega)}\right),$$

*where the constant $C > 0$ depends on $\Omega$, the norms of $\varepsilon$ and $\sigma$, and the coercivity bound on $\varepsilon$ only. In particular, $C$ does not depend on $T$.*

Continuing with the proof of the main theorem, using the uniform energy estimate (3.3.13) it follows that the sequence $\{u_m\}_{m=1}^{\infty}$ is bounded in $L^{\infty}\left(0,T;H_D^1(\Omega)\right)$ and $\{\partial_t u_m\}_{m=1}^{\infty}$ is bounded in $L^2\left(0,T;H_D^1(\Omega)\right)$. Hence, there exists a subsequence $\{u_{m_\ell}\}_{\ell=1}^{\infty} \subset \{u_m\}_{m=1}^{\infty}$ and a limit function $u \in L^{\infty}\left(0,T;H_D^1(\Omega)\right)$ with $\partial_t u \in L^2\left(0,T;H_D^1(\Omega)\right)$ such that

$$\begin{cases} u_{m_l} \overset{w^*}{\rightharpoonup} u & \text{in } L^{\infty}\left(0,T;H_D^1(\Omega)\right) \text{ and,} \\ \partial_t u_{m_l} \overset{w}{\rightharpoonup} \partial_t u & \text{in } L^2\left(0,T;H_D^1(\Omega)\right). \end{cases} \tag{3.3.14}$$

Passing to the limit in (3.3.2) for this subsequence, we establish the limit function $u \in L^{\infty}\left(0,T;H_D^1(\Omega)\right)$ also satisfies the weak form of the equation. By definition, the limit function is a weak solution to the equation. Moreover, by the Aubin–Lions–Simon lemma[1] [69, 158], we can conclude that $u \in C\left([0,T];H^1(\Omega)\right)$.

Passing to the limit in (3.3.13) and using the weak-star sequential lower semi-continuity of the norms, we can establish the same energy estimate holds for the limit function $u \in L^{\infty}\left(0,T;H_D^1(\Omega)\right)$.

It remains to prove that the solution to (3.3.1) is unique. This follows from the energy estimate and linearity of the equation: suppose $u_1$ and $u_2$ are two distinct solutions to equation (3.3.1), then the difference $u_1 - u_2$ is also a solution to the same equation with homogeneous initial and boundary conditions. Applying Lemma 4 to the difference $u_1 - u_2$, we establish

$$||u_1 - u_2||_{L^{\infty}\left(0,T;H_D^1(\Omega)\right)} + ||\partial_t u_1 - \partial_t u_2||_{L^2\left(0,T;H_D^1(\Omega)\right)} = 0. \tag{3.3.15}$$

and so $u_1 = u_2$ in $Q_T$. This concludes the proof of the theorem. □

We now consider the proof of the energy estimates in Lemma 4

[1] See also the statement of Theorem 3 in Section 5.9.2 in [69].

PROOF OF LEMMA 4. Using $u_m(t,\cdot) \in H^1_D(\Omega)$, which exists by Lemma 3, as a test function in the weak form, we obtain for each $0 \leq t \leq T$

$$\int_{Q_t} \varepsilon \left(\partial_t \nabla u_m\right) \cdot \nabla u_m \,\mathrm{d}x\mathrm{d}s + \int_{Q_t} \left[\sigma + \partial_t \varepsilon\right] |\nabla u_m|^2 \,\mathrm{d}x\mathrm{d}s = \int_0^t \langle f, u_m \rangle_{H_D^{-1}(\Omega), H_D^1(\Omega)} \,\mathrm{d}s + \int_0^t \langle \psi, u_m \rangle_{H^{-1/2}(\partial\Omega_N), H^{1/2}(\partial\Omega_N)} \,\mathrm{d}s. \tag{3.3.16}$$

The right-hand side of (3.3.16) can be bounded above using the Cauchy-Schwarz inequality to obtain

$$\text{RHS} \leq \|f\|_{L^2\left(0,t;H_D^{-1}(\Omega)\right)} \|u_m\|_{L^2\left(0,t;H_D^1(\Omega)\right)} + \|\psi\|_{L^2\left(0,t;H^{-1/2}(\partial\Omega_N)\right)} \|u_m\|_{L^2\left(0,t;H^{1/2}(\partial\Omega_N)\right)}. \tag{3.3.17}$$

Since $u_m(t,\cdot) \in H^1_D(\Omega)$ it is possible to bound the second term from above by $\|u_m\|_{L^2\left(0,t;H_D^1(\Omega)\right)}$ using the trace inequality. Estimate (3.3.17) then becomes

$$\text{RHS} \leq C\left(\Omega\right) \left( \|f\|_{L^2(0,t;H^{-1}(\Omega))} + \|\psi\|_{L^2\left(0,t;H^{-1/2}(\partial\Omega_N)\right)} \right) \|u_m\|_{L^2\left(0,t;H_D^1(\Omega)\right)}. \tag{3.3.18}$$

We now turn to the left-hand side and derive a lower bound. By integration by parts, we have

$$\begin{aligned} \text{LHS} &= \frac{1}{2} \int_0^t \varepsilon \partial_t \int_\Omega |\nabla u_m|^2 \,\mathrm{d}x\mathrm{d}t + \int_{Q_t} \left(\sigma + \partial_t \varepsilon\right) |\nabla u_m|^2 \,\mathrm{d}x\mathrm{d}t \\ &= \frac{1}{2} \int_\Omega \varepsilon(t,\cdot) \left|\nabla u_m(t,\cdot)\right|^2 \mathrm{d}x - \frac{1}{2} \int_\Omega \varepsilon\left(0,\cdot\right) \left|\nabla u_m(0,\cdot)\right| \,\mathrm{d}x \\ &\quad - \int_0^t \partial_t \varepsilon \left\|\nabla u_m(t,\cdot)\right\|_{L^2(\Omega)} + \int_{Q_t} \left(\sigma + \partial_t \varepsilon\right) \nabla u_m \cdot \nabla u_m \,\mathrm{d}x\mathrm{d}t. \end{aligned} \tag{3.3.19}$$

Therefore,

$$\text{LHS} \geq \frac{1}{2} \varepsilon_0 C\left(\Omega, T_0, \|\varepsilon\|_{C^1(0,t;L^\infty(\Omega))}\right) \|u_m(t,\cdot)\|^2_{H^1_D(\Omega)} - \|\varepsilon\left(0,\cdot\right)\|_{L^\infty(\Omega)} \|u_0\|^2_{H^1_D(\Omega)} \tag{3.3.20}$$

by applying the Poincaré Inequality on $H^1_D(\Omega)$, the coercivity assumption on $\varepsilon$ and the assumption that $\partial_t \varepsilon(t,\cdot) = 0$ for all $t \geq T_0 > 0$. Combining (3.3.18), (3.3.20), and

integrating both sides with respect to $t$, we deduce

$$\begin{aligned}
&\frac{1}{2}\varepsilon_0 C(\Omega)\,\|u_m(t,\cdot)\|^2_{L^2\left(0,t;H^1_D(\Omega)\right)}\\
&\leq t\left(\|\varepsilon(0,\cdot)\|_{L^\infty(\Omega)}\,\|u_0\|^2_{H^1_D(\Omega)}\right.\\
&\qquad\left.+\,C\left(\Omega,T_0,\|\varepsilon\|_{C^1(0,t;L^\infty(\Omega))}\right)\left(\|f\|_{L^2(0,t;H^{-1}(\Omega))}+\|\psi\|_{L^2\left(0,t;H^{-1/2}(\partial\Omega_N)\right)}\right)\|u_m\|_{L^2\left(0,t;H^1_D(\Omega)\right)}\right),
\end{aligned}$$

which implies

$$\begin{aligned}
\|u_m(t,\cdot)\|_{L^2\left(0,t;H^1_D(\Omega)\right)} \leq C\left(\Omega,\varepsilon_0,\|\varepsilon\|_{C^1(0,t;L^\infty(\Omega))}\right)\Big(t\,\|f\|_{L^2(0,t;H^{-1}(\Omega))}\\
+\|\psi\|_{L^2\left(0,t;H^{-1/2}(\partial\Omega_N)\right)}+\|u_0\|_{H^1_D(\Omega)}\Big).
\end{aligned}\tag{3.3.21}$$

Inserting (3.3.20) into (3.3.18) and using the lower bound (3.3.20)

$$\begin{aligned}
\|u_m(t,\cdot)\|^2_{H^1_D(\Omega)} \leq C\left(\Omega,\varepsilon_0,\|\varepsilon\|_{C^1(0,t;L^\infty(\Omega))}\right)\|u_0\|^2_{H^1_D(\Omega)}\\
+C\left(\Omega,\varepsilon_0,\|\varepsilon\|_{C^1(0,t;L^\infty(\Omega))}\right)t\left(\|f\|^2_{L^2(0,t;H^{-1}(\Omega))}\right.\\
\left.+\|\psi\|^2_{L^2\left(0,t;H^{-1/2}(\partial\Omega_N)\right)}+\|u_0\|^2_{H^1_D(\Omega)}\right).
\end{aligned}$$

Finally, taking the supremum over all $t\in[0,T]$,

$$\begin{aligned}
\|u_m\|_{L^\infty\left(0,T;H^1_D(\Omega)\right)} \leq C\left(\Omega,\varepsilon_0,\|\varepsilon\|_{C^1(0,t;L^\infty(\Omega))}\right)\Big(\sqrt{T}\,\|f\|_{L^2(0,T;H^{-1}(\Omega))}\\
+\sqrt{T}\,\|\psi\|_{L^2(0,T;H^{-1/2}(\partial\Omega_N)}+\|u_0\|_{H^1_D(\Omega)}\Big)
\end{aligned}\tag{3.3.22}$$

and the required bound for $u_m$ follows.

We now establish the required inequality on $\partial_t u_m$. Fix any $v\in H^1_D(\Omega)$ with $\|v\|_{H^1_D(\Omega)}\leq 1$. This $v$ can be decomposed as $v=v^1+v^2$ where $v^1\in E_m$ and $\langle v^2,w\rangle_{H^1_D(\Omega)}=0$ for all $w\in E_m$. Then for a.e. $t\in[0,T]$

$$\begin{aligned}
\int_\Omega \partial_t(\varepsilon\nabla u_m)\cdot\nabla v\,\mathrm{d}x &= \int_\Omega \partial_t(\varepsilon\nabla u_m)\cdot\nabla v^1\,\mathrm{d}x+\\
&\leq \langle\psi,v^1\rangle_{H^{-1/2}(\partial\Omega_N),H^{1/2}(\partial\Omega_N)}+\left\langle f,v^1\right\rangle_{H^{-1}_D,H^1}-\int_\Omega\sigma\nabla u_m\cdot\nabla v^1\,\mathrm{d}x.
\end{aligned}$$

Since $\|v\|_{H^1_D(\Omega)} \leq 1$, inequality (3.3.22) implies

$$\|\operatorname{div}(\partial_t(\varepsilon\nabla u_m))\|^2_{H^{-1}(\Omega)} \leq C\left(\|f\|^2_{H^{-1}(\Omega)} + \|\psi\|^2_{H^{-1/2}(\partial\Omega_N)} + \|u_0\|^2_{H^1_D(\Omega)}\right) \tag{3.3.23}$$

for a.e. $t \in [0,T]$.

Furthermore, since $\varepsilon$ is bounded and coercive we can form the following elliptic PDE for $z_m$ at a.e. $t \in [0,T]$

$$\begin{cases} -\operatorname{div}(\varepsilon(t,\cdot)\nabla z_m) = -\operatorname{div}(\varepsilon(t,\cdot)\partial_t(\nabla u_m)) & \text{in } \Omega, \\ z_m = 0 & \text{on } \partial\Omega_D, \\ \varepsilon(t,\cdot)\nabla z_m \cdot \hat{n} = \partial_t\left(\sum_{k=1}^m \psi_k(t) w_k\right) & \text{on } \partial\Omega_N, \end{cases} \tag{3.3.24}$$

where $\psi_k(t) = \langle \psi(t,\cdot), w_k\rangle_{H^{-1/2}(\partial\Omega_N), H^{1/2}(\partial\Omega_N)}$.

Solutions to (3.3.24) exist by the Lax–Milgram lemma and by uniqueness we have $z_m = \partial_t u_m \in H^1_D(\Omega)$. Moreover,

$$\|\partial_t u_m\|^2_{H^1_D(\Omega)} \leq C\left(\|\operatorname{div}(\partial_t(\varepsilon(t,\cdot)\nabla u_m))\|^2_{H^{-1}(\Omega)} + \|\partial_t\psi\|_{H^{-1/2}(\partial\Omega_N)}\right), \tag{3.3.25}$$

holds for a.e. $t \in [0,T]$. Combining (3.3.23) and (3.3.25), we deduce

$$\|\partial_t u_m\|^2_{H^1_D(\Omega)} \leq C\left(\|f\|^2_{H^{-1}(\Omega)} + \|\psi\|^2_{H^{-1/2}(\partial\Omega_N)} + \|\partial_t\psi\|^2_{H^{-1/2}(\partial\Omega_N)} + \|u_0\|^2_{H^1_D(\Omega)}\right). \tag{3.3.26}$$

Integrating this inequality with respect to $t \in [0,T]$,

$$\|\partial_t u_m\|^2_{L^2\left(0,T;H^1_D(\Omega)\right)} \leq C\left(\|f\|^2_{L^2(0,T;H^{-1}(\Omega))} + \|\psi\|^2_{H^1\left(0,T;H^{-1/2}(\partial\Omega_N)\right)} + \|u_0\|^2_{H^1_D(\Omega)}\right). \tag{3.3.27}$$

Combining (3.3.22) and (3.3.27) the lemma is proven.

□

We remark that since the solutions to (3.3.7) exist for all time, the approximate solutions $u_m$ to (3.3.1) do also. Furthermore, passing to the limit one can show that the solution $u$ to equation (3.3.1), defined as the limit of the $u_m$, exists for all times $t \in \mathbb{R}^+$. We now prove that if the boundary conditions and source terms have compact

support the solution actually decays to zero as time $t \to \infty$. For simplicity we focus our attention on the case when $(\varepsilon, \sigma) \in \mathcal{A}$. The decay of the solution when $(\varepsilon, \sigma) \in \mathcal{A}_{\mathrm{TD}}$ follows as a corollary since for sufficiently large $t$, $\varepsilon$ and $\sigma$ are constant in time.

THEOREM 8. *Suppose that $\varphi \in H^1(\mathbb{R}^+; H^{1/2}(\partial\Omega_D))$, $\psi \in H^1(\mathbb{R}^+; H^{-1/2}(\partial\Omega_N))$, and $f \in H^1(\mathbb{R}^+; H^{-1}(\Omega))$ all have compact support in time. Then the solution $u \in H^1\left(\mathbb{R}^+; H^1_{\partial\Omega_D}(\Omega)\right)$ to (3.3.1) decays to zero as $t \to \infty$ and*

$$\|u\|^2_{L^2(\Omega)} \leq C \exp(-kt)$$

*for some positive constants $C, k > 0$ independent of time.*

PROOF. Fix $T > 0$. Let $u \in C\left([0,T]; H^1_D(\Omega)\right)$ be the solution to (3.3.1) which we decompose as $u = \widehat{u} + \widehat{\varphi}$, where $\widehat{\varphi}$ is a lift of the boundary condition $\varphi \in H^1\left(0, T; H^{1/2}\left(\partial\Omega_D\right)\right)$ for $T > 0$. Then by rearranging (3.3.1), we find $\widehat{u}$ satisfies

$$\begin{aligned}\int_{Q_T} -\partial_t\left(\varepsilon\nabla\widehat{u}\right)\cdot\nabla v + \sigma\nabla\widehat{u}\cdot\nabla v \,\mathrm{d}x\mathrm{d}t = &\int_0^T \langle\psi, v\rangle_{H^{-1/2}(\partial\Omega_N), H^{1/2}(\partial\Omega_N)}\mathrm{d}t \\ &+ \int_0^T \langle f, v\rangle_{H^{-1}(\Omega), H^1_D(\Omega)}\mathrm{d}t \\ &- \int_{Q_T} \left\langle \varepsilon\partial_t\nabla\widehat{\varphi} + \sigma\nabla\widehat{\varphi}, v\right\rangle \,\mathrm{d}t\end{aligned}$$

for all $v \in L^2(0,T; H^1(\Omega))$. Choosing $v = \widehat{u} \in C\left([0,T]; H^1_D(\Omega)\right) \subset L^2\left(0,T; H^1_D(\Omega)\right)$, we obtain

$$\begin{aligned}\int_{Q_T} \frac{1}{2}\partial_t\left(\varepsilon\left|\nabla\widehat{u}\right|^2\right) + \sigma\left|\nabla\widehat{u}\right|^2 \,\mathrm{d}x\mathrm{d}t \leq &\int_0^T \left(\|f\|_{H^{-1}(\Omega)} + \|\psi\|_{H^{-1/2}(\partial\Omega_N)}\right)\|\widehat{u}\|_{H^1_D(\Omega)}\,\mathrm{d}t \\ &+ \int_0^T \|\varepsilon\|_{L^\infty(\Omega)}\|\partial_t\nabla\widehat{\varphi}\|_{L^2(\Omega)}\|\nabla\widehat{u}\|_{L^2(\Omega)}\,\mathrm{d}t \\ &+ \int_0^T \|\sigma\|_{L^\infty(\Omega)}\|\nabla\widehat{\varphi}\|_{L^2(\Omega)}\|\nabla\widehat{u}\|_{L^2(\Omega)}\,\mathrm{d}t.\end{aligned}$$

Using the Poincaré inequality for the function $\widehat{u}(t,\cdot) \in H^1_D(\Omega)$, we combine the two terms on the right hand side to establish

$$\int_{Q_T} \frac{1}{2}\partial_t\left(\varepsilon\left|\nabla\widehat{u}\right|^2\right) + \sigma\left|\nabla\widehat{u}\right|^2 \,\mathrm{d}x\,\mathrm{d}t \leq \int_0^T F\|\nabla\widehat{u}\|_{L^2(\Omega)}\,\mathrm{d}t \tag{3.3.28}$$

with $F$ defined by

$$F(t) := (1 + C_0)\left(\|f\|_{H^{-1}(\Omega)} + \|\psi\|_{H^{-1/2}(\partial\Omega_N)}\right) + \|\varepsilon\|_{L^\infty(\Omega)} \|\partial_t \nabla\widehat{\varphi}\|_{L^2(\Omega)} + \|\sigma\|_{L^\infty(\Omega)} \|\nabla\widehat{\varphi}\|_{L^2(\Omega)}$$

where $C_0$ is the Poincaré constant. In particular, we notice that since $f, \psi$, and $\varphi$ have compact support in time, $\widehat{\varphi}$ does also and

$$\sup_{t\in\mathbb{R}^+} |F(t)| = \sup_{t\in[0,T^*]} |F(t)| < \infty,$$

where $T^*$ is the maximal time that $F(t)$ is non-zero.

To ease notation let $X = \|\nabla\widehat{u}\|^2_{L^2(\Omega)}$, $X_\sigma = \|\nabla\widehat{u}\|^2_{L^2(\Omega_\sigma)}$, and $X_\sigma^\perp = \|\nabla\widehat{u}\|^2_{L^2(\Omega\setminus\Omega_\sigma)}$ where $\Omega_\sigma$ is an open set with Lipschitz boundary where $\sigma \geq \sigma_0 > 0$ for some constant $\sigma_0$. For example, take $\Omega_\sigma$ to be the support of $\sigma$. Then, for a choice $\delta > 0$, (3.3.28) becomes

$$\frac{1}{2}\varepsilon_0 \int_0^T \partial_t X \,\mathrm{d}t + \sigma_0 \int_0^T X_\sigma \,\mathrm{d}t \leq \frac{1}{2\delta} T^* \sup_{t\in[0,T^*]} |F(t)|^2 + \frac{\delta}{2} \int_0^T X \,\mathrm{d}t. \tag{3.3.29}$$

We now look to bound $\int_0^T X_\sigma \,\mathrm{d}t$ from below by $\int_0^T X \,\mathrm{d}t$ for any $T > 0$. Let $R_\sigma : H^1(\Omega) \to H^1(\Omega_\sigma)$ be the restriction operator and let $v = R_\sigma(\widehat{u})$. Since $\partial\Omega_\sigma$ is assumed to be Lipschitz, each $v \in H^1(\Omega_\sigma)$ has a well defined trace on $\partial\Omega_\sigma$ and

$$\|v\|_{H^{1/2}(\partial\Omega_\sigma)} \leq \|v\|_{H^1(\Omega_\sigma)} = \|\widehat{u}\|_{H^1(\Omega_\sigma)}. \tag{3.3.30}$$

Consider now the restriction $R_{\sigma^\perp} : H^1(\Omega) \to H^1(\Omega \setminus \Omega_\sigma)$. Here $w = R_{\sigma^\perp}(u)$ solves the equation

$$\begin{cases} -\operatorname{div}\left(\partial_t\left(\varepsilon\nabla w\right) + \sigma\nabla w\right) = f & \text{in } \Omega\setminus\Omega_\sigma, \\ w(t,\cdot) = 0 & \text{on } (0,T]\times\partial\Omega_D, \\ w(t,\cdot) = v & \text{on } (0,T]\times\partial\Omega_\sigma, \\ \partial_t\left(\varepsilon\nabla w\right)\cdot\hat{n} + \sigma\nabla w\cdot\hat{n} = \psi & \text{on } (0,T]\times\partial\Omega_N, \\ w(0,\cdot) = u_0 & \text{in } \Omega\setminus\Omega_\sigma. \end{cases} \tag{3.3.31}$$

which exists and is unique by Theorem 7. Moreover, since $\widehat{u}$ and $w$ satisfy the same boundary conditions, and the solution is unique, they must be equivalent on $\Omega \setminus \Omega_\sigma$. In particular, we can bound $\widehat{u}$ at a.e. $t \in \mathbb{R}^+$ by

$$\|\widehat{u}\|_{H^1(\Omega_\sigma)} \leq C \left( \|f\|_{H^{-1}(\Omega)} + \|\psi\|_{H^{-1/2}(\partial\Omega_N)} + \|v\|_{H^{1/2}(\partial\Omega_\sigma)} \right).$$

Using inequality (3.3.30), this can be bounded further and

$$\|\widehat{u}\|_{H^1(\Omega\setminus\Omega_\sigma)} \leq C \left( \|f\|_{H^{-1}(\Omega)} + \|\psi\|_{H^{-1/2}(\partial\Omega_N)} + \|\widehat{u}\|_{H^{1/2}(\partial\Omega_\sigma)} \right).$$

By rewriting, we find that there exists a constant $C > 0$ such that

$$\int_0^T X_{\sigma^\perp} \, \mathrm{d}t \leq C \int_0^T X_\sigma \, \mathrm{d}t + T^* \sup_{t\in[0,T^*]} |F(t)|^2 .$$

Furthermore, since $X = X_\sigma + X_{\sigma^\perp}$ we establish that

$$\int_0^T X \, \mathrm{d}t \leq (1 + C) \int_0^T X_\sigma \, \mathrm{d}t + T^* \sup_{t\in[0,T^*]} |F(t)|^2$$

for all $T > 0$. Thus using this inequality in combination with (3.3.29) we obtain, for any $\delta < 1$,

$$\frac{1}{2}\varepsilon_0 \int_0^T \partial_t X \, \mathrm{d}t + \frac{\sigma_0}{1+C} \int_0^T X \, \mathrm{d}t \leq \frac{T^*}{\delta} \left( \frac{C + 1 + \sigma_0}{C+1} \right) \sup_{t\in[0,T^*]} |F(t)|^2 + \frac{\delta}{2} \int_0^T X \, \mathrm{d}t. \tag{3.3.32}$$

In other words, for $\delta$ small enough, writing $Y(t) = \int_0^t X \, \mathrm{d}s$, the bound (3.3.32) becomes

$$Y' + kY \leq C' T^* \sup_{t\in[0,T^*]} |F(t)|^2 ,$$

and the conclusion follows by applying Gronwall's lemma. □

Remark. The reader will note that without the complication that the damping effect, due to the conductive material, only occurs on a subset of the domain this proof would have been relatively standard. In other words, the difficulty in the proof originates in the assumption that the support of $\sigma$ is a proper subset of the domain $\Omega$.

**3.3.2. Model 4.** In preparation for the next section, we now combine Theorem 6, Theorem 7 and Theorem 8 to provide an existence and uniqueness result for Model 4.

THEOREM 9. *Given* $(u_0, U_0) \in \overline{H^1}(\Omega)$, $F = (F_1, \ldots, F_N) \in C_c(\mathbb{R}^+)^N$, *and* $f \in C_c(\mathbb{R}^+; H^{-1}(\Omega))$ *with*

$$\int_0^\infty \left( \sum_{i=1}^N F_i + \langle f, 1 \rangle_{H^{-1}(\Omega), H^1(\Omega)} \right) dt = 0$$

*there exists a unique* $(u, U) \in H^1\left(\mathbb{R}^+; \overline{H^1}(\Omega)\right)$

$$\begin{cases} -div(\varepsilon \nabla \partial_t u + \sigma \nabla u) = f & \text{in } (0,\infty) \times \Omega, \\ u = U_k & \text{on } (0,\infty) \times \partial E_k \text{ for } k = 1, \ldots, N, \\ \int_{\partial E_k} \varepsilon \nabla \partial_t u \cdot \hat{n} ds = F_k & \text{on } (0,\infty) \times \partial E_k \text{ for } k = 1, \ldots, N, \\ \int_{\partial E_k} \varepsilon \nabla \partial_t u \cdot \hat{n} ds = 0 & \text{on } (0,\infty) \times \partial \Omega_B \\ (u, U)_{t=0} = (u_0, U_0) & \text{in } \Omega \times \mathbb{R}^N. \end{cases}$$

*In particular, the operator*

$$\begin{aligned} \mathcal{S} : \overline{H^1}(\Omega) \times C_c\left(\mathbb{R}^+; H^{-1}(\Omega)\right) \times C_c\left(\mathbb{R}^+\right)^N &\to H^1\left(\mathbb{R}^+; \overline{H^1}(\Omega)\right) \\ (u_0, U_0, f, F) &\to (u, U) \end{aligned} \tag{3.3.33}$$

*is continuous. Furthermore, for any* $T > 0$,

$$\begin{aligned} \max_{t \in [0,T]} \|S(u_0, U_0, f, F)\|_{\overline{H^1}(\Omega)} \leq C \Big( \sqrt{T} \Big( &\|f\|_{L^2(0,T;H^{-1}(\Omega))} + \|F\|_{L^2(0,T)^N} \Big) \\ &+ \|(u_0, U_0)\|_{\overline{H^1}(\Omega)} \Big) \end{aligned}$$

*and*

$$\|\partial_t S(u_0, U_0, f, F)\|_{L^2\left(0,T;\overline{H^1}(\Omega)\right)} \leq C \left( \|f\|_{L^2(0,T;H^{-1}(\Omega))} + \|F\|_{L^2(0,T)^N} + \|(u_0, U_0)\|_{\overline{H^1}(\Omega)} \right) \tag{3.3.34}$$

*where the constant* $C$ *depends on* $\Omega$, *the norms of* $\varepsilon$ *and* $\sigma$, *and the coercivity bound on* $\varepsilon$ *only.*

PROOF. The proof of this theorem follows closely the steps of the proof of Theorem 6, Theorem 7, and Theorem 8. We will not repeat all of the details, except for the beginning of the Galerkin method where the existence of approximate solutions exists. The ODE in this case is distinct from the previous cases. The rest of the proof follows identically to Theorem 7.

Similarly to the proof of Theorem 7, we suppose $(w_k)_{k\in\mathbb{N}}$ is an orthonormal eigenbasis in $H_0^1(\Omega)$ for the operator $\operatorname{div}(\varepsilon\nabla\cdot)$, with

$$-\operatorname{div}(\varepsilon\nabla w_k) = \lambda_k w_k \in H_0^1(\Omega).$$

In other to satisfy the boundary condition constraint embedded in the space $\overline{H^1}(\Omega)$, we supplement this basis with the functions $\{e_\ell\}_{\ell=1}^N$ where $e_\ell \in H^1(\Omega)$ is the weak solution to

$$\begin{cases} -\operatorname{div}(\varepsilon\nabla e_\ell) = 0 & \text{in } \Omega, \\ e_\ell = \delta_{kl} & \text{on } \partial E_k, \\ \varepsilon\nabla e_\ell \cdot \hat{n} = 0 & \text{on } \partial\Omega_B, \end{cases}$$

where $\delta_{kl}$ is the Kronecker delta. We construction approximate solutions in $\overline{H^1}(\Omega)$ of the form

$$u_m(t,x) = \left(\sum_{k=1}^m d_k^m(t) w_k(x) + \sum_{\ell=1}^N e_\ell D_\ell^m + c, D_1^m + c, \ldots, D_N^m + c\right),$$

where $c$ is any constant and, $\{d_k^m\}_{k=1}^m$ and $\{D_\ell^m\}_{\ell=1}^N$ are absolutely continuous functions.

We define $b_{\ell k} = \int_\Omega \sigma\nabla e_\ell \cdot \nabla w_k \mathrm{d}x$, $f_k = \langle f, w_k\rangle_{H^{-1}(\Omega),H_0^1(\Omega)}$, $c_{\ell j} = \int_\Omega \sigma\nabla e_\ell \cdot \nabla w_j \mathrm{d}x$, $d_{\ell q} = \int_\Omega \sigma\nabla e_\ell \cdot \nabla e_q \mathrm{d}x$, and $g_\ell = \langle f, e_\ell\rangle_{H^{-1}(\Omega),H_0^1(\Omega)}$. Then by substitution, we deduce the following system of ODEs:

$$\lambda_k \frac{\mathrm{d}}{\mathrm{d}t} d_k^m(t) = \left[f_k - \sum_{j=1}^m a_{kj} d_j^m(t) - \sum_{\ell=1}^N b_{\ell k} D_\ell^m\right],$$

and

$$\int_\Omega \varepsilon\nabla e_\ell \cdot \nabla e_\ell \frac{\mathrm{d}}{\mathrm{d}t} D_\ell^m(t) = \left[g_\ell + \psi_\ell - \sum_{j=1}^m c_{\ell j} d_j^m(t) - \sum_{q=1}^N d_{\ell q} D_\ell^m\right],$$

together with the initial conditions

$$d_k^m(0) + \sum_{\ell=0}^{N} \langle e_\ell, w_k \rangle D_\ell^m(0) = u_0,$$

$$D_\ell^m(0) = U_{0,\ell} \text{ for each } \ell.$$

Given $T > 0$, the existence of absolutely continuous solutions on $[0,T]$ for each $d_1^m, \ldots, d_m^m$ and $D_1^m, \ldots, D_N^m$ follows from Caratheodory's theorem. The proof then continues as in Theorem 7. □

**3.3.3. Model 5.** In this section we prove that there exists a unique weak solution to (2.5.8), the coupled PDE-ODE model, in the space $C\left(0,T;\overline{H^1}(\Omega)\right)$. In other words we provide a proof of the following theorem in the case when $(\varepsilon,\sigma) \in \mathcal{A}$, the case when $(\varepsilon,\sigma) \in \mathcal{A}_{\text{TD}}$ follows similarly.

THEOREM 10. *Let $(\varepsilon,\sigma) \in \mathcal{A}$. Suppose $U_0 \in \mathbb{R}$, $(u,U)|_{t=0} = (u_0, U_0\mathbf{1}) \in H^1(\Omega) \oplus \mathbb{R}^N$, and $\phi \in C^1([0,T])$ with $\phi(0) = 0$ are given. Let $R_k > 0$ and $C_k > 0$ be known constants for each $k = 1, \ldots, N$. Select any electrode to act as the transmitter and denote this electrode by $\partial E_T$. Then there exists a unique $(u,U) \in C\left([0,T]; \overline{H^1}(\Omega)\right)$ satisfying*

$$\begin{cases} -div(\varepsilon\nabla\partial_t u + \sigma\nabla u) = f & \text{in } [0,T]\times\Omega, \\ u = \phi(t) & \text{on } (0,T]\times\partial E_T, \\ u = U_k(t) & \text{on } (0,T]\times\partial E_k \text{ for } k = 1,\ldots,N, k \neq T \\ |\partial E_k|^{-1}\displaystyle\int_{\partial E_k} \varepsilon\nabla u\cdot\hat{n}\,ds = Q_k(t) & \text{on } (0,T]\times\partial E_k \text{ for } k = 1,\ldots,N, k \neq T \\ \varepsilon\nabla u\cdot\hat{n} = 0 & \text{on } [0,T]\times\partial\Omega_B, \\ u = u_0 & \text{in } \Omega, \\ C_k\dfrac{dQ_k}{dt} + R_k^{-1}Q_k = U_k(t) - U_0 & \text{for } k = 1,\ldots,N, k \neq T \\ Q_k(0) = 0 & \text{for } k = 1,\ldots,N, k \neq T. \end{cases} \tag{3.3.35}$$

PROOF OF THEOREM 10. As a first step, we reformulate the above as a fixed point problem. For each $t \in [0,T]$, let $\psi(t) \in H^1(\Omega)$ be the solution of

$$\begin{cases} -\operatorname{div}(\varepsilon\nabla\psi) = 0 & \text{in } \Omega, \\ \psi = \phi(t) & \text{on } \partial E_T, \\ \psi = 0 & \text{on } \partial E_k \text{ for } k = 1,\dots,N, k \neq T \\ \varepsilon\nabla\psi\cdot\hat{n} = 0 & \text{on } \partial\Omega_B. \end{cases} \tag{3.3.36}$$

Then $u$ is a solution of (3.3.35), if and only if $\widetilde{u} = u - \psi$ is a solution of

$$\begin{cases} -\operatorname{div}(\varepsilon\nabla\partial_t\widetilde{u}) - \operatorname{div}(\sigma\nabla\widetilde{u}) = f & \text{in } [0,T]\times\Omega, \\ u = 0 & \text{on } [0,T]\times\partial E_T, \\ u = U_k(t) & \text{on } (0,T]\times\partial E_k \text{ for } k = 1,\dots,N, k\neq T, \\ |\partial E_k|^{-1}\displaystyle\int_{\partial E_k}\varepsilon\nabla u\cdot\hat{n}\mathrm{d}s = \widetilde{Q}_k(t) & \text{on } (0,T]\times\partial E_k \text{ for } k = 1,\dots,N, k\neq T, \\ \varepsilon\nabla u\cdot\hat{n} = 0 & \text{on } [0,T]\times\partial\Omega_B, \\ u = u_0 & \text{in } \Omega, \\ U_k(t) - U_0 - C_k\dfrac{\mathrm{d}}{\mathrm{d}t}\widetilde{Q_k} - R_k^{-1}\widetilde{Q_k} = B_k & \text{for } k = 1,\dots,N, k\neq T \\ \widetilde{Q}_k(0,\cdot) = \widetilde{Q_0} & \text{for } k = 1,\dots,N, k\neq T. \end{cases} \tag{3.3.37}$$

where

$$\begin{aligned} f &= \operatorname{div}(\sigma\nabla\psi), \\ B_k &= C_k\frac{\mathrm{d}}{\mathrm{d}t}\left(|\partial E_k|^{-1}\int_{\partial E_k}\varepsilon\nabla\psi\cdot\hat{n}\mathrm{d}s\right) + R_k^{-1}|\partial E_k|\int_{\partial E_k}\varepsilon\nabla\psi\cdot\hat{n}\mathrm{d}s, \\ \widetilde{Q_0} &= Q_0 - |\partial E_k|^{-1}\int_{\partial E_k}\varepsilon\nabla\psi\cdot\hat{n}\mathrm{d}s. \end{aligned}$$

In other words, using the operator $S$ introduced in (3.3.33), we have

$$(\widetilde{u}, U) = \mathcal{S}(u_0, U_0, f, \partial_t Q).$$

On the other hand, we have

$$\widetilde{Q} = \exp\left(-\frac{t}{R_k C_k}\right)\widetilde{Q_0} + \frac{1}{C_k}\int_0^t \exp\left(\frac{\tau - t}{R_k C_k}\right)\left(U_k(\tau) - U_0 - B_k(\tau)\right)\mathrm{d}\tau,$$

and

$$\frac{\mathrm{d}}{\mathrm{d}t}Q = \mathcal{R}\left(Q_0, U - U_0\mathbf{1} - B\right)$$

where

$$\begin{aligned}\mathcal{R} : \mathbb{R}^N \times C\left([0,T];\mathbb{R}^N\right) &\to C\left([0,T];\mathbb{R}^N\right)\\ (A,F) &\to -\frac{1}{R_k}\left(\exp\left(-\frac{t}{R_k C_k}\right)A_k + \frac{1}{C_k}\int_0^t \exp\left(\frac{\tau - t}{R_k C_k}\right)F_k(\tau)\,\mathrm{d}\tau\right)\\ &\quad + \frac{1}{C_k}F_k, \qquad k = 1,\ldots,N.\end{aligned}$$

Altogether, any solution $(\tilde{u}, U)$ of (3.3.37) satisfies

$$(\widetilde{u}, U) = \mathcal{S}\left(u_0, U_0, f, \mathcal{R}\left(Q_0, U - U_0\mathbf{1} - B\right)\right),$$

and the existence of a solution amounts to establishing the existence of a fixed point, $U$. Since $\mathcal{S}$ and $\mathcal{R}$ are linear in all their arguments, existence and uniqueness will be established by applying Banach's Fixed Point Theorem provided we show

$$\begin{aligned}K : C\left([0,T];\mathbb{R}^N\right) &\to C\left([0,T];\mathbb{R}^N\right)\\ X &\to S\left(0,0,0,\mathcal{R}\left(0,X\right)\right)\end{aligned}$$

is contracting in an appropriate space. We shall use $C([0,T])$ equipped with the norm $\|X\|_\beta = \max_{[0,T]}\exp(-\beta t)\,|X(t)|$, for some $\beta > 0$ to be chosen later. This norm is equivalent to the canonical norm since $\exp(-\beta t) > 0$ for any choice of $\beta$ and for all $t \in \mathbb{R}$.

We have

$$\begin{aligned}|\mathcal{R}(0,X)| &= \left|-\frac{1}{R_k C_k}\int_0^t \exp\left(\frac{\tau - t}{R_k C_k}\right)X_k(\tau)\,\mathrm{d}\tau + \frac{1}{C_k}X(t)\right|\\ &\leq \left(\frac{1}{\underline{RC}}\int_0^t \exp\left(\frac{\tau - t}{\overline{RC}} + \beta\tau\right)\mathrm{d}\tau + \exp(\beta t)\right)\|X\|_\beta,\end{aligned}$$

where $\underline{RC} \leq R_k C_k \leq \overline{RC}$ for all $k$, which yields

$$|\mathcal{R}(0,X)|(t) \leq C \exp(\beta t) \|X\|_\beta$$

for some constant $C$ depending on $\underline{RC}$ and $\overline{RC}$ only. For each $t \in [0,T]$, thanks to the a priori estimates (3.3.34) applied to the interval $(0,t)$, we bound

$$\begin{aligned}
\exp(-\beta t)\, S(0,0,0,\mathcal{R}(0,X))(t) &\leq \exp(-\beta t) \max_{[0,t]} \|S(0,0,0,\mathcal{R}(0,X))\| \\
&\leq \exp(-\beta t)\, C\sqrt{t} \left[\int_0^t \exp(2\beta\tau)\, \mathrm{d}\tau\right]^{1/2} \|X\|_\beta \\
&\leq \frac{C\sqrt{T}}{\sqrt{\beta}} \|X\|_\beta
\end{aligned}$$

where $C$ now depends on $\underline{RC}$,$\overline{RC}$, $\Omega$, the norms of $\varepsilon$ and $\sigma$, and the coercivity bound on $\varepsilon$ only. Taking $\beta = C^2 T + 1$, we obtain

$$\|S(0,0,0,\mathcal{R}(0,X))\|_\beta \leq \sqrt{\frac{C^2 T}{C^2 T + 1}} \|X\|_\beta,$$

which establishes the contractivity as required. □

CHAPTER 4

# Numerical solution and validation of the models

The aim of this chapter is twofold: firstly, we aim to numericallycompute solutions to each of the five models, and secondly, we aim to compare the simulated data to empirically collected sensor data. The first is achieved by applying the Finite Element Method (FEM) to solve the corresponding weak formulation of each model given the sensor input which is represented as boundary conditions. In particular Model 2 and Model 4 use non-standard boundary conditions and in both cases we detail the construction of the associated linear system. The algorithms are implemented using FreeFem++ [87] and the code is included in the appendices. We discuss the convergence, accuracy, and consistency of the algorithms and produce numerical results to illustrate the performance of the numerical solver.

Before the second aim can be addressed, we devise and test algorithms to estimate the model hyper-parameters from sensor measurements. Using simulated data, the accuracy of each method is determined and the best algorithm is chosen. Finally, we are then able to compare simulated measurements with empirically collected sensor data supplied by Zedsen Ltd.

## 4.1. Preliminaries

We begin this chapter with a brief discussion of the FEM. The reader is referred to details can be found in [32, 53] for more details of the FEM. We begin with describing the triangulation of the domain and the finite dimensional approximation spaces defined on this triangulation used in the FEM.

**4.1.1. Triangulations and the space of $P0$ and $P1$ finite elements.** Suppose that $\Omega$ is a bounded domain in $\mathbb{R}^d$ for $d \geq 1$ with a polygonal boundary $\partial\Omega$. A triangulation, $\mathcal{T}$, of $\Omega$ is a finite collection of triangles such that the following hold:

(1) For each $K \in \mathcal{T}$, $K$ is a closed non-empty set;

(2) $\overline{\Omega} = \bigcup_{K\in\mathcal{T}} K$;

(3) The interiors of any two elements $K_1, K_2 \in \mathcal{T}$ are disjoint i.e. $\mathring{K}_1 \cap \mathring{K}_2 = \emptyset$;

(4) No vertex of any triangle lies on the edge of another triangle.

We shall define the constant $h > 0$ to be the maximal diameter of all the triangles in $\mathcal{T}$

$$h := \max_{K\in\mathcal{T}} \operatorname{diam}(K)$$

where appropriate we include $h$ as a subscript and write $\mathcal{T}_h$.

Intuitively, the smaller the value of $h$ the more triangular elements that are in $\mathcal{T}$, and the *finer* the mesh.

Furthermore, we shall suppose the triangulation is regular. A triangulation $\mathcal{T}_h$ is regular if for each $h > 0$, there exists a constant $C \geq 1$ such that for all $K \in \mathcal{T}_h$

$$\frac{h}{\rho_K} \leq C, \tag{4.1.1}$$

where $\rho_K$ is the radius of the largest circle contained in $K$. Condition (4.1.1) prevents the triangles becoming too thin as the mesh is refined. We suppose that all the triangulations considered in this thesis are regular.

In general, a finite element space is a triple $(\mathcal{T}, \mathcal{P}, \mathcal{N})$ consisting of a regular triangulation, a set of functions defined on the triangulation, and a set of nodal variables respectfully [53]. The set of nodal variables is defined implicitly by the choice of functions $\mathcal{P}$: $\mathcal{N}$ is a basis of the algebraic dual to $\mathcal{P}$. In the specific case when $\mathcal{P}$ is the set of piecewise linear functions on $\mathcal{T}$, the set of nodal variables coincides with the vertices of the triangular elements of the mesh.

In particular, we denote the set of all piece-wise constant functions on $\mathcal{T}$ by $P_0$ and the set of all piece-wise linear polynomials as $P_1$. Given a triangulation $\mathcal{T}$, we define for each $N_i \in \mathcal{N}$ the piecewise linear function $\phi_i \in P_1$ such that

$$\phi_i(N_j) = \delta_{ij} \tag{4.1.2}$$

for each $N_j \in \mathcal{N}$. In other words, the function $\phi_i$ is 1 on the node $N_i$, zero at all other nodes, and linear on the edge of each triangle. Furthermore, one can show that the

set $\{\phi_i\}_{i=1}^{M}$, where $M$ is the number of nodes in the triangulation, forms a basis of $P_1$. To emphasise the dependence on the mesh parameter $h > 0$, it is convenient to denote the vector space formed by the span of this basis by $V_h$:

$$V_h := \operatorname{span}\{\phi_1, \ldots, \phi_M\}. \tag{4.1.3}$$

Similarly, the set of functions $\{\psi_i\}_{i=1}^{M_T}$, where $\psi_i = 1$ on the $i$-th triangle and 0 otherwise, forms a basis of $P_0$.

If we are assuming that the domain is polygonal, provided enough nodes are placed on the boundary, the domain can be triangulated exactly. In this case, one can show the following inclusion properties

- $V_h \subset H^1(\Omega)$ and
- $V_{h_1} \subset V_{h_2}$ whenever $0 < h_2 < h_1$.

When both of these nesting conditions hold, the finite element space is said to be conforming.

However, not all finite element spaces are conforming. Most notable to this work, is the case where the domain has curved boundaries in which case the theory of non-conforming finite elements needs to be used. In this thesis, when we consider domains with curved boundaries, we implicitly replace the curved domain $\Omega$ with a sequence of approximating polygonal domains, denoted $\left\{\widetilde{\Omega}_{h_k}\right\}_k$ for some sequence of $h_k > 0$ with $h_k \to 0$, provided

$$\widetilde{\Omega}_{h_k} \longrightarrow \Omega \text{ as } h_k \to 0$$

in some suitable topology. However, while $V_h \subset H^1(\widetilde{\Omega}_h)$ it is not the case for a non-polygonal domain $\Omega$ that $V_h \subset H^1(\Omega)$. Furthermore, the spaces $V_h$ do not necessarily have the nesting property and $V_{h_1} \nsubseteq V_{h_2}$ whenever $0 < h_2 < h_1$. As a consequence, establishing convergence estimates in the non-conformal case is a non-trivial problem.

However, alternative approaches do exist. For example, the use of triangles with curved elements of the mesh is one possibility, which results in either the use of curvilinear finite elements or isoparametric finite elements. From a mathematical point of view, this approach is preferable: the approximating function spaces are once again

conformal as the mesh is refined. However, from a practical perspective it is often far easier to implement the solvers using a sufficiently accurate polygonal domain, that can be refined as appropriate to deliver the required accuracy [25, 32, 68]. For these reasons we adopt the second approach in this thesis.

To summarise, we let $\widetilde{\Omega}_h$ be a polygonal approximation of the domain $\Omega$ such that the boundary nodes of $\partial\Omega$ coincide with those on the boundary $\partial\widetilde{\Omega}_h$. We denote the polygonal representation of the electrode boundaries of $\widetilde{\Omega}_h$ by $\left\{\partial\widetilde{E}_k\right\}_{k=1}^{N}$. We define $V_h$ to be the space of $P_1$ functions on $\mathcal{T}_h$ spanned by the basis $\{\phi_k\}_{k=1}^{M}$ as in (4.1.3). Finally, we allow for the possibility of conforming and non-conforming finite elements to be used. While the numerical solution in either case is the same, the mathematical analysis of the methods requires different approaches.

**4.1.2. The Finite Element Method (FEM).** We briefly summarise the FEM for the following abstract (linear) variational problem: find $u \in V$ such that

$$a(u, v) = f(v) \quad \text{for all} \quad v \in V, \tag{4.1.4}$$

where $a : V \times V \to \mathbb{K}$ is a continuous and coercive bilinear form and the functional $f : V \to \mathbb{K}$ is bounded. We remark that when $\mathbb{K}$ is the complex field $\mathbb{C}$, $a$ is more correctly a continuous, sesquilinear form. A unique solution to this variational problem follows by the Lax-Milgram lemma. The FEM seeks an approximate solution $u_h \in V_h$ to (4.1.4) in a given finite dimensional subspace $V_h \subset V$. Formally, the FEM solves the related variational problem

$$a(u_h, v_h) = f(v_h) \quad \text{for all} \quad v_h \in V_h. \tag{4.1.5}$$

An application of the FEM then becomes a process of constructing the subspace $V_h \subset V$ and numerically solving (4.1.5) for this choice of $V_h$. Mathematically, one can show that under certain conditions, the approximate solutions converge to the true solution as the mesh is refined provided the mesh remains regular. Choosing $V_h$ to be given by (4.1.3) there is an immediate relationship between the dimension of $V_h$ and the size of

the mesh, therefore, increasing the size of the mesh produces more accurate numerical solutions at the expense of a larger linear system of equations to solve.

Additionally, care must be taken to ensure the correct boundary conditions are imposed on the system. Analytically, Dirichlet boundary conditions are often encoded directly into the function space $V$ and this can be done similarly for the approximating space $V_h$ [32]. While this approach is convenient, the boundary of the mesh is required to coincide with the domain boundary. This presents a difficulty when curved domains arise in this thesis, therefore, we adopt the Penalty Boundary Method (PBM) as an alternative. The PBM is a method for solving boundary problems using a regular mesh that covers the true domain boundary [55]. The advantages to this approach are two-fold: firstly, the PBM does not require the mesh boundary to conform to the true domain and secondly, this method has already been implemented natively in FreeFem++ [87].

More explicitly the solution to (4.1.5) is found by deducing a corresponding algebraic system of equations whose solution corresponds to the coefficients of $u_h$ in a chosen basis of $V_h$. Given a basis of $\{\phi_k\}_{k\in K} \subset V_h$ (note the index set $K$ is necessarily finite) the approximate solution $u_h$ can be expressed as

$$u_h = \sum_{k\in K} \alpha_k \phi_k \tag{4.1.6}$$

with constants $\alpha_k \in \mathbb{K}$ for each $k \in K$. Using (4.1.6) and choosing $v_h = \phi_k$ for each $k \in K$, (4.1.5) can be written as the linear system

$$A\alpha = b, \tag{4.1.7}$$

where $A_{ij} = a(\phi_j, \phi_i)$ and $b_i = f(\phi_i)$ for $i, j \in K$. In other-words, once a basis of $V_h$ is chosen, the FEM is equivalent to a problem in linear algebra.

We remark that by virtue of the assumptions on the bilinear form $a$, and the functional $f$, the linear system (4.1.7) is necessarily invertible. Despite always being solvable, for very large meshes this linear system can become very large in which case the choice of basis functions then becomes critical: the guiding principle is to choose

basis functions which impose additional structure on the matrix $A$. Most commonly the basis functions are chosen to have small support which results in a sparse matrix $A$.

The sparsity property of the matrix $A$ allows (4.1.7) to be solved using more efficient algorithms than directly inverting the matrix $A$. The conjugate gradient method is a commonly used example [169]. Furthermore, such choices are necessary in both conforming and non-conforming finite element spaces. We remark that a compromise between the required accuracy of the FEM approximation and computational resources available is often necessary.

When the finite elements are conformal, convergence of the FEM element as $h \to 0$ follows by establishing an a-priori error bounds of the form

$$\|u - u_h\|_V \leq Ch^s \tag{4.1.8}$$

for some rate parameter $s > 0$ and constant $C > 0$ that is independent of the approximation $u_h \in V_h$. Such estimates establish that as the mesh is refined, $h \to 0$, the finite element approximations $u_h \in V_h$ become better approximations of the true solution $u \in V$. However, there is no requirement that the constant $C$ in (4.1.8) is small. Therefore, despite the error decreasing as the mesh is refined there is no guarantee that for a fixed $h > 0$ the error is numerically small.

A posteriori error estimates, where the upper bound depends on the finite element approximation can also be used to prove convergence of a FEM solution when the true solution is known. We do not go into the details in this thesis but refer the reader to [79] for a review. We instead adopt an empirical approach to estimating the rate of convergence and accuracy of the numerical methods that we now outline.

**4.1.3. Testing methodology of the numerical solvers.** To test the solvers, we construct a sequence of polygonal domains $\widetilde{\Omega}_h$ approximating $\Omega$ as $h \to 0$ and consider the convergence of the solution on $\widetilde{\Omega}_h$ to the solution on $\Omega$. To further complicate matters, for the applicable choice of domains in this thesis an analytic solution is not known. We choose as a proxy for the true solution, the solution $u_{h^*}$ for

a *very small* $h^*$ and investigate the rate of convergence of

$$u_h \to u_{h^*} \text{ as } h \to h^*.$$

We remark that this investigation is unable to demonstrate accuracy of the numerical scheme. However, provided that $h^*$ is chosen sufficiently small such that $0 < h^* \ll h$, it is reasonable to extrapolate and presume convergence of the scheme as $h^* \to 0$.

**4.1.4. Discretisation of the parameter spaces $\widetilde{\mathcal{A}}$, $\widetilde{\mathcal{A}}_{\mathbf{p}}$, and $\widetilde{\mathcal{A}}_{\mathbf{c}}$.** We suppose that $\mathcal{T}_h$ is a triangulation of $\widetilde{\Omega}_h$ with $M_T$ triangles and $M$ nodes. We suppose that a basis of space of piecewise constant functions on $\mathcal{T}_h$, denoted $P_0$, is given by $\{\psi_k\}_{k=1}^{M_T}$ such that

$$\max\{\psi_{k_1}, \psi_{k_2}\} = \delta_{k_1,k_2} \text{ for all } k_1, k_2 = 1, \dots, M_T.$$

We discretise the space of material parameters $\mathcal{A}$ using the basis $\{\psi_k\}_{k=1}^{M_T}$. Let $\mathcal{K} \subset \{1, \dots, M_T\}$ be the set of indices of the triangular elements $K \in \mathcal{T}_h$ such that $K \subset \Omega'$, where $\Omega'$ is the subset of $\Omega$ separated from the boundary of $\partial\Omega$ appearing in the definition of $\mathcal{A}$ (see (2.2.2)). We fix a constant $\beta_0 > 0$ and consider the subset of parameter distributions that can be written as

$$\gamma = \beta_0 + \sum_{k \in \mathcal{K}} \beta_k \psi_k$$

with $\beta_k \in \mathbb{C}$ such that $\mathrm{Re}\,(\beta_k) > 0$ and $\mathrm{Im}(\beta_k) \geq 0$ for each $k \in \mathcal{K}$. We denote the space of all such functions by $\widetilde{\mathcal{A}}$:

$$\widetilde{\mathcal{A}} := \left\{ \beta_0 + \sum_{k \in \mathcal{K}} \beta_k \psi_k : \beta_0 > 0, \beta_k \in \mathbb{C} \text{ with } \mathrm{Re}(\beta_k) > \beta_0 \text{ and } \mathrm{Im}(\beta_k) \geq 0 \right\}.$$

The space $\widetilde{\mathcal{A}}$ has dimension equal to the size of $\mathcal{K}$ and is a finite dimensional subspace of $\mathcal{A}$.

Similarly, we discretise the space of admissible permittivities and conductivities by $\widetilde{\mathcal{A}_{\mathrm{p}}}$ and $\widetilde{\mathcal{A}_{\mathrm{c}}}$ respectively where

$$\widetilde{\mathcal{A}_{\mathrm{p}}} := \left\{ \beta_0 + \sum_{k \in \mathcal{K}} \beta_k \psi_k \ : \ \beta_0 > 0, \beta_k \in \mathbb{R} \text{ with } \beta_k \geq 0 \right\}$$

and

$$\widetilde{\mathcal{A}_{\mathrm{c}}} := \left\{ \sum_{k\in\mathcal{K}} \beta_k \psi_k \ : \beta_k \in \mathbb{R} \text{ with } \beta_k \geq 0 \right\}.$$

## 4.2. Numerical solution in the frequency domain

We describe the numerical solution using the FEM of the models stated in the frequency domain, namely Model 1 and Model 2. The implementation of the algorithms in FreeFem++ is given in Appendix B. In this chapter, all vectors $x \in \mathbb{C}^d$ will be considered to be column vectors and square brackets are used to denote block matrices.

**4.2.1. Numerical solution of Model 1.** We begin with describing the FEM solution to Model 1 in the case when the boundary condition is determined by a given vector $U \in \mathbb{C}^N$, a source term $f \in V_h$, and a parameter $\gamma \in \widetilde{\mathcal{A}}$. Namely, we seek a $u_h \in V_h$ such that

$$\begin{cases} -\operatorname{div}(\gamma \nabla u_h) &= f & \text{in} \quad \widetilde{\Omega}_h, \\ u_h &= U_k & \text{on} \quad \partial\widetilde{E}_k \text{ for } k = 1, \ldots, N, \\ \gamma \nabla u_h \cdot \hat{n} &= 0 & \text{on} \quad \partial\widetilde{B}. \end{cases} \tag{4.2.1}$$

We have introduced a source term $f \in V_h$ to aid the development of the numerical schemes in the time dependent case. A numerical solution to Model 1 can be obtained by simply choosing $f = 0$.

We use the Penalty Boundary Method (PBM) to impose the Dirichlet boundary conditions rather than incorporating these constraints into the function space. The PBM imposes the boundary condition by the addition of the penalty term,

$$C \sum_{k=1}^{N} \int_{\partial E_k} (u - U_k)^2 \, \mathrm{d}s$$

for a large positive penalty $C > 0$, into the weak form of the equation. The weak form of equation (4.2.1) then becomes: find $u_h \in V_h$ to minimise the functional

$$\int_{\Omega} \gamma \left|\nabla u_h\right|^2 + C \sum_{k=1}^{N} \int_{\partial E_k} (u_h - U_k)^2 \, \mathrm{d}s.$$

Or equivalently, we seek a solution to the weak form

$$\int_\Omega \gamma \nabla u_h \cdot \nabla v + C \sum_{k=1}^{N} \int_{\partial E_k} u_h v \, \mathrm{d}s - C \sum_{k=1}^{N} \int_{\partial E_k} U_k v \, \mathrm{d}s = 0. \tag{4.2.2}$$

A further discussion of the PBM can be found in [55]. We adopt the PBM, rather than alternatives, due to its implementation the finite element software package FreeFem++ [46, 87]. In FreeFem++, the default value of $C$ is chosen to be $10^{30}$. It is a property of the penalty boundary method that the resulting systems are well-conditioned in both two and three dimensions [54, 55, 131]. Furthermore, the accuracy of the solution is not sensitive to changes in the penalty parameter $C$ [15].

We now discretise the weak form given by (4.2.2). Let $M$ be the number of nodal variables in the mesh. We define the matrix $B \in \mathbb{C}^{M\times M}$ such that

$$B_{ik} = \begin{cases} C & \text{if } \partial\widetilde{E}_k \subset \operatorname{supp}(\phi_i), \\ 0 & \text{otherwise,} \end{cases} \tag{4.2.3}$$

for some large constant $C$. We define the vector $b \in \mathbb{C}^M$ to be

$$b_i = \sum_{k=1}^{N} B_{ik} U_k.$$

The stiffness matrix $A \in \mathbb{C}^{M\times M}$, for a given $\gamma \in \mathcal{A}$, is defined by

$$A(\gamma)_{ji} := \sum_{K\in\mathcal{T}_h} \int_K \gamma \nabla\phi_i \cdot \nabla\overline{\phi}_j \, \mathrm{d}x \quad \text{for} \quad i,j = 1,\ldots,M,$$

where $\{\phi_k\}_{k=1}^M$ is the basis of $V_h$. When there is no risk of confusion, we simply write $A$ instead of $A(\gamma)$.

Any function $u_h \in V_h$ can be expressed in this basis as

$$u_h = \sum_{k=1}^{M} \alpha_k \phi_k \tag{4.2.4}$$

for a choice of coefficients $a_k \in \mathbb{C}$ for each $k = 1, \ldots, M$. Therefore, a function of the form (4.2.4) satisfies (4.2.1) if and only if $\alpha \in \mathbb{C}^N$ satisfies a

$$(A + B)\,\alpha = F + b, \tag{4.2.5}$$

where $F \in \mathbb{C}^M$ is the vector of coefficients representing $f$:

$$f = \sum_{k=1}^{M} F_i \phi_k. \tag{4.2.6}$$

We remark that since $f \in V_h$, this is an exact representation and the vector $F \in \mathbb{C}^M$ is unique.

To summarise, let $\mathbf{A}_1 = A + B$ and $\mathbf{b}_1 = b$, then a numerical solution of (4.2.1) can be written as (4.2.4) where $\alpha \in \mathbb{C}^M$ solves

$$\mathbf{A}_1 \alpha = \mathbf{b}_1. \tag{4.2.7}$$

Recall in this case that the modelled sensor measurements are given by the average boundary flux on each electrodes. Given the vector $\alpha$, the solution to (4.2.7), the average boundary flux can be computed by left-multiplying by a matrix. Let the matrix $L \in \mathbb{C}^{N \times M}$ be the matrix given by

$$L_{ki} = |\partial \widetilde{E}_k|^{-1} \int_{\partial \widetilde{E}_k} \gamma \nabla \phi_i \cdot \hat{n} \, \mathrm{d}s \tag{4.2.8}$$

then the vector of measurements, $Q_h \in \mathbb{C}^N$, is given by

$$Q_h = L\alpha. \tag{4.2.9}$$

Indeed, using (4.2.4), we compute

$$\begin{aligned} \left|\partial \widetilde{E}_k\right|^{-1} \int_{\partial \widetilde{E}_k} \gamma \nabla u_h \cdot \hat{n} \, \mathrm{d}s &= \left|\partial \widetilde{E}_k\right|^{-1} \sum_{i=1}^{n} \alpha_i \int_{\partial \widetilde{E}_k} \gamma \nabla \phi_i \cdot \hat{n} \, \mathrm{d}s \\ &= \sum_{i=1}^{N} L_{ki} \alpha_i \\ &= (L\alpha)_k . \end{aligned}$$

Alternatively, provided $f = 0$, the divergence theorem implies that the measurements can also be calculated by

$$Q_h = \widetilde{L}\alpha \tag{4.2.10}$$

where $\widetilde{L} \in \mathbb{C}^{N\times M}$ is defined component-wise by

$$\widetilde{L}_{ki} = |\partial\widetilde{E}_k|^{-1} \int_{\widetilde{\Omega}_h} \gamma\nabla\phi_i \cdot \nabla g_k \,\mathrm{d}x$$

where $g_k \in V_h$ solve

$$-\Delta g_k = 0 \text{ in } \widetilde{\Omega}_h, g_k = 1 \text{ on } \partial\widetilde{E}_k, g_k = 0 \text{ otherwise.}$$

Numerical experiments have shown that calculating the boundary flux using (4.2.10) instead of (4.2.9) is less sensitive to inaccuracies in meshing the boundary despite the extra computational cost in computing $g_k$ for each $k$ and the numerical evaluation of a two dimensional integral. This is well-known in the field of numerical analysis and is analysed in [16]. We adopt this approach and measure the charge using (4.2.10). However, despite the increase in computational cost, the functions $\{g_k\}_{k=1}^N$ need only be solved once and can be done ahead of time. Therefore, the increased computational cost will not affect the simulations at run-time. Furthermore, we remark that the choice of $g_k$ is not unique. We summarise the numerical procedure to solve Model 1 below.

**Algorithm 1** Pseudo-code solver for Model 1.

**Require:** $U \in \mathbb{C}^N$ and set $f = 0 \in V_h$.
1: Solve (4.2.7) for the vector $\alpha \in \mathbb{C}^M$.
2: Find the solution $u_h$ using (4.2.4) and $\alpha$.
3: Calculate the average flux on each electrode using (4.2.10).

**4.2.2. Numerical solution of Model 2.** We now consider the numerical solution of Model 2, where we are given a vector describing the average boundary flux on each electrode. We remark that this is a weaker condition than the corresponding Neumann problem. In lieu of the well-posedness discussed in Chapter 3, we are required to constrain the solution to be constant on each electrode. We will explicitly describe how this constraint can be encoded into the finite element linear system.

Similar approaches to the FEM solution of models with either shunt-type boundary conditions or the complete electrode model can be found in [83], [183], [145], and [185].

Suppose we are given $\gamma \in \widetilde{\mathcal{A}}$, $f \in V_h$, and $Q \in \mathbb{C}^N_\diamond$ , we wish to find $(u_h, U_h) \in V_h \oplus \mathbb{C}^N$ satisfying

$$\begin{cases} -\operatorname{div}(\gamma \nabla u_h) &= f & \text{in} \quad \widetilde{\Omega}_h, \\ u_h &= (U_h)_k & \text{on} \quad \partial \widetilde{E}_k \text{ for } k = 1, \ldots, N, \\ |\partial \widetilde{E}_k|^{-1} \int_{\partial \widetilde{E}_k} \gamma \nabla u_h \cdot \hat{n} &= Q_k & \text{on} \quad \partial \widetilde{E}_k \text{ for } k = 1, \ldots, N \\ \gamma \nabla u_h \cdot \hat{n} &= 0 & \text{on} \quad \partial \widetilde{B}, \end{cases} \tag{4.2.11}$$

subject to the constraint

$$\sum_{k=1}^{N} (U_h)_k = 0. \tag{4.2.12}$$

We recall this final constraint is necessary for the solution to be unique. We begin by encoding the average flux on the electrodes to be the given vector $Q_k$. If we suppose $u_h$ is written as 4.2.4, then using $\widetilde{L}$, defined by 4.2.10, we can express the average boundary flux constraints as

$$\widetilde{L}\alpha = Q.$$

However, since $\sum_k Q_k = 0$, there are only $N - 1$ unique rows encoded in the above matrix with $N$ rows. In order, to preserve the minimal rank of the matrix, we choose (without loss of generality) to not directly impose the condition on the $N$-th electrode:

$$\left|\partial \widetilde{E}_N\right|^{-1} \int_{\partial \widetilde{E}_N} \gamma \nabla u_h \cdot \hat{n} \, \mathrm{d}s = Q_N. \tag{4.2.13}$$

However, since

$$\int_{\partial \widetilde{\Omega}_h} \gamma \nabla u_h \cdot \hat{n} \, \mathrm{d}s = 0,$$

(4.2.13) will necessarily hold and be implicitly imposed in the system. In practice this amounts to removing the last row of the matrix $\widetilde{L}$. Define the matrix $P \in \mathbb{K}^{(N-1)\times N}$ to be

$$P = \begin{pmatrix} I_{(N-1)\times(N-1)} & \mathbf{0} \end{pmatrix}, \tag{4.2.14}$$

where $I_{(N-1)\times(N-1)}$ is the identity matrix in $\mathbb{K}^{(N-1)\times(N-1)}$ and $\mathbf{0} \in \mathbb{K}^{N-1}$ is the vector of zeroes. The $N-1$ independent constraints can be written concisely as

$$P\widetilde{L}\alpha = PQ. \tag{4.2.15}$$

We now consider the constraint (4.2.12). Let $\mathbf{1} \in \mathbb{C}^N$ be the vector of ones, then can (4.2.12) be written

$$\mathbf{1} \cdot U = 0. \tag{4.2.16}$$

Combining (4.2.7), (4.2.15), and (4.2.16), we deduce $[\alpha, U]^T \in \mathbb{K}^{M+N}$ satisfies

$$\begin{bmatrix} \mathbf{A}_1 & -B \\ P\widetilde{L} & 0 \\ 0 & \mathbf{1}^T \end{bmatrix} \begin{bmatrix} \alpha \\ U \end{bmatrix} = \begin{bmatrix} F \\ PQ \\ 0 \end{bmatrix},$$

where $F \in \mathbb{K}^M$ is given by (4.2.6). Define

$$\mathbf{A}_2 := \begin{bmatrix} \mathbf{A}_1 & -B \\ P\widetilde{L} & 0 \\ 0 & \mathbf{1}^T \end{bmatrix} \in \mathbb{K}^{N+M,N+M} \text{ and } \mathbf{b}_2 = \begin{bmatrix} F \\ PQ \\ 0 \end{bmatrix} \in \mathbb{K}^{N+M},$$

then (4.2.4) is a solution to (4.2.11) if and only if $[\alpha, U] \in \mathbb{K}^{N+M}$ satisfies

$$\mathbf{A}_2 \begin{bmatrix} \alpha \\ U \end{bmatrix} = \mathbf{b}_2. \tag{4.2.17}$$

We remark that since the matrix $\mathbf{A}_1$ has rank $M$, $L$ has rank $N-1$, and the row $\begin{bmatrix} 0 & \mathbf{1}^T \end{bmatrix}$ has rank 1, the matrix $\mathbf{A}_2$ is invertible provided the rows are independent. This is analytically and numerically verifiable and hence a numerical solution to (4.2.17) can be found.

To summarise, Model 2 can be solved numerically by implementing following pseudo-code. This is done in FreeFem++ and the code is provided in Appendix B.

**Algorithm 2** Pseudo-code solver for Model 2.

**Require:** $Q \in \mathbb{C}^N_\diamond$ with and set $f = 0 \in V_h$.
1: Solve (4.2.17) to find the vector $[\alpha, U]^T \in \mathbb{C}^{M+N}$.
2: The measurements are then given directly by the vector $U \in \mathbb{C}^N_\diamond$.

**4.2.3. Testing of the numerical solvers in the frequency domain.** The derivation and numerical solution of (4.2.7) and (4.2.17) have been been implemented by the author using the finite element software package FreeFem++ [87]. As discussed earlier, estimating the accuracy of the solvers in the absence of an analytical solution is difficult. We numerically verify the convergence of the FEM solution to Model 1 and Model 2 as $h \to h^*$, for some fixed but small $h^* > 0$. We also discuss the consistency of the FEM solution to Models 1 and Models 2. We specialise to the planar geometry case and use a domain similar to Figure 2.1.1. The code given in Appendix A defines this sensor geometry used for these tests and generates a mesh in FreeFem++.

*Convergence of Model 1 and Model 2.* We increment the number of nodes on the boundary and solve on a triangulation of each domain. We then consider the projection of $u_{h^*}$ onto the triangulation $\mathcal{T}_h$ using the interpolation operator native to FreeFem++, which we denote by $\pi$.

Since the solution depends linearly on the choice of boundary condition, it suffices to consider the accuracy on a set of basis functions describing the boundary conditions. In our case, due to the discretised nature of the electrodes, this is a finite dimensional space isomorphic to $\mathbb{K}^{N-1}$. We choose the basis given by $\{V_i\}_{i=1}^{N-1} \subset \mathbb{K}^N_\diamond$ with $V_i \in \mathbb{K}^N_\diamond$ defined by

$$(V_i)_k = \begin{cases} 1 & \text{if } k = i, \\ -1 & \text{if } k = i+1, \\ 0 & \text{otherwise.} \end{cases}$$

The space of all admissible boundary conditions is then given by span $\{V_1, \ldots, V_{N-1}\}$.

We consider both the $L^2$ and the $H^1$ norms of the difference on this basis. More precisely, we track, as functions of $h$, $\xi_{L^2}$ and $\xi_{H^1}$ defined by

$$\xi_{L^2}(h) = \frac{1}{N-1} \sum_{i=1}^{N} \left\| u_h(V_i) - \pi\left(u_{h^*}(V_i)\right) \right\|_{L^2(\Omega)}$$

and

$$\xi_{H^1}(h) = \frac{1}{N-1} \sum_{i=1}^{N} \left\| u_h(V_i) - \pi\left(u_{h^*}(V_i)\right) \right\|_{H^1(\Omega)},$$

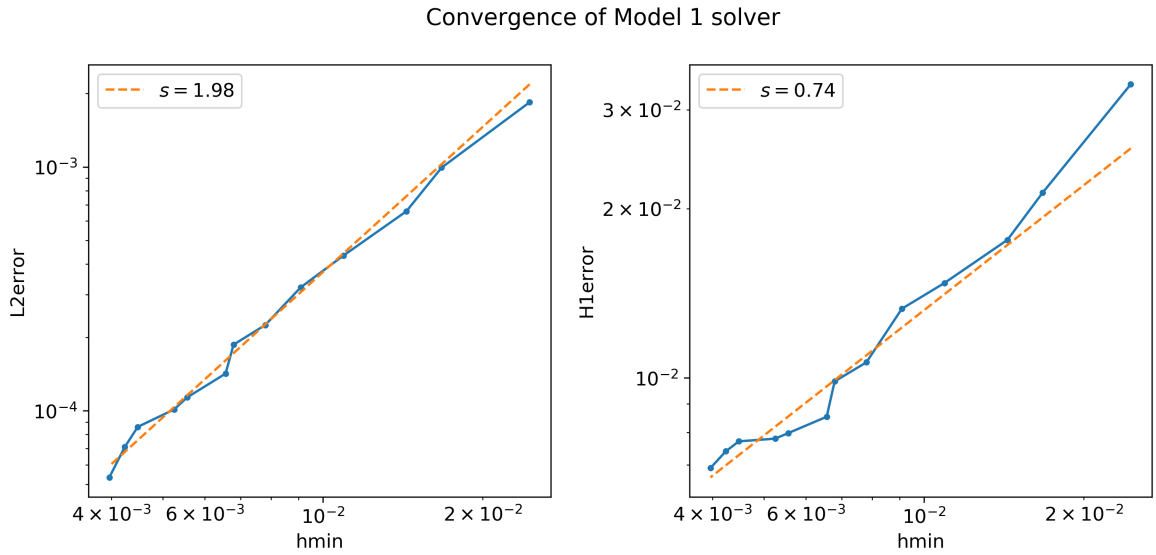



FIGURE 4.2.1. Log-log plot of $\xi_{L^2}$ showing $\xi_{L^2} \sim h^s$ (left) and $\xi_{H^1}$ showing $\xi_{H^1} \sim h^s$ (right) using the solver for Model 1.

where we write $u_h(V_i)$ to be the solution of either Model 1 or Model 2 with the input boundary conditions given by $V_i$.

Tracking these metrics in FreeFem++ as the mesh is refined by placing more nodes on the electrode boundaries we observe that $\xi_{L^2} \to 0$ and $\xi_{H^1} \to 0$ as $h \to 0$ for both the Model 1 solver and the Model 2 solver, see Figure 4.2.1 and Figure 4.2.2. In all cases, we see clearly that the solution is converging as the mesh is refined, although we observe slower convergence rates for Model 2 than for Model 1. Furthermore, we observe that for the Dirichlet solver in Model 1, $\xi_{L^2} \sim h^s$ for $s \approx 1.98$ and $\xi_{H^1} \sim h^s$ for $s \approx 0.74$. This empirical result is as expected as theoretical rate for the convergence with $P_1$ elements is 2.0 in the $L^2$ norm [32]. In the case of Model 2, we observe slower convergence in the $L^2$ norm than anticipated but faster convergence for the $H^1$ norm than expected. This is most likely due to being in the pre-asymptotic regime and we expect that further refinement of the mesh will resolve this discrepancy between the theoretical and observed rates of convergence.

*Consistency of Model 1 and Model 2.* Define the operator

$$S_{\mathrm{D}}^h : \mathbb{K}_\diamond^N \longrightarrow \mathbb{K}_\diamond^N$$

$$U \longmapsto Q_h$$

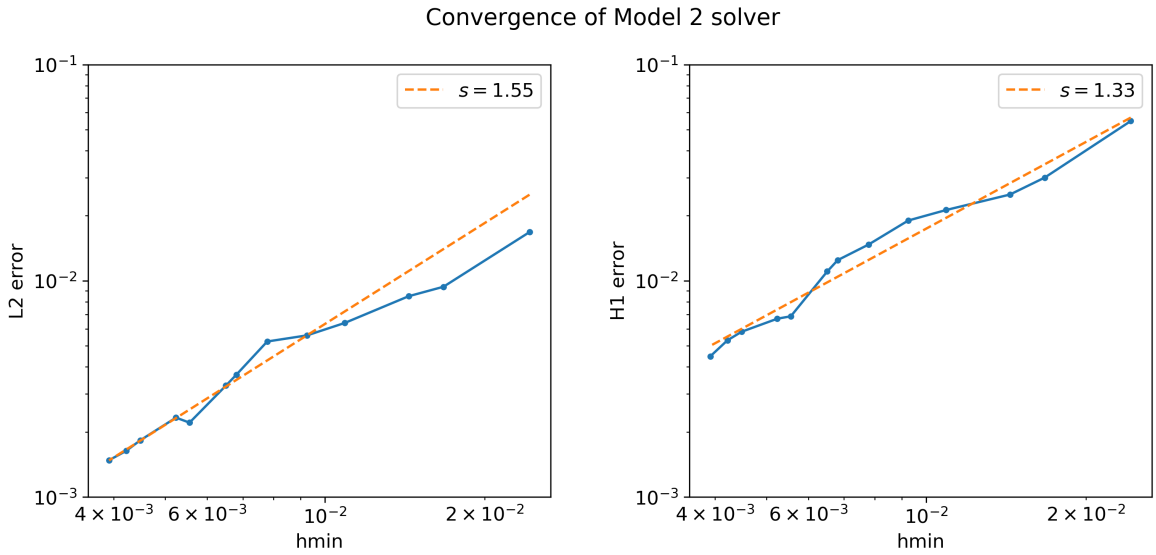



FIGURE 4.2.2. Log-log plot of $\xi_{L^2}$ showing $\xi_{L^2} \sim h^s$ (left) and $\xi_{H^1}$ showing $\xi_{H^1} \sim h^s$ (right) using the solver for Model 2.

where $Q$ is the measured flux of the solution to (4.2.10). Similarly, define the linear operator

$$S_{\mathrm{S}}^h : \mathbb{K}_\diamond^N \longrightarrow \mathbb{K}_\diamond^N$$

$$Q \longmapsto U_h$$

where $U_h$ is the part of the solution to (4.2.17). Since the underlying PDE has a unique solution and as a result specifying either $U$ or $Q$ will result in the same solution in $H_\diamond^1(\Omega)$. In other words, if the numerical solvers are consistent then

$$S_{\mathrm{S}}^h \circ S_{\mathrm{D}}^h \approx \mathrm{Id}_{\mathbb{K}_\diamond^N \to \mathbb{K}_\diamond^N} \tag{4.2.18}$$

and

$$S_{\mathrm{D}}^h \circ S_{\mathrm{S}}^h \approx \mathrm{Id}_{\mathbb{K}_\diamond^N \to \mathbb{K}_\diamond^N}. \tag{4.2.19}$$

We hypothesise that any error observed is due to the imprecise meshing of the electrode boundaries and the numerical error in the FEM solution. We would expect this error to decrease as more nodes are placed on the electrode boundaries increasing the resolution of the mesh and enforcing $\widetilde{\Omega}_h$ to better approximate $\Omega$.

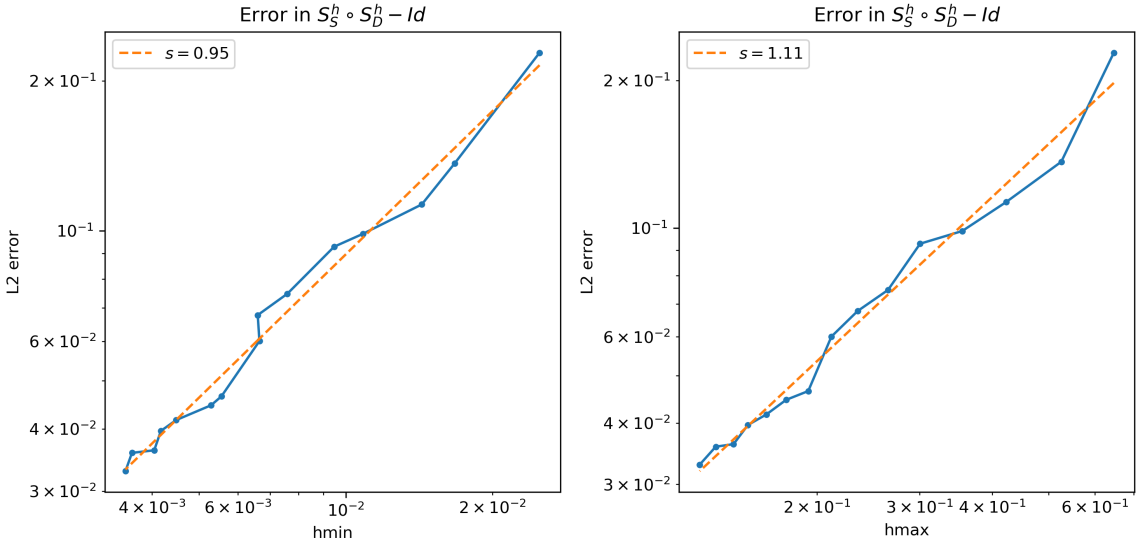



FIGURE 4.2.3. Log-log plot of $\xi_{\mathrm{SD}}$ showing $\xi_{\mathrm{SD}} \approx Ch^s$ where $h$ is given by $\min_{K\in\mathcal{T}_h} h$ (left) and $\max_{K\in\mathcal{T}_h} h$ (right).

Once again, since each of the operators are linear it is sufficient to verify (4.2.18) and (4.2.19) for the basis of $\mathbb{K}^N_\diamond$, $\{V_k\}_{k=1}^N$, defined previously. We calculate

$$\xi_{\mathrm{SD}}(h) := \frac{1}{N-1}\sum_{i=1}^{N-1} \left\| S_{\mathrm{S}}^h\left(S_{\mathrm{D}}^h\left(V_i\right)\right) - V_i \right\|_{\mathbb{K}^N}$$

and

$$\xi_{DS}(h) := \frac{1}{N-1}\sum_{i=1}^{N-1} \left\| S_{\mathrm{D}}^h\left(S_{\mathrm{S}}^h\left(V_i\right)\right) - V_i \right\|_{\mathbb{K}^N}.$$

We track the mesh resolution by recording the minimum shape parameter $\min_{K\in\mathcal{T}_h} h$ and the maximum shape parameter $\max_{K\in\mathcal{T}_h} h$. We remark that since non-uniform triangulations are used, we expect slightly different rates of convergence to be observed for each representation of the typical length scale. Figure (4.2.3) and (4.2.4) demonstrate that the error is dependent on the mesh resolution, which decreases as the mesh is refined.

Furthermore, expressing $\xi_{\mathrm{SD}}$ as relative percentage we see reasonable agreement in (4.2.18) and in (4.2.19), see Figure (4.2.5).

Using these empirical results, we conclude that the implementation of the algorithms produces consistent and convergent solutions. Therefore, the code is suitable to be used to generate simulated test data.

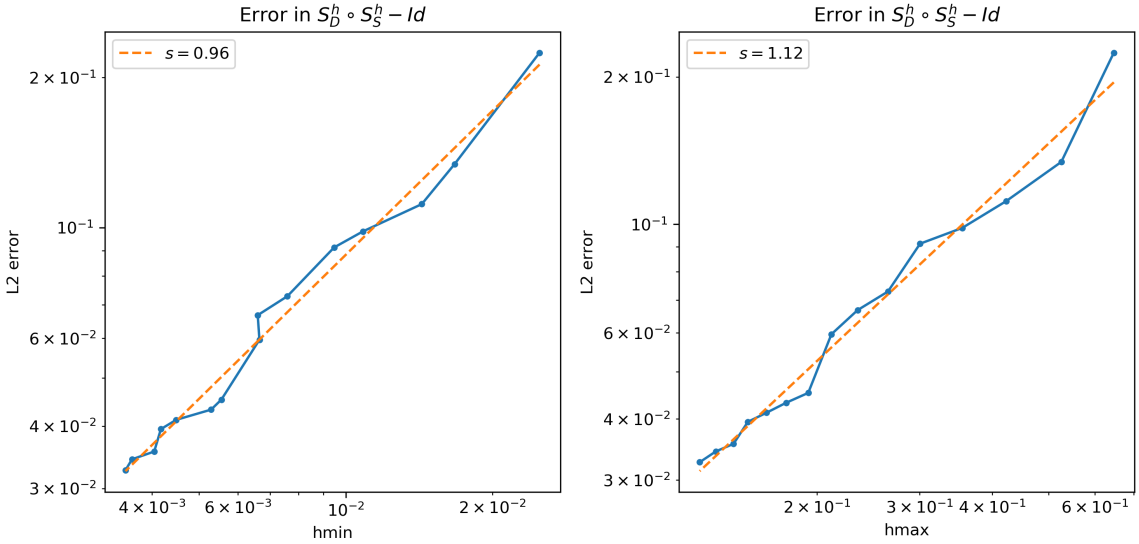



FIGURE 4.2.4. Log-log plot of $\xi_{\mathrm{DS}}$ showing $\xi_{\mathrm{DS}} \approx Ch^s$ where $h$ is given by $\min_{K\in\mathcal{T}_h} h$ (left) and $\max_{K\in\mathcal{T}_h} h$ (right).

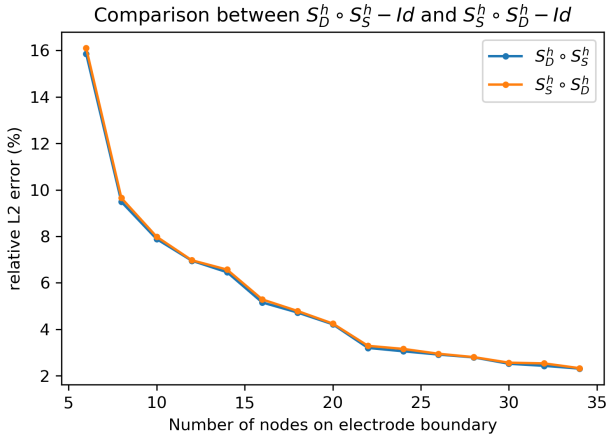



FIGURE 4.2.5. Relative error $\xi_0$ as a function of the number of mesh elements $N_T$.

## 4.3. Numerical solution in the time domain

We now discuss the numerical solution of the models in the time domain. We solve in the time domain using a time stepping scheme and solve in space using the FEM. We suppose the time interval $[0, T]$ is subdivided into $N_T \in \mathbb{N}$ segments of equal length $d = T/N_T$ which we denote by $t_0, \ldots, t_{N_T-1}$. All of the algorithms are implemented in FreeFem++ using the code given in Appendix C.

**4.3.1. Model 3.** We begin with describing the equivalent linear system for Model 3 when Dirichlet boundary conditions, described by the vector $U \in \mathbb{R}^N$, are imposed on the electrodes. The FEM problem in space then becomes: given $U \in \mathbb{R}^N$ and $f \in C(0,T;V_h)$, find $u_h \in V_h$ for every $t \in [0,T]$

$$\begin{cases} -\operatorname{div}(\varepsilon \partial_t \nabla u_h) - \operatorname{div}(\sigma \nabla u_h) = f(t,\cdot) & \text{in } \Omega_h, \\ u_h = U_k & \text{on } \partial E_k \text{ for } k = 1,\dots,N, \\ \varepsilon \nabla u_h \cdot \hat{n} = 0 & \text{on } \partial B, \\ u_h(0,\cdot) = 0 & \text{in } \Omega. \end{cases} \tag{4.3.1}$$

We use a backward discretisation scheme to discretise the time derivative and write

$$\partial_t \nabla u_h|_{t_{n+1}} = d^{-1}\left(\nabla u_h^{n+1} - \nabla u_h^n\right) \tag{4.3.2}$$

for $n = 0,\dots,N_t - 1$, where $u_h^n = u_h(t_n,\cdot) \in V_h$. By substitution and rearrangement, we establish that $u_h^{n+1}$ solves

$$\begin{cases} -\operatorname{div}\left((\varepsilon + d\,\sigma)\nabla u_h^{n+1}\right) = d\, f(t_{n+1},\cdot) + \operatorname{div}(\varepsilon \nabla u_h^n) & \text{in } \Omega_h, \\ u_h^{n+1} = U_k(t_{n+1}) & \text{on } \partial E_k \text{ for } k = 1,\dots,N, \\ \varepsilon \nabla u_h^{n+1} \cdot \hat{n} = 0 & \text{on } \partial B, \end{cases} \tag{4.3.3}$$

for each $n = 0,\dots,N-1$. Associating each $u_h^{n+1} \in V_h$ to the representation vector $\alpha^{n+1} \in \mathbb{R}^M$ and $f(t_n,\cdot) \in V_h$ to $F^n \in \mathbb{R}^M$, (4.3.3) can be represented by the equivalent system of equations

$$(A(\varepsilon + d\sigma) + B)\,\alpha^{n+1} = BU^{n+1} + d\,F^{n+1} - (A(\varepsilon) + B)\,\alpha^n \tag{4.3.4}$$

where

$$A_{ji}(\varepsilon) := \sum_{K \in \mathcal{T}_h} \int_K \varepsilon \nabla \phi_i \cdot \nabla \phi_j \,\mathrm{d}x \quad \text{for} \quad i,j = 1,\dots,M,$$

and

$$B_{ik} = \begin{cases} C & \text{if } \partial \widetilde{E}_k \subset \operatorname{supp}(\phi_i), \\ 0 & \text{otherwise,} \end{cases}$$

for some large $C > 0$. Therefore, given $\alpha^0 \in \mathbb{R}^M$, we can solve inductively to find $\alpha^n \in \mathbb{R}^N$ for all $n = 1, \dots, N_T$.

The measurements in this case correspond to the average flux at each $t_0, \dots, t_{N_T}$. This can be computed using the matrix $\widetilde{L}$, defined by (4.2.10), by

$$Q^{n+1} = \widetilde{L}\alpha^{n+1}.$$

Therefore, the simulated measurements are given by the vector-valued time series $Q^0, \dots, Q^{N_T}$. We summarise this procedure in the following pseudo-code.

**Algorithm 3** Pseudo-code solver for Model 3.

**Require:** $U \in C(0, T; \mathbb{R}^N)$ and set $f = 0 \in V_h$.
1: Initialise $n = 0$ and $\alpha^0 = 0 \in \mathbb{R}^N$.
2: **while** $n < N_T$ **do**
3: Solve (4.3.4) using $U^{n+1}$ to find $\alpha^{n+1}$.
4: Measure the average flux on the electrodes using $Q^{n+1} := L\alpha^{n+1}$.
5: Increment $n$: $n \leftarrow n + 1$.
6: **end while**
7: The measurements are then given by the time series $Q^0, \dots, Q^{N_T}$.

**4.3.2. Model 4.** We further generalise this to the case when only the average flux $Q \in C(0, T; \mathbb{R}^N)$ is known and prescribed on the boundary. That is we deduce the equivalent linear system to find $(u_h, U) \in V_h \times \mathbb{R}^N$ for each time $t \in [0, T]$ such that

$$\begin{cases} -\operatorname{div}(\varepsilon \partial_t \nabla u_h) - \operatorname{div}(\sigma \nabla u_h) = f(t, \cdot) & \text{in } \Omega_h, \\ u_h = U_k & \text{on } \partial E_k \text{ for } k = 1, \dots, N, \\ |\partial E_k|^{-1} \displaystyle\int_{\partial E_k} \varepsilon \nabla u_h \cdot \hat{n} = Q_k & \text{on } \partial E_k \text{ for } k = 1, \dots, N, \\ u_h(0, x) = 0 & \text{in } \Omega_h, \end{cases}$$

subject to $\sum_{k=1}^N U_k(t) = 0$ for every $t \in [0, T]$ and $u_h(0, \cdot) = 0$.

Using (4.3.2), we discretise this system of equations in time

$$\begin{cases} -\operatorname{div}\left((\varepsilon + d\sigma)\,\nabla u_h^{n+1}\right) = d\,f(t_{n+1},\cdot) + \operatorname{div}\left(\varepsilon \nabla u_h^n\right) & \text{in } \Omega_h, \\ u_h^{n+1} = U_k^{n+1} & \text{on } \partial E_k \text{ for } k = 1,\dots,N, \\ |\partial E_k|^{-1} \displaystyle\int_{\partial E_k} \varepsilon \nabla u_h^{n+1} \cdot \hat{n} = Q_k^{n+1} & \text{on } \partial E_k \text{ for } k = 1,\dots,N, \end{cases} \tag{4.3.5}$$

subject to $\sum_{k=1}^N U_k^n = 0$ for every $n = 0,\dots,N_T - 1$ and $u_h(0,\cdot) = 0$.

Written in terms of the representative vectors $\alpha^n \in \mathbb{R}^M$ and $U^n \in \mathbb{R}^N$ this becomes the linear system

$$\begin{bmatrix} A(\varepsilon + d\cdot\sigma) + B & -B \\ L & 0 \\ 0 & \mathbf{1}^T \end{bmatrix} \begin{bmatrix} \alpha^{n+1} \\ U^{n+1} \end{bmatrix} = \begin{bmatrix} d\,F^{n+1} - (A(\varepsilon) + B)\cdot\alpha^n \\ \widetilde{Q}\,(t_{n+1}) \\ 0 \end{bmatrix}, \tag{4.3.6}$$

where the matrix $L$ is defined by (4.2.8) and $\mathbf{1} \in \mathbb{R}^N$ is the vector of ones. This system can be solved inductively and the numerical solution at $t_n$, namely $u_h(t_n,\cdot)$, can be found given the initial conditions $\alpha^0 \in \mathbb{R}^M$ and $U^0 \in \mathbb{R}^N$.

**Algorithm 4** Pseudo-code solver for Model 4.

**Require:** $Q(t_n) \in \mathbb{C}^N$ with $\sum_k Q_k = 0$ for each $n = 1,\dots,N_T$ and set $f = 0 \in V_h$.
1: Initialise $n = 0$ and $\alpha^0 = 0 \in \mathbb{R}^N$.
2: **while** $n < N_T$ **do**
3: Solve (4.3.6) using $Q^n$ to find $[\alpha^{n+1}, U^{n+1}]^T \in \mathbb{R}^{M+N}$.
4: Increment $n$: $n \leftarrow n + 1$.
5: **end while**
6: The measurements are then given directly by the vector $U^{n+1} \in \mathbb{R}^N$ for each $n = 0,\dots,N-1$.

**4.3.3. Model 5.** We now consider the numerical solution of Model 5, the coupled PDE and ODE system given by (2.5.8). While it is possible to solve the ODE directly in our case, we choose to adopt a time-stepping procedure to obtain a numerical solution. By doing this, the same numerical procedure can be used if more complex ODEs are imposed on each of the electrode boundaries. Before giving the details, we introduce an indexing convention for the electrodes. While this may appear initially cumbersome there are benefits when fitting to real or simulated data: for different

choices of transmitting electrode $\partial E_I$, the solution of the ODE can be written in terms of same coefficient matrices ($Z_1$ and $Z_2$ defined below).

Let $\mathcal{I}$ be the set of indices corresponding to the transmitter (or injecting) electrode(s), which in our case is the singleton set $\mathcal{I} = \{I\}$. Denote the complement of the set $\mathcal{I}$ in $\{1, \dots, N\}$ by $\mathcal{I}^c$: $\mathcal{I}^c := \{1, \dots, N\} \setminus \mathcal{I}$. In other-words, $\mathcal{I}^c$ corresponds to the electrode indices where the flux condition will be imposed and $\mathcal{I}$ the electrode indices where the Dirichlet conditions will be imposed. Let $\{e_i\}_{i=1}^N$ be the standard basis of $\mathbb{R}^N$ and define for any $\mathcal{I} \subset \{1, \dots, N\}$, $P_{\mathcal{I}} \in \mathbb{R}^{|\mathcal{I}| \times N}$ to be the matrix with rows $e_k$ for $k \in \mathcal{I}$. Namely, let $\mathcal{I} := \{p_1, \dots, p_{|\mathcal{I}|}\}$ then

$$P_{\mathcal{I}} := \begin{pmatrix} e_{p_1} \\ \vdots \\ e_{p_{|\mathcal{I}|}} \end{pmatrix} \in \mathbb{R}^{|\mathcal{I}| \times N}.$$

More verbosely, given a vector $X \in \mathbb{R}^N$ and multiplying by $P$ returns the vector $PX \in \mathbb{R}^{|\mathcal{I}|}$ where only the entries of $X$ indexed by $\mathcal{I}$ remain. We denote the identity matrix in $\mathbb{R}^{N \times N}$ by $I_{N \times N}$.

We begin by considering the discretisation of the $N - 1$ ODEs:

$$\partial_t Q_k + (R_k C_k)^{-1} Q_k = C_k^{-1}(U_k - U_0) \tag{4.3.7}$$

for each $k = 1, \dots, N$ with $k \neq I$ where the constants $R_k, C_k > 0$ and $U_0 \in \mathbb{R}$ are known. Using $P_{\mathcal{I}^c}$ this can be written as a matrix system of equations in terms of $\widetilde{Q}(t) := P_{\mathcal{I}^c} Q(t) \in \mathbb{R}^{N-1}$ and $\widetilde{U}(t) := P_{\mathcal{I}^c} U(t) \in \mathbb{R}^{N-1}$ for each $t \in [0, T]$ as

$$\partial_t \widetilde{Q} + (P_{\mathcal{I}^c} Z_1)\, \widetilde{Q} = (P_{\mathcal{I}^c} Z_2) \left( \widetilde{U} - U_0 \mathbf{1}_{\mathbb{R}^{N-1}} \right) \tag{4.3.8}$$

where $Z_1, Z_2 \in \mathbb{R}^{N \times N}$ are diagonal matrices given by

$$Z_1 = \begin{pmatrix} (R_1 C_1)^{-1} & & 0 \\ & \ddots & \\ 0 & & (R_N C_N)^{-1} \end{pmatrix} \text{ and } Z_2 = \begin{pmatrix} (C_1)^{-1} & & 0 \\ & \ddots & \\ 0 & & (C_N)^{-1} \end{pmatrix}.$$

Writing $\widetilde{Q}^n := \widetilde{Q}(t_n)$ and $\widetilde{U}^n := \widetilde{U}(t_n)$ , the differential equation (4.3.8) can be written in discretised form as

$$\left(\widetilde{Q}^{n+1} - \widetilde{Q}^n\right) + dP_{\mathcal{I}^c} Z_1 \widetilde{Q}^{n+1} = dP_{\mathcal{I}^c} Z_2 \left(\widetilde{U}^n - U_0 \mathbf{1}_{\mathbb{R}^{N-1}}\right). \tag{4.3.9}$$

Rearranging (4.3.9), we express $\widetilde{Q}^{n+1}$ in terms of $\widetilde{Q}^n$ and $\widetilde{U}^n$:

$$\widetilde{Q}^{n+1} = d \cdot \left(P_{\mathcal{I}^c} I_{N\times N} + dP_{\mathcal{I}^c} Z_1\right)^{-1} P_{\mathcal{I}^c} Z_2 \left(\widetilde{U}^n - U_0 \mathbf{1}\right) + P_{\mathcal{I}^c} I_{N\times N} \widetilde{Q}^n. \tag{4.3.10}$$

Therefore, given $\widetilde{U}^n$ for $n = 0, \ldots, N_T$, (4.3.10) can be solved inductively to find $\widetilde{Q}^n$ for each $n = 0, \ldots, N_T$. Higher order methods are also possible and for long time simulations of the electric field are desirable although we do not give the details here.

We consider a numerical solution of the PDE given $\widetilde{Q}^n$ for each $n = 0, \ldots, N_T + 1$ and $U_I \in C([0, T])$ . Discretising the equation in the same way as in the previous sections, we wish to deduce a linear system of equations equivalent to finding $u_h^{n+1} \in V_h$ for any $n = 0, \ldots, N_T - 1$ such that

$$\begin{cases} -\operatorname{div}\left((\varepsilon + d\sigma)\nabla u_h^{n+1}\right) = d\, f(t_{n+1}, \cdot) + \operatorname{div}\left(\varepsilon \nabla u_h^n\right) & \text{in } \Omega_h, \\ u_h^{n+1} = U_I(t_{n+1}) & \text{on } \partial E_I, \\ u_h^{n+1} = U_k^{n+1} & \text{on } \partial E_k \text{ for } k \in \mathcal{I}^c, \\ |\partial E_k|^{-1} \displaystyle\int_{\partial E_k} \varepsilon \nabla u_h^{n+1} \cdot \hat{n} = Q_k^{n+1} & \text{on } \partial E_k \text{ for } k \in \mathcal{I}^c, \\ \varepsilon \nabla u_h \cdot \hat{n} = 0 & \text{on } \partial B, \\ u_h(0) = 0 & \text{in } \Omega_h. \end{cases} \tag{4.3.11}$$

This is a time-dependent PDE with mixed boundary conditions: a Dirichlet condition is imposed on $\partial E_I$, average flux conditions are imposed on $\partial E_k$ for $k \in \mathcal{I}^c$, and a zero Neumann condition is imposed on $\partial\Omega_B$. The resulting linear system is a combination of (4.3.4) and (4.3.6). Indeed, encoding the Dirichlet constraints as in (4.3.4), we have that

$$\left(A(\varepsilon + d\sigma) + B\right)\alpha^{n+1} = BU^{n+1} + d\, F^{n+1} - \left(A(\varepsilon) + B\right)\alpha^n, \tag{4.3.12}$$

where $\alpha^n \in \mathbb{R}^M$ are the coefficients of $u_h^n$ in the $\{\phi_i\}$ basis of $V_h$. However, since only the condition on $\partial E_I$ is known, which we write as $P_{\mathcal{I}} U^{n+1}$, we partition $BU^{n+1}$ as

$$BU^{n+1} = BP_{\mathcal{I}^c}^T P_{\mathcal{I}^c} U^{n+1} + BP_{\mathcal{I}}^T P_{\mathcal{I}} U^{n+1}, \tag{4.3.13}$$

where, for example, the product $BP_{\mathcal{I}}^T$ extracts the column of $B$ corresponding to $\partial E_I$. The average flux conditions can be written in terms of the matrix $L \in \mathbb{R}^{N\times N}$, defined component wise by

$$L_{ki} := \left|\partial \widetilde{E}_k\right|^{-1} \int_{\partial \widetilde{E}_k} \varepsilon \nabla \phi_i \cdot \hat{n} \, \mathrm{d}s,$$

as

$$P_{\mathcal{I}^c} L \alpha^{n+1} = P_{\mathcal{I}^c} Q^{n+1}. \tag{4.3.14}$$

Combining (4.3.12), (4.3.13), and (4.3.14) we write the vector of unknowns $\left[\alpha^{n+1}, P_{\mathcal{I}^c} U^{n+1}\right]^T \in \mathbb{R}^{M\times(N-1)}$ as the solution to

$$\begin{bmatrix} A(\varepsilon + d\,\sigma) + B & -BP_{\mathcal{I}^c}^T \\ P_{\mathcal{I}^c} L & 0 \end{bmatrix} \begin{bmatrix} \alpha^{n+1} \\ P_{\mathcal{I}^c} U^{n+1} \end{bmatrix} = \begin{bmatrix} d\,F^{n+1} + BP_{\mathcal{I}}^T P_{\mathcal{I}} U^{n+1} - (A(\varepsilon) + B)\,\alpha^n \\ P_{\mathcal{I}^c} \cdot Q^{n+1} \end{bmatrix}. \tag{4.3.15}$$

Using the ODE solver (4.3.10) and the PDE solver (4.3.15) alternately, we can inductively solve for $u_h^n$ and $U^n$ for each $n = 0, \ldots, N_T$ provided $U_I \in C(0,T)$, $Q^0 \in \mathbb{R}^N$, and $U_0 \in \mathbb{R}$ are given. Pseudo-code for this solver is given below and code written for FreeFem++ is given in Appendix C.

**Algorithm 5** Couple ODE-PDE solver for Model 5.

**Require:** $Q^0 \in \mathbb{R}^N$, $U_I \in C(0,T)$, $f \in C(0,T;V_h)$, and $U_0 \in \mathbb{R}$.
1: Initialise $n = 0$.
2: Discretise the functions $F^n = f(t_n)$ and $U_I^n(t_n)$ for each $n$.
3: **while** $n < N_T$ **do**
4: Solve (4.3.15) using $Q^n$, $F^n$ and $U_I^n$ to find $U^{n+1}$.
5: Solve (4.3.10) using $U^{n+1}$ to find $Q^{n+1}$.
6: Increment $n$: $n \leftarrow n+1$.
7: **end while**
8: The measurements are then given by the time series $U^n$ for $n = 0, \ldots, N_T$.

**4.3.4. Testing of the time dependent numerical schemes.** It suffices to check the convergence of the ODE solver, since the same solvers have already been

tested. In contrast to the PDE, the ODE can be solved analytically and a solution found for each choice of $U(t)-U_0$. In the simplest case that $U(t)-U_0 \equiv 1$, the solution of the ODE

$$\partial_t Q + z_1 Q = z_2 \text{ with } Q(0) = 0$$

is given by

$$Q(t) = z_1^{-1} z_2 \left(1 - e^{-z_1 t}\right), \text{ for } t > 0.$$

We choose $N_T$ for different integer values spanning 10 to 20000 (corresponding to $d$ from 0.1 to $10^{-5}$) and compare the numerical solution obtained with the analytic solution derived above. Choosing $z_1 = 3$ and $z_2 = 2$, we establish that the numerical solution is stable on the time interval $[0, T]$ for all values of $d$ tested, Figure 4.3.1a. Moreover, provided $N_T > 2000$ the maximal error in this case is at most $10^{-4}$.

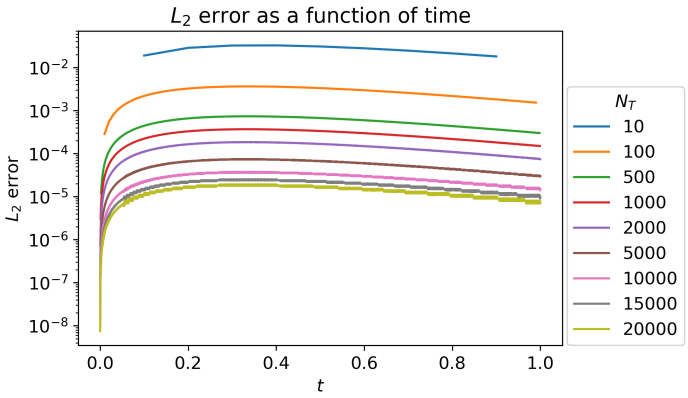
Finally we remark that the global truncation error is of order $d$ as expected, see Figure 4.3.1b. These results further justifies our decision to not develop higher order methods to solve the ODE since for $d$ between 0.1 and $10^{-5}$, the error in solving the ODE in time is significantly less than the error made when solving the PDE in space.

## 4.4. Fitting of the model parameters

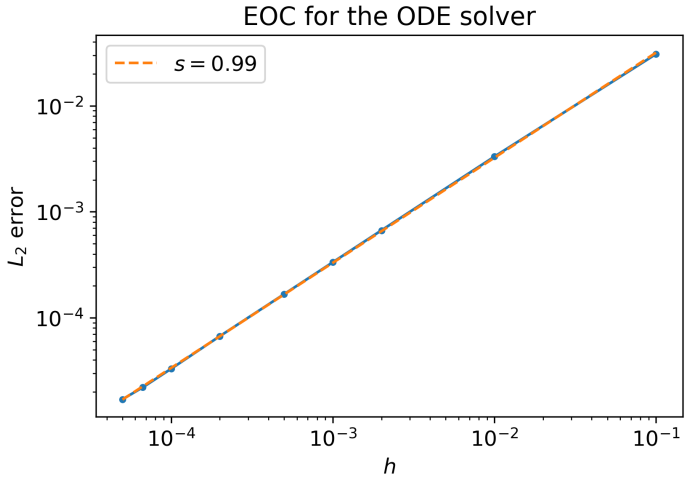
In this section we describe a procedure for fitting the parameters $R_k$ and $C_k$ appearing in Model 5 to simulated data. We remark that this parameter fitting problem can be considered as an inverse problem in its own right, however, unlike the inverse problems discussed in the next chapter, this inverse problem is overdetermined. For the remainder of this chapter, we shall suppose that the material parameters $\varepsilon \in \mathcal{A}_{\mathrm{p}}$ and $\sigma \in \mathcal{A}_{\mathrm{c}}$ are known and fixed.

**4.4.1. Full data case.** In this section we suppose that we have knowledge of $U \in C\left([0,T]\,;\mathbb{R}^N\right)$ and $Q \in C^1\left([0,T]\,;\mathbb{R}^N\right)$. We choose $\mathcal{I} = \{T\}$ to be the indexing set of the transmitter $\partial E_T$ and $\mathcal{I}^c := \{1,\dots,N\} \setminus \{T\}$ to be the remainder. By virtue of the model, we have that for each $k \in \mathcal{I}^c$, $U_k$ and $Q_k$ satisfy

$$z_1^k \partial_t Q_k + z_2^k Q_k = (U_k - U_0), \tag{4.4.1}$$




(A) Demonstration of the solver stability in $[0, T]$




(B) Global truncation error as a function of step size $h$.

FIGURE 4.3.1. Convergence of the ODE solver.

for some coefficients $z_1^k, z_2^k > 0$. Note that we have redefined the coefficients, by writing $z_1^k = C_k$ and $z_2^k = R_k$. While it seems redundant, it is convenient when more complex ODEs are introduced since $z_1^k$ and $z_2^k$ will not be given in such a nice form in terms of the circuit parameters.

The problem then becomes to determine the coefficients $z_1^k$ and $z_2^k$ for each $k \in \mathcal{I}^c$ given time series approximations of $Q_k$ and $U_k$ at the distinct time points $\{t_i\}_{i=1}^{N_T}$ with $t_i \in [0, T]$. We suppose that the $\{t_i\}_{i=1}^{N_T}$ are ordered such that $0 = t_1 < \cdots < t_i < t_{i+1} < \cdots < t_{N_T} = T$. Considered as an inverse problem, this amounts to determining $2(N-1)$ unknown parameters from $N_T(N-1)$ measurements. For convenience, we suppose that the time points are equally spaced and consider without loss of generality

the case when $k = 1$. Indeed, since the ODEs for each $k$ are uncoupled the same estimation procedure can be repeated for each $k$ independently to estimate $z_1^k$ and $z_2^k$.

We discuss two methods for determining the unknown coefficients: the first uses the time series data of $U_k$ and $Q_k$ to approximate $\partial_t Q_k$ while the second uses the same data to approximate $\int_0^T Q \, \mathrm{d}t$ and $\int_0^T U \, \mathrm{d}t$. In both cases the accuracy is dependent on the sampling resolution of the time series. Therefore, we suppose that $N_T$ is large (greater than 100) to ensure that $t_{i+1} - t_i$ is small for each $i = 0, \ldots, N_T - 1$. Using either method an overdetermined system of equations is established and we choose $z_1$ and $z_2$ to correspond to the least squares solution. To avoid confusion, in this chapter we denote by $d$ the step size in the time domain and the characteristic mesh size in space by $h$.

We remark for this particular ODE an alternative approach exists by using the analytical solution of (4.4.1)

$$Q(t) = e^{-z_2 z_1^{-1} t} \left( Q_0 + z_1^{-1} \int_0^t (U(s) - U_0) e^{z_2 z_1^{-1} s} \, \mathrm{d}s \right). \tag{4.4.2}$$

Given the measurements of $\{Q(t_i)\}_{i=1}^{N_T}$, it is in principle possible to choose the parameters $(z_1, z_2)$ to satisfy

$$(z_1, z_2) := \arg\min_{(\alpha,\beta)\in\mathbb{R}^+\times\mathbb{R}^+} \frac{1}{2} \left\| Q(t_i) - \widetilde{Q}(t_i) \right\|_{\mathbb{R}^{N_T}}^2$$

where

$$\widetilde{Q}_k(t_i) = e^{-\alpha^{-1}\beta t} \left( Q_0 + \alpha^{-1} \int_0^t (U(s) - U_0) e^{\alpha^{-1}\beta s} \, \mathrm{d}s \right).$$

However, this is a non-trivial minimisation procedure and since $U(t)$ is only known as a time series $\{U(t_i)\}_{i=1}^{N_T}$ numerical integration will need to be used and this approach becomes similar to Method 2 discussed below.

4.4.1.1. *Method 1: Using a finite difference approximation.* Using $\{Q(t_i)\}_{i=1}^{N_T}$ and $\{U(t_i)\}_{i=1}^{N_T}$, we discretise (4.4.1) as

$$z_1 d^{-1} \left( Q\left(t_{i+1}\right) - Q\left(t_i\right) \right) + z_2 Q\left(t_{i+1}\right) = \left( U\left(t_{i+1}\right) - U_0 \right) \tag{4.4.3}$$

for each $i = 1, \ldots, N_T - 1$. Written as a system of $N_T - 1$ equations, this becomes

$$\begin{pmatrix} Q_2 - Q_1 & d\,Q_2 \\ \vdots & \vdots \\ Q_{N_T} - Q_{N_T-1} & d\,Q_{N_T} \end{pmatrix} \begin{pmatrix} z_1 \\ z_2 \end{pmatrix} = d \begin{pmatrix} U_2 - U_0 \\ \vdots \\ U_{N_T} - U_0 \end{pmatrix}, \tag{4.4.4}$$

where $Q(t_i) = Q_i$ and $U(t_i) = U_i$. Writing (4.4.4) as

$$A_1 \begin{pmatrix} z_1 \\ z_2 \end{pmatrix} = b_1,$$

for matrices $A_1 \in \mathbb{R}^{N_T-1,2}$ and $b_1 \in \mathbb{R}^{N_T-1}$ , the least squares approximation of $(z_1, z_2)^T \in \mathbb{R}^2$ is given by the solution of the normal equations

$$A_1^T A_1 \begin{pmatrix} z_1 \\ z_2 \end{pmatrix} = A_1^T b_1. \tag{4.4.5}$$

The accuracy of the method is dependent on the error being committed in approximating $\partial_t Q$ discretely. If $N_T$ is very large, than the approximation given by (4.4.3) is likely to be small, however, if $N_T$ is not large enough additional approximation errors may be introduced. We therefore, introduce a second order method for comparison: replacing (4.4.3) by

$$z_1(2d)^{-1}\left(Q\left(t_{i+2}\right) - Q\left(t_i\right)\right) + z_2 Q\left(t_{i+1}\right) = \left(U\left(t_{i+1}\right) - U_0\right).$$

In addition to the initial value of $U(t_0)$ given by $U_0$, this method requires $U(t_1)$. In the case when $U(t_1)$ is not known then a single step of the first order scheme is used to estimate $U(t_1)$ from $U(t_0)$. The system of $N_T - 2$ constraints, then becomes

$$A_2 \begin{pmatrix} z_1 \\ z_2 \end{pmatrix} = b_2$$

where

$$A_2 := \begin{pmatrix} Q_3 - Q_1 & (2d)Q_2 \\ \vdots & \vdots \\ Q_{N_T} - Q_{N_T-2} & (2d)Q_{N_T-1} \end{pmatrix} \text{ and } b_2 = d \begin{pmatrix} U_2 - U_0 \\ \vdots \\ U_{N_T-1} - U_0 \end{pmatrix}.$$

Once again, the least squares approximation of $z_1$ and $z_2$ is the solution of the equation

$$A_2^T A_2 \begin{pmatrix} z_1 \\ z_2 \end{pmatrix} = A_2^T b_2. \tag{4.4.6}$$

We compare numerically the accuracy of the estimated parameters found by solving (4.4.5) and (4.4.6). We first describe the generation of the test data. Choosing $U(t) - U_0 = 1$ for all $t$, we find using (4.4.2) that $Q(t) = z_2^{-1}\left(1 - e^{-z_2 z_1^{-1} t}\right)$ subject to $Q(0) = 0$. We sample this $Q(t)$ at times $t \in \{t_1, \ldots, t_{N_T}\}$ where $t_{i+1} = t_i + d$ and $d = T/N_T$, these samples are dependent on the parameter $d$ and we denote them by $Q_d \in \mathbb{R}^{N_T}$. For each sample $Q_d \in \mathbb{R}^{N_T}$, the systems (4.4.5) and (4.4.6) are solved and the solution, written as $\left(z_1^d, z_2^d\right)$, is compared to the true choice of parameters, denoted by $(z_1^{\text{true}}, z_2^{\text{true}})$. We consider the error function defined by

$$d \mapsto \left\| \left(z_1^d, z_2^d\right) - \left(z_1^{\text{true}}, z_2^{\text{true}}\right) \right\|_{\mathbb{R}^2} \tag{4.4.7}$$

for each method.

The numerical results for two different choices $(z_1^{\text{true}}, z_2^{\text{true}})$ are shown in Figure 4.4.1. We see that as the step size $d$ decreases, the estimated parameters $\left(z_1^d, z_2^d\right)$ converge to the true parameters in both cases. Furthermore, comparing the order of convergence, we establish that using (4.4.6) is a higher order method than solving (4.4.5) as expected. It is also appears that the accuracy of the parameter estimation, for a given step size, is dependent on the magnitude of the true parameter, however, further investigation is needed to make this observation robust.

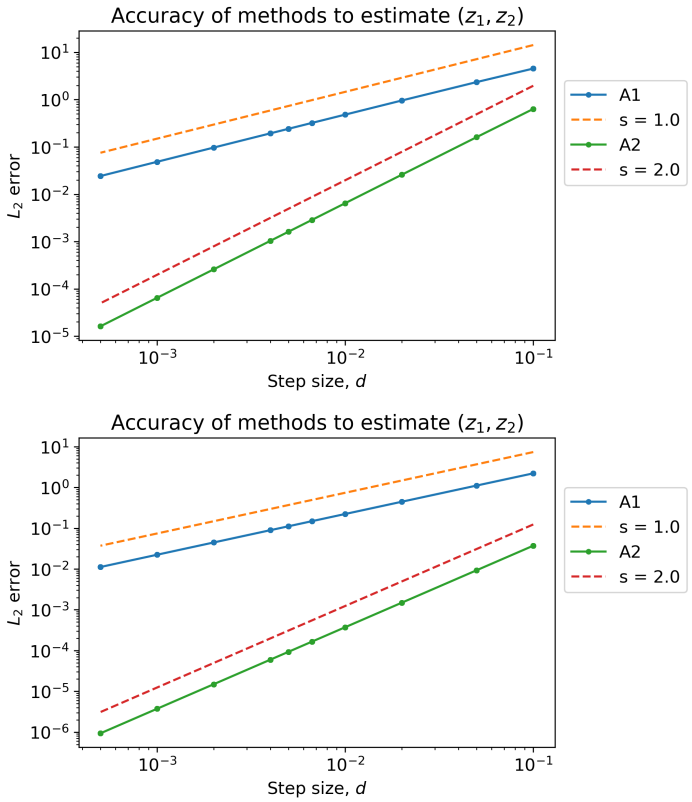



FIGURE 4.4.1. $L^2$ error as a function $d$ for the parameters estimated by solving (4.4.5) and (4.4.6) for $(z_1^{\text{true}}, z_2^{\text{true}}) = (0.5, 2)$ (top) and $(z_1^{\text{true}}, z_2^{\text{true}}) = (2, 1)$ (bottom).

4.4.1.2. *Method 2: Using numerical integration.* Integrating the ODE we obtain that for any $s_1, s_2 \in [0, T]$ with $s_1 < s_2$

$$z_1 \left(Q(s_2) - Q(s_1)\right) + z_2 \int_{s_1}^{s_2} Q \, \mathrm{d}t = \int_{s_1}^{s_2} \left(U_k - U_0\right) \, \mathrm{d}t \tag{4.4.8}$$

for each $k \in \mathcal{I}^c$. Using the closed Newton–Cotes formula we write

$$\int_{s_1}^{s_2} Q \, \mathrm{d}t \approx \sum_{i=1}^{n} w_i Q(t_i) \text{ and } \int_{s_1}^{s_2} U(t) \, \mathrm{d}t \approx \sum_{i=1}^{n} w_i U(t_i) \tag{4.4.9}$$

where $t_i = id + s_1$ and $d = (s_2 - s_1)/n$ with $n$ being the number of sampling points between $s_1$ and $s_2$. The $w_i$ are a choice of weights and are determined in closed form by $n$.

Given a time series of $Q$ and $U$ at the time points $\{t_1, \ldots, t_N\}$, we choose $s_1, s_2 \in \{t_1, \ldots, t_{N_T}\}$ where $s_1 < s_2$ are $n \geq 1$ apart i.e. if $s_1 = t_i$ and $s_2 = t_j$ then $j - i = n$.

Exhausting all such choices of $s_1$ and $s_2$ for a fixed $n$, we deduce $N_T - n$ constraints by combining (4.4.8) and (4.4.9).

More explicitly, when $n = 1$ (4.4.9) becomes the trapezium rule with

$$\int_{t_i}^{t_{i+1}} Q \, \mathrm{d}t \approx \frac{1}{2} \left(t_{i+1} - t_i\right) \left(Q(t_{i+1}) + Q(t_i)\right)$$

and

$$\int_{t_{i+1}}^{t_{i+1}} U \, \mathrm{d}t \approx \frac{1}{2} (t_{i+1} - t_i) \left(U(t_{i+1}) + U(t_i)\right).$$

Denoting $d = t_{i+1} - t_i$, which we assume to be constant for all $i$, the system of constraints becomes

$$\begin{pmatrix} Q_2 - Q_1 & \frac{1}{2} d \left(Q_2 + Q_1\right) \\ \vdots & \vdots \\ Q_{N_T} - Q_{N_T - 1} & \frac{1}{2} d \left(Q_{N_T} + Q_{N_T - 1}\right) \end{pmatrix} \begin{pmatrix} z_1 \\ z_2 \end{pmatrix} = \frac{1}{2} d \begin{pmatrix} U_2 + U_1 \\ \vdots \\ U_{N_T} + U_{N_T - 1} \end{pmatrix}, \quad (4.4.10)$$

written alternatively as

$$A_3 \begin{pmatrix} z_1 \\ z_2 \end{pmatrix} = b_3$$

for the matrix $A_3 \in \mathbb{R}^{N_T - 1, 2}$ and vector $b \in \mathbb{R}^{N_T - 1}$ defined by comparison with (4.4.10). Once again the least squares estimate of $z_1$ and $z_2$ is given by solving

$$A_3^T A_3 \begin{pmatrix} z_1 \\ z_2 \end{pmatrix} = A_3^T b_3. \quad (4.4.11)$$

For comparison we also consider the system of constraints when $n = 2$. In this case the numerical integration becomes equivalent to Simpson's rule and the resulting linear system of constraints is written in terms of $A_4 \in \mathbb{R}^{N_T - 2, 2}$ and $b \in \mathbb{R}^{N_T - 2}$ as

$$A_4 \begin{pmatrix} z_1 \\ z_2 \end{pmatrix} = b_4$$

where

$$A_4 := \begin{pmatrix} Q_3 - Q_1 & \frac{1}{3}d\left(Q_3 + 4Q_2 + Q_1\right) \\ \vdots & \vdots \\ Q_{N_T} - Q_{N_T-2} & \frac{1}{3}d\left(Q_{N_T} + 4Q_{N_T-1} + Q_{N_T-2}\right) \end{pmatrix} \tag{4.4.12}$$

and

$$b_4 = \frac{1}{3}d \begin{pmatrix} (U_3 + 4U_2 + U_1) \\ \vdots \\ (U_{N_T} + 4U_{N_T-1} + U_{N_T-2}) \end{pmatrix}.$$

Using this system the estimated parameters $z_1$ and $z_2$ satisfy

$$A_4^T A_4 \begin{pmatrix} z_1 \\ z_2 \end{pmatrix} = A_4^T b_4. \tag{4.4.13}$$

Using the test data $Q_d$ calculated previously, we compare the parameters estimated by solving (4.4.11) and (4.4.13). The relationship between the error and the step size $d$ can be seen in Figure 4.4.2. Firstly, we observe and achieve very good accuracy rates using these methods for modest values of the parameter $d$. The peculiar behaviour of method (4.4.13) at small step sizes that can be seen is likely to be a result of floating point rounding errors. If using this method in practice, care should be taken to ensure that such errors do not propagate through the solver.

4.4.1.3. *Stability of the solution to (4.4.6) and (4.4.13).* We compare the sensitivity of the estimated parameters subject to normally distributed additive noise in the time series $\{Q(t_i)\}_{i=1}^{N_T}$ and $\{U(t_i)\}_{i=1}^{N_T}$. We suppose that $\mu \sim N(0,1)$ and denote the standard deviation of the noise by $\sigma > 0$. We consider additive measurement noise that is proportional to the measurement signal, namely,

$$\widetilde{Q}(t_i) = Q(t_i)(1 + \sigma\mu) \text{ and } \widetilde{U}(t_i) = U(t_i)(1 + \sigma\mu) \text{ for } i = 1, \ldots, N_T.$$

For the test case described previously, example noisy measurements are shown in Figure 4.4.3.

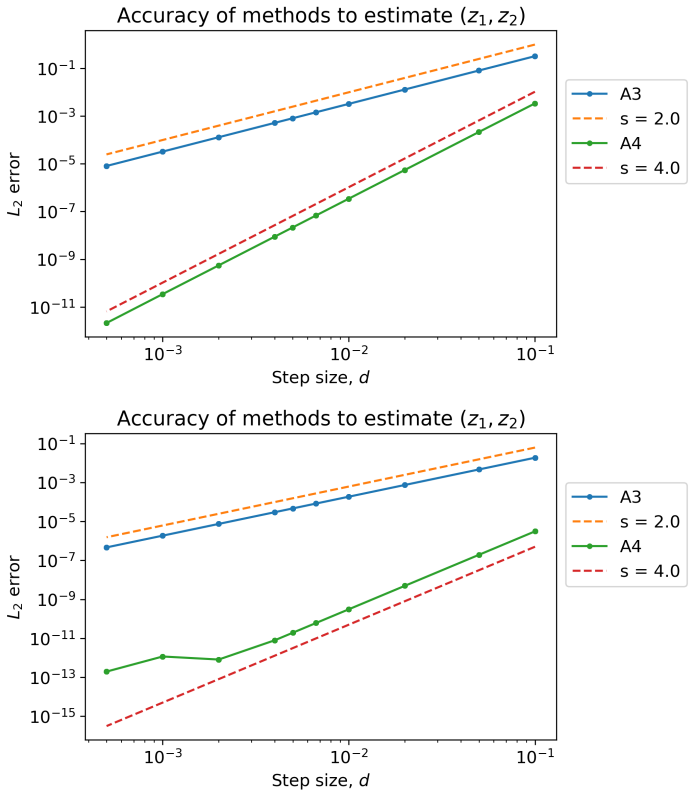



FIGURE 4.4.2. $L^2$ error as a function of the step size $d$ for the parameters estimated by solving (4.4.11) and (4.4.13) for $(z_1^{\text{true}}, z_2^{\text{true}}) = (0.5, 2)$ (top) and $(z_1^{\text{true}}, z_2^{\text{true}}) = (2, 1)$ (bottom).

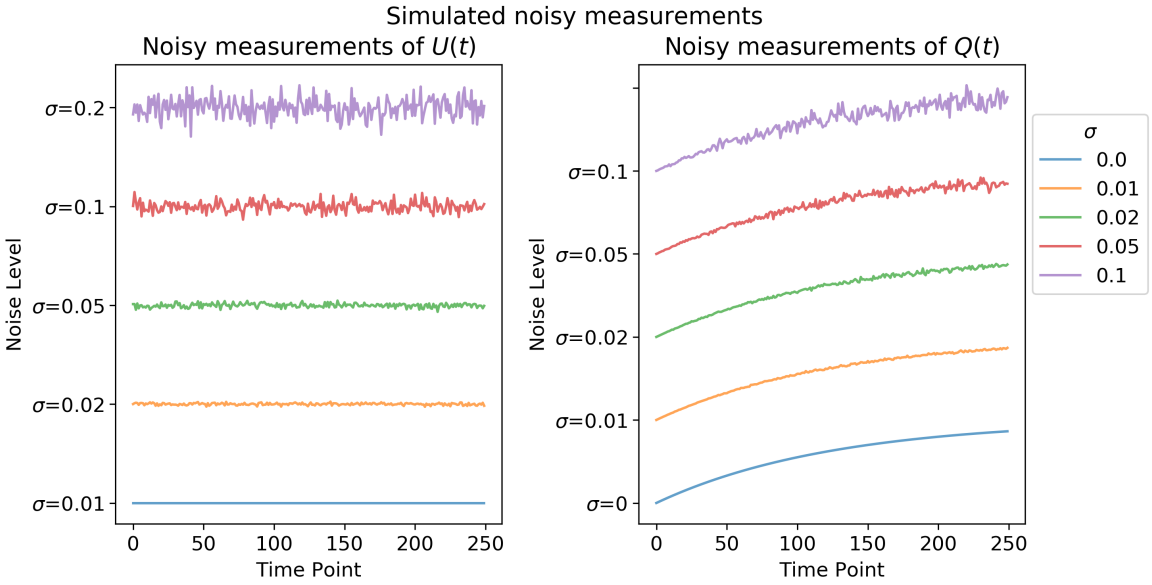



FIGURE 4.4.3. Example noisy measurements used for different values of $\sigma$. The measurements are vertically offset to allow for easier comparison.

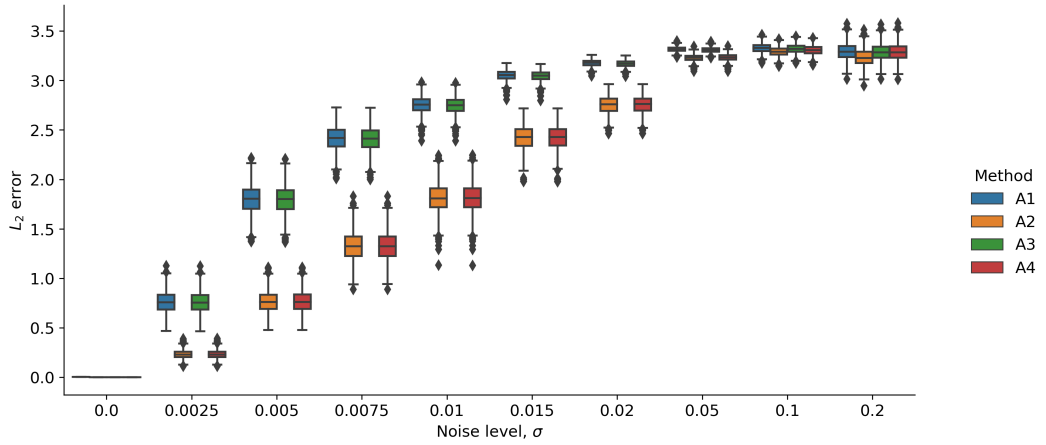



FIGURE 4.4.4. $L^2$ error as a function of the noise level $\sigma$ for all four methods. The true parameters are chosen to be $(z_1^{\text{true}}, z_2^{\text{true}}) = (2, 1)$.

Using the measurements with additive noise, we use the procedures described above to estimate $(z_1^\sigma, z_2^\sigma)$ and measure the distribution of

$$\sigma \longmapsto \left\| (z_1, z_2) - (z_1^{\text{true}}, z_2^{\text{true}}) \right\|_{\mathbb{R}^2}$$

where $z_1, z_2$ are found using solver (4.4.6) and (4.4.13). The results are shown in Figure 4.4.4. We see that a small addition of noice reduces the accuracy of the parameter estimation significantly. We also see that the higher order methods, A2 and A4, are more stable in the presence of measurement noise.

In conclusion, by comparing Figure 4.4.1 with Figure 4.4.2 and considering Figure 4.4.4, we find that the parameters found using (4.4.13) are more accurate than using (4.4.6). Furthermore, we see that the solutions to system (4.4.13) are as stable as the solutions of system (4.4.6). Therefore, we conclude that estimating the parameters using system (4.4.13) is preferable both in terms of accuracy and stability.

Although this analysis is not sufficient to determine the optimal method for estimating the parameters $z_1$ and $z_2$, we believe the accuracy obtained is sufficient for the purposes of this thesis. Improvements are likely to be possible using a weighted least squares to counteract measurement noise as well as investigating higher order integral methods. Preprocessing the data to remove measurement noise is also likely to improve the stability of the solvers and reduce the sensitivity to noice. However,

investigating these modifications is beyond the scope of this thesis. We conclude this section by summarising the algorithm that will be used to estimate $z_1$ and $z_2$.

**Algorithm 6** Procedure used to find $(z_1, z_2)$ in the full data case.

**Require:** The set of indices $\mathcal{I}^c$.
**Require:** The data $Q_k \in \mathbb{R}^{N_T}$, $U_k \in \mathbb{R}^{N_T}$ for each $k \in \mathcal{I}^c$.
1: **for** $k \in \mathcal{I}^c$ **do**
2: Compute the matrix $A_4$ and the vector $b_4$ defined in (4.4.12) using $Q_k$ and $U_k$.
3: Solve $A_4^T A_4 x = A_4^T b_4$ to find $(z_1^k, z_2^k)$.
4: **end for**
5: Return $(z_1^k, z_2^k)$ for each $k \in \mathcal{I}^c$.

**4.4.2. Partial data case.** We consider the case when $U_k(t)$ is known on all of the electrodes $k \in \mathcal{I}^c$ but that $Q_k(t)$ is not known for any $k = 1, \dots, N$. This situation resembles the data available in practice. Due to the lack of $Q_k(t)$ the procedure described above cannot be directly applied, however, we estimate $Q_k(t)$ by solving the PDE for a known $\varepsilon$ and $\sigma$ with boundary conditions given by the measurements $U_k(t)$ .

Let $w \in H^1(0, T; H^1(\Omega))$ be the solution to

$$\begin{cases} -\operatorname{div}(\varepsilon \partial_t \nabla w) - \operatorname{div}(\sigma \nabla w) = 0 & \text{in } [0,T] \times \Omega \\ w = U_k & \text{on } [0,T] \times \partial E_k \text{ for } k = 1, \dots, N \\ \varepsilon \nabla w \cdot \hat{n} = 0 & \text{on } [0,T] \times \partial \Omega_B. \end{cases} \tag{4.4.14}$$

Then by the uniqueness of the PDE, we must have $w = u$, where $u$ solves Model 5, and therefore,

$$|\partial E_k|^{-1} \int_{\partial E_k} \varepsilon \nabla w \cdot \hat{n} \, \mathrm{d}s = Q_k \text{ for } k \in \mathcal{I}^c.$$

Then, using $U_k(t)$ and $Q_k(t)$ for each $k \in \mathcal{I}^c$ the $\left(z_1^k, z_2^k\right)$ parameters can be estimated using Algorithm 6. This is summarised in the pseudo-code given by Algorithm 7.

To find the parameters $\left(z_1^k, z_2^k\right)$ for $k \in \mathcal{I}$ it is necessary to have access to data for different choices of $\mathcal{I}$. We denote the choices by $\{\mathcal{I}_j\}_{j=1}^P$ and suppose that $k = 1, \dots, N$, $k \in \mathcal{I}_j$ for at least one $j$. In other words, we suppose that each electrode acts a transmitter in at least once. In a system with $N$ electrodes, choosing $\mathcal{I}_j = \{j\}$ for

**Algorithm 7** Procedure used to find $(z_1, z_2)$ in the case when only the $U_k$ are known.

**Require:** The set of indices $\mathcal{I}^c$.
**Require:** The material parameters of $\varepsilon$ and $\sigma$.
**Require:** The data $U_k \in \mathbb{R}^{N_T}$ for each $k \in \mathcal{I}^c$.
**Require:** The sensor input $U_k \in \mathbb{R}^{N_T}$ for each $k \in \mathcal{I}$.
1: Solve (4.4.14) for the given $U_k$ for $k = 1, \ldots, N$ to find $w$.
2: Using (4.3.14) measure the average flux of $w$ on each $\partial E_k$. Denote this by $Q_k$.
3: **for** $k \in \mathcal{I}^c$ **do**
4: Compute the matrix $A_4$ and the vector $b_4$ defined in (4.4.12) using $Q_k$ and $U_k$.
5: Solve $A_4^T A_4 x = A_4^T b_4$ to find $(z_1^k, z_2^k)$.
6: **end for**
7: Return $(z_1^k, z_2^k)$ for each $k \in \mathcal{I}^c$.

$j = 1, \ldots, N$ gives such a system. Furthermore, this results in $N - 1$ estimations of each $\left(z_1^k, z_2^k\right)$ for each $k$, in which case it is reasonable to average the estimated parameters.

We test this procedure in the case of $N = 10$ for the case $\mathcal{I} = \{1\}$. We select the input pulse on $\mathcal{I}$ to be the sigmoid function defined by

$$\phi(t) = \frac{1}{1 + \exp\left(-15(t - 0.5)\right)}, \tag{4.4.15}$$

for $t \in [0, 3]$. We choose $N_T = 600$ and so $d = 1/200$. The mesh in space is fixed and includes over $20,000$ triangular elements with $h \approx 0.076$. The material parameters are chosen to be $\varepsilon = 1$ and $\sigma = 1$ corresponding to a measurement of an 'empty sensor'. We fix a choice of the parameters $z_1$ and $z_2$ for $k = 2, \ldots, N$. The values chosen can be seen in Figure 4.4.6 and the simulated $U_k$ and $Q_k$ can be seen in Figure 4.4.5.

Using the simulated $U_k$ and $Q_k$, Algorithm 7 is used to estimate the unknown parameters. A comparison between the true and estimated parameters is given in Figure (4.4.6). Visually we see a reasonable agreement between the true and the estimated parameters, however, it appears that the estimated parameters are consistently below the true value for $z_1$. It is unclear where this originates from but exploratory testing seems to indicate that this difference is mesh dependent and so is potentially a consequence of the polygonal approximation of the electrode boundaries.

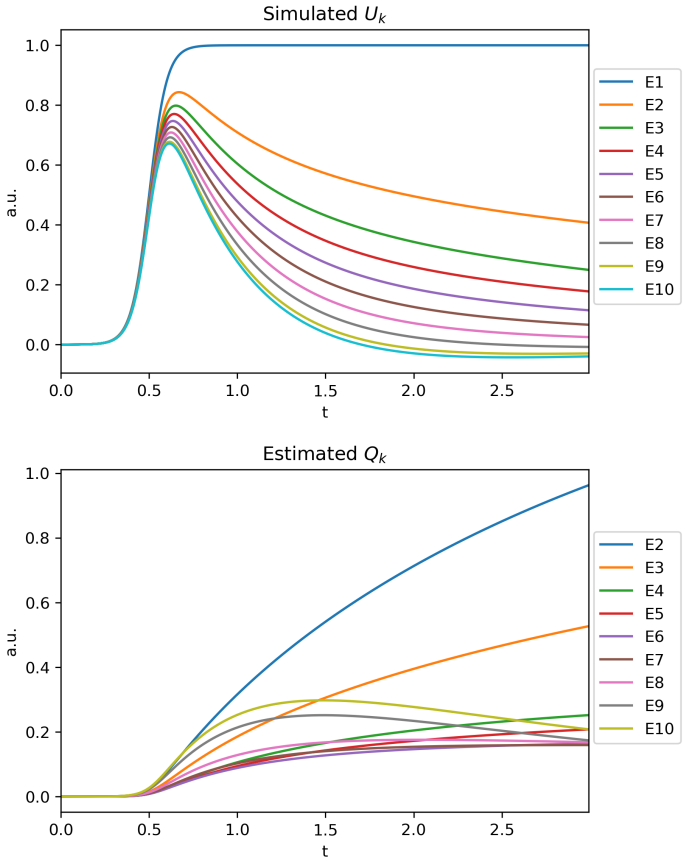



FIGURE 4.4.5. Simulated $U_k$ (left) and $Q_k$ (right). On $E_1$ the function given by(4.4.15) is applied.

## 4.5. Comparison of the models to real data

In this section we use Algorithm 7 to estimate the parameters $(z_1^k, z_2^k)$ using real sensor data supplied by Zedsen Ltd. The data supplied is collected by a planar sensor with 15 electrodes with no object in the sensing volume. Therefore, we suppose that the material parameters are $\varepsilon = 1$ in the sensing volume. We set $\sigma = 0$ throughout the domain. We model the Zedsen transmit function by the sigmoid function

$$\phi(t) = \frac{1}{1 + \exp\left(-60(t - 0.03)\right)}, \tag{4.5.1}$$

where the parameters were chosen to reflect the true transmit signal used. The Zedsen data consists of the measurements from 5 electrodes adjacent to the transmitter and sampled over 250 time points. The data has been scaled by the maximum possible measurement (the value 4095) and thus the measurements are represented by a real number between 0 and 1 as can be seen in Figure 4.5.1: by eye the data looks reasonable

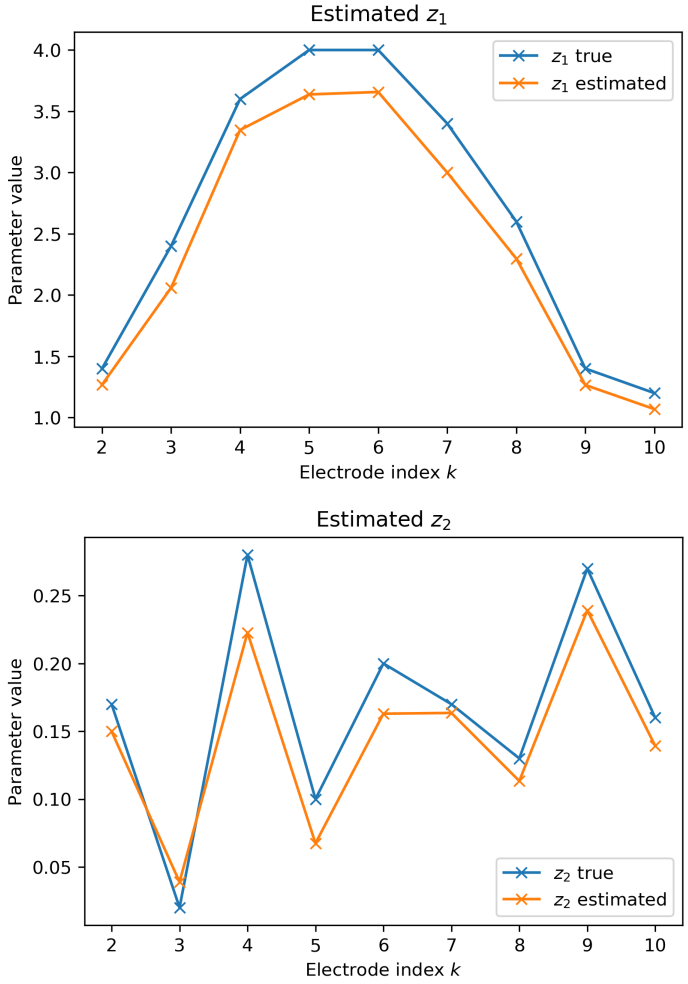



FIGURE 4.4.6. The estimated parameters $z_1$ and $z_2$ for $k = 2, \ldots, 10$ using Algorithm 7.

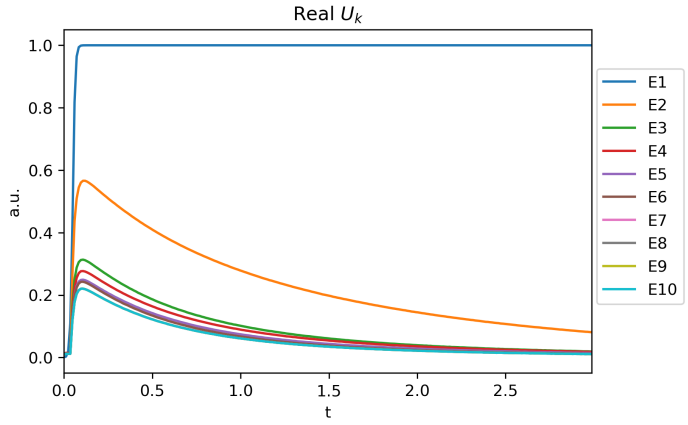



FIGURE 4.5.1. Plot of the real sensor measurements and the true transmit function.

and is qualitatively similar to the measurements predicted in the simulated case as shown in Figure 4.4.5.

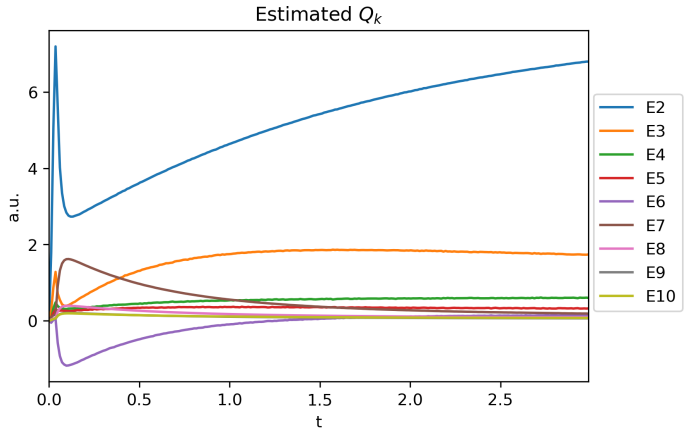



FIGURE 4.5.2. The estimated parameters $z_1$ and $z_2$ for $k = 2, \ldots, 10$ using Algorithm 7.

Using the measurements $\{U_k(t)\}_{k=1}^N$, we estimate $\{Q_k(t)\}_{k=1}^N$ by solving the PDE. The estimated $\{Q_k(t)\}_{k=1}^N$ can be seen in Figure 4.5.2. By considering the estimated charge $\{Q_k(t)\}_{k=1}^N$ we see peculiar behaviour. The author expects this due to (4.5.1) not approximating the true impulse function preventing the model from accurately reproducing the data. Modifying the transmit function, or using empirical measurements of the true transmit function, is the next logical step.

CHAPTER 5

# ECT as an inverse problem

In this chapter we discuss the inverse problem associated with EFS. The forward problem can be considered as a mapping from the space of admissible material parameters into the the set of all sensor input–output pairs. Formally, let $\mathcal{L}(X, Y)$ be the space of all bounded linear operators between Banach spaces $X$ and $Y$. We shall suppose that $X$ is the space of sensor inputs (the boundary conditions of the PDE) and $Y$ is the space of all possible measurements (for example the average flux on each electrode). In practice the spaces $X$ and $Y$ are finite dimensional, however, it is mathematically convenient to adopt the more general framework and consider $X$ and $Y$ to be Banach spaces. Let $\mathcal{A}$ be the space of all admissible parameters, then the forward problem is the operator

$$\mathcal{F} : \mathcal{A} \longrightarrow \mathcal{L}(X, Y),$$

where $X$, $Y$, and $\mathcal{L}$ are specific to the model being used. The inverse problem then becomes establishing the operator (should it exist)

$$\mathcal{F}^{-1} : \mathcal{L}(X, Y) \longrightarrow \mathcal{A}.$$

The aim of this chapter is to establish the operator $\mathcal{F}$ and $\mathcal{F}^{-1}$ associated to each of the five models introduced in Chapter 2. Once the operators have been defined, we discuss the discretisation of the problem and describe procedures for estimating the finite dimensional form of $\mathcal{F}(\gamma)$ from both simulated and real sensor measurements. We first consider the full-data problem and explicitly prove equivalence for different measurement paradigms. In particular, we define a novel measurement paradigm, which we call the *two electrode problem with mixed boundary conditions*, characterised by taking sequential, rather than concurrent, electrode measurements. The difficulty,

and novelty, of this measurement paradigm is there does not exist an immediate superposition principle due to the mixed boundary conditions. This measurement paradigm is motivated by considering the sensors developed by Zedsen Ltd. We then consider the partial data problem and consider novel approaches to estimate the missing data using weak assumptions on the distribution of the unknown parameter.

We begin with a motivating example of an inverse problem: the so called Calderón problem first introduced by Calderón himself in [37].

**5.0.1. Motivating example: the Calderón problem.** We begin by defining the Dirichlet-to-Neumann (DtN) and the Neumann-to-Dirichlet maps (NtD). For now, we suppose the electric potential is given as the unique solution to

$$-\operatorname{div}(\gamma \nabla u) = 0 \text{ in } \Omega \tag{5.0.1}$$

with Dirichlet boundary conditions

$$u = \varphi \text{ on } \partial\Omega \text{ with } \varphi \in H^{1/2}(\partial\Omega).$$

This corresponds to Model 1 with continuum boundary conditions (case 1 in Table 1). For this $u \in H^1(\Omega)$, let $m$ be the flux restricted to the boundary of the domain:

$$m = \gamma \nabla u \cdot \hat{n} \text{ on } \partial\Omega. \tag{5.0.2}$$

Typically, $m \in H^{-1/2}(\partial\Omega)$ which allows us to define the operator

$$\Lambda_\gamma : H^{1/2}(\partial\Omega) \longrightarrow H^{-1/2}(\partial\Omega)$$

$$\varphi \longmapsto m.$$

The operator $\Lambda_\gamma$ is known as the Dirichlet-to-Neumann (DtN) operator. We shall establish later that $\Lambda_\gamma \in \mathcal{L}\left(H^{1/2}(\partial\Omega), H^{-1/2}(\partial\Omega)\right)$. The forward problem can then be stated as

$$\mathcal{F} : \gamma \longmapsto \Lambda_\gamma$$

and the associated inverse problem becomes:

PROBLEM 1 (The Calderón problem). Given $\Lambda_\gamma$, find $\gamma \in \mathcal{A}$.

Alternatively, choosing $Y = H^{-1/2}(\partial\Omega)$ and $X_\diamond = H^{1/2}_\diamond(\partial\Omega)$ the Neumann-to-Dirichlet (NtD) operator is the operator

$$N_\gamma : H^{-1/2}_\diamond(\partial\Omega) \longrightarrow H^{1/2}_\diamond(\partial\Omega)$$
$$f \longmapsto u|_{\partial\Omega},$$

where $u \in H^1_\diamond(\Omega)$ solves 5.0.1 with boundary conditions

$$\gamma\nabla u \cdot \hat{n} = f \text{ on } \partial\Omega.$$

The forward problem is described by the operator

$$\mathcal{F} : \gamma \longmapsto N_\gamma,$$

and the associated inverse problem becomes

PROBLEM 2 (The Calderón problem 2). Given $N_\gamma$, find $\gamma \in \mathcal{A}$.

Referring to both of these as the Calderón problem is not incorrect since $\Lambda_\gamma^{-1} = N_\gamma$, provided $\Lambda_\gamma$ is restricted to $H^{1/2}_\diamond(\partial\Omega)$, and the equivalence of the inverse problems follows. However, for sake of this exposition we assume that the Calderón problem is written in terms of the Dirichlet-to-Neumann operator.

First proposed in [37], the Calderón problem has attracted substantial attention from the mathematical community with research focussing on four themes: identifiability, stability, partial boundary data, and numerical reconstruction. We discuss each of these in turn and briefly survey results the literature for the Calderón problem. A more detailed exposition can be found in the review papers [29, 179, 180].

**Identifiability of the parameter.** Most fundamental is the problem of identifiability: namely, given $\Lambda_\gamma$, does there indeed exists a unique $\gamma \in \mathcal{A}$. The existence of a parameter $\gamma \in \mathcal{A}$ is immediate from the definition and construction of the operator $\Lambda_\gamma$, however, this does not give a uniqueness result for $\gamma \in \mathcal{A}$. In other words, we wish to determine under what conditions, $\Lambda_{\gamma_1} = \Lambda_{\gamma_2}$ implies $\gamma_1 = \gamma_2$. Colloquially, this

statement is often referred to as the solvability of the inverse problem: is knowledge of the boundary data sufficient to determine the unknown parameter? If this is true, the parameter $\gamma$ is said to be *identifiable*. For the Calderón problem the answer relies on the dimension of the space. We briefly illustrate this by discussing a well-known counterexample, which demonstrates the non-identifiability of the parameter in one dimension [112].

In one dimension, only the determination of constant parameters is possible and as such the unknown parameter $\gamma$ is not identifiable. We illustrate this using an example on the domain $[0, 1]$. Given boundary conditions $u(0) = U_0$ and $u(1) = U_1$, the function $u$ solves

$$(\gamma(x)u'(x))' = 0 \text{ for } x \in [0, 1],$$

where $\cdot'$ denotes derivative with respect to $x$. In the inverse problem, we suppose that $\gamma(x)$ is unknown but the measurement $m_0 = \gamma(0)u'(0)$ is known. We wish to demonstrate that a general $\gamma$ cannot be determined from $m_0$ alone.

Integrating with respect to $x$, we establish

$$\gamma(x)u'(x) = C$$

for some $C \in \mathbb{R}$ and all $x \in [0, 1]$. Moreover, by choosing $x = 0$ it follows $C = m_0$. Integrating again in $x$, we establish

$$u(1) - u(0) = m_0 \int_0^1 \frac{1}{\gamma(x)} \, \mathrm{d}x.$$

In other words, for any choice of boundary conditions $u(1)$ and $u(0)$ it is only possible determine the reciprocal average of the parameter $\gamma(x)$ given by:

$$\int_0^1 \frac{1}{\gamma(x)} \, \mathrm{d}x = \frac{U_1 - U_0}{m_0}.$$

Consequently, a general parameter distribution $\gamma(x)$ cannot be determined from boundary measurements alone. However, restricting to constant parameter distributions,

$\gamma(x) = \gamma_0$ for some $\gamma_0 > 0$, we can write

$$\gamma_0 = \frac{m_0}{U_1 - U_0}.$$

This highlights a general principle: by restricting the class of admissible parameters it is often possible to turn a non-identifiable inverse problem into a solvable one.

Contrastingly—and rather surprisingly—in two dimensions, the parameter $\gamma \in \mathcal{A}$ can be determined from knowledge of the DtN map alone [13]. This result is the main theoretical underpinning of this work. An earlier, but directly relevant result to this thesis, is the possibilty to reconstruct piecewise analytic functions from knowledge of the boundary data [113].

For dimensions three and higher, if that the isotropic conductivity is sufficiently smooth, namely $\gamma \in C^2(\Omega)$, then knowledge of the DtN map is sufficient to determine the unknown coefficient [173]. This result can be extended further to also include Lipschitz conductivities [33]. However, the $L^\infty(\Omega)$ identifiability result for dimensions greater than three is still open. We combine this into the following result.

THEOREM (Identifiability of the Calderón problem). *Let $\Omega \subset \mathbb{K}^n$ be a bounded $C^2$ domain. Suppose that either*

*(1) $\gamma_1, \gamma_2 \in \mathcal{A}$ when $n = 2$, or*

*(2) $\gamma_1, \gamma_2$ are strictly positive functions in $C^2(\Omega)$ when $n \geq 3$, or*

*(3) $\gamma_1, \gamma_2$ are piecewise analytic functions*

*In each case, if $\Lambda_{\gamma_1} = \Lambda_{\gamma_2}$, then $\gamma_1 = \gamma_2$ in $\Omega$.*

PROOF. The method of proof is different for each $n$. When $n = 2$, see [13] and when $n \geq 3$ see [173]. For the piecewise analytic case, see [113]. □

**Stability of the inverse problem.** The stability of the problem is equivalent to understanding the dependence of the unknown parameter $\gamma \in \mathcal{A}$ on the data $\Lambda_\gamma$. An understanding of the stability is vital for the reliability of a reconstruction procedure particularly in the case where the measurements are affected by measurement errors.

It is well known that for the Calderón problem continuous dependence does not hold: namely, that for an arbitrary choice of $\gamma_1, \gamma_2 \in \mathcal{A}$, an $L^\infty(\Omega)$ estimate of the form

$$\|\gamma_1 - \gamma_2\|_{L^\infty(\Omega)} \leq C \, \|\Lambda_{\gamma_2} - \Lambda_{\gamma_2}\|_{H^{-1/2}(\partial\Omega)} \tag{5.0.3}$$

for some constant $C > 0$ is not possible [6]. As an illustration, we construct an explicit counter example in the case when $\Omega$ is the unit ball in $\mathbb{R}^2$ where we show that $\Lambda_{\gamma_1}$ can become arbitrarily close to $\Lambda_{\gamma_2}$ despite $\gamma_1$ not being close to $\gamma_2$ in the $L^\infty$ norm:the same construction is discussed in [88] and in [31]. Let $B(r_0) \subset \Omega$ be the ball centred at $r_0 > 0$. For a fixed $0 < r_0 < 1$, consider the coefficients $\gamma_1 = 1$ and $\gamma_2 = 1 + \chi_{B(r_0)}$, where $\chi_{B(r_0)}$ is the characteristic function of the set $B(r_0)$. Considering the $L^\infty$ norm of the difference, there holds

$$\|\gamma_1 - \gamma_2\|_{L^\infty(\Omega)} = 1$$

for any choice of $r_0 > 0$.

Due to the rotational symmetry of parameters $\gamma_1$ and $\gamma_2$, equation (5.0.1) is separable. Therefore, given any choice of boundary condition $\varphi \in H^{1/2}(\partial\Omega)$, which can be written as

$$\varphi(\theta) = \sum_{n\in\mathbb{Z}} \widehat{\varphi}(n) e^{\mathrm{i}\, n\theta}$$

where

$$\|\varphi\|^2_{H^{1/2}(\partial\Omega)} = \sum_{n\in\mathbb{Z}} |n| \, |\widehat{\varphi}(n)|^2 < \infty.$$

The solution to (5.0.1), when $\gamma = \gamma_1$, can be written as

$$u_1(r,\theta) = \sum_{n\in\mathbb{Z}} \widehat{\varphi}(n) e^{\mathrm{i}\, n\theta} r^{|n|}.$$

We calculate the associated Neumann data to each such $\varphi$ to be

$$\Lambda_{\gamma_1}(\varphi) = \sum_{n\in\mathbb{Z}} |n| \, \widehat{\varphi}(n) e^{\mathrm{i}\, n\theta}.$$

Similarly, when $\gamma = \gamma_2$ the solution can be written as

$$u(r,\theta) = \begin{cases} A_1 \sum_{n\in\mathbb{Z}} \widehat{\varphi}(n) r^n e^{\mathrm{i}\, n\theta} & \text{when } r \le r_0, \\ \sum_{n\in\mathbb{Z}} \left[A_2 r^n + A_3 r^{-n}\right] \widehat{\varphi}(n) e^{\mathrm{i}\, n\theta} & \text{when } r_0 < r \le 1, \end{cases}$$

for some constants $A_1, A_2$, and $A_3$. By imposing the boundary conditions and continuity conditions on the internal boundary we establish explicit forms of the coefficients $A_1$, $A_2$, and $A_3$.

Imposing the boundary conditions implies

$$A_2 + A_3 = 1. \tag{5.0.4}$$

Defining $u_1 := u$ on $B(r_0)$ and $u_2 := u$ on $B(1) \setminus B(r_0)$, we constrain the solution to be continuous at $r = r_0$ namely,

$$u_1(r_0,\theta) = u_2(r_0,\theta) \text{ for all } \theta \in [0, 2\pi).$$

Additionally, we suppose that the normal derivative on $\partial B(r_0)$ is also continuous with

$$2\partial_r u_1(r,\theta) = \partial_r u_2(r_0,\theta) \text{ for all } \theta \in [0, 2\pi),$$

where in both cases $\partial_r$ is the derivative in the direction of increasing $r$. For these constraints to be true we require

$$\begin{cases} A_1 r_0^n = A_2 r_0^n + A_3 r_0^{-n} \\ 2A_1 n r_0^{n-1} = A_2 n r_0^{n-1} - A_3 n r_0^{-n-1} \end{cases} \tag{5.0.5}$$

holds for every $n \in \mathbb{Z} \setminus \{0\}$. Solving (5.0.4) and (5.0.5) for the unknowns $A_1$,$A_2$, and $A_3$, we find

$$A_1 = \frac{2}{3 - r_0^{2n}}, A_2 = \frac{3}{3 - r_0^{2n}}, \text{ and } A_3 = -\frac{r_0^{2n}}{3 - r_0^{2n}}.$$

We calculate the Neumann data as follows:

$$\begin{aligned}\Lambda_{\gamma_2}(\varphi)|_{r=1} &= \sum_{n\in\mathbb{Z}\setminus\{0\}} \left(|n|\, A_2 - |n|\, A_3\right) \widehat{\varphi}(n) e^{\mathrm{i}\, n\theta} \\ &= \sum_{n\in\mathbb{Z}} |n| \left(\frac{3 + r_0^{2|n|}}{3 - r_0^{2|n|}}\right) \widehat{\varphi}(n) e^{\mathrm{i}\, n\theta}.\end{aligned}$$

Now

$$\begin{aligned}\left\|\Lambda_{\gamma_2}(\varphi) - \Lambda_{\gamma_1}(\varphi)\right\|^2_{H^{-1/2}(\partial\Omega)} &= \sum_{n\in\mathbb{Z}} (1+n^2)^{-1/2} n^2 \left(\frac{2r_0^{2|n|}}{3 - r_0^{2|n|}}\right)^2 \left|\widehat{\varphi}(n)\right|^2 \\ &\leq \max_{n\geq 1} \left(\sqrt{\frac{n^2}{1+n^2}} \left(\frac{2r_0^{2|n|}}{3 - r_0^{2|n|}}\right)^2\right) \sum_{n\in\mathbb{Z}} |n| \left|\widehat{\varphi}(n)\right|^2 \\ &\leq r_0^4 \left\|\varphi\right\|^2_{H^{1/2}(\partial\Omega)}.\end{aligned}$$

As a result, it follows that

$$\left\|\Lambda_{\gamma_2} - \Lambda_{\gamma_1}\right\|_{\mathcal{L}\left(H^{1/2}(\partial\Omega);H^{-1/2}(\partial\Omega)\right)} \leq r_0^2.$$

Therefore, as $r_0 \to 0$, $\|\Lambda_{\gamma_1} - \Lambda_{\gamma_2}\| \to 0$ despite $\|\gamma_1 - \gamma_2\|_{L^\infty(\Omega)} = 1$ preventing an estimate of the form (5.0.3) existing for an arbitrary choice of parameters in $\mathcal{A}$.

However, by imposing additional regularity on the parameters $\gamma_1$ and $\gamma_2$, logarithmic-type stability estimates can be established. In two dimensions, $\gamma_1, \gamma_2 \in C^\alpha(\Omega)$ for $0 < \alpha < 1$ is sufficient [21] and when $n \geq 3$, $\gamma_1, \gamma_2 \in H^{2+s}(\Omega)$ for $s > n/2$ suffices [6]. More precisely, we combine these results into the following theorem.

THEOREM. *Let $\Omega \subset \mathbb{K}^n$ be a bounded Lipschitz domain. Suppose*

*(1) $\gamma_1, \gamma_2 \in H^{2+s}(\Omega)$ for $s > \frac{n}{2}$ when $n \geq 3$,*

*(2) $\gamma_1, \gamma_2 \in C^\alpha(\Omega)$ for $0 < \alpha < 1$ when $n = 2$.*

*Then there exists constants $C = C\left(\Omega, n, s, \|\gamma_1\|, \|\gamma_2\|\right)$ and $p \in (0,1)$ such that*

$$\left\|\gamma_1 - \gamma_2\right\|_{L^\infty(\Omega)} \leq V_p\left(\left\|\Lambda_{\gamma_2} - \Lambda_{\gamma_2}\right\|\right), \tag{5.0.6}$$

*where*

$$V_p : \rho \to C\left|\log(\rho)\right|^{-p}. \tag{5.0.7}$$

PROOF. For the $n = 2$ case, see [21] and when $n \geq 3$ see [6]. □

Furthermore, the estimate (5.0.6) is optimal up to the value of the exponent $p$ in (5.0.7) [127]. In other words, even if parameters are assumed to be $C^\infty$ a logarithmic-type stability estimate is the best that can be achieved. There have been attempts to consider what additional assumptions are required on the parameters to guarantee better stability. Most relevant to this work is the existence of a Lipschitz stability estimate for piecewise constant parameters $\gamma \in \mathcal{A}$ [7].

It is conjectured that the stability is 'better' near the boundary of the domain and the stability degrades further into the domain. For inclusions of the type $\gamma(x) = \gamma_0(x)+\gamma_1(x)\chi_D$ where $\chi_D$ is the characteristic function of an open, compactly contained subset of the interior of $\Omega$, this has been established quantitatively in [138]. However, a complete analytic description of depth stability is not currently known.

**The partial boundary data problem.** The previous discussions suppose that the boundary data is known on the whole boundary $\partial\Omega$. Practically, this is often not feasible as part of the boundary may be inaccessible or too large to cover with electrodes. Let $\Gamma \subset \partial\Omega$ be an open subset and denote $H^{1/2}_\Gamma(\partial\Omega) \subset H^{1/2}(\partial\Omega)$ to be the set of functions with support in $\Gamma$. The partial DtN map is given by

$$\begin{aligned} \Lambda_\gamma|_\Gamma : H^{1/2}_\Gamma(\partial\Omega) &\longrightarrow H^{-1/2}(\Gamma) \\ \varphi &\longmapsto \gamma\nabla u \cdot \hat{n}|_\Gamma \end{aligned}$$

where $u \in H^1(\Omega)$ solves

$$\begin{cases} \operatorname{div}(\gamma\nabla u) = 0 & \text{in } \Omega, \\ u = \varphi & \text{on } \partial\Omega. \end{cases}$$

Establishing identifiability and stability results for the partial data operator has been the topic of research over the last few decades [179]. Since less control of the boundary input is available, the results obtained often require stronger assumptions on the permittivity, or only hold in a weaker form. In particular, the parameter $\gamma \in \mathcal{A}$ is identifiable if $\Omega$ is assumed to be convex [109] or $\Gamma$ covers at least half of the boundary [35].

**Numerical reconstruction algorithms.** Of significant practical interest is the development of numerical algorithms to estimate the parameter $\gamma \in \mathcal{A}$ from finitely many evaluations of the DtN map $\Lambda_\gamma$ or the partial DtN map $\Lambda_\gamma|_\Gamma$. Since only finitely many evaluations are available, $\gamma \in \mathcal{A}$ certainly cannot be identifiable. Instead, the inverse problem is regularised and the space of admissible parameters is restricted to ensure at a unique parameter $\gamma$ can be found. We discuss this in more detail in Chapter 6. Despite these difficulties, convergent reconstruction algorithms to determine the parameter are known. The first of these was introduced in [137], although many other algorithms have since been proposed and implemented [202]. We postpone a further discussion of such algorithms until the next chapter.

Finally, we remark that this is not intended to be an exhaustive list and many more interesting questions can be posed and studied. We depart from this discussion and to formally define and establish properties of the DtN and NtD operators.

## 5.1. The $\Lambda_\gamma$ and $N_\gamma$ operators

We begin by proving that the DtN map is well defined as a mapping into $L^2(\partial\Omega)$. We then establish that $\Lambda_\gamma$ and $N_\gamma$ are bounded linear operators and prove that, under a restricted set of sensor inputs, $\Lambda_\gamma^{-1} = N_\gamma$.

**5.1.1. The Dirichlet-to-Neumann (DtN) Operator.** We define the Dirichlet-to-Neumann operator as follows: for any $\gamma \in \mathcal{A}$

$$\begin{aligned} \Lambda_\gamma : H^{1/2}(\partial\Omega) &\to H^{-1/2}(\partial\Omega) \\ \varphi &\mapsto f \end{aligned} \tag{5.1.1}$$

where $f = \gamma\nabla u \cdot \hat{n}|_{\partial\Omega}$. This operator is well-defined by choosing $F = \gamma\nabla u$ in the following lemma, also see [108].

LEMMA 5. *Let $\Omega$ be an open, bounded domain with Lipschitz boundary given by $\partial\Omega$. Suppose $F \in L^2(\Omega;\mathbb{K}^d)$ for $d \in \mathbb{N}$ and div$(F) \in L^2(\Omega)$ then $F \cdot \hat{n} \in H^{-1/2}(\partial\Omega)$ can be defined by the duality pairing*

$$\langle F \cdot \hat{n}, \psi \rangle_{H^{-1/2}(\partial\Omega), H^{1/2}(\partial\Omega)} = \int_\Omega div(F)\widetilde{\psi}\, dx + \int_\Omega F \cdot \nabla\widetilde{\psi}\, dx$$

*where* $\widetilde{\psi} \in H^1(\Omega)$ *is any extension of* $\psi \in H^{1/2}(\partial\Omega)$.

Proof of Lemma 5. We begin by considering the case of a smooth compactly supported test function $\psi \in C^\infty(\overline{\Omega}; \mathbb{C})$. Applying Green's theorem, we compute

$$\begin{aligned}\int_{\partial\Omega} \psi F \cdot \hat{n}\, \mathrm{d}s &= \int_\Omega \operatorname{div}(\psi F)\, \mathrm{d}x \\ &= \int_\Omega \operatorname{div}(F)\psi\, \mathrm{d}x + \int_\Omega F \cdot \nabla\psi\, \mathrm{d}x.\end{aligned}$$

Using this identity, it follows

$$\begin{aligned}\int_{\partial\Omega} \psi F \cdot \hat{n}\, \mathrm{d}s &\leq \|\operatorname{div}(F)\|_{L^2(\Omega)} \|\psi\|_{L^2(\Omega)} + \|F\|_{L^2(\Omega)} \|\nabla\psi\|_{L^2(\Omega)} \\ &\leq \|\psi\|_{H^1(\Omega)} \left( \|\operatorname{div}(F)\|_{L^2(\Omega)} + \|F\|_{L^2(\Omega)} \right).\end{aligned}$$

Given $\psi \in H^{1/2}(\Omega)$ , let $\widetilde{\psi} \in H^1(\Omega)$ be an extension of $\psi$ such that $\left\|\widetilde{\psi}\right\|_{H^1(\Omega)} \leq c\, \|\psi\|_{H^{1/2}(\Omega)}$. Then, since $C^\infty(\overline{\Omega}; \mathbb{C})$ is dense in $H^1(\Omega; \mathbb{C})$, we establish

$$\langle \psi, F \cdot \hat{n} \rangle_{H^{1/2}(\partial\Omega;\mathbb{C}), H^{-1/2}(\partial\Omega;\mathbb{C})} \leq C\, \|\psi\|_{H^{1/2}(\Omega)} \left( \|\operatorname{div}(F)\|_{L^2(\Omega)} + \|F\|_{L^2(\Omega)} \right), \quad (5.1.2)$$

for some constant $C > 0$. Since this holds for all $\psi \in H^{1/2}(\partial\Omega)$ the result follows by taking the supremum of 5.1.2 over all $\psi$ such that $\|\psi\|_{H^{1/2}(\partial\Omega)} = 1$. □

The above result guarantees that the DtN operator is well-defined when the boundary of the domain is Lipschitz. We now establish that when the boundary of the domain is $C^2$, the image of $H^{1/2}(\partial\Omega)$ under the DtN operator lies in the more regular space $L^2(\partial\Omega)$. A similar, improved regularity result can also be shown in the case when $\Omega$ is convex.

Theorem 11. *Suppose that* $\gamma \in \mathcal{A}$ *and* $\Omega \subset \mathbb{R}^d$ *is an open, bounded and connected domain for* $d \geq 2$. *Let* $u \in H^1(\Omega)$ *be the weak solution to*

$$\begin{cases} div(\gamma\nabla u) = 0 & \text{in } \Omega, \\ u = \varphi & \text{on } \partial\Omega, \end{cases} \quad (5.1.3)$$

*for a given boundary condition $\varphi \in H^{3/2}(\partial\Omega)$. If $\partial\Omega \in C^2$, then*

$$\gamma\nabla u \cdot \hat{n} \in L^2(\partial\Omega)$$

*and*

$$\|\gamma\nabla u \cdot \hat{n}\|_{L^2(\partial\Omega)} \leq C \|u\|_{H^1(\Omega)},$$

*with the constant $C > 0$ depending on $\gamma \in \mathcal{A}$.*

PROOF. Recall that $\gamma \in \mathcal{A}$ is constant in $\Omega \setminus \Omega'$ (see (2.2.2)), and $d(\partial\Omega, \Omega') > \delta_2 > 0$. Let $\Omega''$ be a smooth open set such that $\Omega' \subset \Omega'' \subset \Omega$. . On $\Omega \setminus \Omega'$, $u$ is a solution of the constant coefficient elliptic boundary-value problem

$$\operatorname{div}(\gamma\nabla u) = 0 \text{ in } \Omega \setminus \Omega'.$$

In particular, $u \in H^2(\Omega \setminus \Omega'')$ and

$$\|u\|_{H^2(\Omega\setminus\Omega'')} \leq C \|\varphi\|_{H^{3/2}(\partial\Omega)} + \|u\|_{H^{3/2}(\partial\Omega')} \leq C \left( \|\varphi\|_{H^{3/2}(\partial\Omega)} + \|u\|_{H^1(\Omega)} \right),$$

see, for example [69, Chapter 6, Theorem 2]. Since $\partial\Omega \in C^2$ we can construct a $C^1$ extension of the normal vector as follows: let $N \in C^1\left(\overline{\Omega}; \mathbb{R}^d\right)$ be a function such that $N|_{\partial\Omega} = \hat{n}$ where $\hat{n}$ is the (outward) pointing normal to $\partial\Omega$ and $N = 0$ on $\Omega'$. Then $\psi = N \cdot \nabla u \in H^1(\Omega)$, with a trace $N \cdot \nabla u \in H^{1/2}(\partial\Omega)$ and so by construction, $\psi|_{\partial\Omega} = \nabla u \cdot \hat{n}$. Testing equation (5.1.3) against $\psi$ , we establish

$$\int_{\partial\Omega} \gamma\nabla u \cdot \hat{n}\, \psi \, \mathrm{d}s = \int_\Omega \gamma\nabla u \cdot \nabla\psi \, \mathrm{d}x, \tag{5.1.4}$$

which becomes

$$\int_{\partial\Omega} \gamma \left(\nabla u \cdot \hat{n}\right)^2 \mathrm{d}s = \int_\Omega \gamma\nabla u \cdot \nabla \left(N \cdot \nabla u\right) \mathrm{d}x. \tag{5.1.5}$$

Note that since $\gamma \in \mathcal{A}$ is constant in $\Omega \setminus \Omega'$, we write the right hand side as

$$\int_\Omega \gamma\nabla u \cdot \nabla(N \cdot \nabla u) \, \mathrm{d}x = \gamma \int_\Omega \nabla u \cdot \nabla(N \cdot \nabla u) \, \mathrm{d}x. \tag{5.1.6}$$

Using the repeated indices notation, we compute that

$$\int_\Omega \gamma \nabla u \cdot \nabla (N \cdot \nabla u)\, \mathrm{d}x = \int_\Omega \gamma \partial_i u\, \partial_i N_k\, \partial_k u\, \mathrm{d}x + \int_\Omega \gamma \partial_i u\, N_k\, \partial_{ik} u\, \mathrm{d}x.$$

We consider each of these terms separately; the first can be immediately bounded by

$$\left| \int_\Omega \gamma \partial_i u\, \partial_i N_k\, \partial_k u\, \mathrm{d}x \right| \leq \|\gamma\|_{L^\infty(\Omega)} \|N\|_{C^1(\Omega)} \|\nabla u\|^2_{L^2(\Omega)}. \tag{5.1.7}$$

For the second term, we use the identity

$$\mathrm{div}\left(|\nabla u|^2 N\right) = |\nabla u|^2 \mathrm{div}(N) + N \cdot \nabla \left(|\nabla u|^2\right),$$

to give

$$\int_\Omega N.\nabla \left(|\nabla u|^2\right)\, \mathrm{d}x = \int_\Omega \mathrm{div}\left(|\nabla u|^2 N\right)\, \mathrm{d}x - \int_\Omega |\nabla u|^2 \mathrm{div}(N)\, \mathrm{d}x.$$

Applying Green's theorem, we calculate

$$\begin{aligned} \int_\Omega \partial_i u\, N_k\, \partial_{ik} u\, \mathrm{d}x &= \frac{1}{2} \int_{\partial\Omega} |\nabla u|^2 N \cdot \hat{n}\, \mathrm{d}s - \frac{1}{2} \int_\Omega |\nabla u|^2 \mathrm{div}(N)\, \mathrm{d}x \\ &= \int_{\partial\Omega} |\nabla u \cdot \hat{n}|^2\, \mathrm{d}s - \frac{1}{2} \int_{\partial\Omega} \left| \left(\mathrm{Id} - NN^T\right) \nabla u \right|^2 \mathrm{d}s \\ &\quad - \frac{1}{2} \int_\Omega |\nabla u|^2 \mathrm{div}(N)\, \mathrm{d}x. \end{aligned} \tag{5.1.8}$$

Bounding each term, we obtain

$$\begin{aligned} \frac{1}{2} \left| \int_\Omega (N.\nabla) |\nabla u|^2\, \mathrm{d}x \right| &\leq \|\partial_n u\|^2_{L^2(\partial\Omega)} - \frac{1}{2} \left\| \left(\mathrm{Id} - NN^T\right) \nabla u \right\|^2_{L^2(\partial\Omega)} \\ &\quad + \left( \|\mathrm{div}(N)\|_{L^\infty(\Omega)} \right) \|\nabla u\|^2_{L^2(\Omega)}. \end{aligned} \tag{5.1.9}$$

Combining (5.1.5), (5.1.7), and (5.1.9)

$$\begin{aligned} \int_{\partial\Omega} \gamma\, |\nabla u \cdot \hat{n}|^2\, \mathrm{d}s \leq C \|\gamma\|_{L^\infty(\Omega)} \Big( &\|N\|_{C^1(\Omega)} \\ &+ \|\mathrm{div}(N)\|_{L^2(\partial\Omega)} \Big) \|\nabla u\|^2_{L^2(\Omega)}, \end{aligned}$$

for some constant $C > 0$. Therefore, $\gamma \nabla u \cdot \hat{n} \in L^2(\partial\Omega)$ as required. □

**5.1.2. The Neumann-to-Dirichlet (NtD) Operator.** We defined the Neumann-to-Dirichlet operator as follows: for any $\gamma \in \mathcal{A}$

$$\begin{aligned} N_\gamma : H_\diamond^{-1/2}(\partial\Omega) &\to H_\diamond^{1/2}(\partial\Omega) \\ f &\mapsto u|_{\partial\Omega}, \end{aligned} \tag{5.1.10}$$

with $u \in H_\diamond^1(\Omega)$ solving

$$\begin{cases} \operatorname{div}(\gamma\nabla u) = 0 & \text{in } \Omega, \\ \gamma\nabla u \cdot \hat{n} = f & \text{on } \partial\Omega. \end{cases} \tag{5.1.11}$$

Defined in this way, the operator $N_\gamma$ can be written as

$$N_\gamma = T \circ S_N(f)$$

where $S_N : H_\diamond^{-1/2}(\partial\Omega) \longrightarrow H^1(\Omega)$ is the solution operator of (5.1.11) and $T$ is the trace operator. Restricted to the space $H_\diamond^{-1/2}(\partial\Omega)$, the operator $S_N$ is well defined by Theorem 5: there exists a unique $u \in H^1(\Omega)$ for each $f \in H_\diamond^{-1/2}(\partial\Omega)$ solving (5.1.11). Then by the trace theorem [69, 70], $T(u) = u|_{\partial\Omega}$ exists and is unique. As a consequence, $N_\gamma$ is well-defined.

**5.1.3. Properties of the DtN and NtD Operators.** We state and prove useful properties of the DtN and NtD operators.

LEMMA 6. *For any $\gamma \in \mathcal{A}$, let $\Lambda_\gamma$ be the operator defined by (5.1.1) and $N_\gamma$ be the operator defined by (6). Then the following properties hold:*

*(1) For any $\varphi_1$, $\varphi_2 \in H^{1/2}(\partial\Omega)$*

$$\Lambda_\gamma(\varphi_1 + \varphi_2) = \Lambda_\gamma(\varphi_1) + \Lambda_\gamma(\varphi_2).$$

*Similarly, for any $f_1, f_2 \in H^{-1/2}(\partial\Omega)$*

$$N_\gamma(f_1 + f_2) = N_\gamma(f_1) + N_\gamma(f_2).$$

*(2) For any $\varphi \in H^{1/2}(\partial\Omega)$, we have that*

$$\int_{\partial\Omega} \Lambda_\gamma(\varphi)\, ds = 0.$$

*Equivalently, Range*$(\Lambda_\gamma) \subseteq H_\diamond^{-1/2}(\partial\Omega)$.

*(3) If* $\varphi \equiv C$ *for some* $C \in \mathbb{K}$, *then*

$$\Lambda_\gamma(\varphi) = 0.$$

*And conversely, if* $\Lambda_\gamma(\varphi) = 0$ *then* $\varphi = C$ *for some* $C \in \mathbb{K}$.

*(4) For any* $\varphi \in H^{1/2}(\partial\Omega)$,

$$N_\gamma(\Lambda_\gamma(\varphi)) = \varphi + C$$

*for some constant* $C \in \mathbb{K}$. *Similarly, for all* $f \in H_\diamond^{-1/2}(\partial\Omega)$

$$\Lambda_\gamma(N_\gamma(f)) = f.$$

PROOF. We prove each of the parts independently.

(1) For any $\varphi \in H^{1/2}(\partial\Omega)$, write the solution to (5.1.3) as $u(\varphi)$. Then given $\varphi_1, \varphi_2 \in H^{1/2}(\partial\Omega)$, $w \in H^1(\Omega)$ defined by

$$w := u(\varphi_1) + u(\varphi_2)$$

satisfies

$$\operatorname{div}(\gamma\nabla w) = 0$$

by the linearity of the divergence operator. On the boundary,

$$w|_{\partial\Omega} = \varphi_1 + \varphi_2.$$

By uniqueness of (5.1.3) established in Theorem5, $w$ must be equal to $w = u(\varphi_1 + \varphi_2)$. Finally, by linearity of the gradient operator, the boundary flux is also linear and the conclusion follows. Arguing similarly the linearity of $N_\gamma$ is established.

(2) For any $\varphi \in H^{1/2}(\partial\Omega)$, the weak solution of (5.1.3), denoted $u \in H^1(\Omega)$ satisfies

$$\int_\Omega \gamma\nabla u \cdot \nabla v \,\mathrm{d}x = \int_{\partial\Omega} \gamma\nabla u \cdot \hat{n} v \,\mathrm{d}s \tag{5.1.12}$$

for all $v \in H^1(\Omega)$ with $u = \varphi$ on $\partial\Omega$. By substitution, it follows

$$\int_\Omega \gamma \nabla u \cdot \nabla v \, \mathrm{d}x = \int_{\partial\Omega} \Lambda_\gamma(\varphi) v \, \mathrm{d}s \tag{5.1.13}$$

for all $v \in H^1(\Omega; \mathbb{C})$. Choosing $v \equiv 1$, we obtain

$$\int_{\partial\Omega} \Lambda_\gamma(\varphi) \, \mathrm{d}s \ = 0$$

for all $\varphi \in H^{1/2}(\partial\Omega)$ as required.

(3) Suppose that $\varphi \equiv C$ for some $C \in \mathbb{K}$. Then $u \equiv C$ is the unique solution to (5.1.3) for this choice of boundary condition and

$$\int_\Omega \gamma \nabla u \cdot \nabla v \, \mathrm{d}x = 0$$

for all $v \in H^1(\Omega)$. Using (5.1.13), this becomes

$$\int_{\partial\Omega} \Lambda_\gamma(C) v \, \mathrm{d}s = 0$$

for all $v \in H^1(\Omega)$, which implies $\Lambda_\gamma(C) = 0$. Conversely, if $\Lambda_\gamma(\varphi) = 0$, then for any $v \in H^1(\Omega)$

$$\int_{\partial\Omega} \Lambda_\gamma(\varphi) v \, \mathrm{d}s = 0.$$

Choosing $v = u$ (or $v = \overline{u}$ when $\mathbb{K} = \mathbb{C}$), it follows

$$\int_\Omega \gamma |\nabla u|^2 \, \mathrm{d}x = 0.$$

Since $\gamma > 0$ in $\Omega$, we have that $\nabla u \equiv 0$, i.e. $u \equiv C$ for some $C \in \mathbb{K}$.

(4) Take any $\varphi \in H^{1/2}(\partial\Omega)$ then by definition $\Lambda_\gamma(\varphi) = \gamma \nabla u \cdot \hat{n}|_{\partial\Omega}$ where $u$ satisfies (5.1.12) for all $v \in H^1(\Omega; \mathbb{C})$. Let $f = \Lambda_\gamma(\varphi)$. By part (2) we have that $\int_{\partial\Omega} f \, \mathrm{d}s = 0$ and so the operator $N_\gamma$ can be applied to $f$ and $N_\gamma(f) = T(w)$, where $T$ is the trace operator and $w$ satisfies

$$\int_\Omega \gamma \nabla w \cdot \nabla v \, \mathrm{d}x = \int_{\partial\Omega} f \, v \, \mathrm{d}x \tag{5.1.14}$$

for all $v \in H^1(\Omega)$ subject to the constraint that $\int_\Omega w \, \mathrm{d}x = 0$. Equating (5.1.12) and (5.1.14), we establish the identity

$$\int_\Omega \gamma \nabla u \cdot \nabla v \, \mathrm{d}x = \int_\Omega \gamma \nabla w \cdot \nabla v \, \mathrm{d}x$$

for all $v \in H^1(\Omega)$. And so $w = u + C$ for some $C \in \mathbb{C}$. We remark that an explicit form of the constant $C$, namely $C = -\int_{\partial\Omega} \varphi \, \mathrm{d}x$, can be obtained. Running the argument in reverse we establish that

$$\Lambda_\gamma(N_\gamma(f)) = f$$

for all $f \in H_\diamond^{-1/2}(\partial\Omega; \mathbb{C})$.

□

We remark that property 4, implies $\Lambda_\gamma$ restricted to $H_\diamond^{1/2}(\partial\Omega)$ is the inverse of $N_\gamma$ and vice versa. As mentioned previously this implies the information encoded by $\Lambda_\gamma$ and $N_\gamma$ is identical since one determines the other. However, $\Lambda_\gamma$ is mapping into a less regular space, whereas $N_\gamma$ is a smoothing operator. For this reason, it would be preferable to develop reconstruction algorithms for the $N_\gamma$ operator. However, as mentioned in previous chapters, this choice of boundary condition is non-physical: the boundary flux is not known to be spatially uniform on the electrodes. Once again we make use of the shunt model to reflect the nature of the electrodes. We discuss this in more detail in the next section where the operators $\Lambda_\gamma$ and $N_\gamma$ are discretised.

## 5.2. The finite dimensional DtN and NtD operators

In this section we describe the finite dimensional form of the operators $\Lambda_\gamma$ and $N_\gamma$. In all practical applications, the action of either $\Lambda_\gamma$ or $N_\gamma$ is known only for a finite number of linearly independent functions. This reflects the constraint that only finitely many sensor measurements are available. Let $M \in \mathbb{N}$ and suppose that the space of all sensor inputs is a finite dimensional set $\{\varphi_1, \ldots, \varphi_M\} \subset H_\diamond^{1/2}(\partial\Omega)$, where $\varphi_i \neq 0$ for each $i$. If we further suppose that $\{\varphi_i\}_{i=1}^M$ are linearly independent, then $\{\varphi_i\}_{i=1}^M$ is a basis of $V := \operatorname{span}\{\varphi_1, \ldots, \varphi_M\}$. Under the action of the DtN map, the

image of the space is given by

$$\Lambda_\gamma(V) = \operatorname{span}\{\Lambda_\gamma(\varphi_1), \ldots, \Lambda_\gamma(\varphi_M)\}$$

by the linearity of $\Lambda_\gamma$ (Lemma 6). A basis of $\Lambda_\gamma(V)$ is given by $\{f_i\}_{i=1}^M$ where $f_i = \Lambda_\gamma(\varphi_i)$. After fixing this basis, $\Lambda_\gamma$ can be uniquely represented by a matrix $[\Lambda]_{ij} \in \mathbb{K}^{M\times M}$ where

$$\Lambda_\gamma(\varphi_j) = \sum_{i=1}^{M} [\Lambda]_{ij} f_i.$$

The matrix depends on $\gamma \in \mathcal{A}$ and the inverse problem becomes: given $[\Lambda] \in \mathbb{K}^{M\times M}$, find $\gamma \in \mathcal{A}$. However, as expected this problem is not well-posed and the space $\mathcal{A}$ must be restricted in order to ensure that a unique parameter exists. Rather than pursue this abstract setting, we modify the approach to better reflect the physical properties of the electrodes. In particular, we do the following:

- choose the functions $\varphi_i$ such that $\varphi_i|_{\partial E_j}$ is constant for each $i$ and $j$;
- and introduce a measurement operator to record spatial averages of $\Lambda_\gamma(\varphi)$ on each electrode.

We begin by addressing the second of these and define the measurement operator

$$\begin{aligned} P : L^2_\diamond(\partial\Omega;\mathbb{K}) &\longrightarrow \mathbb{K}^N_\diamond \\ f &\longmapsto |\partial E_k|^{-1} \int_{\partial E_k} f \,\mathrm{d}s. \end{aligned}$$

If we assume that the boundary of each electrode $\partial E_k$ is $C^2$, therefore applying Theorem 11 we establish $\Lambda_\gamma(\varphi) \in L^2(\partial\Omega)$. Moreover, using Lemma 6 we must have that $\int_{\partial\Omega} \Lambda_\gamma(\varphi)\,\mathrm{d}s = 0$ for all $\varphi \in H^{1/2}(\partial\Omega)$ and $\Lambda_\gamma(\varphi) \in L^2_\diamond(\partial\Omega)$. Given any $\varphi \in H^{1/2}(\partial\Omega)$, the vector $m := P \circ \Lambda_\gamma(\varphi)$ describes the average boundary flux on each electrode.

In the models derived previously, it was assumed that the electric potential is spatially constant on each electrode. Therefore, the space of all boundary voltage

patterns on a sensor with $N$ electrodes is an injection into $H^{1/2}_{\diamond}(\partial\Omega)$ given by

$$\begin{aligned} L : \mathbb{K}^N_{\diamond} &\longrightarrow H^{1/2}_{\diamond}(\partial\Omega) \\ U &\longmapsto \sum_{k=1}^{N} U_k \, \chi_k \end{aligned} \tag{5.2.1}$$

where $\chi_k \in H^{1/2}(\partial\Omega; \mathbb{K})$ is such that

$$\chi_k(x) := \begin{cases} |\partial E_k|^{-1} & \text{if } x \in \partial E_k, \\ 0 & \text{if } x \notin \partial E_k. \end{cases}$$

Let $e_1, \ldots, e_N$ be the standard basis of $\mathbb{K}^N$ and let $V := \operatorname{span}\{L(e_1), \ldots, L(e_N)\} \subset H^{1/2}(\partial\Omega)$. The dimension of the space $\Lambda_\gamma(V)$ is given by the rank-nullity theorem

$$\dim\left(\Lambda_\gamma(V)\right) = \dim(V) - \dim\left(\operatorname{Ker}\left(\Lambda_\gamma\right)\right) = N - 1$$

since $\operatorname{Ker}(\Lambda_\gamma) = \operatorname{span}\{\mathbf{1} \in \mathbb{K}^N\} \subset V$ from Lemma 6 part 3.

LEMMA 7. *The space $V \subset H^{1/2}(\partial\Omega)$ defined by*

$$V := \mathit{span}\{L(e_1), \ldots, L(e_N)\}$$

*where $e_1, \ldots, e_N$ are the standard basis of of $\mathbb{K}^N$ can be decomposed as*

$$V = \mathit{Ker}(\Lambda_\gamma) \oplus V^{\perp}$$

*where*

$$V^{\perp} := \mathit{span}\left\{L(d_2^1), \ldots, L(d_N^1)\right\}$$

*and $d_j^1 := e_1 - e_j$.*

PROOF. Fix $j = 2, \ldots, N$. Observe $L(d_j^1) \notin \operatorname{Ker}(\Lambda_\gamma)$ by Lemma 6 part 3, otherwise $L(d_j^1)$ would be constant. ThereforeKer$(\Lambda_\gamma) \cap V^{\perp} = \emptyset$. It is then sufficient to show that for each $i = 1, \ldots, N$, $L(e_i)$ can be written as $L(e_i) = a + b_i$ for some $v_1 \in \operatorname{Ker}(\Lambda_\gamma)$

and $v_2 \in V^\perp$. When $k = 1, \dots, N$, we write

$$e_k = \frac{1}{N}\mathbf{1} + \frac{1}{N}\sum_{j\neq k}\left(d_j^1 - d_k^1\right)$$

where we have used the convention that $d_1^1 = 0$. Noting that $\frac{1}{N}\mathbf{1} \in \mathrm{Ker}(\Lambda_\gamma)$ and $\frac{1}{N}\sum_{j\neq k}\left(d_j^1 - d_k^1\right) \in V^\perp$, the result follows. □

Furthermore, we have $V^\perp \subset H_\diamond^{1/2}(\partial\Omega)$. Indeed, for any $j = 2, \dots, N$ we calculate

$$\begin{aligned}\sum_{k=1}^{N}\int_{\partial E_k} L(d_j^1)\,\mathrm{d}s &= \int_{\partial E_1}\chi_1\,\mathrm{d}s - \int_{\partial E_j}\chi_j\,\mathrm{d}s\\ &= |\partial E_1|\,|\partial E_1|^{-1} - |\partial E_j|\,|\partial E_j|^{-1}\\ &= 0.\end{aligned}$$

After redefining the operator

$$\begin{aligned}L : \mathbb{K}_\diamond^N &\longrightarrow H_\diamond^{1/2}(\partial\Omega)\\ U &\longmapsto \sum_{k=1}^{N} U_k\,\chi_k,\end{aligned} \tag{5.2.2}$$

the finite dimensional form of the DtN operator is the mapping defined by

$$\begin{aligned}\widetilde{\Lambda}_\gamma : \mathbb{K}_\diamond^N &\longrightarrow \mathbb{K}_\diamond^N\\ U &\longmapsto P\circ\Lambda_\gamma\circ L(U).\end{aligned}$$

Similarly, the finite dimensional NtD operator is defined by

$$\begin{aligned}\widetilde{N}_\gamma : \mathbb{K}_\diamond^N &\longrightarrow \mathbb{K}_\diamond^N\\ Q &\longmapsto P\circ N_\gamma\circ L(Q).\end{aligned}$$

This is well defined due to the inclusion $H_\diamond^{1/2}(\partial\Omega;\mathbb{K}) \subset H_\diamond^{-1/2}(\partial\Omega)$.

Unlike in the continuum case

$$\widetilde{\Lambda}_\gamma \circ \widetilde{N}_\gamma \neq \mathrm{Id}_{\mathbb{K}_\diamond^N\to\mathbb{K}_\diamond^N}$$

and

$$\widetilde{N}_\gamma \circ \widetilde{\Lambda}_\gamma \neq \mathrm{Id}_{\mathbb{K}_\diamond^N\to\mathbb{K}_\diamond^N}.$$

In other words, part 4 of Lemma 6 does not hold in the finite dimensional setting.

It is the shunt model introduced in Chapter 2 that provides the true inverse to $\widetilde{\Lambda}_\gamma$ in finite dimensions. We define the operator

$$\widetilde{S}_\gamma : \mathbb{K}^N_\diamond \longrightarrow \mathbb{K}^N_\diamond$$

$$Q \longmapsto U$$

where $(u, U) \in H^1(\Omega)$ is the unique solution to

$$\begin{cases} -\operatorname{div}(\gamma \nabla u) = 0 & \text{in } \Omega, \\ u = U_k & \text{on } \partial E_k, \\ |\partial E_k|^{-1} \displaystyle\int_{\partial E_k} \gamma \nabla u \cdot \hat{n} \, \mathrm{d}s = Q_k & \text{on } \partial E_k. \end{cases} \tag{5.2.3}$$

Then by uniqueness of the solution to (5.2.3) given in Theorem 6, we have

$$\widetilde{\Lambda}_\gamma \circ \widetilde{S}_\gamma = \mathrm{Id}_{\mathbb{K}^N_\diamond \to \mathbb{K}^N_\diamond}$$

and, as a consequence,

$$\widetilde{S}_\gamma \circ \widetilde{\Lambda}_\gamma = \mathrm{Id}_{\mathbb{K}^N_\diamond \to \mathbb{K}^N_\diamond}.$$

These relationships have been numerically verified as a method of validating the numerical code in Section 4.2.3. The results can be seen in Figure 4.2.5.

## 5.3. Estimation of $\widetilde{\Lambda}_\gamma$ and $\widetilde{S}_\gamma$ from data

We fix the basis of $\mathbb{K}^N_\diamond$ to be $\left\{d^1_j\right\}_{j=2}^N$ and denote the unique matrix representation of the operators $\widetilde{\Lambda}_\gamma$ and $\widetilde{S}_\gamma$ in this basis by $[\widetilde{\Lambda}_\gamma]$ and $[\widetilde{S}_\gamma]$ respectively. This is possible since each operator is a linear automorphism of $\mathbb{K}^N_\diamond$. The aim of this section is to describe a procedure to estimate $[\widetilde{\Lambda}_\gamma]$ and $[\widetilde{S}_\gamma]$ using the measurements from each of the models described previously. This is not immediate as the measurements from each of the models discussed previously are in the basis $\{e_j\}_{j=1}^N$, that is, in $\mathbb{K}^N$ not in $\mathbb{K}^N_\diamond$ . Let $M$ denote the matrix of measurements and we specialise to four cases or measurement paradigms:

**Paradigm 1** For $i, j = 1, \ldots, N$ with $i \neq j$

$$M_{ij} = P\Lambda_\gamma L(e_j) \cdot e_i;$$

**Paradigm 2** For $j = 2, \ldots, N$ and $k = 1, \ldots, N$

$$M_{ij} = \widetilde{S}_\gamma \left(d_j^1\right) \cdot e_i;$$

**Paradigm 3** For $i, j = 1, \ldots, N$ with $i \neq j$

$$M_{ij} = \widetilde{S}_\gamma(d_j^i) \cdot d_j^i;$$

**Paradigm 4** For $1 \leq i < j \leq N$ with $|i - j| \leq L$ for some $L \in \mathbb{N}$, $L < N$,

$$M_{ij} = \widetilde{S}_\gamma(d_j^i) \cdot d_j^i$$

in a planar geometry. In a circular geometry, we suppose that $M_{ij}$ is known for $1 \leq i < j \leq N$ where $\min\left(|i - j + N|, |i - j - N|, |i - j|\right) \leq L$ for some $L \in \mathbb{N}$, $L < N$.

By counting the number of admissible indices in each case, we compute that measurement paradigms 1-3 have $N(N-1)$ measurements whereas paradigm 4 has only $(N-1)(N-L-1)/2$ measurements. However, for paradigms 1-3 we will demonstrate that the measurements are not independent and that there are inherent redundancies in the measurements. Despite these redundancies, we establish that there are sufficient independent measurements to estimate $\left[\widetilde{S}_\gamma\right]$. Whereas in paradigm 4, the fewer number of measurements prevents $\left[\widetilde{S}_\gamma\right]$ from being determined. In more abstract terms, we prove that measurement paradigms 1, 2, and 3 are equivalent by constructing a bijection between the measurements in each case.

We show that paradigm 3 is equivalent to the 'two electrode problem'. The principle of taking sequential electric field measurements between only two electrodes eliminates the cumbersome hardware needed for concurrent measurements on many electrodes. Therefore, potentially allowing for faster measurement procedures to be

employed without compromising on the amount of data or the number of independent measurements. This is the practical motivation for considering Paradigm 4.

The last case considered addresses the commonly encountered situation when only measurements between near electrodes are recorded. This limitation is due to practical considerations: electrodes that are far apart lead to measurements that have poor signal to noise ratios, typically below the sensitivity threshold of the measurement apparatus.

Finally, we remark that while the measurements in each case can be considered in isolation, by mapping to the 'standard form' the same reconstruction algorithms can be developed independently of the measurement paradigm and then applied to each case. We remark that this approach is often used by practitioners. We consider such reconstruction algorithms in Chapter 6.

**5.3.1. Measurement paradigm 1.** Considering first the DtN map, we suppose that the matrix of measurements $M \in \mathbb{K}^{N\times N}$ is given component-wise by

$$M_{ij} = P\Lambda_\gamma L(e_j)\cdot e_i, \tag{5.3.1}$$

for $i,j = 1,\dots,N$. This measurement matrix corresponds to the Model 1 as defined by (2.5.2) when $\mathcal{I} = \{1,\dots,N\}$. While it may appear that there are $N^2$ measurements, in fact some of these measurements are redundant.

LEMMA 8. *Given the measurement matrix as defined by (5.3.1). Then*

for each $i,j = 1,\dots,N$ with $i \neq j$

$$|\partial E_i| M_{ij} = |\partial E_j| M_{ji},$$

and for each $j = 1,\dots,N$

$$M_{jj} = -\sum_{k\neq j} |\partial E_k|\, M_{kj}. \tag{5.3.2}$$

PROOF. Writing out the measurements explicitly, we have

$$M_{ij} = |\partial E_i|^{-1} \int_{\partial E_i} \gamma \nabla u_j \cdot \hat{n}\, \mathrm{d}s$$

where $u_j \in H^1(\Omega)$ solves

$$\begin{cases} -\operatorname{div}(\gamma \nabla u_j) = 0 & \text{in } \Omega, \\ u_j = L(e_j) & \text{on } \bigcup_{k=1}^{N} \partial E_k, \\ \gamma \nabla u_j \cdot \hat{n} = 0 & \text{on } \partial\Omega_B. \end{cases}$$

Since $u_i|_{\partial\Omega}$ is the indicator function of $\partial E_i$ in $\partial\Omega$, by testing against $u_i$, $M_{ij}$ can be expressed as

$$|\partial E_i| M_{ij} = \int_{\partial\Omega} \gamma \nabla u_j \cdot \hat{n} u_i \, \mathrm{d}s.$$

Using Green's theorem twice, this becomes

$$\begin{aligned} \int_{\partial\Omega} \gamma \nabla u_j \cdot \hat{n} u_i \, \mathrm{d}s &= \int_{\Omega} \gamma \nabla u_j \cdot \nabla u_i \, \mathrm{d}s \\ &= \int_{\partial\Omega} \gamma \nabla u_i \cdot \hat{n} u_j \, \mathrm{d}s \\ &= |\partial E_j| M_{ji} \end{aligned}$$

as required.

For the second relationship, testing the equation against $1 \in H^1(\Omega)$

$$\int_{\Omega} \gamma \nabla u_j \cdot \nabla 1 \, \mathrm{d}x = \int_{\partial\Omega} \gamma \nabla u_j \cdot \hat{n} 1 \, \mathrm{d}s.$$

Therefore,

$$\sum_{k=1}^{N} \int_{\partial E_k} \gamma \nabla u_j \cdot \hat{n} \, \mathrm{d}s = 0$$

and the result follows. □

We have shown that the matrix $M_{ij}$ in this case is symmetric. As a result there are only $N(N-1)/2$ possible independent measurements, and not $N^2$ as appears at first glance. We now describe relationships that enable the matrix representation of $\widetilde{\Lambda}_\gamma$, defined component-wise by

$$\left[\widetilde{\Lambda}_\gamma\right]_{ij} := \widetilde{\Lambda}_\gamma(d^1_{j+1}) \cdot d^1_{i+1},$$

in terms of the matrix $M$.

LEMMA 9. *For each $i, j = 1, \ldots, N-1$ the following relationships hold:*

*If $i \neq j$ then,*

$$\widetilde{\Lambda}_\gamma(d^1_{j+1}) \cdot d^1_{i+1} = \sum_{k=2}^{N} M_{1k} - M_{1,i+1} - M_{j+1,1} - M_{i+1,j+1},$$

*and if $i = j$,*

$$\widetilde{\Lambda}_\gamma(d^1_{i+1}) \cdot d^1_{i+1} = \sum_{k=2}^{N} (M_{k1} + M_{k,i+1}) - (M_{1,i+1} + M_{i+1,1}).$$

PROOF. We begin with establishing the identity

$$P\Lambda_\gamma L(e_i) - P\Lambda_\gamma L(e_j) = \widetilde{\Lambda}_\gamma\left(d^1_j\right) - \widetilde{\Lambda}_\gamma\left(d^1_i\right)$$

for each $i, j = 1, \ldots, N$ using the convention that $d^1_1 = 0$. Using linearity, we calculate

$$\begin{aligned} P\Lambda_\gamma L(e_i) - P\Lambda_\gamma L(e_j) &= P\Lambda_\gamma L(e_i - e_j) \\ &= P\Lambda_\gamma L(e_i - e_1 - e_j + e_1) \\ &= P\Lambda_\gamma L(d^1_j - d^1_i) \\ &= \widetilde{\Lambda}_\gamma\left(d^1_j\right) - \widetilde{\Lambda}_\gamma\left(d^1_i\right) \end{aligned}$$

since $P\Lambda_\gamma L|_{\mathbb{K}^N_\diamond} = \widetilde{\Lambda}_\gamma$. Furthermore, for each $i, j = 1, \ldots, N-1$ there holds

$$\begin{aligned} \widetilde{\Lambda}_\gamma(d^1_{j+1}) \cdot d^1_{i+1} &= (P\Lambda_\gamma L(e_1) - P\Lambda_\gamma L(e_{j+1})) \cdot (e_1 - e_{i+1}) \\ &= (P\Lambda_\gamma L(e_1) - P\Lambda_\gamma L(e_{j+1})) \cdot e_1 + (P\Lambda_\gamma L(e_1) - P\Lambda_\gamma L(e_{j+1})) \cdot e_{i+1} \\ &= M_{11} - M_{1,j+1} + M_{i+1,1} - M_{i+1,j+1}. \end{aligned}$$

Finally, using 5.3.2 to estimate $M_{11}$ the result follows when $i \neq j$. Similarly, when $i = j$, (5.3.2) can be used to $M_{i+1,i+1}$ to establish the required result. □

To summarise, Lemma 9provides $(N-1)^2$ that can be used to estimate $\left[\widetilde{\Lambda}_\gamma\right]$ from the measurement matrix $M$. We recall that $\left[\widetilde{S}_\gamma\right]$ can be found by computing $\left[\widetilde{\Lambda}_\gamma\right]^{-1}$.

**5.3.2. Measurement paradigm 2.** We now consider measurements as given by

$$M_{ij} = \widetilde{S}_\gamma\left(d^1_{j+1}\right) \cdot e_i, \tag{5.3.3}$$

for $i = 1, \ldots, N$ and $j = 1, \ldots, N-1$. In this form, all $N(N-1)$ possible measurements are expressed. However, not all these measurements are linearly independent which leads to redundancies in the measurement matrix. Nevertheless, we are still able to extract the $(N-1)^2$ entries of the matrix $\left[\widetilde{S}_\gamma\right]$ in the basis $\left\{d_j^1\right\}_{j=2}^N$. Establishing this result is the purpose of this section and we begin by making explicit the relationships between the measurements.

LEMMA 10. *Given the matrix of measurements defined by (5.3.3), then for each* $j = 1, \ldots, N-1$

$$\sum_{k=1}^{N} M_{kj} = 0.$$

*For each* $i, j = 1, \ldots, N-1$

$$M_{1j} - M_{i+1,j} = M_{1i} - M_{j+1,i} \tag{5.3.4}$$

PROOF. By the definition, we have that for any $Q \in \mathbb{K}_\diamond^N$,

$$\sum_{k=1}^{N} \widetilde{S}_\gamma(Q) \cdot e_k = 0.$$

For each $j = 1, \ldots, N-1$, by choosing $Q = d_{j+1}^1$ the first relationship follows.

For each $d_j^1$, denote the solution to (5.2.3) with boundary conditions given by $d_{i+1}^1$ by $u_i$: namely,

$$S_\gamma(d_{i+1}^1) = \left(u_i, (M_{ki})_{k=1}^N\right),$$

where

$$\int_\Omega \gamma \nabla u_i \cdot \nabla v \, \mathrm{d}x = d_{i+1}^1 \cdot V \tag{5.3.5}$$

holds for all $(v, V) \in \overline{H}^1(\Omega)$ by (3.2.17). Setting $\left(\overline{v}, \overline{V}\right) = S_\gamma(d_{j+1}^1)$ in (5.3.5), we establish

$$\begin{aligned}\int_\Omega \gamma \nabla u_j \cdot \nabla u_i \,\mathrm{d}x &= \sum_{k=1}^{N} \left(d_{j+1}^1\right)_k M_{ki} \\ &= \sum_{k=1}^{N} \left(\delta_{1k} M_{1i} - \delta_{j+1,k} M_{j+1,i}\right) \\ &= M_{1i} - M_{j+1,i}.\end{aligned} \tag{5.3.6}$$

Interchanging the roles of $i$ and $j$, we deduce

$$\int_\Omega \gamma \nabla u_i \cdot \nabla u_j \,\mathrm{d}x = M_{1j} - M_{i+1,j}. \tag{5.3.7}$$

Finally, by equating (5.3.6) and (5.3.7) the result follows. □

Recall the definition of the matrix representation of the operator $\widetilde{S}_\gamma$ in the basis $\left\{d_j^1\right\}_{j=2}^N$ as

$$\left[\widetilde{S}_\gamma\right]_{ij} = \widetilde{S}_\gamma(d_{j+1}^1) \cdot d_{i+1}^1.$$

In terms of the entries $\left[\widetilde{S}_\gamma\right]_{ij}$ the relationships described by (5.3.4) become more natural: namely,

$$\left[\widetilde{S}_\gamma\right]_{ij} = \left[\widetilde{S}_\gamma\right]_{ji} \tag{5.3.8}$$

for each $i, j = 1, \ldots, N-1$ with $i \neq j$. In other words, the matrix $\left[\widetilde{S}_\gamma\right]$ is symmetric. We now state explicitly the relationships between the entries of the matrix $\left[\widetilde{S}_\gamma\right]$ and the measurement matrix $M_{ij}$.

LEMMA 11. *The matrix $[S_\gamma]_{ij}$ can be written in terms of $M_{ij}$ using the following relationships:*

For each $i, j = 1, \ldots, N-1$ with $j \neq i$

$$[S_\gamma]_{ij} = M_{1j} - M_{i+1,j},$$

and for $i = j$

$$[S_\gamma]_{jj} = M_{1j} + \sum_{k \neq j} M_{kj}.$$

PROOF. We argue by calculation: for each $i, j = 1, \ldots, N-1$ with $i \neq j$

$$\begin{aligned} S_\gamma\left(d_{j+1}^1\right) \cdot d_{i+1}^1 &= S_\gamma\left(d_{j+1}^1\right) \cdot e_1 - S_\gamma\left(d_{j+1}^1\right) \cdot e_{i+1} \\ &= M_{1j} - M_{i+1,j}. \end{aligned} \tag{5.3.9}$$

Since we do not have access to $M_{j,j+1}$, using Lemma 10 we write

$$M_{j,j+1} = -\sum_{k \neq j} M_{k,j+1}.$$

Thus

$$S_\gamma\left(d_{j+1}^1\right) \cdot d_{j+1}^1 = M_{1j} + \sum_{k \neq j} M_{kj}$$

as required. □

**5.3.3. Measurement paradigm 3: The two electrode problem with mixed boundary conditions.** We consider the third measurement paradigm where the measurements are assumed to be

$$M_{ij} = \widetilde{S}_\gamma\left(d_j^i\right) \cdot d_j^i \tag{5.3.10}$$

for $i, j = 1, \ldots, N$ with $i \neq j$. As in both cases discussed above, this appears to contain $N(N-1)$ measurements.

We begin by establishing the symmetry property present in the matrix $M_{ij}$. Namely, arguing by linearity of the operator $\widetilde{S}_\gamma$ we establish

$$M_{ij} = \widetilde{S}_\gamma\left(d_j^i\right) \cdot d_j^i = -\widetilde{S}_\gamma\left(d_i^j\right) \cdot d_j^i = \widetilde{S}_\gamma\left(d_i^j\right) \cdot d_i^j = M_{ji}.$$

As a result, we only have access at most to $N(N-1)/2$ independent measurements. We now describe the process of establishing relationships between the elements of $\left[\widetilde{S}_\gamma\right]_{ij}$, that is, the matrix representation of $\widetilde{S}_\gamma$ in the basis $\left(d_j^1\right)_{2 \leq j \leq N}$ from the matrix of measurements $M_{ij}$.

For convenience, and without loss of generality, we only consider the measurement elements indexed by $(i, j)$ where $1 \leq i < j \leq N$. This enumerates the complete set of $\frac{1}{2}N(N-1)$ possible measurements.

LEMMA 12. *With measurements $M_{ij}$ given by (5.3.10). The following relationships hold:*

(1) If $i = 1$, then
$$\left[\widetilde{S}_\gamma\right]_{jj} = M_{1,j+1}$$
for each $j = 1, \ldots, N-1$. The diagonal of the matrix $\left[\widetilde{S}_\gamma\right]$ is given by the measurements.

(2) If $i = 2, \ldots, N$ then the following identities hold
$$2\left[\widetilde{S}_\gamma\right]_{i-1,j} = -M_{i,j+1} + M_{1,j+1} + M_{1,i}$$
for each $j = i+1, \ldots, N-1$.

PROOF. When $i = 1$, this follows immediately from the definition of $\left[\widetilde{S}_\gamma\right]_{jj}$. When $1 < i \leq N$, expressing the vector $d^i_{j+1} = d^1_{j+1} - d^1_i$, we calculate

$$\begin{aligned} M_{i,j+1} &= S_\gamma\left(d^i_{j+1}\right) \cdot d^i_{j+1} \\ &= S_\gamma\left(d^1_{j+1} - d^1_i\right) \cdot \left(d^1_{j+1} - d^1_i\right) \\ &= S_\gamma(d^1_{j+1}) \cdot d^1_{j+1} - S_\gamma\left(d^1_{j+1}\right) \cdot d^1_i - S_\gamma(d^1_i) \cdot d^1_{j+1} + S_\gamma\left(d^1_i\right) \cdot d^1_i. \end{aligned}$$

Therefore,
$$\left[\widetilde{S}_\gamma\right]_{jj} - \left[\widetilde{S}_\gamma\right]_{i-1,j} - \left[\widetilde{S}_\gamma\right]_{j,i-1} + \left[\widetilde{S}_\gamma\right]_{i-1,i-1} = M_{i,j+1}$$
for $i = 2, \ldots, N$ and $j = i, \ldots, N-1$. Replacing $\left[\widetilde{S}_\gamma\right]_{i-1,i-1}$ by $M_{1,i}$ and $\left[\widetilde{S}_\gamma\right]_{jj}$ by $M_{1,j+1}$ in the identity above, and using the symmetry of $\left[\widetilde{S}_\gamma\right]$ shown in (5.3.8), the conclusion follows. □

**Justification for measurement paradigm 3.** We now consider the practical relevance of measurement paradigm 3 by proving equivalence with the 'two electrode' problem. Let $\mathcal{I} = \{i, j\} \subset \{1, \ldots, N\}$ be a set of two distinct indices $i$ and $j$. Suppose

$u_{ij} \in H^1(\Omega;\mathbb{C})$ is the solution to mixed problem

$$\begin{cases} -\operatorname{div}(\gamma\nabla u_{ij}) = 0, \text{ in } \Omega, \\ \qquad\qquad u_{ij} = 1 \text{ on } \partial E_i, \\ \qquad\qquad u_{ij} = 0 \text{ on } \partial E_j, \\ \qquad \gamma\nabla u_{ij}\cdot\hat{n} = 0 \text{ on } \partial\Omega_B \cup \left(\bigcup_{k\neq i, k\neq j} \partial E_k\right). \end{cases} \tag{5.3.11}$$

The measurements are then

$$m_{ij} := |\partial E_j|^{-1} \int_{\partial E_j} \gamma\nabla u_{ij}\cdot\hat{n}\,\mathrm{d}s. \tag{5.3.12}$$

This produces a set of $N(N-1)$ measurements indexed by the tuples $(i,j)$ where $i,j \in \{1,\dots,N\}$ with $i \neq j$. Practically, the measurements obtained using the two electrode problem are sequential unlike in paradigms 1 and 2 where measurements are taken across all electrodes simultaneously. We now argue that the sequential 'two electrode' measurements are equivalent to (5.3.10).

Recall that for any $\gamma \in \mathcal{A}$ and any choice of $\mathcal{I}$

$$\int_{\partial\Omega} \gamma\nabla u_{ij}\cdot\hat{n}\,\mathrm{d}s = 0,$$

therefore,

$$\int_{\partial E_i} \gamma\nabla u_{ij}\cdot\hat{n}\,\mathrm{d}s = -\int_{\partial E_j} \gamma\nabla u_{ij}\cdot\hat{n}\,\mathrm{d}s = -m_{ij}|\partial E_j|$$

We define the vector $Q^{ij} \in \mathbb{K}^N_\diamond$ by

$$Q^{ij}_k := \begin{cases} -m_{ij} & \text{when } k = i, \\ m_{ij} & \text{when } k = j, \\ 0 & \text{otherwise.} \end{cases}$$

Then by construction and the definition of $u_{ij}$, for each $k = 1,\dots,N$

$$|\partial E_k|^{-1} \int_{\partial E_k} \gamma\nabla u_{ij}\cdot\hat{n}\,\mathrm{d}s = Q^{ij}_k.$$

Alternatively, this can be expressed in terms of $d_j^i$ as

$$Q^{ij} = -m_{ij} d_j^i. \tag{5.3.13}$$

Considering (5.3.11) as a Dirichlet problem instead, let $U^{ij} \in \mathbb{K}^N$ be the such that

$$\left(U^{ij}\right)_k = u^{ij}|_{\partial E_k}.$$

This is well-defined since the function $u^{ij}$ is constant on each electrode by the choice of boundary conditions. More explicitly, we have

$$\left(U^{ij}\right)_i = 1, \left(U^{ij}\right)_j = 0, \text{ and } \left(U^{ij}\right)_k \in \mathbb{K}$$

for $k = 1, \ldots, N$ with $k \neq i$ and $k \neq j$. Define the vector $\widetilde{U}^{ij} \in \mathbb{K}^N_\diamond$ to be

$$\widetilde{U}^{ij} := U^{ij} - \overline{U^{ij}}\mathbf{1}$$

where $\overline{U^{ij}} = |\partial E|^{-1} \sum_{k=1}^N |\partial E_k| \left(U^{ij}\right)_k \in \mathbb{K}$ with $|\partial E| = \sum_{k=1}^N |\partial E_k|$ and $\mathbf{1} \in \mathbb{K}^N$ is the vector of ones. Then

$$\begin{aligned}
\sum_{k=1}^N \int_{\partial E_k} \left(u_k^{ij} - \overline{U^{ij}}\right) \mathrm{d}s &= \sum_{k=1}^N |\partial E_k| \left(U_k^{ij} - \overline{U^{ij}}\right) \\
&= \sum_{k=1}^N |\partial E_k| \, U_k^{ij} - |\partial E| \, \overline{U^{ij}} \\
&= 0.
\end{aligned}$$

We remark that when the electrodes are of size $|\partial E_k| = 1$, $\overline{U^{ij}}$ becomes the average of the vector $U^{ij}$.

Although none of the entries of $\widetilde{U}^{ij}$ are unknown, the image of $\widetilde{U}^{ij}$ under the linear map $\widetilde{\Lambda}_\gamma$ is known. Namely,

$$\widetilde{\Lambda}_\gamma \left(\widetilde{U}^{ij}\right) = Q^{ij}. \tag{5.3.14}$$

Substituting (5.3.13) into (5.3.14) and using $\widetilde{S}_\gamma \circ \widetilde{\Lambda}_\gamma = \mathrm{Id}$, this becomes

$$\widetilde{S}_\gamma \left(m_{ij} d_j^i\right) = U^{ij} - \overline{U^{ij}}\mathbf{1}. \tag{5.3.15}$$

Noticing the $i$-th and $j$-th elements are given by

$$\widetilde{S}_\gamma\left(m_{ij}d_j^i\right)\cdot e_i = 1 - \overline{U^{ij}}\mathbf{1}$$

and

$$\widetilde{S}_\gamma\left(m_{ij}d_j^i\right)\cdot e_j = -\overline{U^{ij}}\mathbf{1},$$

we deduce

$$\widetilde{S}_\gamma\left(m_{ij}d_j^i\right)\cdot d_j^i = 1.$$

In other-words, using the linearity of $\widetilde{S}_\gamma$ the measurements (5.3.10) can be written in terms of the $m_{ij}$ where

$$M_{ij} = \frac{1}{m_{ij}}$$

for each $1 \leq i < j \leq N$.

**5.3.4. Measurement paradigm 4: A partial data problem.** We consider, as a fourth measurement paradigm, a partial data form of paradigm 3: the measurements are given by

$$M_{ij} = \widetilde{S}_\gamma\left(d_j^i\right)\cdot d_j^i \tag{5.3.16}$$

for $i, j = 1, \ldots, N$ with $i \neq j$ and $d(i,j) \leq 1$ for some function $d(i,j)$ depends on the distance between electrodes $E_i$ and $E_j$. The placement and naming convention of the electrodes in both the circular and planar cases defines the distance function $d(i,j)$. In the case of a circular boundary with equally spaced electrodes whose middle point is located at $R\exp\left(2\pi\frac{i-1}{N}\mathrm{i}\right)$, one can set

$$d : (i,j) \longmapsto \frac{\min\left(|i-j+N|, |i-j-N|, |i-j|\right)}{L},$$

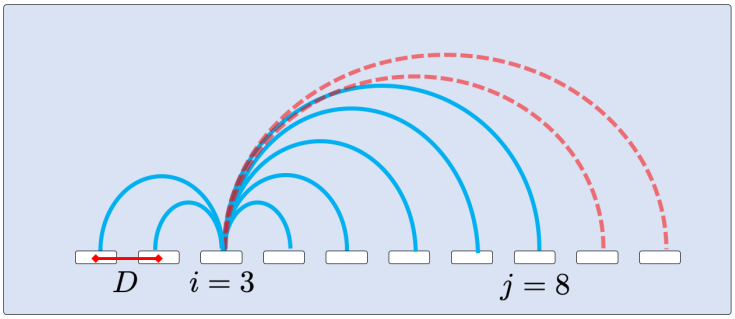
for some fixed $L \in \mathbb{N}$ with $L < N$. Similarly, in the case of a planar sensor, with equally spaces electrodes separated by a distance $D > 0$, one can set

$$d : (i,j) \longmapsto \frac{|i-j|}{L}$$

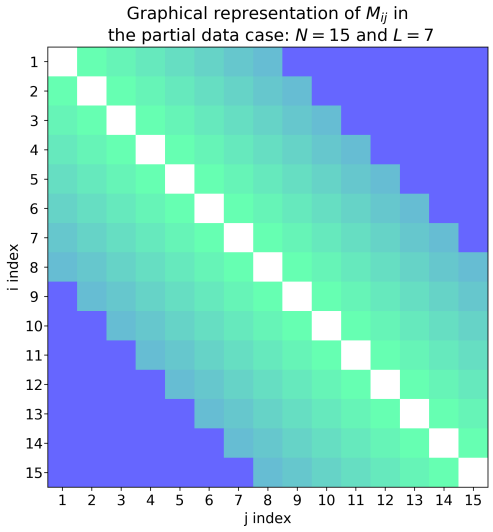
with $L \in \mathbb{N}$ with $L < N$.

In both cases, the integer $L$ determines the number of electrodes on either side of the emitter that are being considered. We argue that this paradigm is practically relevant: when $i$ and $j$ are far apart, the measured signal in the two electrode problem given by (5.3.12) becomes very small, critically less than the sensitivity of the measurement apparatus and thus cannot be measured. Instead, we suppose that the measurements are only known for $i$ and $j$ within $L$ electrodes of each other. In practice, $L$ is not large, often chosen to be 5 in the cases considered here. As an example, Figure 5.3.1a shows the particular measurements that are missing in the case when $L = 5$ on a planar sensor with 10 electrodes.

Since the measurements are in the same form as (5.3.10), we establish $N(N-1-L)/2$ relationships using Lemma 12. However, $\left[\widetilde{S}_\gamma\right]$ cannot be found in its entirety as measurements are missing, creating off diagonal bands of missing entries in the matrix as seen in Figure 5.3.1b. In the following chapter, we consider methods to estimate the missing data which, coupled with Lemma 12, can be used to estimate $\left[\widetilde{S}_\gamma\right]$.




(A) Diagram showing the missing measurements in the planar case when $N = 10$ and $L = 5$. The known measurements are shown in blue. In contrast, the missing measurements, shown in red, are $\widetilde{S}_\gamma\left(d_9^3\right) \cdot d_9^3$ and $\widetilde{S}_\gamma\left(d_{10}^3\right) \cdot d_{10}^3$. The unit length between the midpoint of each electrode is shown and denoted $D$.




(B) Graphical representation of the matrix $M_{ij}$ showing the missing elements in blue.

FIGURE 5.3.1. Diagrams demonstrating the origin of the missing measurements and their place in the matrix $M_{ij}$.

CHAPTER 6

# Reconstruction algorithms

We consider algorithms to numerical estimate the *unknown* parameter $\gamma \in \mathcal{A}$ given either $\Lambda_\gamma$ in the continuum setting or $\widetilde{S}_\gamma$ in the finite dimensional setting. While the practically relevant problem is the later, considering the functional analytic framework is once again useful. We call such algorithms *numerical reconstruction algorithms*. Of particular relevance to this thesis are the developments made to improve the algorithms used in the reconstruction: namely, improving the accuracy of the forward model used [8, 110], the use of regularisation techniques (for example [101]), and the encoding of a priori information on the material distribution [140].

The importance of developing stable and accurate numerical procedures to estimate the parameters has been considered by many authors over the past few decades [58, 202]. Historically, the first reconstruction algorithm, the celebrated $\bar{\partial}$-method was developed by Nachmann [137]. This cultivated interest in this problem and many alternative approaches have been presented: each with their own advantages and disadvantages. Broadly speaking, the reconstruction algorithms proposed to date use either deterministic, Bayesian, or a Neural Network methods, although combined approaches have been proposed. The number of deterministic algorithms currently employed by far outweighs the other two categories although recently algorithms built on neural networks have started to out perform the deterministic approaches.

The most widely used algorithms rely on linearisation methods [20, 120, 202, 203]. In such methods, the forward problem is linearised about a known parameter and the inverse problem associated linear problem is expressed as a minimisation problem. Many techniques have been employed to solve the resulting system, of which the most successful has been based on an iterative Landweber minimisation procedure [120, 199]. Regularising the system using specialised regularisation methods can also be shown to improve the reconstructions [148].

However, while the accuracy of reconstructions can be improved using iterative approaches the accuracy remains limited by the fundamental linearisation assumption: only small perturbations of the background parameter distribution can be estimated [51, 58, 171, 202].

Alternative approaches have been considered that avoid such stringent linearisation assumptions. One approach is to rephrase the reconstruction as a PDE constrained minimisation procedure and use numerical techniques from optimisation theory to find a solution. An early example of this approach was proposed by Wexler [193, 194] and expanded by Kohn and Vogelius in [113]. The methods developed vary from non-iterative approximation methods to iterative Newton-type methods, see the review paper [49] or the last chapter of [96] for an overview. This approach has been shown to perform well and is capable of recovering non-linear properties of the parameter $\gamma \in \mathcal{A}$ [41, 101, 129, 157, 160]. Non-linear reconstruction algorithms have also shown promise [160].

More recently representing the unknown coefficient as a Neural Network has been shown to outperform conventional methods in particular cases [77, 129, 147, 152]. While this area of study remains in its infancy, it is an exciting area for development. Similarly, improvements have been seen using Bayesian reconstruction techniques [38, 39, 64, 102, 114, 140, 174]. We do not discuss neural networks or Bayesian methods in detail here but refer the interested reader to the aforementioned references. Additionally, we mention work done to reconstruct three dimensional parameters [17, 42, 90, 106, 199].

Determining the accuracy of each reconstruction algorithm is non-trivial. Not only due to the care needed in order to avoid committing an 'inverse crime' (see Chapter 1), the accuracy of the reconstruction is known to be dependent on the unknown parameter distribution [94, 181, 182]. In particular, the accuracy of the reconstruction is known to be dependent on the distance between the object and the electrodes. As a result there is the potential to over estimate the accuracy of an algorithm if the test cases used are particularly favourable to the specific algorithm being tested.

A more robust approach would be to test the algorithms on a very large number of randomly generated parameter distributions and consider the statistical distribution of the accuracy for this ensemble of cases. However, this is beyond the scope of this thesis. Instead, we adopt the conventional approach and specialise to a single test case in order to illustrate the potential for parameter reconstruction for the specific planar geometry of interest. We are particularly mindful of this when reporting the accuracy of the algorithms in the case of a planar sensor array since this geometry has not been considered by many authors, an exception being the work on Open EIT described in [207]. We choose simple test cases inspired by the practical application.

The author has implemented the reconstruction algorithms in FreeFem++ and all of the numerics are done using simulated data generated by methods described in Chapter 4. We remark that open-source simulation and reconstruction computational environments do exist: examples include EIDORS [2] and pyEIT [121].

This chapter is structured in two parts. In the first part, we review numerical procedures that can be used to estimate the complex valued parameter $\gamma \in \mathcal{A}$ in the full data case using both linearisation and optimisation based approaches. In the minimisation algorithm, we introduce an adjoint problem to calculate the gradient step which significantly reduces the computational time. In the second part, we consider the partial data case relevant to measurement paradigm 4 introduced in the previous chapter. In particular, we devise algorithms to estimate the missing data using a priori assumptions on the parameter $\gamma$. We consider the case when either $\gamma$ is symmetric or when $\gamma$ can be considered a small perturbation from a known background $\gamma_0 \in \mathcal{A}$ and present novel algorithms that can be used in the estimate the missing data. Finally, we present numerical evidence showing the resulting error committed by estimating the missing matrix entries can be considered small in certain circumstances.

## 6.1. Parameter reconstruction in the full data case

We define the space of admissible parameter perturbations: given a known, fixed background distribution $\gamma_0 \in \mathcal{A}$, we define

$$\mathcal{A}_0 := \{\delta\gamma \in L^\infty(\Omega) : \gamma_0 + \delta\gamma \in \mathcal{A}\}\,.$$

We discretise this set in the following way: let $\Omega \subset\subset \Omega$ and define a set of functions, which we call pixels, as $\{\psi_p\}_{p\in P}$ where

- for any $p \in P$

$$\psi_p \in L^\infty(\Omega) \text{ and } \psi_p \equiv 0 \text{ in } \Omega' \setminus \Omega;$$

- for any $x \in \Omega$

$$\psi_p(x) \in \{0, 1\}\,;$$

- and for any $p, q \in P$

$$\int_\Omega \psi_p\, \psi_q \,\mathrm{d}x = 0.$$

We consider the restricted class of admissible perturbations that can be identified uniquely with a vector $\beta \in \mathbb{K}^P$ by

$$\delta\gamma = \sum_{p\in P} \beta_p \psi_p \text{ where } \beta_p \geq 0 \text{ for each } p \in P. \tag{6.1.1}$$

For a given set of pixels, we denote the set of all perturbations of the form (6.1.1) by $\widetilde{\mathcal{A}}_0$. While we do not specify explicitly the construction of the pixels in order to maintain the generality of our approach to different applications; when testing the algorithms we define a rectangular grid of equally sized square pixels for convenience, see 6.1.6.

Throughout this chapter we shall denote the forward problem by $\mathcal{F}$ defined by

$$\mathcal{F} : \gamma \longmapsto \left[\widetilde{S}_\gamma\right] \tag{6.1.2}$$

where $\left[\widetilde{S}_\gamma\right] \in \mathbb{K}^{N-1,N-1}$ is the matrix representation of the operator $\widetilde{S}_\gamma$ in the basis $\left\{d_j^1\right\}_{j=2}^N$. We recall the operator

$$\widetilde{S}_\gamma : \mathbb{K}_\diamond^N \longrightarrow \mathbb{K}_\diamond^N$$

$$Q \longmapsto U$$

where $(u, U) \in \overline{H}^1(\Omega)$ solves

$$\begin{cases} -\operatorname{div}(\gamma \nabla u) = 0 & \text{in } \Omega, \\ |\partial E_k|^{-1} \displaystyle\int_{\partial E_k} \gamma \nabla u \cdot \hat{n} \, \mathrm{d}s = Q_k & \text{on } \partial E_k \text{ for } k = 1, \ldots, N, \\ u = U_k & \text{on } \partial E_k \text{ for } k = 1, \ldots, N, \\ \gamma \nabla u \cdot \hat{n} = 0 & \text{on } \partial \Omega_B. \end{cases} \tag{6.1.3}$$

The estimation of the matrix $\left[\widetilde{S}_\gamma\right]$ from sensor measurements was discussed in Chapter 5.3.

**6.1.1. A linearised approach to reconstruction.** In this section we deduce the linearisation of the operator $\mathcal{F}$, defined in (6.1.2), and consider a least-squares solution of the associated inverse problem. Suppose that a parameter $\gamma_0 \in \mathcal{A}$ is known. Then expanding $\mathcal{F}(\gamma)$ about $\gamma_0$, we write

$$\mathcal{F}(\gamma_0 + \delta\gamma) = \mathcal{F}(\gamma_0) + \mathrm{d}\mathcal{F}(\gamma_0)[\delta\gamma] + \text{h.o.t.}$$

where $\delta\gamma \in \mathcal{A}_0$ is a small perturbation of $\gamma_0$ and $\mathrm{d}\mathcal{F}$ is the first variation of $\mathcal{F}$ in the direction $\delta\gamma$ at $\gamma_0$. Written in discretised form, the linearised problem becomes for each $i, j = 1, \ldots, N-1$

$$\left[\widetilde{S}\left(\gamma_0 + \sum_{p \in P} \beta_p \psi_p\right)\right]_{ij} = \left[\widetilde{S}(\gamma_0)\right]_{ij} + \sum_{p \in P} \left[\mathrm{d}\widetilde{S}_{\gamma_0}\right]_{ijp} \beta_p \tag{6.1.4}$$

where $\beta \in \mathbb{K}^P$ is the associated vector to $\delta\gamma \in \widetilde{\mathcal{A}}_0$ in (6.1.1) and $\left[\mathrm{d}\widetilde{S}_{\gamma_0}\right]_{i\cdot} \in \mathbb{K}^{(N-1)\times P}$ is the Jacobian matrix for each $i = 1, \ldots, N-1$. After rearranging (6.1.4), we write

$$\sum_{p\in P} \left[\mathrm{d}\widetilde{S}_{\gamma_0}\right]_{ijp} \beta_p = \left[\widetilde{S}\left(\gamma\right)\right]_{ij} - \left[\widetilde{S}(\gamma_0)\right]_{ij} \tag{6.1.5}$$

and notice that both terms on the right hand side are the known sensor measurements: $\left[\widetilde{S}\left(\gamma\right)\right]$ being the matrix of measurements for the unknown parameter $\gamma$ and $\left[\widetilde{S}\left(\gamma_0\right)\right]$ being the measurements for the known background parameter $\gamma_0$.

We denote $\mathbf{A} \in \mathbb{K}^{(N-1)\times(N-1)\times P}$ by

$$\mathbf{A}_{ijp} := \left[\mathrm{d}\widetilde{S}_{\gamma_0}\left(\psi_p\right)\right]_{ij}$$

and thus, provided $\mathrm{d}\widetilde{S}_{\gamma_0}$ can be computed, (6.1.5) becomes

$$\sum_{p\in P} \mathbf{A}_{ijp}\overline{\beta_p} = \mathbf{B}_{ij} \tag{6.1.6}$$

where

$$\mathbf{B}_{ij} := \left[\widetilde{S}\left(\gamma\right)\right]_{ij} - \left[\widetilde{S}(\gamma_0)\right]_{ij}.$$

We consider the computation of $\mathrm{d}\widetilde{S}_{\gamma_0}$ in the subsequent section. In practice, 6.1.6 is then serialised to produce a matrix system: define $A \in \mathbb{K}^{M\times P}$ and $b \in \mathbb{K}^M$ where $M = (N-1)^2$, (6.1.6) becomes

$$\sum_{p\in P} A_{ip}\overline{\beta_p} = b_i. \tag{6.1.7}$$

The inverse problem associated to (6.1.7) is to find the vector $\overline{\beta} \in \mathbb{K}^P$ given the matrix $A \in \mathbb{K}^{M\times P}$ and the vector of measurements $b \in \mathbb{K}^M$. That is we are interested in finding a matrix $R$ such that

$$\overline{\beta} = Rb. \tag{6.1.8}$$

In the case when $M = P$—the number of measurements being equal to the number of parameter unknowns—the natural candidate for $R$ is the inverse matrix $A^{-1}$ (provided

it exists). However, in most practical applications $P > M$ and the system is underdetermined and thus further restrictions on the components of $\overline{\beta}$ are required. These are often imposed using regularisation techniques.

One can rephrase (6.1.8) as a least squares problem: define the cost function

$$J\left(\overline{\beta}\right) = \sum_{i=1}^{M} w_i^2 (b_i - A\overline{\beta})^T (b_i - A\overline{\beta})$$

where the transpose denotes the conjugate transpose in the complex case and $w_i$ are chosen weights. Then the discretised reconstruction of $\gamma$ is then given by

$$\gamma = \gamma_0 + \sum_p \widehat{\beta}_p \psi_p \text{ where } \widehat{\beta} := \arg\min_{\overline{\beta} \in \mathbb{K}^P} J(\overline{\beta}).$$

In particular, $\widehat{\beta} \in \mathbb{K}^P$ is the solution to the set of normal equations given by

$$\left(A^T W A\right) \widehat{\beta} = A^T W b. \tag{6.1.9}$$

Before considering methods for computing the matrix $A$, we briefly describe how appropriate choices of the weight matrix $W$ regularise the inverse problem.

6.1.1.1. *Using the Truncated Singular Valued Decomposition.* We begin by stating the singular valued decomposition of a complex valued matrix.

THEOREM 12 (Singular Valued Decomposition (SVD)). *Let $A \in \mathbb{C}^{N \times M}$ be a matrix of rank $r$. The there exists a factorisation of $A$, which we call the SVD, such that*

$$A = U \Sigma V^T \tag{6.1.10}$$

*where $U \in \mathbb{C}^{N \times N}$ and $V \in \mathbb{C}^{M \times M}$ are unitary matrices, and $\Sigma \in \mathbb{R}^{N \times M}$ is a diagonal matrix with $r$ non-negative entries, which we denoted by $\sigma_1, \ldots, \sigma_r$. This decomposition is unique if we suppose that the singular values are ordered as $\sigma_1 \geq \sigma_2 \geq \cdots \geq \sigma_r > 0$.*

We apply the SVD decomposition to the matrix $A \in \mathbb{K}^{M \times P}$ to obtain

$$A = U \Sigma V^T \tag{6.1.11}$$

where $U \in \mathbb{K}^{M\times M}$, $V \in \mathbb{K}^{P\times P}$, and $\Sigma \in \mathbb{K}^{M\times P}$. . Then the SVD of the matrix product $A^TA$ is given by

$$A^TA = V\Sigma^T\Sigma V^T \tag{6.1.12}$$

where $\Sigma^T\Sigma \in \mathbb{K}^{P\times P}$ is the diagonal matrix with diagonal

$$\left(\Sigma^T\Sigma\right)_{ii} = \begin{cases} \sigma_i^2 & \text{for } i = 1,\dots,p, \\ 0 & \text{otherwise.} \end{cases} \tag{6.1.13}$$

Using this decomposition the solution to the normal equations (6.1.9) can be expressed as

$$\begin{aligned} \hat{\beta} &= V\left(\Sigma^T\Sigma\right)^{-1}V^TS^Tb \\ &= V\left(\Sigma^T\Sigma\right)^{-1}\Sigma^TU^Tb \end{aligned} \tag{6.1.14}$$

where $\left(\Sigma^T\Sigma\right)^{-1}$ is the diagonal matrix with diagonal elements given by

$$\left(\Sigma^T\Sigma\right)^{-1}_{ii} = \begin{cases} 1/\sigma_i^2 & \text{if } i = 1,\dots,r, \\ 0 & \text{otherwise.} \end{cases} \tag{6.1.15}$$

This matrix is known as the pseudo-inverse of the matrix. As such (6.1.14) can be written simply as

$$\hat{\beta} = V\Sigma^{-1}U^Tb \tag{6.1.16}$$

where $\Sigma^{-1}$ is the pseudo-inverse of the matrix $\Sigma$, namely,

$$\left(\Sigma^{-1}\right)_{ii} = \begin{cases} 1/\sigma_i & \text{if } i = 1,\dots,p, \\ 0 & \text{otherwise.} \end{cases} \tag{6.1.17}$$

The truncated singular valued decomposition (TSVD) modifies the pseudo-inverse and instead gives a solution to the normal equations as

$$\hat{\beta} = V\Sigma_\alpha^{-1}U^Tb \tag{6.1.18}$$

where $\Sigma_\alpha^{-1}$ is the diagonal matrix given by

$$\left(\Sigma_\alpha^{-1}\right)_{ii} = \begin{cases} w_i/\sigma_i & \text{if } i = 1, \dots, r, \\ 0 & \text{otherwise,} \end{cases} \tag{6.1.19}$$

for some choice of weights $w_1, \dots, w_r$ that depend on the regularisation parameter $\alpha > 0$. We consider the weights to be chosen by a hard-filter

$$w_i = \begin{cases} 1 & \text{if } \sigma_i > \alpha, \\ 0 & \text{if } \sigma_i \leq \alpha, \end{cases} \tag{6.1.20}$$

for $i = 1, \dots, r$, or by a high-pass filter

$$w_i = \frac{\sigma_i^2}{\sigma_i^2 + \alpha} \tag{6.1.21}$$

for $i = 1, \dots, r$. In Lemma (13), we will show that the choice of weights given by (6.1.21) is equivalent to adding a Tikhonov regularisation term to the cost functional $J_1(\beta)$.

6.1.1.2. *Using the Tikhonov Regularisation.* The Tikhonov method regularises the solution to the least squares problem by imposing additional constraints on the solution obtained. That is the minimisation problem becomes

$$\hat{\beta} = \arg\min_{\beta \in \mathbb{K}^{N_p}} \left( |A\beta - b|^2 + \alpha \, |\beta - \beta_0|^2 \right) \tag{6.1.22}$$

with $\beta_0$ encoding the prior information on the parameter distribution, and $\alpha > 0$ is the regularisation coefficient. In the case when $\beta_0$ is zero, the system of normal equations becomes

$$\left(A^T A + \alpha I\right) \hat{\beta} = A^T b. \tag{6.1.23}$$

We make the connection to the TSVD method explicit.

LEMMA 13. *If $\beta_0 = 0$ then the solution $\hat{\beta}$ to (6.1.23) is equivalent to the solution by TSVD (6.1.18) with the choice of weights given by (6.1.21).*

PROOF. Let the matrices $U$, $V$, and $\Sigma$ be defined as in equation (6.1.11). Let $v_i$ be the vector associated to the singular value $\sigma_i$ of the matrix $A$ then

$$\left(A^T A + \alpha I\right) v_i = \left(\sigma_i^2 + \alpha\right) v_i \tag{6.1.24}$$

and so $\sigma_i^2 + \alpha$ is a singular value of the matrix $S^T S + \alpha I$. Taking the SVD of the matrix $S^T S + \alpha I$ then becomes

$$A^T A + \alpha I = V \widetilde{\Sigma} V^T$$

where

$$\left(\widetilde{\Sigma}\right)_{ii} = \begin{cases} \sigma_i^2 + \alpha & \text{if } i = 1, \ldots, r, \\ 0 & \text{otherwise.} \end{cases} \tag{6.1.25}$$

Taking then the inverse of $S^T S + \alpha I$, equation (6.1.23) we get that

$$\hat{\beta} = V \widetilde{\Sigma}^{-1} \Sigma^T U^T b,$$

where

$$\left(\widetilde{\Sigma}^{-1}\Sigma\right)_{ii} = \begin{cases} \frac{\sigma_i}{\sigma_i^2 + \alpha} & \text{for } i = 1, \ldots, r \\ 0 & \text{otherwise.} \end{cases} \tag{6.1.26}$$

The RHS is then equivalent to the TSVD method with the choice of weights given by (6.1.21). □

**6.1.2. Rephrasing the reconstruction problem as a minimisation problem.** We now consider the inverse problem as a minimisation problem for the functional

$$J_1(\gamma; Q) = |\widetilde{S}_\gamma(Q) - U|^2, \tag{6.1.27}$$

where $Q \in \mathbb{K}_\diamond^N$, $U = \widetilde{S}_\gamma(Q)$ and $\gamma \in \mathcal{A}$.. We estimate the true parameter $\gamma \in \mathcal{A}$ by $\widehat{\gamma} \in \mathcal{A}$ defined as

$$\widehat{\gamma} := \arg\min_{\gamma \in \mathcal{A}} \sum_{i=1}^{M} J_1(\gamma; Q_i), \tag{6.1.28}$$

where $M \in \mathbb{N}$ and $Q_i \in \mathbb{K}^N$ for each $i = 1, \ldots, K$. This can be considered as a PDE constrained minimisation problem since an evaluation of $\widetilde{S}_\gamma$ requires the solution of the PDE given by equation (6.1.3).

We restrict to a subset of admissible parameter distributions that are perturbations from a known background. Let $\gamma_0 \in \mathcal{A}$ be the known background parameter distribution and $\delta\gamma \in \mathcal{A}_0$ the perturbation where

$$\mathcal{A}_0 := \{\delta\gamma \in L^\infty(\Omega) : \gamma_0 + \delta\gamma \in \mathcal{A}\}.$$

We discuss computing directly $\mathrm{d}\widetilde{S}_{\gamma_0}(Q)[\delta\gamma]$ for any $\delta\gamma \in \mathcal{A}_0$ without the need for first discretising $\delta\gamma$ into pixels. The main advantage of being able to computing $\mathrm{d}\widetilde{S}_{\gamma_0}(Q)[\delta\gamma]$, is the ability to use gradient-based iterative minimisation algorithms where at each iteration the gradient vector can be updated. Despite these algorithms being computationally more expensive than solving 6.1.7, due to requiring the gradient to be updated at each step, we expect more accurate reconstructions to be obtained. We formalise the computation of the first variation of $\widetilde{S}_\gamma$ in the following section.

We remark that Newton methods can also be developed. In particular, using the linearisation of $\widetilde{S}_\gamma$ about $\gamma_0$, we write

$$\widetilde{S}_\gamma(Q) = \widetilde{S}_{\gamma_0}(Q) + \mathrm{d}\widetilde{S}_{\gamma_0}(Q)[\delta\gamma] + \text{h.o.t.}.$$

Using this approximation, minimising (6.1.27) is equivalent to minimising

$$J_2(\gamma_0; Q) = |\mathrm{d}\widetilde{S}_{\gamma_0}(Q)[\delta\gamma] - (U - U_0)|^2. \tag{6.1.29}$$

Subsequently, we estimate the true parameter $\gamma \in \mathcal{A}$ by $\gamma = \gamma_0 + \widehat{\delta\gamma}$ where

$$\widehat{\delta\gamma} := \arg\min_{\delta\gamma \in \mathcal{A}_0} \sum_{i=1}^{M} J_2(\delta\gamma; \gamma_0, Q_i).$$

However, we do not consider Newton methods in detail in this thesis.

**6.1.3. The first variation of $J_1(\gamma)$ and $J_2(\gamma)$.** We begin with the formal definition of the first variation of a function between Banach spaces.

DEFINITION 7. Suppose that $X$ and $Y$ are Banach spaces and $F : X \to Y$. Let $U \subset X$ be an open set and $u \in U$. *The first variation* of $F$ at $u \in U$ in the direction $v \in X$ is the linear map $v \mapsto \mathrm{d}F(u)[v]$ where

$$\mathrm{d}F(u)[v] := \frac{\mathrm{d}}{\mathrm{d}h} F(u + hv)|_{h=0}.$$

The functional $\mathrm{d}F(u)[v]$ is also known as the Gateaux differential of $F$ at $u \in U$ in the direction $v$.

**The first variation of $S_\gamma(Q)$.** In the following Lemma we calculate the first and second variations of the map $S_\gamma : \gamma \to (u, U)$ where $(u, U) \in \overline{H}^1(\Omega)$ solves (6.1.3). We note that this calculation allows for $\mathrm{d}\widetilde{S}_\gamma$ to be computed.

LEMMA 14. *Fix $\gamma \in \mathcal{A}$ and Let $(u, U) \in \overline{H}^1(\Omega)$ be the weak solution to (6.1.3) for a given $Q \in \mathbb{K}_\diamond^N$.*

*(1) The first variation of the map $\gamma \mapsto S_\gamma(Q)$ is the linear map*

$$dS_\gamma(Q) : \mathcal{A}_0 \to \overline{H}^1(\Omega; \mathbb{C})$$

$$\delta\gamma \mapsto (v, V)$$

*where $(v, V) \in \overline{H}^1(\Omega; \mathbb{C})$ is the weak solution to*

$$\int_\Omega \gamma \nabla v \cdot \nabla \psi \, dx = -\int_\Omega \delta\gamma \nabla u \cdot \nabla \psi \, dx, \qquad \text{for all } (\psi, \Psi) \in \overline{H}^1(\Omega; \mathbb{C}). \tag{6.1.30}$$

*In other-words, $(v, V) \in \overline{H}^1(\Omega)$ solves*

$$\begin{cases} -div(\gamma \nabla v) = div(\delta\gamma \nabla u) & \text{in } \Omega, \\ |\partial E_k|^{-1} \displaystyle\int_{\partial E_k} \gamma \nabla v \cdot \hat{n} \, ds = 0 & \text{on } \partial E_k \text{ for } k = 1, \dots, N, \\ v = V_k & \text{on } \partial E_k \text{ for } k = 1, \dots, N, \\ \gamma \nabla v \cdot \hat{n} = 0 & \text{on } \partial\Omega_B, \end{cases}$$

*for each $\delta\gamma \in \mathcal{A}_0$.*

PROOF. For $h \in \mathbb{R}$ the function $(u(\gamma + h\delta\gamma), U(\gamma + h\delta\gamma)) \in \overline{H}^1(\Omega; \mathbb{C})$ satisfies

$$\int_\Omega (\gamma + h\delta\gamma)\nabla u(\gamma + h\delta\gamma) \cdot \nabla\psi \, \mathrm{d}x - \sum_{k=1}^{N} Q_k \Psi_k = 0 \text{ for all } (\psi, \Psi) \in \overline{H}^1(\Omega).$$

Differentiating this expression with respect to $h$ and setting $h = 0$ we obtain

$$\int_\Omega \delta\gamma \nabla u\,(\gamma) \cdot \nabla\psi \, \mathrm{d}x + \int_\Omega \gamma \nabla\left(\mathrm{d}u\,[\delta\gamma]\right) \cdot \nabla\psi \, \mathrm{d}x = 0 \text{ for all } (\psi, \Psi) \in \overline{H}^1(\Omega),$$

and conclude that $\mathrm{d}S_\gamma(Q)\,[\delta\gamma]$ satisfies (6.1.30). On the other hand, the solution $(v, V) \in \overline{H}^1(\Omega)$ to (6.1.30) exists and is unique, therefore, $(v, V) = \mathrm{d}S_\gamma(Q)\,[\delta\gamma]$ as required. □

**The adjoint $\mathbf{d}\widetilde{S}_\gamma(Q)$.** While (6.1.30) can be used to compute the first variation $\mathrm{d}\widetilde{S}_\gamma$, this approach is computationally expensive since a $\mathrm{d}u[\delta\gamma]$ needs to be found for each choice of direction $\delta\gamma$. We offer an alternative using the adjoint of the operator $\mathrm{d}\widetilde{S}_\gamma$.

DEFINITION 8. The adjoint operator $\left(\mathrm{d}\widetilde{S}_\gamma\,(Q)\right)^* : \mathbb{K}^N_\diamond \longrightarrow L^1(\Omega; \mathbb{C})$ is the unique operator such that for any $W \in \mathbb{K}^N_\diamond$ and $\delta\gamma \in \mathcal{A}_0$

$$\left\langle \mathrm{d}\widetilde{S}_\gamma\,(Q)\,[\delta\gamma]\,, W \right\rangle_{\mathbb{K}^N_\diamond, \mathbb{K}^N_\diamond} = \left\langle \delta\gamma, \left(\mathrm{d}\widetilde{S}_\gamma\,(Q)\right)^* [W] \right\rangle_{L^\infty(\Omega;\mathbb{C}), L^1(\Omega;\mathbb{C})}. \tag{6.1.31}$$

We give a useful characterisation of the adjoint operator in the following theorem.

THEOREM 13. *The adjoint of the operator $d\widetilde{S}_\gamma\,(Q) : \mathcal{A}_0 \to \mathbb{K}^N_\diamond$ is given by*

$$\left(d\widetilde{S}_\gamma\,(Q)\right)^* : \mathbb{K}^N_\diamond \to L^1(\Omega; \mathbb{C})$$

$$W \mapsto -\nabla p \cdot \nabla u$$

*where* $(p, P) \in \overline{H}^1(\Omega)$ *is the weak solution to the adjoint problem*

$$\begin{cases} -\,div\,(\gamma \nabla p) = 0 & \text{in } \Omega, \\ |\partial E_k|^{-1} \displaystyle\int_{\partial E_k} \gamma \nabla p \cdot \hat{n}\, ds = W_k & \text{on } \partial E_k \text{ for } k = 1, \ldots, N, \\ p = P_k & \text{on } \partial E_k \text{ for } k = 1, \ldots, N, \\ \gamma \nabla p \cdot \hat{n} = 0 & \text{on } \partial \Omega_B, \end{cases} \tag{6.1.32}$$

*and* $(u, U) \in \overline{H}^1(\Omega)$ *solves (6.1.3).*

Proof. The weak form of equation (6.1.32) is given by

$$\int_\Omega \gamma \nabla p \cdot \nabla \psi \, \mathrm{d}x = \sum_{k=1}^{N} W_k \Psi_k \text{ for all } (\psi, \Psi) \in \overline{H}^1(\Omega). \tag{6.1.33}$$

Additionally, for any $\delta\gamma \in \mathcal{A}_0$, the weak form for $(v, V) := \mathrm{d}S_\gamma(Q)\,[\delta\gamma]$ is given by (6.1.30): namely,

$$\int_\Omega \gamma \nabla u \cdot \nabla v \, \mathrm{d}x = -\int_\Omega \delta\gamma \nabla u \cdot \nabla v \, \mathrm{d}x \text{ for all } (\psi, \Psi) \in \overline{H}^1(\Omega).$$

Setting $(\psi, \Psi) = (v, V)$ in (6.1.33) and $(\psi, \Psi) = (p, P)$ in (6.1.30), we establish the

$$\sum_{k=1}^{N} W_k V_k = -\int_\Omega \delta\gamma \nabla u \cdot \nabla p \, \mathrm{d}x \tag{6.1.34}$$

as required. □

**First variation of $J_1(\gamma)$.** We use the adjoint operator established above to express the first variation of $J_1(\gamma)$ with respect to $\delta\gamma \in \mathcal{A}_0$.

Corollary 1. *Suppose that* $\delta\gamma \in \mathcal{A}_0$ *and* $Q \in \mathbb{K}_\diamond^N$. *Then the first variation of* $J_1(\gamma)$ *in the direction* $\delta\gamma$ *is given by*

$$dJ(\gamma)[\delta\gamma] = \left\langle d\widetilde{S}_\gamma\,(Q)\,[\delta\gamma]\,, \widetilde{S}_\gamma\,(Q) - U \right\rangle_{\mathbb{K}_\diamond^N, \mathbb{K}_\diamond^N} \tag{6.1.35}$$

$$= -\sum_{i=1}^{M} \int_\Omega \delta\gamma \nabla u_i \cdot \nabla p_i \, dx \tag{6.1.36}$$

*with* $(p_i, P_i) \in \overline{H}^1(\Omega)$ *the weak solution of*

$$\int_\Omega \gamma \nabla p_i \cdot \nabla \psi \, dx = \sum_{k=1}^{N} \left( \widetilde{S}_{\gamma_0}(Q_i) - U_i \right)_k \Psi_k \text{ for all } (\psi, \Psi) \in \overline{H}^1(\Omega).$$

Proof. Recall the definition of $J_1(\gamma)$ to be

$$J_1(\gamma) = \frac{1}{2} \sum_{i=1}^{M} \left| \widetilde{S}_\gamma(Q_i) - U \right|^2.$$

Directly computing the first variation, we establish for any perturbation $\delta\gamma \in \mathcal{A}_0$

$$\mathrm{d}J_1(\gamma)[\delta\gamma] = \sum_{i=1}^{M} \left\langle \mathrm{d}\widetilde{S}_\gamma(Q_i)[\delta\gamma], \widetilde{S}_\gamma(Q_i) - U_i \right\rangle_{\mathbb{K}^N_\diamond, \mathbb{K}^N_\diamond} .$$

We look to write this in terms of the adjoint variable as in Theorem 13: let $(p_i, P_i) \in \overline{H}^1(\Omega; \mathbb{C})$ be the solution to

$$\begin{cases} -\operatorname{div}(\gamma \nabla p_i) = 0 & \text{in } \Omega, \\ |\partial E_k|^{-1} \displaystyle\int_{\partial E_k} \gamma \nabla p_i \cdot \hat{n} \, \mathrm{d}s = \left( \widetilde{S}_\gamma(Q_i) - U_i \right)_k & \text{on } \partial E_k \text{ for } k = 1, \dots, N, \\ p_i = (P_i)_k & \text{on } \partial E_k \text{ for } k = 1, \dots, N, \\ \gamma \nabla p_i \cdot \hat{n} = 0 & \text{on } \partial\Omega_B, \end{cases} \tag{6.1.37}$$

for each $i = 1, \dots, M$. Then, using Theorem 13, we write

$$\mathrm{d}J_1(\gamma)[\delta\gamma] = -\sum_{i=1}^{M} \int_\Omega \delta\gamma \nabla u_i \cdot \nabla p_i \, \mathrm{d}x \tag{6.1.38}$$

as required. □

**6.1.4. Minimisation of the functional $J_1(\gamma)$ using gradient descent.** The calculations above allow for the gradient-based minimisation of $J_1(\gamma)$ to be used. By iteratively computing $\{\gamma_n\}_{n=1}^{M_I}$, for some $M_I > 0$,

$$\gamma_{n+1} = \gamma_n - s\,\delta\gamma \text{ where } \delta\gamma = \sum_{i=1}^{M} \nabla u_i \cdot \nabla p_i \tag{6.1.39}$$

with $u_i$, $p_i$ are defined in (6.1.35) and $M$ being the number of measurements. This choice of update ensures that the functional $J_1(\gamma_{n+1}) \leq J_2(\gamma_n)$ for some $s > 0$. By

substituting this choice of $\delta\gamma$ into (6.1.38), we establish

$$\mathrm{d}J_1(\gamma)[\delta\gamma] = -\sum_{i=1}^{M} |\nabla u_i \cdot \nabla p_i|^2 < 0.$$

Therefore, if $J_1(\gamma)$ is $C^1$, for each $n = 1, \ldots, M_I$ there exists an $s_n > 0$ such that $J_1(\gamma_{n+1}) \leq J_1(\gamma_n)$. We note two difficulties with this approach: the first, as discussed in [101], is the insufficient regularity of each update $\delta\gamma$ in (6.1.39) for each gradient step. The second difficulty, as with all gradient descent algorithms, arises in a procedure to find an optimal $s > 0$. To address the first difficulty, we regularise the gradient step $\delta\gamma$ using the Sobolev gradient [101] and for the second, we adopt a step size rule based of Barzilai and Borwein [23]. We consider each of these problems in turn.

**Sobolev gradient of $\delta\gamma$.** In this thesis, we adopt the approach proposed in [101], where the update $\delta\gamma \in L^\infty(\Omega)$ is replaced by a regularised form

$$\widehat{\delta\gamma} := q|_{\Omega'}$$

$q \in H^1(\Omega)$ given as the solution to

$$\begin{cases} -\Delta q + kq = \delta\gamma & \text{in } \Omega, \\ \quad q = 0 & \text{on } \partial E_k \text{ for } k = 1, \ldots, N, \\ \quad q = 0 & \text{on } \partial\Omega_B, \end{cases} \tag{6.1.40}$$

for some $k > 0$. We remark that the restriction to $\Omega'$ ensures that $\widehat{\delta\gamma}|_{\partial\Omega} = 0$ and a solution to (6.1.40) exists by a similar argument as those presented in Chapter (3).

There is a significant and real risk that this approach would 'over-smooth' the update at each step. While this approach produces smooth reconstructions, any sharp edges or material features are unlikely to be accurately resolved. An investigation as to which would be the optimal PDE to solve to regularise the update while preserving the material boundaries is beyond the scope of this thesis.

**BB step size rule.** The difficulty of selecting an optimal choice of step size parameter $s > 0$ is common to all gradient based minimisation algorithms. The classical

'Steepest Descent' method, first proposed by Cauchy in 1847 [44], is to choose a fixed—but small—choice at each step. However, this is often computationally inefficient. Many alternatives have been proposed. Most common are variants of a line-search algorithm where selecting an optimal choice of $s$ is considered itself as a one dimensional minimisation problem. However, in our case a line search procedure is computationally expensive since many evaluations of the functional $J_1(\gamma)$ will be required.

Therefore, we consider an alternative method to estimate the parameter $s$ in a line search that doesn't require many evaluations of the functional $J_1$. In particular, we combine the gradient update from the previous step with the update from the current step to estimate the second derivative. This approach, developed by Barzilai and Borwein, can significantly accelerate the convergence [23] without a significant increase in computational cost, albeit with a small increase in computational memory. We shall refer to this choice of $s > 0$ as the BB step rule throughout this Chapter.

More explicitly, at each step we choose $s_n > 0$ to be

$$s_n = \arg\min_{s>0} \left\| (\gamma_n - \gamma_{n-1}) - s(d_n - d_{n-1}) \right\|^2 . \tag{6.1.41}$$

Where by definition we have $d_n = \delta\gamma_n - \delta\gamma_{n-1}$. A solution of the least squares problem can be found by differentiating (6.1.41) with respect to $s$. The optimal step size $s_n$ then satisfies

$$0 = (d_n - d_{n-1})^T \left[ \delta\gamma_n - s_n(d_n - d_{n-1}) \right],$$

namely,

$$s_n = \frac{(d_n - d_{n-1})^T \delta\gamma_n}{(d_n - d_{n-1})^T (d_n - d_{n-1})}. \tag{6.1.42}$$

Alternatively, the step size can be chosen to be the least squares solution to

$$s_n = \arg\min_{s>0} \left\| s\,(\gamma_n - \gamma_{n-1}) - (d_n - d_{n-1}) \right\|^2 . \tag{6.1.43}$$

The optimal step size in this case is then

$$s_n = \frac{(d_n - d_{n-1})^T (d_n - d_{n-1})}{(d_n - d_{n-1})^T \delta\gamma_n}. \tag{6.1.44}$$

The choice of step size between (6.1.42) and (6.1.44) is dependent on the conditioning of the problem: we have found that alternating between these choices performs well.

**6.1.5. Summary of the gradient-based minimisation procedure.** We summarise the implementation of the gradient descent method using pseudo-code below. This procedure uses as a termination condition that the value of the cost functional is reduced to $\alpha^{-1}$ of its original value. This condition is chosen for convenience and has performed well in the numerical testing presented in the subsequent section.

**Algorithm 8** Procedure to reconstruct $\gamma$ using an iterative gradient descent method.

**Require:** The input-measurement pairs $(Q_i, U_i)$ for each $i = 1, \ldots, M$.
**Require:** The background material parameter $\gamma_0$.
**Require:** Set the precision to be $\alpha = 0.01$ (say) and require a maximum number of iterations $M_I$.
1: **while** $J_1(\gamma_n) \geq \alpha J(\gamma_0)$ and $n < M_I$. **do**
2: Evaluate $\widetilde{S}_{\gamma_n}(Q_i) - U_i$ for $i = 1, \ldots, M$. Call this $W_i$.
3: Find the update $\delta\gamma$ by solving the adjoint problem (6.1.37).
4: Regularise the update $\delta\gamma$ by solving either (6.1.40).
5: Restrict the update to $\Omega'$.
6: Calculate the BB step size using either (6.1.42) or (6.1.44).
7: Compute new estimate, $\gamma_{n+1} = \gamma_n - s\widehat{\delta\gamma}$.
8: Increment $n$.
9: **end while**
10: Return estimate $\gamma_n$.

However, due to the lack of regularisation in the functional $J_1$, reconstructions produced using (8) can only expected to be accurate if the initial guess $\gamma_0$ is close to the true but unknown parameter. Improvements to the accuracy of the above method can be achieved by further regularising the functional $J_1$. For example, the addition of an $L^1$-sparcity term in the cost functional, namely

$$\widetilde{J}_1(\gamma) = J_1(\gamma) + \lambda \left\| \delta\gamma \right\|_{L^1(\Omega)},$$

has been shown to improve the accuracy in specific circumstances [101]. A further discussion is beyond the scope of this thesis and the optimal choice of regularisation remains an active area of research.

**6.1.6. Numerical comparison.** In this section we consider preliminary testing of the reconstruction algorithms discussed above on a single chosen test case shown in Figure 6.1.2a. We use a planar sensor with 10 equally spaced, identical electrodes with rounded corners. The measurement data is simulated by solving Model 2 for the basis functions $\left\{d_j^1\right\}_{j=2}^N$ on a very fine mesh. This mesh is also used to generate the sensitivity matrix used in the linearised reconstruction algorithm. In contrast, the reconstructions are conducted in a coarser mesh to prevent an inverse crime being committed.

Additionally, we have avoided tweaking the regularisation parameters in order to prevent reporting over-optimistic accuracy statistics: the linearised system of equations is regularised with a fixed Tikhonov parameter $\alpha = 0.1$ and each iteration of the gradient descent algorithm regularised by solving (6.1.40) with $k = 1.5$ and $k = 0.75$. Two regularisation parameters are chosen for the gradient descent algorithm to allow for comparison. We calculate the value of the cost functional $J_1$ and the relative $L^2$ error of $\gamma$ at each iteration step. The relative $L^2$ error is defined

$$\text{Relative } L^2 \text{ error } = 100\frac{\|\gamma_n - \gamma_{\text{true}}\|_{L^2(\Omega)}}{\|\gamma_{\text{true}}\|_{L^2(\Omega)}},$$

where $\gamma_n$ is the reconstructed parameter at iteration $n$ and $\gamma_{\text{true}}$ is the known parameter distribution.

The gradient-based algorithm is initialised with the parameter distribution equal to the background $\gamma_0$. While it is reasonable to use the output of the linearisation algorithm as the initial distribution, the results shown in Figure 6.1.1 demonstrates this does not increase the accuracy after a few iterations of gradient descent. We also observe slow convergence of the algorithm to the true parameter. We remark that the percentage $L^2$ error does not decrease uniformly, this is due to the step size parameter $s$ being chosen to ensure $J$ is reduced at each step.

These results show that it is possible to develop algorithms to reconstruct material parameters using a planar sensor geometry. The resulting reconstructions are shown in Figure 6.1.2 and Figure 6.1.3. While the quantitative measurements of the accuracy

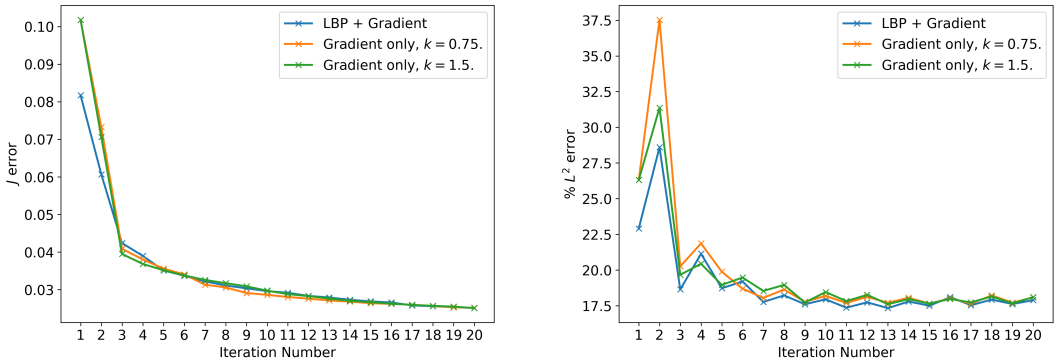



FIGURE 6.1.1. Convergence of the reconstruction as iteration number increase. Error measured using the function $J$ (left) and using the percentage $L^2$ error.

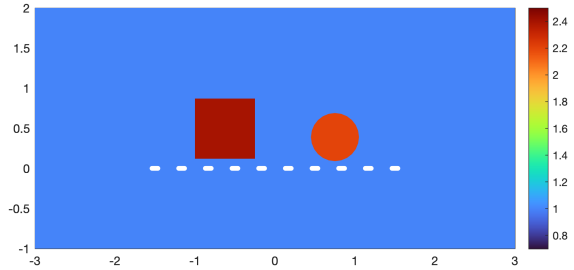
estimate the $L^2$ relative error in the region of 20% this is a positive first step. Although the accuracy statistics reported by other authors are better, these studies have used different sensor geometries than considered here. In light of the reconstructions presented in 6.1.2 and Figure 6.1.3, we observe that the reconstructions appear to be more accurate near the electrodes than far away. This is particularly relevant to this specific planar geometry as the sensing volume is not enclosed by the electrodes. We acknowledge that father testing is required to replicate these results in different test scenarios. Furthermore, the accuracy is likely to be improved after optimisation of the regularisation parameters.

## 6.2. Parameter reconstruction in the partial data case

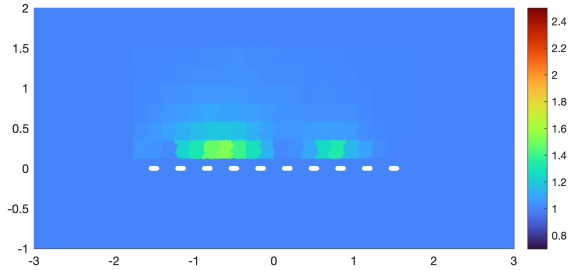
In this section we discuss the estimation of the missing data in the partial data problem arising from measurement paradigm 4 introduced in Chapter 5.3.4. Recall that in this case the measurements are given by

$$M_{ij} = \widetilde{S}_\gamma \left( d_j^i \right) \cdot d_j^i \tag{6.2.1}$$

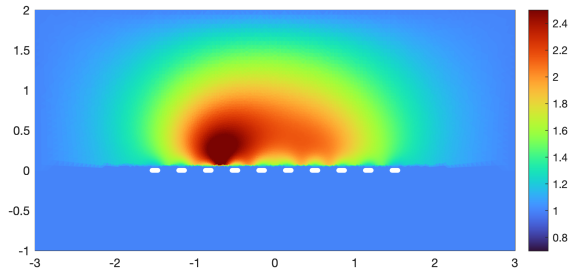
for $1 \leq i < j \leq N$ with $i$ and $j$ at most separated by $L$. We consider imposing additional constraints to allow for the missing entries, seen graphically in Figure 5.3.1b, to be determined from either assumptions on $\gamma$, or estimated using the measurements of a known parameter distribution $\gamma_0 \in \mathcal{A}$. We begin by considering the case when



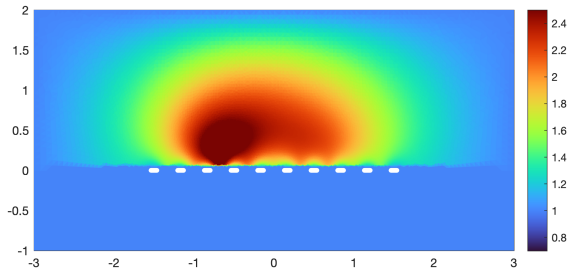
(A) True parameter distribution.



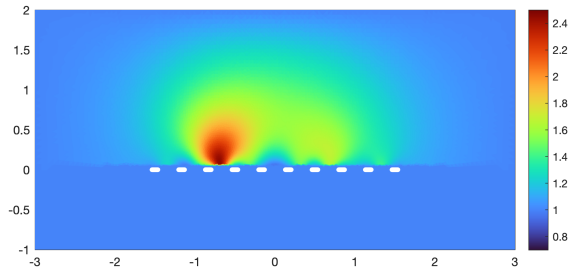
(B) Reconstruction using a single linearisation step. Tikhonov regularisation has been used with $\alpha = 0.1$.



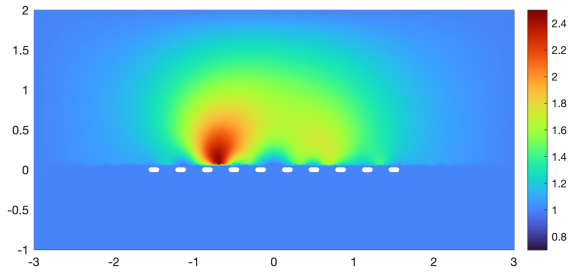
(C) First iteration of gradient descent with $k = 1.5$.



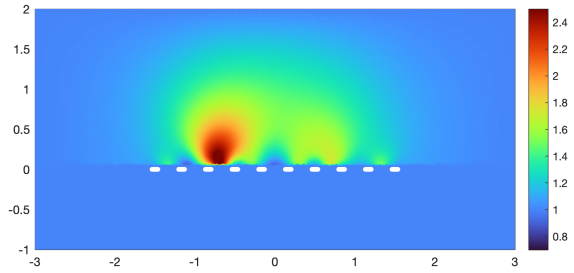
(D) First iteration of gradient descent with $k = 0.75$.



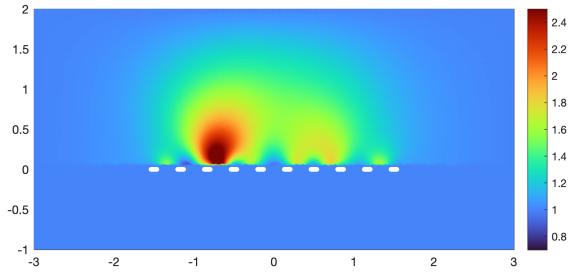
(E) Third iteration of gradient descent with $k = 1.5$.



(F) Third iteration of gradient descent with $k = 0.75$.



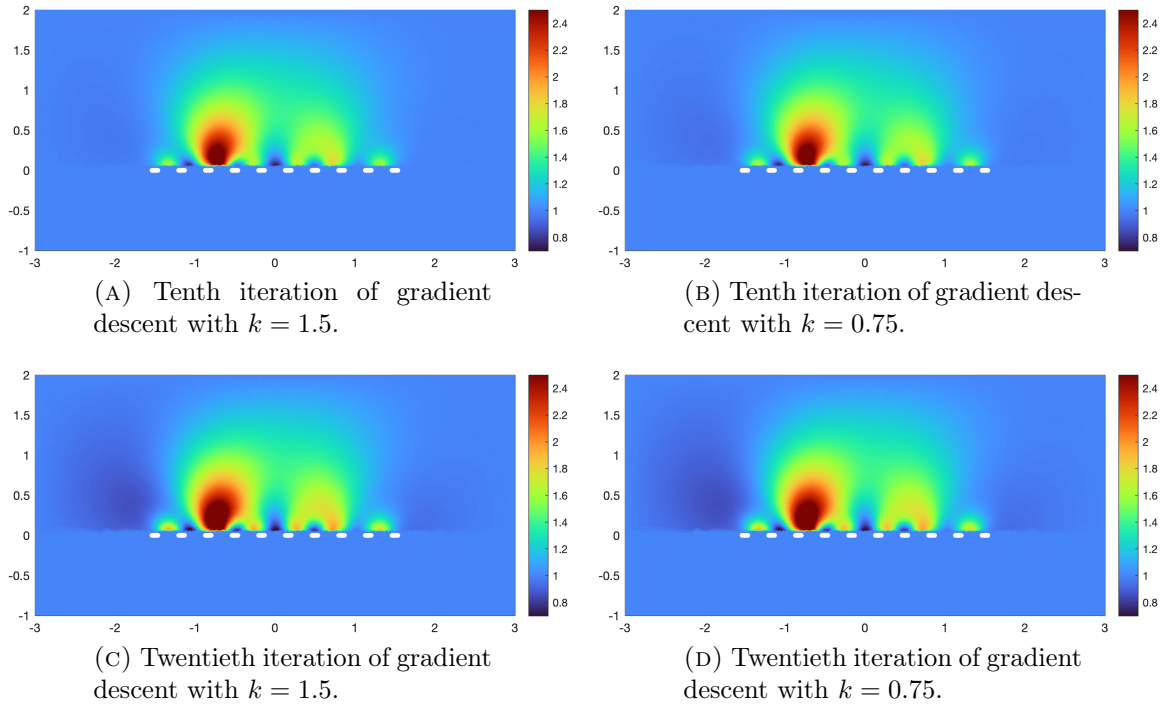
(G) Fifth iteration of gradient descent with $k = 1.5$.



(H) Fifth iteration of gradient descent with $k = 0.75$.

FIGURE 6.1.2. Comparison of reconstruction algorithms for an unknown parameter.

$\gamma \in \mathcal{A}$ is symmetric about the mid-line of the sensor before considering the case when the support of $\delta\gamma$ is small. We specialise to the case of planar sensor case throughout this section.



(A) Tenth iteration of gradient descent with $k = 1.5$.

(B) Tenth iteration of gradient descent with $k = 0.75$.

(C) Twentieth iteration of gradient descent with $k = 1.5$.

(D) Twentieth iteration of gradient descent with $k = 0.75$.

FIGURE 6.1.3. Comparison of reconstruction algorithms for an unknown parameter.

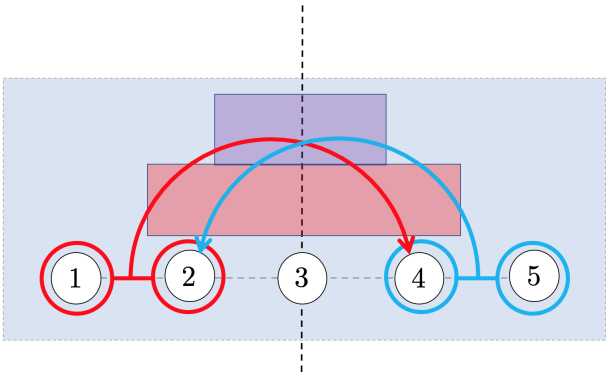



FIGURE 6.2.1. Example of two symmetric measurements: $\widetilde{S}_\gamma\left(d_2^1\right) \cdot e_4 = \widetilde{S}_\gamma\left(d_4^5\right) \cdot e_2$.

**6.2.1. The symmetric case.** Suppose that $\gamma \in \mathcal{A}$ is symmetric about the vertical mid-line of the sensor. In this case, to each measurement $\widetilde{S}(d_j^1) \cdot d_i^1$ for $i, j = 2, \ldots, N$ there is a corresponding measurement symmetric measurement. Graphically this can be seen in Figure 6.2.1 where the symmetry between two measurements are shown. This constraint has the effect of reducing the number of degrees of freedom in the full, but unknown, matrix $\left[\widetilde{S}_\gamma\right]$.

More precisely, if $\gamma$ is symmetric then

$$\widetilde{S}_\gamma\left(d^1_{j+1}\right)\cdot d^1_{i+1} = \widetilde{S}_\gamma\left(d^N_{N-j+1}\right)\cdot d^N_{N-i+1} \tag{6.2.2}$$

for $i,j = 2,\ldots,N$ with $i \neq j$. Written in terms of the $\left\{d^1_j\right\}_{j=2}^N$ basis, 6.2.2 becomes

$$\widetilde{S}_\gamma\left(d^1_{j+1}\right)\cdot d^1_{i+1} = \widetilde{S}_\gamma\left(d^1_{N-j+1} - d^1_N\right)\cdot\left(d^1_{N-i+1} - d^1_N\right)$$

for $i,j = 2,\ldots,N$ or equivalently,

$$\left[\widetilde{S}_\gamma\right]_{ij} = \left[\widetilde{S}_\gamma\right]_{N-j,N-i} - \left[\widetilde{S}_\gamma\right]_{N-i,N-1} - \left[\widetilde{S}_\gamma\right]_{N-1,N-j} + \left[\widetilde{S}_\gamma\right]_{N-1.N-1} \tag{6.2.3}$$

for $i,j = 1,\ldots,N-1$.

Each of these relationships are independent, however, when combined with the relationships given by (6.2.1), there are inherent dependencies which reduces the number of independent relationships available to determine $\left[\widetilde{S}_\gamma\right]$. We explore this numerically. The relationships described in Lemma 6.2.2 are combined with relationships that impose symmetry of the matrix $\left[\widetilde{S}_\gamma\right]$ and the rank of this matrix. When $L$ is chosen to be equal to $N$ the rank of this matrix is equal to $(N-1)^2$ recovering the previous result that in the full data case, $\left[\widetilde{S}_\gamma\right]$ can be determined by paradigm 3. However, when $L$ is chosen to be less than $N$ the matrix has a lower rank.

Similarly, we construct a matrix of constraints using (6.2.3) and calculate the rank of the constraints. We find that there are further redundancies in the constraints given by (6.2.3). Finally, we combine the constraint matrix with the measurement matrix and consider the rank of this combined matrix. The results are shown in Figure 6.2.2 for $L = 5$ and $L = 7$. In both cases it is clear that the rank of the combined matrix is less than $(N-1)^2$, the target rank, and hence the inclusion of the additional symmetry constraints are insufficient to enable $[\widetilde{S}_\gamma]$ to be estimated from measurements alone.

To summarise, we have established that despite being intuitive and reasonable, assuming only that the parameter $\gamma \in \mathcal{A}$ is symmetric is insufficient to recover the full-data problem from the partial-data problem.

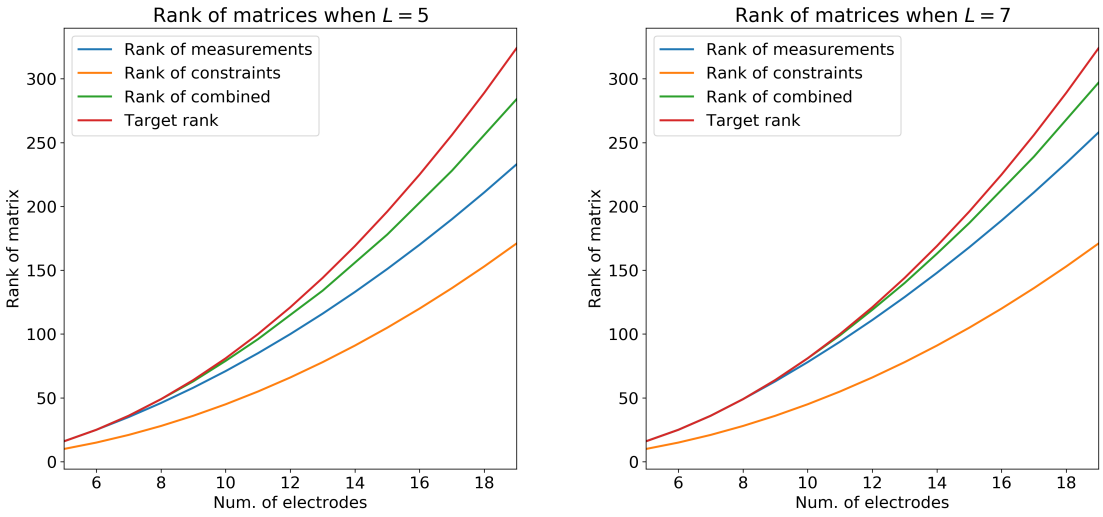



FIGURE 6.2.2. The rank of the between the linear systems of equation resulting from the measurements, the constraints, and the combined matrix for $L = 5$ and $L = 7$.

**6.2.2. Using background measurements.** We now suppose the parameter $\gamma \in \mathcal{A}$ can be decomposed as

$$\gamma = \gamma_0 + \delta\gamma$$

for some $\delta\gamma \in \mathcal{A}_0$ and a known $\gamma_0 \in \mathcal{A}$, provided that the support of $\delta\gamma$ is small. In this case we describe an alternative where the full-data measurements of $\gamma_0$ are used to estimate the missing entries in $\gamma$. The rationale being that away from the perturbation $\delta\gamma$, the electric potential field $u(\gamma)$ can be reasonably approximated by $u(\gamma_0)$.

**Estimation by extension.** The simplest approach is to estimate the missing elements, $M_{ij}$ where $j > i + L$, by setting them equal to $M_{i,i+L}$. This is unlikely to give an accurate estimation and will certainly over estimate the electric potential away from the source. However, this method has the advantage of not require the measurement, or solution of the forward problem, for the background $\gamma_0$.

**Splicing measurements.** Alternatively, if the full measurement data corresponding to the background $\gamma_0$ is known, then one could set the missing entries equal to the background:

$$M_{ij} := \widetilde{S}_{\gamma_0}\left(d^i_j\right) \cdot d^i_j$$

when $|j-i| > L$ or in the notation introduced previously, $d(i,j) > 1$. This corresponds to the setting the upper triangle and lower triangular components of the measurement matrix equal to the background: these are indicated by the blue regions in Figure 5.3.1b. While this is very convenient, it is likely to reduce the sensitivity of the measurements and may introduce sudden changes in the decay of the measurements. It is likely that these would estimate introduce artefacts into any resulting reconstructions. However, if it can be justified that the missing entries are far from the support of $\delta\gamma$ then this is a reasonable approach to adopt.

**Constraining the decay.** In order to prevent sudden changes in the measurements being introduced using the above method, we consider an alternative. Rather than directly splicing the background measurements into $M_{ij}$, we propose to constrain the missing values to decay at the same rate as the background measurements. The rationale being that since the electric potential decays away from the source $d_j^i$ the measurements would be expected to decay to zero also. It is reasonable, as a first approximation, to assume the same decay electric potential associated to $\gamma_0$.

Define

$$\alpha_0(i,j) := \frac{\widetilde{S}_{\gamma_0}\left(d_{j+1}^i\right) \cdot d_{j+1}^i}{\widetilde{S}_{\gamma_0}\left(d_j^i\right) \cdot d_j^i},$$

and

$$\alpha_\gamma(i,j) := \frac{M_{ij+1}}{M_{i,j}}$$

for each $i,j = 1,\ldots,N$ with $i \neq j$. We then look to impose

$$\alpha_\gamma\left(d_j^i\right) = \alpha_0\left(d_j^i\right) \tag{6.2.4}$$

when $i = 1,\ldots,N-L$ and when $j = i+L,\ldots,N$. In other words, we estimate the missing entries of $M_{ij}$ inductively. For example, beginning with $M_{i,i+L}$, which is known, we estimate $M_{i,i+L+1}$ according to the formula

$$M_{i,i+L+1} = \alpha_0(i,j) M_{i,i+L}.$$

More generally, we use

$$M_{i,i+L+j} = \alpha_0(i,j) M_{i,i+L+j-1}$$

for $j = 1, \ldots, N - i - L$ to estimate the missing data.

We remark that both of the last two approaches require knowledge and access to the full data corresponding to the background $\gamma_0$. In a simulation environment this data is readily accessible, however, in practice this data unlikely to be measure-able. In this case, it would be necessary to use a model of the electric field to estimate the measurements corresponding to $\gamma_0$. This would introduce a systematic error, originating from the model error, into the estimation of $\left[\widetilde{S}_\gamma\right]$. This error would likely be visible as artefacts in the subsequent parameter reconstruction.

**6.2.3. Numerical comparison.** We compare the error made when estimating the missing entries of $\left[\widetilde{S}_\gamma\right]$ using each of the procedures discussed above. We include, as a comparison, the case where the missing entries are simply set to zero. It is reasonable that for accurate reconstructions to eventually be obtained, the missing data must be estimated in such a way to minimise the error encoded into the measurement matrix. We measure this error by calculating the $L^2$ norm between the estimated measurement matrix, denoted $M_{ij}$, to the full data matrix denoted $M_{ij}^{\text{true}}$ (collected using measurement paradigm 3). Namely, we calculate

$$\xi := \sqrt{\sum_{i=1}^{N} \sum_{j=1, j\neq i}^{N} \left| M_{ij} - M_{ij}^{\text{true}} \right|^2}.$$

For the purposes of exposition, we choose $\gamma := 1 + \delta\gamma$ where

$$\delta\gamma = \begin{cases} 1 & \text{in } \mathcal{O} \\ 0 & \text{in } \Omega \setminus \mathcal{O} \end{cases}$$

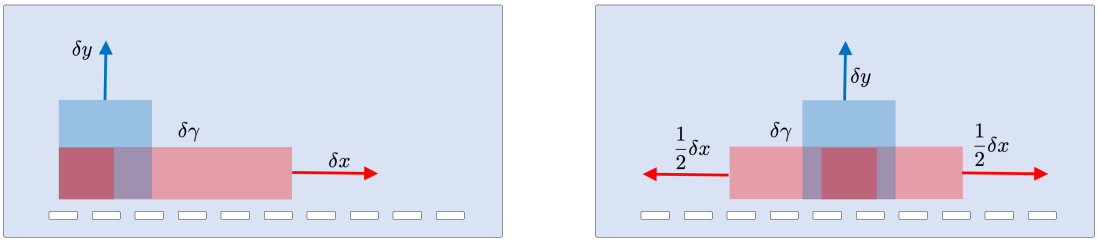
and $\mathcal{O} \subset \Omega'$ is chosen to be a square of side length 0.5 located to the left of the domain as in Figure 6.2.3a or to the centre as in Figure 6.2.3b.The numerically estimated values of $\xi$ are reported in Table 1.

| Location of $\delta\gamma$ | $L$ | Setting missing entries to zero | Extend by the last measurement | Splicing in background measurements | Fitting the decay |
|---|---|---|---|---|---|
| Left | 8 | 1.17 | 0.071 | 0.0324 | 0.0227 |
| Left | 7 | 1.95 | 0.172 | 0.0534 | 0.0369 |
| Left | 6 | 2.65 | 0.328 | 0.0684 | 0.0483 |
| Left | 5 | 3.27 | 0.552 | 0.0804 | 0.0588 |
| Centre | 8 | 1.19 | 0.0748 | 0.0145 | 0.00682 |
| Centre | 7 | 1.98 | 0.189 | 0.0264 | 0.0198 |
| Centre | 6 | 2.67 | 0.364 | 0.0398 | 0.0521 |
| Centre | 5 | 3.28 | 0.614 | 0.0573 | 0.0582 |

TABLE 1. The $L^2$ mismatch error between the estimated matrix $M_{ij}$ and the full matrix $M_{ij}^{\text{true}}$ for each of the estimation methods discussed.

Considering Table 1 it is immediate that as $L$ increases, the difference between $M_{ij}$ and $M_{ij}^{\text{true}}$ decreases, or in other words, $M_{ij}$ becomes a better approximation to $M_{ij}^{\text{true}}$. This is to be expected as a larger $L$ results in fewer missing entries to be estimated. In all cases, we observe that estimating the missing entries by fitting the decay of the background field introduces the smallest error. It is curious to observe that the location of the perturbation also has an effect on the accuracy: the perturbation being in the centre of the sensor produces a matrix $M_{ij}$ that more closely resembles $M_{ij}^{\text{true}}$ than when the perturbation is on the left of the sensor.

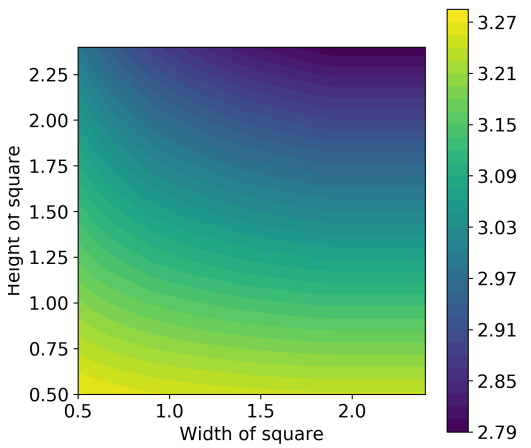
We explore numerically the dependence of the error $\xi$ on the support of $\delta\gamma$. In particular, we conduct a grid search where the support of $\delta\gamma$ is increased both parallel to the electrodes and perpendicular. We again initialise the perturbation with a square of side length 0.5 positioned either on the left of the sensor or in the centre. The width and height of the square is increased, producing in a rectangular perturbation $\delta\gamma$ of difference sizes: a graphical illustration of this process is shown in Figure 6.2.3a and Figure 6.2.3b. This experiment parameterises the error $\xi$ as a function of the width and the height of the perturbation. The results are shown as two-dimensional plots in Figure 6.2.4 and Figure 6.2.5 for each of the procedures used to estimate the missing data.



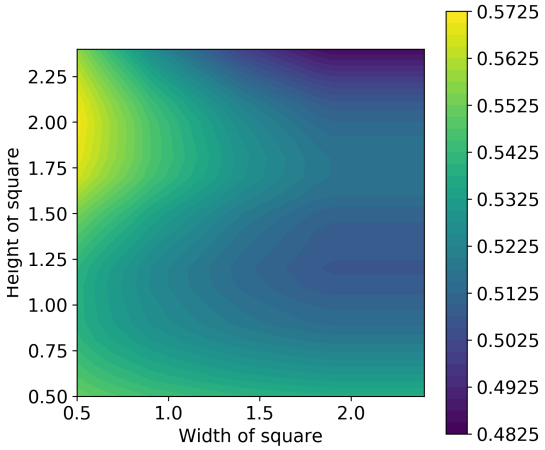

(A) Placement on the left. (B) Placement at the centre.

FIGURE 6.2.3. Diagram showing the position of the perturbation $\delta\gamma$ in each case. The arrows illustrate the stretch of the rectangle in the grid search to estimate the dependence of the estimation accuracy on the support of $\delta\gamma$.

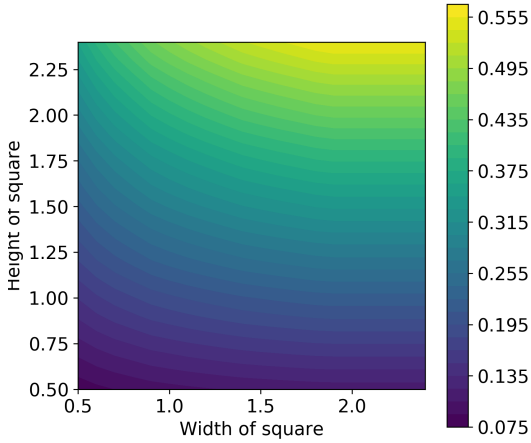
The results of this numerical experiment are intriguing: there is a clear dependence on the support of $\delta\gamma$ on the accuracy of the estimated matrix $M_{ij}$. Furthermore, the plots are not symmetric indicating that the error is dependence is not symmetric in the $x$ and $y$ directions. Therefore, the location, shape, and orientation of the parameter distribution will affect the optimal choice of procedure to estimate the missing components. However, this information is not available a priori and hence a universal procedure to estimate the missing data is not possible to develop.



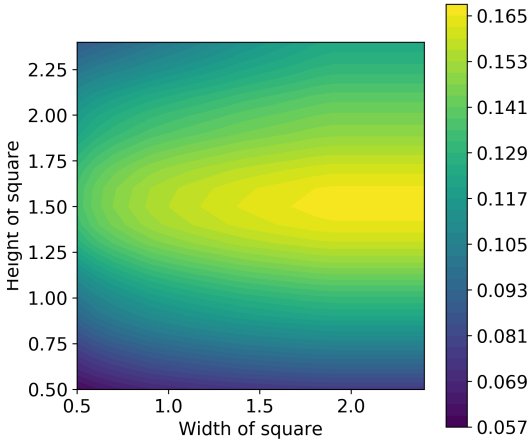

(A) Setting missing values equal to zero.




(B) Extending by a fixed value.

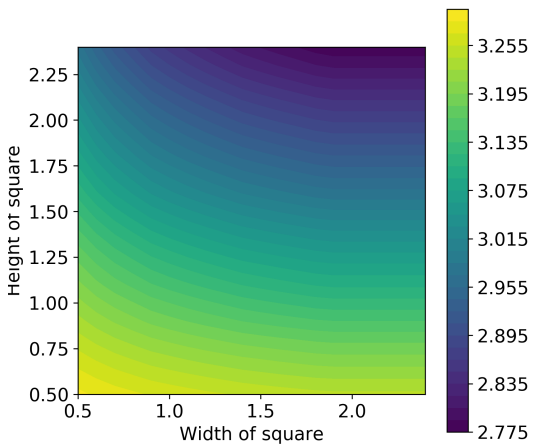



(C) Splicing in the values of the background.

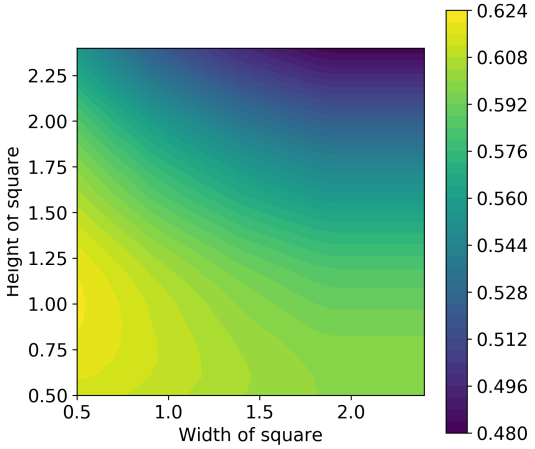



(D) Fitting the missing values using the decay estimates.

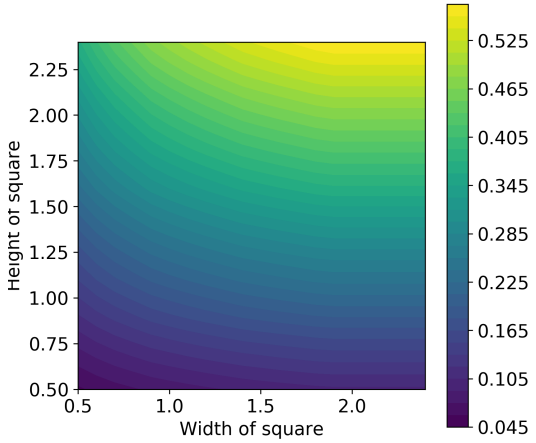
FIGURE 6.2.4. The $L^2$ error between the estimated $\left[\widetilde{S}_\gamma\right]$ using the partial data and each of the methods described previously. The width and height correspond to the rectangle positioned at the left hand side as in Figure 6.2.3a.



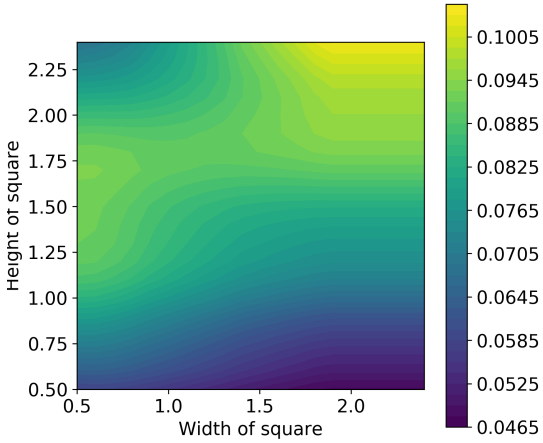

(A) Setting missing values equal to zero.




(B) Extending by a fixed value.




(C) Splicing in the values of the background.




(D) Fitting the missing values using the decay estimates.

FIGURE 6.2.5. The $L^2$ error between the estimated $\left[\widetilde{S}_\gamma\right]$ using the partial data and each of the methods described previously. The width and height correspond to the rectangle positioned in the middle of the sensor as in Figure 6.2.3b.

CHAPTER 7

# Conclusion and next steps

In the first three chapters of this thesis we have derived five models from Maxwell's equations to describe the electric field in the sensing volume of an EFS device: Model 1 and Model 2 are stated in the frequency domain, and Model 3, Model 4, and Model 5 describe the evolution of the electric field in time. Despite the differences, all of the models share commonalities. Firstly, each of the five models adopts the quasi-static assumption. We have investigated the validity of this assumption analytically and presented an original argument to justify its use in Lemma 2. Secondly, in each model the electrodes are described by boundary conditions of the PDE. We advocate this approach and demonstrate that boundary conditions can be chosen to model the physical properties of the electrodes and operation of the sensor. If voltage signals are used as sensor inputs then this can be modelled using spatially constant Dirichlet boundary conditions (as in Model 1 and Model 3), whereas injecting current into the electrodes requires a weakened form of Neumann-type boundary conditions—the so-called shunt boundary conditions adopted in Model 2 and Model 4. The development of the time-dependent approach is the first significant novelty of this thesis. We establish existence and uniqueness of a solution in this case in Theorem 7.

The fifth model considered in this thesis couples a model of the measurement circuit to a PDE model of the electric field withng shunt boundary conditions. Beginning from the observation that the electric circuit used in the measurement of the electric field affects the electric field inside the domain, particularly in the case of time-dependent measurements, we have developed a coupled PDE and ODE model to describe this interaction. We have proven an existence and uniqueness result for this model (see Theorem 10) using a fixed point argument.

In Chapter 4, we have described and implemented numerical procedures to solve each of the five models using the Finite Element Method. We then discussed the

estimation of model hyper-parameters using simulated sensor measurements in both the full data and partial cases. We also explored the agreement between the simulated data and real sensor data supplied by Zedsen Ltd. This study has had mixed results: while the simulated and real measurements show qualitative similarities, further work needs to be done to establish quantitative accuracy of the model. To the best of the author's knowledge, this is the first such comparison between a time-dependent model and the time-dependent measurements taken by Zedsen's sensors.

In Chapter 5, we present a unified approach to the inverse problem associated with each of the five models. We explicitly discuss four measurement paradigms used by EFS sensors. We prove constructively the equivalence of the first three measurement paradigms. In each case, a procedure is devised to estimate the discretised DtN operator $\widetilde{\Lambda}_\gamma$ or its (discretised) inverse $\widetilde{S}_\gamma$. However, measurements in the form of measurement paradigm four are insufficient to estimate the operator $\widetilde{S}_\gamma$.

We describe and test reconstruction algorithms for the material parameters in Chapter 6. We consider two numerical algorithms, the first solves by least squares the linearised problem and the second is a gradient-based minimisation algorithm. We have demonstrated that, while the latter provides greater reconstructive accuracy there is a significant computational cost over the former. In particular, these algorithms can be directly applied to simulated or real sensor data is in the form of measurement paradigm 1, 2, or 3.

Finally, we described, implemented, and compared algorithms that can be used to estimate the missing data in measurement paradigm 4. We have demonstrated that when the perturbation of $\gamma$ from a background $\gamma_0$ has small support, the measurements can be reasonably approximated by the electric potential of the background. We quantify the error committed by this estimation, although quantifying the effect of this error on parameter reconstruction is a topic of further research.

## 7.1. Next steps

We conclude this thesis with a few speculative remarks. The tantalising benefits proffered by EFS technologies means that interest and development of sensors will

continue. From the author's perspective, it is expected that significant developments will be made in the field of medical diagnostics as sensors are developed with particular applications in mind. Many devices are currently only prototypes, but as an understanding of the technology improves, the sensors can be developed to increase the sensitivity and specificity of the measurements. We discuss briefly how the approach proposed in this thesis could be used to optimise the sensitivity of the measurements and the specificity of the measurements to a particular material, or more specifically, blood parameters.

A significant limitation of the use of EFS for medical applications is the difficulty of ensuring that the electric field penetrates sufficiently far into the domain. The region of the sensing volume penetrated by the electric field is primarily determined by the configuration and shape of the electrodes. Recently measurements of the electric field, generated by electrodes to mimic the vasculature of the wrist, has been able to measure blood glucose concentration [85]. Using the model developed in this work we propose an alternative: by noticing that the shape of the electric field is changed by the parameters $\{(C_k, R_k)\}_{k=1}^{N}$, it is possible to optimise the choice of parameters to increase sensitivity at a specific region in the sensing volume. If hardware is developed that allows for the capacitor and resistor connected to the electrodes to be controlled in real-time, then the region of the sensing volume being scanned could be dynamically controlled. This could potentially increase the resolution of EFS devices and unlock further applications.

It as an interesting, and highly applicable, question to consider the optimal choice of frequencies for sampling a particular mixture of materials. For example, the relative concentrations of constituent materials in complex mixtures can be distinguished by sampling at specific frequencies. This has been empirically observed in [107] where blood plasma with different blood glucose concentrations at different concentrations is tested. It is shown that dependence of the permittivity and conductivity on the glucose concentrations is greater at higher frequencies ($\approx$ 20GHz) than at lower frequencies ($\approx$ 1GHz). While this is an ex-vivo study comparing glucose concentrations 40 times greater than physiological range, it demonstrates the importance of selecting

appropriate frequencies for an application. Developing reconstruction algorithms that make optimal use of multi-frequency data to estimate many material parameters (more than 3) concurrently would be a significant step forward.

Similar optimisation problems arise in the time-dependent case. In particular, the optimal choice of input signals $\phi_1, \ldots, \phi_N \in C([0,T])$, which is the analogue of the frequency selection, is critical. Furthermore, the optimal reconstruction of material parameters from multiple time-dependent input signals is an interesting avenue for further research. While the extraction of parameters from multi-frequency data has been considered in the literature, and the advantages of a spectroscopic approach reported, it remains an open question whether the same can be achieved with time-dependent measurements. Time-dependent measurements offer advantages of spectroscopic measurements due to the higher rate of data acquisition and the ability to sample multiple frequencies simultaneously. Furthermore, it is an open problem if the addition of transient data improves the conditioning of the inverse problem [57]. We hope that the work contained in this thesis, and the forthcoming publications, demonstrates that time dependent measurements, while not a panacea, can be used to determine material parameters and unlock the benefits of EFS technologies for new applications.

# Appendices

## A. Code to define geometry and mesh

FreeFem++ code to define the planar geometry with 10 electrodes.

```
1
2  verbosity = 0;
3
4  real R = 1.5; // Radius of the computational domain
5  real r = 0.015;// Radius of the electrodes
6
7  int NE = 10;// Number of electrodes
8  real sl = 2*R-1; // Total length of sensor: I.e. allow 0.5 at each end of the
       ↪  sensor.
9  real gapelecratio = 1.0; //Ratio of the gap length and the electrode length.
10 real El = sl/(NE-1+(NE-1)*gapelecratio); //Length of the rectangular part of
       ↪ each electrode
11
12 real Mt = r/2; //membrane thickness
13
14 // Define the location of the center of each electrode.
15 real[int] xloc(NE);
16 for(int i=0; i<NE; i++){
17   xloc[i] = -R+0.5*(2*R-sl)+i*El+i*gapelecratio*El;
18 }
19
20 // Define the boundary of the electrodes
21 macro electrode(x0, El, strA, strB, strC, strD, i)
22 border strA(t=-El/2+r, El/2-r){x = x0+t; y = r; label = i-1;};
23 border strB(t=-El/2+r, El/2-r){x = x0+t; y = -r; label = i-1;};
24 border strC(t=-pi/2, pi/2){x = x0-El/2+r-r*cos(-t); y = r*sin(t); label = i
       ↪ -1;};
25 border strD(t=-pi/2, pi/2){x = x0+El/2-r+r*cos(t); y = r*sin(t); label = i
       ↪ -1;};
26 //
27
28 electrode(xloc[0], El, E11,E12,E13,E14, 1);
29 electrode(xloc[1], El, E21,E22,E23,E24, 2);
30 electrode(xloc[2], El, E31,E32,E33,E34, 3);
31 electrode(xloc[3], El, E41,E42,E43,E44, 4);
32 electrode(xloc[4], El, E51,E52,E53,E54, 5);
```

```
33  electrode(xloc[5], El, E61,E62,E63,E64, 6);
34  electrode(xloc[6], El, E71,E72,E73,E74, 7);
35  electrode(xloc[7], El, E81,E82,E83,E84, 8);
36  electrode(xloc[8], El, E91,E92,E93,E94, 9);
37  electrode(xloc[9], El, E101,E102,E103,E104, 10);
38
39  // Computational domain
40  border bottom(t=-1.5*R, 1.5*R){x = t; y=-R/2; label = 100;};
41  border top(t=-1.5*R, 1.5*R){x = t; y = R; label = 100;};
42  border left(t=-R/2, R){x = -1.5*R; y=t; label = 100;};
43  border right(t=-R/2, R){x = 1.5*R; y=t; label = 100;};
44
45  // boundary of the membrane
46  border membrane1(t=-R+0.25, R-0.25){x = t; y=-r-Mt; label = 100;};
47  border membrane2(t=-R+0.25, R-0.25){x = t; y=+r+Mt; label = 100;};
48  border membrane3(t=-r-Mt, r+Mt){x = R-0.25; y=t; label = 100;};
49  border membrane4(t=-r-Mt, r+Mt){x = -R+0.25; y=t; label = 100;};
50
51  /*
52  Define the mesh.
53
54  MM is the mesh resolution parameter.
55  MM = number of nodes on the straight part of the electrodes.
56
57  */
58
59  int MM = 8; // Mesh res. param.; num. of nodes on straight part of the elecs.
60
61  macro elecMesh(E11, E12, E13, E14)
62  E11(MM)+E12(-MM)+E13(MM*(pi*r)/(El-2*r))+E14(-MM*(pi*r)/(El-2*r))
63  //
64
65  mesh Th = buildmesh(
66  bottom(10*MM)+top(-0.5*10*MM)+left(-0.75*10*MM)+right(0.75*10*MM)
67  +elecMesh(E11, E12, E13, E14)
68  +elecMesh(E21, E22, E23, E24)
69  +elecMesh(E31, E32, E33, E34)
70  +elecMesh(E41, E42, E43, E44)
71  +elecMesh(E51, E52, E53, E54)
72  +elecMesh(E61, E62, E63, E64)
73  +elecMesh(E71, E72, E73, E74)
74  +elecMesh(E81, E82, E83, E84)
75  +elecMesh(E91, E92, E93, E94)
76  +elecMesh(E101, E102, E103, E104)
77  );
```

## B. Code for the solution of Model 1 and Model 2

FreeFem++ code to solve the Dirichlet problem and measure the average flux on each electrode. The shunt model. Requires the code from Appendix A.

```
//Define H^(1/2) indicator functions of the electrodes
Vh1[int] phi(NE);
for(int i=0; i<NE; i++){
  solve laplace(uu, vv)=int2d(Th)(grad(uu)'*grad(vv))+on(0,1,2,3,4,5,6,7,8,9,
      ↪ uu=0)+on(i, uu=1);
  phi[i][] = uu[];
}

macro BCform(i, Th)
varf BC#i(uu, vv) = on(i, uu = 1.0);
varf L#i(uu, vv) = int1d(Th, i)(ielecPerim*gamma*grad(vv)'*[N.x,N.y]);

real[int] b#i = BC#i(0, Vh1);
real[int] l#i = L#i(0, Vh1);
//

func real[int] solveDiri(real[int] &U, real[int] &F){

  varf a2(uu, vv) = int2d(Th)(gamma*grad(uu)'*grad(vv))
                  +on(0,1,2,3,4,5,6,7,8,9,uu = 1.0);

  BCform(0, Th)
  BCform(1, Th)
  BCform(2, Th)
  BCform(3, Th)
  BCform(4, Th)
  BCform(5, Th)
  BCform(6, Th)
  BCform(7, Th)
  BCform(8, Th)
  BCform(9, Th)

  matrix A2 = a2(Vh1, Vh1);
  matrix B = [[b0,b1,b2,b3,b4,b5,b6,b7,b8,b9]];

  //Solve for u
  real[int] b = B*U;
  b += F;
  uu[] = A2^-1*b;

  //Measure flux using 2D integral.

  real[int] Q2(NE); Q2 = 0.0;
  for(int i=0; i<NE; i++){
```

```
    Q2[i] = -int2d(Th)(gamma*grad(uu)'*grad(phi[i]))*ielecPerim;
  };

  real[int] Output = [uu[], Q2];
  return Output;

}


// Shunt solver
func real[int] solveShunt(real[int] &Q, real[int] &F){

  varf a2(uu, vv) = int2d(Th)(gamma*grad(uu)'*grad(vv))
                  +on(0,1,2,3,4,5,6,7,8,9,uu = 1.0);

  BCform(0, Th)
  BCform(1, Th)
  BCform(2, Th)
  BCform(3, Th)
  BCform(4, Th)
  BCform(5, Th)
  BCform(6, Th)
  BCform(7, Th)
  BCform(8, Th)
  BCform(9, Th)

matrix A2 = a2(Vh1, Vh1);
matrix B = [[b0,b1,b2,b3,b4,b5,b6,b7,b8,b9]];

//Integral constraints to impose average flux
matrix L = [[l0,l1,l2,l3,l4,l5,l6,l7,l8]];
// Constaint \sum U_k=0

real[int] onevec(NE); onevec = 1;
matrix ones = [[onevec']];

//Form system
matrix AA = [[A2, B],[L',0], [0, ones]];
set(AA, solver = UMFPACK);

//Define the RHS of the system, Q is N-1 vector, F is vector of source term
Vh1 uu = 0.0;
real[int] bvec(Vh1.ndof); bvec = F;
real[int] bb = [bvec, Q(0:NE-2), 0];

// Solve the system and extract the solution (uu, U)
real[int] U(NE); U = 0.0;
real[int] sol = AA^-1*bb;
[uu[], U] = sol;
```

```
return sol;
};
```

## C. Code for the solution of Model 3 and Model 4

FreeFem++ code to solve the shunt model using the time-stepping procedure described in Algorithm 4. Requires the code from Appendix A and Appendix B.

```
func real[int] TPulse(real[int] &t, real s){
  real[int] out(t.n); out = 0.0;
  for(int i=0; i<t.n; i++){out[i] = sin(s*t[i]*2*pi); }
    return out;
}


func real[int, int] solveTimeProblemShunt(real[int] &V, real[int] &TPulse){

  real[int] U(NE);
  Vh1 uold; uold = 0.0;
  real[int] Q(NE);
  int size = NE+Vh1.ndof;
  real[int,int] output(TPulse.n, size);

  for(int i=1; i<Nt; i++){
    for(int k=0; k<NE; k++){ Q[k] = V[k]*TPulse[i];}
    real[int] F = F2*uold[];
    [uold[], U] = solveShunt(Q, F);
    real[int] sol = [uold[], U];
    output(i,:) = sol;
  }
  return output;
}
```

## D. Code for the solution of Model 5

FreeFem++ code to solve the coupled ODE and PDE model. Requires the definition of the geometry from Appendix A. In this case, a Dirichlet condition is imposed on electrode 1 and shunt conditions are imposed o the remaining electrodes.

```

func real[int] ODEsolver(real[int] &F, real[int] &Q, real ht, real[int] &zk1,
    ↪ real[int] &zk2){
  /*

  Code to solve the ODE for a single time step.

  */
```

```
  real[int,int] A(NE, NE); A = 0.0;
  real[int] RHS(NE); RHS = 0.0;
  for(int i=0; i<NE; i++){A(i,i) = 1.0/(zk1[i]+ht*zk2[i]);}
  for(int i=0; i<NE; i++){Q[i] = zk1[i]*Q[i];}
  real[int] tmp = ht*F+Q;
  real[int] Qnew = A*tmp;
  return Qnew;
}

func real[int] solveShuntNew(real[int] &Q, real[int] &F, int trans, real BC){
  /*

  Solve the forward model with Shunt condition on electrodes 2,..,10.
  And Dirichlet on 1.

  */

  matrix L = [[ l1,l2, l3,l4,l5,l6,l7,l8,l9]];
  matrix B = [[b1,b2,b3,b4,b5,b6,b7,b8,b9]];
  real[int] flagvec(NE); flagvec = 0.0; flagvec[trans] = 1;
  matrix AA = [[A2, B],[L',0]];
  set(AA, solver = UMFPACK);
  real[int] bvec = F-b0*BC;
  real[int] bb = [bvec, Q(1:NE-1)];

  real[int] sol = AA^-1*bb;

  return sol;
};


real[int] tpulsevec = TPulse(tvec, s);
Umat = 0.0;
uu = 0.0;
for(int i=1; i<Nt; i++){
  U[0] = tpulsevec[i];
  real[int] F = F2*uu[];
  Q = ODEsolver(U, Q, ht, z1est, z2est);
  [uu[], U(1:NE-1)] = solveShuntNew(Q, F, 0, U[0]);
  uu = -uu;
  Umat(i,:) = U;
}
```

# Bibliography


[1] A. Adler, R. Gaburro, and W. Lionheart. *Electrical Impedance Tomography*, pages 701–762. Springer New York, New York, NY, 2015.

[2] A. Adler and W. R. Lionheart. Uses and abuses of eidors: an extensible software base for eit. *Physiological measurement*, 27(5):S25, 2006.

[3] E. Al Hosani. *Electrical Capacitance Tomography for Real-Time Monitoring of Process Pipelines*. PhD thesis, University of Bath, 2016.

[4] G. S. Alberti. *On Local Constraints and Regularity of PDE in Electromagnetics. Applications to Hybrid Imaging Inverse Problems*. PhD thesis, Oxford University, 2014.

[5] G. S. Alberti and Y. Capdeboscq. *Lectures on Elliptic Methods for Hybrid Inverse Problems*, volume 25 of *Cours Spécialisés*. Société Mathématique de France, Paris, 2018.

[6] G. Alessandrini. Stable determination of conductivity by boundary measurements. *Applicable Analysis*, 27(1-3):153–172, 1988.

[7] G. Alessandrini and S. Vessella. Lipschitz stability for the inverse conductivity problem. *Advances in Applied Mathematics*, 35(2):207–241, Aug. 2005.

[8] K. Alme and S. Mylvaganam. Electrical capacitance tomography—sensor models, design, simulations, and experimental verification. *IEEE Sensors Journal*, 6(5):1256–1266, 2006.

[9] H. Ammari. *An Introduction to Mathematics of Emerging Biomedical Imaging*, volume 62 of *Mathématiques & Applications*. Springer, 2008.

[10] H. Ammari and K. Hamdache. Global existence and regularity of solutions to a system of nonlinear Maxwell equations. *Journal of Mathematical Analysis and Applications*, 286(1):51–63, 2003.

[11] C. Amrouche and N. E. H. Seloula. L$^p$-theory for vector potentials and Sobolev's inequalities for vector fields: Application to the Stokes equations with pressure boundary conditions. *Mathematical Models and Methods in Applied Sciences*, 23(1):37–92, 2013.

[12] M. Assenheimer, O. Laver-Moskovitz, D. Malonek, D. Manor, U. Nahaliel, R. Nitzan, and A. Saad. The T-SCANT technology: Electrical impedance as a diagnostic tool for breast cancer detection. *Physiological Measurement*, 22(1):1–8, 2001.

[13] K. Astala and L. Päivärinta. Calderón's inverse conductivity problem in the plane. *Annals of Mathematics. Second Series*, 163(1):265–299, 2006.

[14] A. Babin and A. Figotin. Nonlinear Maxwell equations in inhomogeneous media. *Communications in Mathematical Physics*, 241(2-3):519–581, 2003.

[15] I. Babuška. The finite element method with penalty. *Mathematics of Computation*, 27(122):221–228, 1973.

[16] I. Babuška and A. Miller. A feedback finite element method with a posteriori error estimation: Part i. the finite element method and some basic properties of the a posteriori error estimator. *Computer Methods in Applied Mechanics and Engineering*, 61(1):1–40, 1987.

[17] R. Banasiak and M. Soleimani. Shape based reconstruction of experimental data in 3D electrical capacitance tomography. *NDT & E International*, 43(3):241–249, 2010.

[18] H. Banks, V. Bokil, and N. Gibson. Analysis of stability and dispersion in a finite element method for Debye and Lorentz dispersive media. *Numerical Methods for Partial Differential Equations*, 25(4):885–917, 2009.

[19] H. Banks and N. Gibson. Electromagnetic inverse problems involving distributions of dielectric mechanisms and parameters. *Quarterly of Applied Mathematics*, 64(4):749–795, 2006.

[20] D. C. Barber and B. H. Brown. Applied potential tomography. *Journal of Physics E: Scientific Instruments*, 17(9):723, 1984.

[21] T. Barceló, D. Faraco, and A. Ruiz. Stability of Calderón inverse conductivity problem in the plane. *Journal de Mathématiques Pures et Appliquées*, 88(6):522–556, 2007.

[22] E. Barsoukov and J. R. Macdonald, editors. *Impedance Spectroscopy: Theory, Experiment, and Applications*. Wiley, second edition, 2018.

[23] J. Barzilai and J. M. Borwein. Two-point step size gradient methods. *IMA Journal of Numerical Analysis*, 8(1):141–148, 1988.

[24] M. Beck, M. Byars, T. Dyakowski, R. Waterfall, R. He, S. Wang, and W. Yang. Principles and industrial applications of electrical capacitance tomography. *Measurement and Control*, 30(7):197–200, 1997.

[25] C. Bernardi. Optimal Finite-Element Interpolation on Curved Domains. *SIAM Journal on Numerical Analysis*, 26(5):1212–1240, Oct. 1989.

[26] I. G. Bikker, S. Leonhardt, J. Bakker, and D. Gommers. Lung volume calculated from electrical impedance tomography in ICU patients at different PEEP levels. *Intensive Care Medicine*, 35(8):1362–1367, 2009.

[27] A. Binley and A. Kemna. DC resistivity and induced polarization methods. In *Hydrogeophysics*, pages 129–156. Springer, 2005.

[28] D. F. Bleil. Induced polarization: A method of geophysical prospecting. *Geophysics*, 18(3):636–661, 1953.

[29] L. Borcea. Electrical impedance tomography. *Inverse problems*, 18(6):R99, 2002.

[30] F. Braun, M. Proença, J. Solà, J.-P. Thiran, and A. Adler. A versatile noise performance metric for electrical impedance tomography algorithms. *IEEE Transactions on Biomedical Engineering*, 64(10):2321–2330, 2017.

[31] W. R. Breckon. *Image reconstruction in electrical impedance tomography*. PhD thesis, Oxford Polytechnic, 1990.

[32] S. Brenner and R. Scott. *The Mathematical Theory of Finite Element Methods*. Springer-Verlag, 2008.

[33] R. Brown and G. Uhlmann. Uniqueness in the inverse conductivity problem for non-smooth conductivities in two dimensions. *Communications in Partial Differential Equations*, 22(5-6):1009–1027, 1997.

[34] P. Brunet, R. Clément, and C. Bouvier. Monitoring soil water content and deficit using electrical resistivity tomography (ert)–a case study in the cevennes area, france. *Journal of Hydrology*, 380(1-2):146–153, 2010.

[35] A. L. Bukhgeim and G. Uhlmann. Recovering a potential from partial Cauchy data. *Communications in Partial Differential Equations*, 27(3-4):653–668, 2002.

[36] K. Busch, G. von Freymann, S. Linden, S. Mingaleev, L. Tkeshelashvili, and M. Wegener. Periodic nanostructures for photonics. *Physics Reports*, 444(3):101–202, 2007.

[37] A. P. Calderón. On an inverse boundary value problem. In *Seminar on Numerical Analysis and Its Applications to Continuum Physics*, pages 65–73, Rio de Janeiro, 1980.

[38] D. Calvetti, M. Dunlop, E. Somersalo, and A. Stuart. Iterative updating of model error for Bayesian inversion. *Inverse Problems*, 34(2):025008, 2018.

[39] D. Calvetti, S. Nakkireddy, and E. Somersalo. A Bayesian filtering approach to layer stripping for electrical impedance tomography. *Inverse Problems*, 36(5):055014, Apr. 2020.

[40] Z. Cao, L. Xu, W. Fan, and H. Wang. Electrical capacitance tomography for sensors of square cross sections using Calderon's method. *IEEE Transactions on Instrumentation and Measurement*, 60(3):900–907, 2010.

[41] Y. Capdeboscq, J. Fehrenbach, F. de Gournay, and O. Kavian. Imaging by modification: Numerical reconstruction of local conductivities from corresponding power density measurements. *SIAM Journal on Imaging Sciences*, 2(4):1003–1030, 2009.

[42] Y. Capdeboscq, H. Mamigonians, A. Sulaimalebbe, and V. Tshitoyan. Combining Radon transform and electrical capacitance tomography for a 2d+1 imaging device. *Inverse Problems.*, 34(10):104001, 2018.

[43] E. Cardarelli, G. De Donno, I. Oliveti, and C. Scatigno. Assessing the state of conservation of a masonry building through the combined use of electrical and seismic tomography. In *Near Surface Geoscience 2016-22nd European Meeting of Environmental and Engineering Geophysics*, volume 2016, pages cp–495.

European Association of Geoscientists & Engineers, 2016.

[44] A. Cauchy. Méthodes générales pour la résolution des systémes d'équations simultanées. *CR. Acad. Sci. Par.*, 25:536–538, 1847.

[45] M. Cessenat. *Mathematical Methods in Electromagnetism: Linear Theory and Applications*, volume 41. World Scientific, 1996.

[46] T. Chacón Rebollo, D. Franco Coronil, and F. Hecht. A Petrov-Galerkin multilayer discretization to second order elliptic boundary value problems. *Comput. Math. Appl.*, 77(12):3068–3086, 2019.

[47] D. K. L. Chakraborti and D. W. Selvamurthy. Clinical application of electrical impedance tomography in the present health scenario of India. *Journal of Physics: Conference Series*, 224:012069, 2010.

[48] C. E. Chavez, F. Alonzo-Atienza, and D. Álvarez. Avoiding the inverse crime in the inverse problem of electrocardiography: Estimating the shape and location of cardiac ischemia. In *Computing in Cardiology*. IEEE, 2013.

[49] M. Cheney, D. Isaacson, and J. C. Newell. Electrical impedance tomography. *SIAM review*, 41(1):85–101, 1999.

[50] K.-S. Cheng, D. Isaacson, J. Newell, and D. G. Gisser. Electrode models for electric current computed tomography. *IEEE Transactions on Biomedical Engineering*, 36(9):918–924, 1989.

[51] V. Chitturi and N. Farrukh. Spatial resolution in electrical impedance tomography: A topical review. *Journal of Electrical Bioimpedance*, 8(1):66–78, July 2017.

[52] P. M. Church, P. M. Wort, S. Gagnon, and J. E. McFee. Performance assessment of an electrical impedance tomography detector for mine-like objects. In *Detection and Remediation Technologies for Mines and Mine-like Targets VI*, volume 4394, pages 120–131. International Society for Optics and Photonics, 2001.

[53] P. G. Ciarlet. *The Finite Element Method for Elliptic Problems*. SIAM, 2002.

[54] B. W. Clark and D. C. Anderson. Finite element analysis in 3d using the penalty boundary method. In *International Design Engineering Technical Conferences and Computers and Information in Engineering Conference*, volume 36223, pages

289–297, 2002.

[55] B. W. Clark and D. C. Anderson. The penalty boundary method. *Finite Elements in Analysis and Design*, 39(5):387–401, Mar. 2003.

[56] D. Colton and R. Kress. *Inverse Acoustic and Electromagnetic Scattering Theory*. Springer, fourth edition, 2019.

[57] M. Crabb and W. Lionheart. The sensitivity in time domain EIT. In *Proceedings of the 18th International Conference on Biomedical Applications of Electrical Impedance Tomography*, page 11, 2017.

[58] Z. Cui, Q. Wang, Q. Xue, W. Fan, L. Zhang, Z. Cao, B. Sun, H. Wang, and W. Yang. A review on image reconstruction algorithms for electrical capacitance/resistance tomography. *Sensor Review*, 2016.

[59] W. Deabes, A. Sheta, K. E. Bouazza, and M. Abdelrahman. Application of electrical capacitance tomography for imaging conductive materials in industrial processes. *Journal of Sensors*, 2019.

[60] D. Dean, T. Ramanathan, D. Machado, and R. Sundararajan. Electrical impedance spectroscopy study of biological tissues. *Journal of electrostatics*, 66(3-4):165–177, 2008.

[61] S. Dholakia. *Assessment and Optimisation of the Pancreas Allograft*. PhD thesis, University of Oxford, 2019.

[62] E. Di Nezza, G. Palatucci, and E. Valdinoci. Hitchhiker's guide to the fractional Sobolev spaces. *Bulletin des sciences mathématiques*, 136(5):521–573, 2012.

[63] K. Dines and R. J. Lytle. Analysis of electrical conductivity imaging. *Geophysics*, 46(7):1025–1036, 1981.

[64] M. M. Dunlop and A. M. Stuart. The Bayesian formulation of EIT: Analysis and algorithms. *Inverse Problems & Imaging*, 10(4):1007, 2016.

[65] A. Elcrat and P. Bassanini. Mathematical theory of electromagnetism. *SIAM e-Lecture Notes*, 2:09001–1, 2009.

[66] L. C. Enfield and D. S. Holder. Electrical impedance tomography of brain function: Overview and technical considerations. *International Journal of Biomedical Imaging*, 4(2):199–200, 2002.

[67] T. S. England. Dielectric Properties of the Human Body for Wave-lengths in the 1–10 cm. Range. *Nature*, 166(4220):480–481, 1950.

[68] A. Ern and J.-L. Guermond. *Theory and Practice of Finite Elements*. Springer-Verlag, 2004.

[69] L. C. Evans. *Partial Differential Equations*. American Mathematical Society, second edition, 2010.

[70] L. C. Evans and R. F. Gariepy. *Measure Theory and Fine Properties of Functions*. Textbooks in Mathematics. CRC Press, 2015.

[71] W. Fang. Modeling of electrical capacitance tomography with the use of complete electrode model. *Measurement Science and Technology*, 27(10):105401, 2016.

[72] M. Flatscher, M. Neumayer, and T. Bretterklieber. Impedance matched electrical capacitance tomography system: Front-end design and system analysis. *Measurement Science and Technology*, 30(10):104002, 2019.

[73] G. Flores-Cosío, E. Herrera-López, M. Arellano-Plaza, A. Gschaedler-Mathis, M. Kirchmayr, and L. Amaya-Delgado. Application of dielectric spectroscopy to unravel the physiological state of microorganisms: current state, prospects and limits. *Applied Microbiology and Biotechnology*, 104:6101–6113, 2020.

[74] I. Frerichs, M. B. P. Amato, A. H. van Kaam, D. G. Tingay, Z. Zhao, B. Grychtol, M. Bodenstein, H. Gagnon, S. H. Böhm, E. Teschner, O. Stenqvist, T. Mauri, V. Torsani, L. Camporota, A. Schibler, G. K. Wolf, D. Gommers, S. Leonhardt, and A. Adler. Chest electrical impedance tomography examination, data analysis, terminology, clinical use and recommendations: Consensus statement of the translational EIT development study group. *Thorax*, 72(1):83–93, 2017.

[75] H. Fricke and S. Morse. The electric capacity of tumors of the breast. *The Journal of Cancer Research*, 10(3):340–376, 1926.

[76] C. Gabriel, S. Gabriel, and E. Corthout. The dielectric properties of biological tissues: I. literature survey. *Physics in Medicine and Biology*, 41(11):2231–2249, 1996.

[77] H. Garbaa, L. Jackowska-Strumillo, K. Grudzien, and A. Romanowski. Neural network approach to ECT inverse problem solving for estimation of gravitational

solids flow. In *2014 Federated Conference on Computer Science and Information Systems*, 2014.

[78] B. Gowry, A. B. Shahriman, and M. Paulraj. Electrical bio-impedance as a promising prognostic alternative in detecting breast cancer: A review. In *2nd International Conference on Biomedical Engineering*, 2015.

[79] T. Grätsch and K.-J. Bathe. A posteriori error estimation techniques in practical finite element analysis. *Computers & Structures*, 83(4-5):235–265, Jan. 2005.

[80] M. Grossi and B. Riccò. Electrical impedance spectroscopy (EIS) for biological analysis and food characterization: A review. *Journal of Sensors and Sensor Systems*, 6:303–325, 2017.

[81] Q. Guo, M. Ye, W. Yang, and Z. Liu. A machine learning approach for electrical capacitance tomography measurement of gas–solid fluidized beds. *AIChE Journal*, 65(6), 2019.

[82] J. Hadamard. *Lectures on Cauchy's Problem in Linear Partial Differential Equations*. Yale University Press, 1923.

[83] H. Hakula, N. Hyvönen, and T. Tuominen. On the hp-adaptive solution of complete electrode model forward problems of electrical impedance tomography. *Journal of computational and applied mathematics*, 236(18):4645–4659, 2012.

[84] R. J. Halter, A. Hartov, and K. D. Paulsen. A broadband high-frequency electrical impedance tomography system for breast imaging. *IEEE Transactions on Biomedical Engineering*, 55(2):650–659, 2008.

[85] J. Hanna, M. Bteich, Y. Tawk, A. H. Ramadan, B. Dia, F. A. Asadallah, A. Eid, R. Kanj, J. Costantine, and A. A. Eid. Noninvasive, wearable, and tunable electromagnetic multisensing system for continuous glucose monitoring, mimicking vasculature anatomy. *Science Advances*, 6(24):eaba5320, June 2020.

[86] A. M. Hassan and M. El-Shenawee. Review of electromagnetic techniques for breast cancer detection. *IEEE Reviews in Biomedical Engineering*, 4:103–118, 2011.

[87] F. Hecht. New development in FreeFem++. *Journal of Numerical Mathematics*, 20(3-4):251–265, 2012.

[88] D. S. Holder. *Electrical Impedance Tomography: Methods, History and Applications*. CRC Press, 2004.

[89] T. A. Hope and S. E. Iles. Technology review: The use of electrical impedance scanning in the detection of breast cancer. *Breast Cancer Research*, 6(2):69–74, 2004.

[90] L. Horesh, M. Schweiger, S. Arridge, and D. Holder. Large-scale non-linear 3D reconstruction algorithms for electrical impedance tomography of the human head. In *World Congress on Medical Physics and Biomedical Engineering*, pages 3862–3865. Springer, 2006.

[91] X. Hu and W. Yang. Planar capacitive sensors–designs and applications. *Sensor Review*, 30(1):24–39, 2010.

[92] S. M. Huang. Impedence Sensors – Dielectric Systems. In M. S. Beck and R. A. Williams, editors, *Process Tomography: Principles, Techniques and Applications*, pages 49–62. Butterworth-Heinemann, 1995.

[93] J. A. Huisman, E. Zimmermann, M. Kelter, Y. Zhao, T. H. Bukhary, and H. Vereecken. Advances in spectral electrical impedance tomography (EIT) for near-surface geophysical exploration. In *AGU Fall Meeting Abstracts*, volume 2016, pages NS13A–04, 2016.

[94] T. Ide, H. Isozaki, S. Nakata, S. Siltanen, and G. Uhlmann. Probing for electrical inclusions with complex spherical waves. *Communications on Pure and Applied Mathematics*, 60(10):1415–1442, 2007.

[95] D. Isaacson, J. L. Mueller, J. C. Newell, and S. Siltanen. Imaging cardiac activity by the D-bar method for electrical impedance tomography. *Physiological Measurement*, 27(5):S43, 2006.

[96] V. Isakov. *Inverse Problems for Partial Differential Equations*. Applied Mathematical Sciences. New York: Springer, 2006.

[97] I. Ismail, J. C. Gamio, S. F. A. Bukhari, and W. Q. Yang. Tomography for multi-phase flow measurement in the oil industry. *Flow Measurement and Instrumentation*, 16(2):145–155, 2005.

[98] J. D. Jackson. *Classical Electrodynamics*. John Wiley & Sons, 1975.

[99] G. Y. Jang, G. Ayoub, Y. E. Kim, T. I. Oh, C. R. Chung, G. Y. Suh, and E. J. Woo. Integrated EIT system for functional lung ventilation imaging. *Biomedical Engineering Online*, 18(1):83, 2019.

[100] A. J. Jaworski and T. Dyakowski. Application of electrical capacitance tomography for measurement of gas–solids flow characteristics in a pneumatic conveying system. *Measurement Science and Technology*, 12, 2001.

[101] B. Jin, T. Khan, and P. Maass. A reconstruction algorithm for electrical impedance tomography based on sparsity regularization. *International Journal for Numerical Methods in Engineering*, 89(3):337–353, 2012.

[102] J. Kaipio, V. Kolehmainen, E. Somersalo, and M. Vauhkonen. Statistical inversion and Monte Carlo sampling methods in electrical impedance tomography. *Inverse Problems*, 16(5):1487–1522, 2000.

[103] J. Kaipio and E. Somersalo. *Statistical and Computational Inverse Problems*. Springer-Verlag, 2005.

[104] Y. P. Kalmykov, W. T. Coffey, D. S. Crothers, and S. V. Titov. Microscopic models for dielectric relaxation in disordered systems. *Physical Review E*, 70(4):041103, 2004.

[105] K. C. Kao. *Dielectric Phenomena in Solids*. Elsevier, 2004.

[106] T.-J. Kao, D. Isaacson, J. C. Newell, and G. J. Saulnier. A 3D reconstruction algorithm for EIT using a handheld probe for breast cancer detection. *Physiological Measurement*, 27(5):S1–S11, 2006.

[107] T. Karacolak, E. C. Moreland, and E. Topsakal. Cole–Cole model for glucose-dependent dielectric properties of blood plasma for continuous glucose monitoring. *Microwave and Optical Technology Letters*, 55(5):1160–1164, 2013.

[108] O. Kavian. Lectures on parameter identification. de Gruyter, 2003.

[109] C. E. Kenig, J. Sjöstrand, and G. Uhlmann. The Calderón problem with partial data. *Annals of Mathematics. Second Series*, 165(2):567–591, 2007.

[110] S. Khan and L. Finkelstein. Mathematical modelling in measurement and instrumentation. *Measurement and Control*, 44(9):277–282, 2011.

[111] B. S. Kim, G. Boverman, J. C. Newell, G. J. Saulnier, and D. Isaacson. The complete electrode model for EIT in a mammography geometry. *Physiological measurement*, 28(7):S57–S69, July 2007.

[112] A. Kirsch. *An Introduction to the Mathematical Theory of Inverse Problems*. Springer, 2011.

[113] R. Kohn and M. Vogelius. Determining conductivity by boundary measurements. *Communications on Pure and Applied Mathematics*, 37(3):289–298, 1984.

[114] V. Kolehmainen, M. Lassas, and P. Ola. Electrical impedance tomography problem with inaccurately known boundary and contact impedances. *IEEE transactions on medical imaging*, 27(10):1404–1414, 2008.

[115] P. Kuchment. Mathematics of hybrid imaging: A brief review. Springer, 2012.

[116] L. D. Landau, J. Bell, M. Kearsley, L. Pitaevskii, E. Lifshitz, and J. Sykes. *Electrodynamics of Continuous Media*. Elsevier, 2013.

[117] R. Lee, S.-M. Lee, H. J. Kim, S. Y. Kim, M. Son, J. H. Song, K. Lkhamsuren, I. H. Park, I. H. Choi, Y. N. Park, J.-S. Shin, and K.-H. Yoo. Dielectric imaging for differentiation between cancer and inflammation in vivo. *Scientific Reports*, 2017.

[118] L. Lévy, P. Maurya, J. Byrdina, Sand Vandemeulebrouck, F. Sigmundsson, K. Árnason, T. Ricci, D. Deldicque, M. Roger, B. Gibert, et al. Electrical resistivity tomography and time-domain induced polarization field investigations of geothermal areas at krafla, iceland: comparison to borehole and laboratory frequency-domain electrical observations. *Geophysical Journal International*, 218(3):1469–1489, 2019.

[119] Y. Li and M. Soleimani. Imaging conductive materials with high frequency electrical capacitance tomography. *Measurement*, 46(9):3355–3361, 2013.

[120] W. R. B. Lionheart. EIT reconstruction algorithms: Pitfalls, challenges and recent developments. *Physiological Measurement*, 25(1):125–142, 2004.

[121] B. Liu, B. Yang, C. Xu, J. Xia, M. Dai, Z. Ji, F. You, X. Dong, X. Shi, and F. Fu. pyeit: A python based framework for electrical impedance tomography. *SoftwareX*, 7:304–308, 2018.

[122] S. Liu, W. Q. Yang, H. Wang, F. Jiang, and Y. Su. Investigation of square fluidized beds using capacitance tomography: Preliminary results. *Measurement Science and Technology*, 2001.

[123] M. H. Loke and R. D. Barker. Rapid least-squares inversion of apparent resistivity pseudosections by a quasi-newton method 1. *Geophysical prospecting*, 44(1):131–152, 1996.

[124] A. Malich, T. Boehm, M. Facius, M. G. Freesmeyer, M. Fleck, R. Anderson, and W. A. Kaiser. Differentiation of mammographically suspicious lesions: Evaluation of breast ultrasound, MRI mammography and electrical impedance scanning as adjunctive technologies in breast cancer detection. *Clinical Radiology*, 56(4):278–283, 2001.

[125] A. Malich, T. Böhm, M. Facius, M. Freessmeyer, M. Fleck, R. Anderson, and W. A. Kaiser. Additional value of electrical impedance scanning: Experience of 240 histologically-proven breast lesions. *European Journal of Cancer*, 37(18):2324–2330, 2001.

[126] A. Malich, T. Fritsch, R. Anderson, T. Boehm, M. G. Freesmeyer, M. Fleck, and W. A. Kaiser. Electrical impedance scanning for classifying suspicious breast lesions: First results. *European Radiology*, 10(10):1555–1561, 2000.

[127] N. Mandache. Exponential instability in an inverse problem for the Schrödinger equation. *Inverse Problems*, 17(5), 2001.

[128] S. Mansouri, T. Alhadidi, and M. B. Azouz. Breast cancer detection using low-frequency bioimpedance device. *Breast Cancer: Targets and Therapy*, 12:109, 2020.

[129] Q. Marashdeh, W. Warsito, L. Fan, and F. Teixeira. A nonlinear image reconstruction technique for ECT using a combined neural network approach. *Measurement Science and Technology*, 17(8):2097, 2006.

[130] G. Martín, R. Martín, M. Brieva, and L. Santamaría. Electrical impedance scanning in breast cancer imaging: Correlation with mammographic and histologic diagnosis. *European Radiology*, 12(6):1471–1478, 2002.

[131] B. Maury. Numerical analysis of a finite element/volume penalty method. *SIAM Journal on Numerical Analysis*, 47(2):1126–1148, 2009.

[132] J. C. Maxwell. VIII. A dynamical theory of the electromagnetic field. *Philosophical Transactions of the Royal Society of London*, (155):459–512, 1865.

[133] A. McEwan, A. Romsauerova, R. Yerworth, L. Horesh, R. Bayford, and D. Holder. Design and calibration of a compact multi-frequency EIT system for acute stroke imaging. *Physiological Measurement*, 27(5):S199–210, 2006.

[134] M. Melloul, A. Paz, G. Ohana, O. Laver, D. Michalevich, R. Koren, Y. Wolloch, and R. Gal. Double-phase 99mTc-Sestamibi scintimammography and trans-scan in diagnosing breast cancer. *Journal of Nuclear Medicine*, 40(3):376–380, 1999.

[135] P. Monk. *Finite Element Methods for Maxwell's Equations*. Oxford University Press, 2003.

[136] J. L. Mueller and S. Siltanen. *Linear and nonlinear inverse problems with practical applications*. SIAM, 2012.

[137] A. I. Nachman. Reconstructions from boundary measurements. *Annals of Mathematics. Second Series*, 128(3):531–576, 1988.

[138] S. Nagayasu, G. Uhlmann, and J.-N. Wang. A depth-dependent stability estimate in electrical impedance tomography. *Inverse Problems*, 25(7):075001, July 2009.

[139] E. Y. K. Ng, S. V. Sree, K. H. Ng, and G. Kaw. The use of tissue electrical characteristics for breast cancer detection: A perspective review. *Technology in Cancer Research & Treatment*, 7(4):295–308, 2008.

[140] G. K. Nicholls and C. Fox. Prior modeling and posterior sampling in impedance imaging. In *Bayesian Inference for Inverse Problems*, 1998.

[141] F. L. Pedrotti, L. M. Pedrotti, and L. S. Pedrotti. *Introduction to Optics*. Cambridge University Press, 2017.

[142] C. Perlet, M. Kessler, S. Lenington, H. Sittek, and M. Reiser. Electrical impedance measurement of the breast: Effect of hormonal changes associated with the menstrual cycle. *European Radiology*, 10(10):1550–1554, 2000.

[143] G. Piperno, E. H. Frei, and M. Moshitzky. Breast cancer screening by impedance measurements. *Frontiers of Medical and Biological Engineering*, 2(2):111–117,

1990.

[144] G. Piperno and S. Lenington. Breast electrical impedance and estrogen use in postmenopausal women. *Maturitas*, 41(1):17–22, 2002.

[145] N. Polydorides and W. R. Lionheart. A matlab toolkit for three-dimensional electrical impedance tomography: a contribution to the electrical impedance and diffuse optical reconstruction software project. *Measurement science and technology*, 13(12):1871, 2002.

[146] F. Poupaud and M. Remaki. Existence et unicité des solutions du système de Maxwell pour des milieux hétérogènes non réguliers. *Comptes Rendus de l'Académie des Sciences*, 330(2):99–103, 2000.

[147] C. Pradeep, Y. Ru, and S. Mylvaganam. Interface detection in pipe separators Using ECT: Performance with reduced number of sensing electrodes. In *2011 IEEE Sensors Applications Symposium*, pages 221–226, Feb. 2011.

[148] N. V. Ranade and D. C. Gharpure. Enhancing sharp features by locally relaxing regularization for reconstructed images in electrical impedance tomography. *Journal of Electrical Bioimpedance*, 10(1):2–13, 2019.

[149] Z. Ren. *Exploration of Medical Applications of Electrical Capacitance Tomography*. PhD thesis, The University of Manchester, 2015.

[150] A. E. Rittscher, A. Sulaimalebbe, Y. Capdeboscq, and J. Rittscher. Foreign object detection and quantification of fat content using a novel multiplexing electric field sensor. *arXiv preprint arXiv:1806.08596*, 2018.

[151] A. Romsauerova, A. McEwan, L. Horesh, R. Yerworth, R. H. Bayford, and D. S. Holder. Multi-frequency electrical impedance tomography (EIT) of the adult human head: Initial findings in brain tumours, arteriovenous malformations and chronic stroke, development of an analysis method and calibration. *Physiological Measurement*, 27(5):S147–161, 2006.

[152] Y. Ru, C. Pradeep, and S. Mylvaganam. Neural networks in electrical capacitance tomography (ECT)-based interface detection. *Measurement Science and Technology*, 22(10):104006, 2011.

[153] I. Saied and M. Meribout. Electronic hardware design of electrical capacitance tomography systems. *Philosophical Transactions of the Royal Society A*, 374(2070), 2016.

[154] B. K. P. Scaife. *Principles of Dielectrics*. Oxford University Press, 1998.

[155] H. P. Schwan. Electrical properties of tissue and cell suspensions. In *Advances in Biological and Medical Physics*, volume 5, pages 147–209. Elsevier, 1957.

[156] B. Schweizer. On Friedrichs inequality, Helmholtz decomposition, vector potentials, and the div-curl lemma. In *Trends in Applications of Mathematics to Mechanics*. Springer, 2018.

[157] J. K. Seo and E. J. Woo. *Nonlinear Inverse Problems in Imaging*. Wiley, 2012.

[158] J. Simon. Compact sets in the space $L^{\mathrm{p}}(0,T;B)$. *Annali di Matematica Pura ed Applicata. Series IV*, 146:65–96, 1987.

[159] V. G. Sirtoli, K. Morcelles, and P. Bertemes-Filho. Electrical properties of phantoms for mimicking breast tissue. In *39th Annual International Conference of the IEEE Engineering in Medicine and Biology Society (EMBC)*, pages 157–160, 2017.

[160] M. Soleimani and W. R. Lionheart. Nonlinear image reconstruction for electrical capacitance tomography using experimental data. *Measurement Science and Technology*, 16(10):1987, 2005.

[161] E. Somersalo, M. Cheney, and D. Isaacson. Existence and uniqueness for electrode models for electric current computed tomography. *SIAM Journal on Applied Mathematics*, 52(4):1023–1040, 1992.

[162] N. K. Soni, A. Hartov, C. Kogel, S. P. Poplack, and K. D. Paulsen. Multi-frequency electrical impedance tomography of the breast: New clinical results. *Physiological Measurement*, 25(1):301–314, 2004.

[163] M. Spitz. Local wellposedness of nonlinear Maxwell equations with perfectly conducting boundary conditions. *Journal of Differential Equations*, 266(8):5012–5063, 2019.

[164] S. Stefanesco, C. Schlumberger, and M. Schlumberger. Sur la distribution électrique potentielle autour d'une prise de terre ponctuelle dans un terrain à

couches horizontales, homogènes et isotropes. *Journal de Physique et le Radium*, 1(4):132–140, 1930.

[165] G. Steiner, H. Wegleiter, and D. Watzenig. A dual mode ultrasound and electrical capacitance process tomography sensor. In *IEEE Sensors*, 2005.

[166] A. Stojadinovic, O. Moskovitz, Z. Gallimidi, S. Fields, A. D. Brooks, R. Brem, R. N. Mucciola, M. Singh, M. Maniscalco-Theberge, H. E. Rockette, D. Gur, and C. D. Shriver. Prospective study of electrical impedance scanning for identifying young women at risk for breast cancer. *Breast Cancer Research and Treatment*, 97(2):179, 2006.

[167] A. Stojadinovic, A. Nissan, Z. Gallimidi, S. Lenington, W. Logan, M. Zuley, A. Yeshaya, M. Shimonov, M. Melloul, S. Fields, T. Allweis, R. Ginor, D. Gur, and C. D. Shriver. Electrical impedance scanning for the early detection of breast cancer in young women: Preliminary results of a multicenter prospective clinical trial. *Journal of Clinical Oncology*, 23(12):2703–2715, 2005.

[168] A. Stojadinovic, A. Nissan, C. D. Shriver, E. A. Mittendorf, M. D. Akin, V. Dickerson, S. Lenington, L. D. Platt, T. Stavros, S. R. Goldstein, O. Moskovitz, Z. Gallimidi, S. I. Fields, A. Yeshaya, T. M. Allweis, R. Manassa, I. Pappo, R. X. Ginor, R. B. D'Agostino, and D. Gur. Electrical impedance scanning as a new breast cancer risk stratification tool for young women. *Journal of Surgical Oncology*, 97(2):112–120, 2008.

[169] G. Strang and G. J. Fix. *An analysis of the finite element method.* Prentice-Hall, Inc., 1973.

[170] A. M. Stuart. Inverse problems: A Bayesian perspective. *Acta Numerica*, 19:451–559, 2010.

[171] B. Sun, S. Yue, Z. Cui, and H. Wang. A new linear back projection algorithm to electrical tomography based on measuring data decomposition. *Measurement Science and Technology*, 26(12):125402, 2015.

[172] A. Surowiec, S. Stuchly, J. Barr, and A. Swarup. Dielectric properties of breast carcinoma and the surrounding tissues. *IEEE Transactions on Biomedical Engineering*, 35(4):257–263, 1988.

[173] J. Sylvester and G. Uhlmann. A global uniqueness theorem for an inverse boundary value problem. *Annals of Mathematics.*, 125(1):153–169, 1987.

[174] L. Taghizadeh, A. Karimi, B. Stadlbauer, W. J. Weninger, E. Kaniusas, and C. Heitzinger. Bayesian inversion for electrical-impedance tomography in medical imaging using the nonlinear Poisson–Boltzmann equation. *Computer Methods in Applied Mechanics and Engineering*, 365:112959, June 2020.

[175] A. Tarantola. *Inverse Problem Theory and Methods for Model Parameter Estimation.* SIAM, 2005.

[176] A. Tarasov and K. Titov. On the use of the Cole–Cole equations in spectral induced polarization. *Geophysical Journal International*, 195(1):352–356, 2013.

[177] E. ToolBox. Electrical conductivity of elements and other materials. https://www.engineeringtoolbox.com/conductors-d_1381.html, 2008.

[178] E. ToolBox. Relative permittvity - the dielectric constant. https://www.engineeringtoolbox.com/relative-permittivity-d_1660.html, 2010.

[179] G. Uhlmann. Developments in inverse problems since Calderón's foundational paper. In *Harmonic Analysis and Partial Differential Equations.* University of Chicago Press, 1999.

[180] G. Uhlmann. 30 Years of Calderón's Problem. *Séminaire Laurent Schwartz — EDP et applications*, 2012.

[181] G. Uhlmann and J.-N. Wang. Reconstructing Discontinuities Using Complex Geometrical Optics Solutions. *SIAM Journal on Applied Mathematics*, 68(4):1026–1044, Jan. 2008.

[182] G. Uhlmann, J.-N. Wang, and C.-T. Wu. Reconstruction of inclusions in an elastic body. *Journal de Mathématiques Pures et Appliquées*, 91(6):569–582, June 2009.

[183] M. Vauhkonen. *Electrical impedance tomography and prior information.* PhD thesis, University of Kuopio, 1997.

[184] P. Vauhkonen, M. Vauhkonen, T. Savolainen, and J. Kaipio. Three-dimensional electrical impedance tomography based on the complete electrode model. *IEEE Transactions on Biomedical Engineering*, 46(9), 1999.

[185] P. J. Vauhkonen, M. Vauhkonen, T. Savolainen, and J. P. Kaipio. Three-dimensional electrical impedance tomography based on the complete electrode model. *IEEE Transactions on Biomedical Engineering*, 46(9):1150–1160, 1999.

[186] B. Wang, W. Zhang, Z. Huang, H. Ji, and H. Li. Modeling and optimal design of sensor for capacitively coupled electrical resistance tomography system. *Flow Measurement and Instrumentation*, 31:3–9, 2013.

[187] R. C. Waterfall, R. He, N. B. White, and C. M. Beck. Combustion imaging from electrical impedance measurements. *Measurement Science and Technology*, 7(3):369–374, 1996.

[188] D. Watzenig. Recovery of inclusion shape by statistical inversion of non-stationary tomographic measurement data. *International journal of information & systems sciences*, 2(4):469–483, 2006.

[189] D. Watzenig and C. Fox. A review of statistical modelling and inference for electrical capacitance tomography. *Measurement Science and Technology*, 20(5):052002, 2009.

[190] J. G. Webster. *Electrical impedance tomography*. Adam Hilger series on biomedical engineering. Hilger, Bristol, 1990.

[191] M. Weigand and A. Kemna. Relationship between cole–cole model parameters and spectral decomposition parameters derived from sip data. *Geophysical Journal International*, 205(3):1414–1419, 2016.

[192] A. Wersebe, K. Siegmann, U. Krainick, N. Fersis, U. Vogel, C. D. Claussen, and M. Müller-Schimpfle. Diagnostic Potential of Targeted Electrical Impedance Scanning in Classifying Suspicious Breast Lesions:. *Investigative Radiology*, 37(2):65–72, 2002.

[193] A. Wexler. Electrical impedance imaging in two and three dimensions. *Clinical Physics and Physiological Measurement*, 9(4A):29, 1988.

[194] A. Wexler, B. Fry, and M. R. Neuman. Impedance-computed tomography algorithm and system. *Applied Optics*, 24(23):3985–3992, 1985.

[195] R. B. White. Using electrical capacitance tomography to monitor gas voids in a packed bed of solids. *Measurement Science and Technology*, 13(12):1842–1847,

2002.

[196] P. M. Wort, P. M. Church, and S. Gagnon. Preliminary assessment of electrical impedance tomography technology to detect mine-like objects. In *Detection and Remediation Technologies for Mines and Mine-like Targets IV*, volume 3710, pages 895–905. International Society for Optics and Photonics, 1999.

[197] Z. Xu, F. Wu, X. Yang, and Y. Li. Measurement of gas-oil two-phase flow patterns by using CNN algorithm based on dual ECT sensors with venturi tube. *Sensors*, 20(4), 2020.

[198] X. Xun, J. Cao, B. Mallick, A. Maity, and R. J. Carroll. Parameter estimation of partial differential equation models. *Journal of the American Statistical Association*, 108(503):1009–1020, 2013.

[199] H. Yan, Y. F. Wang, Y. G. Zhou, and Y. H. Sun. 3D ECT reconstruction by an improved Landweber iteration algorithm. *Flow Measurement and Instrumentation*, 37:92–98, 2014.

[200] W. Yang. Design of electrical capacitance tomography sensors. *Measurement Science and Technology*, 21(4):042001, 2010.

[201] W. Yang, Y. Li, Z. Wu, D. Tsamakis, D. Learmonth, C.-G. Xie, S. Huang, C. Lenn, and A. Cutler. Multiphase flow measurement by electrical capacitance tomography. In *IEEE International Conference on Imaging Systems and Techniques*, 2011.

[202] W. Yang and L. Peng. Image reconstruction algorithms for electrical capacitance tomography. *Measurement Science and Technology*, 14(1):R1, 2002.

[203] W. Yang, D. Spink, T. York, and H. McCann. An image-reconstruction algorithm based on Landweber's iteration method for electrical-capacitance tomography. *Measurement Science and Technology*, 10(11):1065, 1999.

[204] W. Yang, A. Stott, M. Beck, and C. Xie. Development of capacitance tomographic imaging systems for oil pipeline measurements. *Review of Scientific Instruments*, 66(8):4326–4332, 1995.

[205] D.-S. Yoo. The dielectric properties of cancerous tissues in a nude mouse xenograft model. *Bioelectromagnetics*, 25(7):492–497, 2004.

[206] X. Zhang, W. Wang, G. Sze, D. Barber, and C. Chatwin. An image reconstruction algorithm for 3-D electrical impedance mammography. *IEEE Transactions on Medical Imaging*, 33(12):2223–2241, 2014.

[207] X.-J. Zhang, M.-Y. Chen, W. He, and C.-H. He. Modeling and simulation of open electrical impedance tomography. *International Journal of Applied Electromagnetics and Mechanics*, 33(1-2):713–720, 2010.

[208] X. Zhao, H. Zhuang, S.-C. Yoon, Y. Dong, W. Wang, and W. Zhao. Electrical impedance spectroscopy for quality assessment of meat and fish: A review on basic principles, measurement methods, and recent advances. *Journal of Food Quality*, 2017.

[209] E. Zimmermann, A. Kemna, J. Berwix, W. Glaas, and H. Vereecken. Eit measurement system with high phase accuracy for the imaging of spectral induced polarization properties of soils and sediments. *Measurement Science and Technology*, 19(9):094010, 2008.

[210] K. Zonge, J. Wynn, and S. Urquhart. Resistivity, induced polarization, and complex resistivity. In *Near-surface geophysics*, pages 265–300. 2005.

[211] Y. Zou and Z. Guo. A review of electrical impedance techniques for breast cancer detection. *Medical Engineering & Physics*, 25(2):79–90, 2003.

[212] J. Zuluaga-Gomez, N. Zerhouni, Z. A. Masry, C. Devalland, and C. Varnier. A survey of breast cancer screening techniques: Thermography and electrical impedance tomography. *Journal of Medical Engineering & Technology*, 43(5):305–322, 2019.